

**REGIONAL SITE RESPONSE AND UPPERMOST MANTLE SEISMIC
STRUCTURE OF CENTRAL AND EASTERN UNITED STATES**

A Dissertation presented to the Faculty of
the Graduate School at the University of Missouri-Columbia

In Partial Fulfillment of
the Requirements for the Degree Doctor of Philosophy

By

Rayan Yassminh

Dr. Eric Sandvol, Dissertation Supervisor

December 2019

The undersigned, appointed by the dean of the Graduate School, have examined the
dissertation entitled

**REGIONAL SITE RESPONSE AND UPPERMOST MANTLE SEISMIC
STRUCTURE OF CENTRAL AND EASTERN UNITED STATES**

presented by Rayan Yassminh, a candidate for the degree of Doctor of Philosophy,
and hereby certify that, in their opinion, it is worthy of acceptance.

Professor Eric Sandvol

Professor Francisco Gomez

Professor Mian Liu

Professor Brent Rosenblad

ACKNOWLEDGEMENTS

I would like to express my special appreciation to my advisor Professor Eric Sandvol. Thank you for encouraging me to grow as a research scientist. You have been a great mentor to me through these years.

I would also like to thank my committee members, Professors Paco Gomez, Mian Liu and Brent Rosenblad for serving as my committee members and for providing critical and helpful comments that led to major improvements in this dissertation. I would also like to express my gratitude to all the professors in the Department of Geological Sciences who offered me valuable courses and advice throughout graduate school.

Finally, I would like to express my deepest gratitude to my beloved family and friends for their love and support through all these years.

TABLE OF CONTENTS

ACKNOWLEDGEMENT.....	I
LIST OF FIGURES	VIII
ABSTRACT.....	XVIII
1 Chapter1: Introduction	1
1.1 Outlines of the dissertation.....	3
1.2 References	4
2 Chapter 2: Geological Background.....	5
2.1 Seismicity of the CEUS.....	8
2.2 Regional Seismic waves.....	9
2.3 Attenuation:.....	11
2.3.1 Scattering attenuation.....	12
2.3.2 Intrinsic attenuation	13
2.4 Site Response	15
2.4.1 The causes of the amplification	15
2.5 Temperature of the uppermost mantle:	18
2.6 Methods.....	21

2.6.1	HVSR Method	21
2.6.2	Travel time tomography.....	24
2.6.3	Reverse -Two Station Method	26
2.6.4	Modified Two -Station Method (TSM).	29
2.6.5	Resolution tomographic model.....	32
2.7	Figures.....	34
2.8	References	48
3	Chapter 3: Investigation of the Regional Site Response in the Central and Eastern United States	56
3.1	Introduction	57
3.2	Data and Methods.....	61
3.2.1	HVSR Method	62
3.2.2	RTS Method.....	64
3.3	Results	66
3.3.1	HVSR Method	66
3.3.2	RTS Method.....	68
3.4	Discussion	70
3.5	Conclusions	75
3.6	Data and Resources	76
3.7	Acknowledgments.....	77

3.8	Tables	77
3.9	Figures	78
3.10	Supplementary figures:	96
3.11	References	113
4	Chapter 4: Uppermost Mantle Seismic Structure beneath Central and Eastern United States	122
4.1	Introduction	123
4.1.1	Geology, Geophysical, and Geochemical Background:	126
4.2	Data and Methods.....	129
4.2.1	Sn attenuation.....	129
4.2.2	Q Tomography	130
4.2.3	Travel Time Tomography	132
4.2.4	Resolution models.....	133
4.3	Results	134
4.4	Discussion	136
4.4.1	Northern Mid-Continent	137
4.4.2	East Coast:	138
4.4.3	Central U.S.....	139
4.4.4	Southern CEUS.....	141
4.5	Temperature Implications	142

4.5.1	Temperature Model.....	143
4.5.2	Model resolution:	144
4.5.3	Results and discussion of the temperature model.....	145
4.6	Conclusions	150
4.7	Tables	152
4.8	Figures.....	153
4.9	Supplementary Figures.....	162
4.10	References	172
5	Chapter 5: Investigation of Local & Regional Site Response in the Central U.S.	
	189	
5.1	Introduction	190
5.2	Geological and Geophysical background of CUSSO	193
5.3	Observed Seismic Records.....	195
5.3.1	Data analysis.....	195
5.3.2	Magnitude effect	196
5.3.3	Azimuthal effect.....	197
5.4	Synthetic data	197
5.4.1	Local Model	198
5.4.2	Velocity effects	199
5.4.3	Simplified Local Model ($f < 13$ Hz).....	199

5.4.4	Regional models:	200
5.4.5	Basin effects:.....	200
5.5	Discussion	201
5.6	Conclusions	207
5.7	Tables	208
5.8	Figures.....	210
5.9	Supplement figures.....	228
5.10	References	230
6	Chapter 6: Conclusions:	240
	Vita.....	242

LIST OF FIGURES

Figure 2.1. The study region with the main geological provinces, basins, and glaciation limits.....	34
Figure 2.2 The seismicity map of CEUS. The orange circles are the size of the earthquakes recorded between 1980-2015 in addition to the historical events. The blue triangles are the USArray seismic stations.	35
Figure 2.3 The bars are oriented parallel to σ Hmax; the thin lines span the 95% confidence interval. Each bar is divided into 5 segments, coloured as the 0.025, 0.16, 0.5, 0.84 and 0.975 quantiles of $A\phi$ (that is, ± 2 standard deviation range) (<i>Levandowski et al., 2018</i>).....	36
Figure 2.4 Regional seismic wave arrivals with time and distances. Pn, Snand Lg are regional phases while Pg and Sg are local phases added as a reference (Borman P. (Ed.)2002).	37
Figure 2.5. Example of Sn attenuation in eastern U.S.. Yellow star is the seismic events. The red array varies based on back-azimuth and the green array varies based on the distance from the events.....	38
Figure 2.6. Sketch simplifies the local site effect on the seismic waves. Thick black line is the fault. Yellow star is the event.....	39
Figure 2.7. Mineral composition and phase transformations in the mantle after (Helffrich and Wood, 2001; Kennedy and Kennedy, 1976; Stixrude and Lithgow-Bertelloni, 2007)	40

Figure 2.8. Sketch shows the horizontal and vertical motion in the bedrock and sediments. 41

Figure 2.9. Sketch shows the Sn ray-path: two crustal arms and the uppermost mantle arm. This sketch shows tomographic cells as well..... 42

Figure 2.10. The geometry for the application of Reverse Two Station Method (RTS) for Q measurement **Figure 2.11.** The geometry for the application of TSM for Q measurement. 43

Figure 2.11. Example of TSM. (a) location of the event and the two stations L56A and Q58A. (b) the spectra of the Sn phases and noise..... 46

Figure 2.12 Checker board of Pn travel time tomography. 47

Figure 3.1. Map of the Central and Eastern U.S. (CEUS), including the main geologic provinces and the limits of continental glaciers from the last major ice ages..... 78

Figure 3.2. (a) The fundamental frequency (F_0) from ambient noise Noise_HVSR, (b) the fundamental frequency (F_0) from earthquake records EQ_HVSR. Note the high F_0 values in the Appalachians (red) and low F_0 values in the coastal plains (blue)..... 79

Figure 3.3. (a) The maximum peak HVSR values from ambient noise (Noise_HVSR), (b) The maximum peak HVSR values from earthquake records (EQ_HVSR). Note the high HVSR values (red) in regions covered in the past by glaciation..... 80

Figure 3.4. HVSR values recorded at four stations. Station (triangle) and event (star) locations are shown at the top of (a), (b), (c), and (d), respectively, with

solid lines representing path. In the HVSR plots at bottom, all lines represent a horizontal to vertical spectral ratio recorded at a particular station, with dashed lines representing the HVSRs of earthquake records and solid lines representing the HVSRs of ambient noise. Note the difference in peak frequencies and amplitudes between the ambient noise and earthquake records. 81

Figure 3.5. (a) The probability density of HVSR (EQ_HVSR/Noise_HVSR) and F_0 (EQ_HVSR/Noise_HVSR). The gray circles represent F_0 and the black triangles represent HVSR. (b) F_0 ratios versus frequency band 0.5-10Hz. (c) HVSR ratios versus frequency band 0.5-10Hz. $F_0 < 2.5$ Hz shows a high discrepancy between EQ_HVSR and Noise_HVSR for both F_0 and HVSR. 82

Figure 3.6. A simplified geologic map of Wisconsin and its subsurface geology. Note that the HVSR (Noise) is high in the north (metamorphic rocks) compared with the south (sedimentary rocks; see Fig. S4 for F_0 map)..... 83

Figure 3.7.(a) Location of station 060A (triangle) and path and location of two recorded events (stars). (b) H/V spectra (dashed lines) of seismic events recorded at 060A (shown in a) and H/V spectra (solid lines) of ambient noise. 84

Figure 3.8. The vertical and horizontal RTS amplification of central frequency 1.0 Hz versus RTS amplification of the central frequencies: 2.0Hz, 3.0 Hz, 4.0 Hz. The color of the circles represents the topographic locations: black=basin, green= shield, red=mountain, and blue= uplift. (g) and (h)

shows the horizontal and vertical RTS amplification versus four frequency bands using the boxplots..... 85

Figure 3.9. (a) Horizontal amplification values resulting from the RTS method at a central frequency of 1.0 Hz. (b) Horizontal amplification at a central frequency of 3.0 Hz. (see Fig. S5 for results at central frequencies of 2.0 and 4.0 Hz). Note that positive amplification (red) appears to correlate with basins. 86

Figure 3.10. (a) Vertical amplification values resulting from the RTS method at a central frequency of 1.0 Hz. (b) Vertical amplification values resulting from the RTS method at a central frequency of 3.0 Hz. Note the positive amplification (red) in the basins (see Fig. S6 for results at central frequencies of 2.0 and 4.0 Hz)...... 87

Figure 3.11. Horizontal to vertical ratio of amplification at central frequencies of 1.0,2.0,3.0 and 4.0 Hz. The H/Z ratio is high in the basins (red)..... 88

Figure 3.12. A comparison of HVSR and RTS results at central frequencies of 1.0 and 3.0 Hz. black circles represent positive correlations, while gray circles show no correlation. Correlation between HVSR and RTS is seen to increase in basins (Illinois and Michigan) at higher frequencies (see the electronic supplements figure S9). 89

Figure 3.13. A comparison of sediment thickness and RTS results at central frequencies of 1.0 and 2.0 Hz. Black circles represent positive correlation while gray circles show a negative correlation. Note that a positive correlation occurs for sediment thicknesses ≤ 4 km while negative correlation

is found for sediment thicknesses >4 km (see Fig. S11 for results at central frequencies of 3.0 and 4 Hz). 90

Figure 3.14. Maps representing V_{s30m} measurements in the northern Mississippi Embayment. In all maps, varying shades of gray represent V_{s30m} measurements based on topographic slope, with dark gray representing low V_{s30m} and light gray to white representing high V_{s30m} . Contours (in meters) represent sediment thickness values (Dart, 1992; Dart and Swolfs, 1998). In (a), triangles represent measured V_{s30m} , with warm colors representing low V_{s30m} and cool colors representing high V_{s30m} . (b) Circles represent HVSR values calculated in this study, with warm colors representing high HVSR and cool colors representing low HVSR. (c) $V_s(R/Z)$ is the shallow velocity model from Ni et al. (2014). (d) and (e) show the vertical and horizontal RTS site response values calculated in this study, respectively, with warm colors generally representing amplification and cool colors generally representing deamplification. Note the negative correlation between the (e) horizontal RTS and the (c) $V_s(R/Z)$ (see Fig. S13 for comparisons between V_{s30m} , sediment thickness and the noise fundamental frequency F_0 , Fig. S14 for comparisons between V_{s30m} , sediment thickness, and the HVSR and F_0 of EQ/NOISE)..... 91

Figure 3.15. (a) Shallow V_s versus HVSR, (b) shallow V_s versus fundamental frequency F_0 , (c) Shallow V_s versus HVSR at a central frequency of 1.0 Hz (d), shallow V_s versus HVSR at a central frequency of 2.0 Hz, (e) shallow V_s versus horizontal RTS amplification at a central frequency of 1.0 Hz, (f)

shallow Vs versus horizontal RTS amplification at a central frequency of 2.0 Hz, (g) shallow Vs versus vertical RTS amplification at a central frequency of 1.0 Hz, (h) shallow Vs versus vertical RTS amplification at a central frequency of 2.0 Hz (see Figs. S16 and S17 for shallow Vs versus all the frequency bands of HVSR and RTS). 93

Figure 3.16. Shallow Vs versus HVSR at four frequency bands: (a) 0.5-1.5 Hz, (b) 1.5-2.5 Hz, (c) 2.5-3.5 Hz, and (d) 3.5-10 Hz. Note that HVSR has a negative trend with velocity for lower frequencies. 94

Figure 3.17. Shallow Vs versus horizontal RTS amplification and vertical RTS amplification at four frequency bands 1.0 Hz, 2.0Hz, 3.0Hz, and 4.0 Hz. 95

Figure 4.1 Central and Eastern U.S. crustal and physiographic provinces. Dashed red lines represent the crustal provinces. Green lines represent the rift zones (Whitmeyer & Karlstrom, 2007). NMSZ is New Madrid Seismic Zone. 153

Figure 4.2. Checkerboard test of QSn resulted from the modified tomographic code. Synthetic data was generated with 30% perturbations. 154

Figure 4.3(a) Lateral variations in Pn wave velocity beneath the continental United States. Notice the negative anomaly in northern Reelfoot Rift (RFR), Illinois basin, beneath New England and the positive anomaly beneath north western CEUS, South Carolina and NMSZ..... 155

Figure 4.4 (a) Lateral variations in Sn wave velocity beneath central and eastern continental United States, Notice the negative anomaly beneath Illinois basin

and southern Reelfoot Rift (RFR), and notice the positive anomaly beneath NMSZ and South Caroli..... 156

Figure 4.5 (a) Lateral variations of the velocity ratio (V_{Pn}/V_{Sn}) beneath the continental United States. Notice the low V_{Pn}/V_{Sn} ratio beneath NMSZ and the high V_{Pn}/V_{Sn} ratio beneath southern the Appalachian (Northern Georgia) and center Illinois. (b) Lateral standard deviation of the bootstrapped ratio..... 157

Figure 4.6. Lateral variations in S_n attenuation (attenuation = $Q-1$) for frequency 1 Hz beneath the CEUS. Notice the low Q beneath New England, Mississippi embayment, and central and southern Georgia 158

Figure 4.7 Flow chart represents the grid search algorithm applied to estimating the temperature of the uppermost mantle. 159

Figure 4.8. (a) the standard deviation (std) of the bootstrap result of the (TP_{nSn}) temperature model. (b) the mean of the bootstrap result (TP_{nSn}) of the temperature model. (c) the standard deviation (std) of the bootstrap result of the composition model. 160

Figure 4.9. Upper most mantle temperature variation beneath CEUS for (a) Temperature resulted from inverting both S_n and P_n velocity, (b) Temperature resulted from inverting S_n velocity, (c) Temperature resulted from inverting P_n velocity. Notice the high temperature. 161

Figure 5.1 CUSSO location and geological uintes beneath CUSSO..... 210

Figure 5.2 (a) The map shows locations of the analyzed earthquakes (stars), CUSSO (triangle), and the geological units surrounding the CUSSO. Graphs

indicate attributes of the earthquakes used: (b) magnitude, (c) distance, (d) depth, and (e) back-azimuth.....	211
Figure 5.3 (a) The horizontal to vertical ratio of Tf30m, (b) the horizontal to vertical ratio of TF270m, (d) the vertical TF of the upper 30m, (e) the vertical TF of the upper 270m, (g) the horizontal TF of the upper 30m, and (g) the horizontal TF of Upper 270m, (c,f,i) the HVSR at the earth surface, at depth 30m and at 270m, respectively.	212
Figure 5.4(a-b) Variation of the amplitude of the TF270 and the F0 with distance. (c-d) Variation of the amplitude of TF270m and F0 with the back-azimuth. (e-f) The amplitude of the TF30m and the F0 versus the distances in km. (g-h) Amplitude of TF30m and F0.....	213
Figure 5.5(a) HVSR of the events where each line represents an event and the solid black line represents the averaged HVSR. (b) The maximum amplitude of HVSR versus the distance (km), (c) F0 versus the distance (km). (d) The maximum amplitude HVSR versus the back azimuth.....	214
Figure 5.6 A sketch of the local model. The red star represents the earthquake location, blue squares are the vertical array of virtual seismometers, blue and green lines represent the dipping bedrock models, and the red line represent the wavy bedrock model.....	215
Figure 5.7. (a) Results of the 2D simulation models. (b) first model, (c) second model, (d) third model, (e) fourth model and (f) fifth model.	216
Figure 5.8Simplified local models (three-layer local model). (a) The horizontal amplification to vertical amplification ratio, (b) vertical amplification,	

(c)horizontal amplification, (c) HVSR at the earth surface, and (d) velocity models.....	217
Figure 5.9 The regional model sketch conducted to test the basin effect on regional seismic waves, where the yellow star represents the earthquake location. Points are the two arrays of virtual seismometers, yellow is the surface array and the black is the bedrock.....	218
Figure 5.10 The three regional models: model1, model2, and model3; (a-c) shows the HVSR, (d-f) vertical amplification / horizontal amplification ratio, (g-h) vertical amplification (j-k) show the horizontal amplification, and (m) the velocity models simulated.	219
Figure 5.11 The Model1, (a) sketch of the upper 3km of the regional model1, (b) horizontal amplification versus distance, (c) F0 of horizontal amplification versus distance, (d) vertical amplification versus distance, (e) F0 of vertical amplification versus distance	220
Figure 5.12 The Model2, (a) a sketch of the upper 3km of the regional model2, (b) horizontal amplification versus distance, (c) F0 of horizontal amplification versus distance, (d) vertical amplification versus distance, (e) F0 of vertical amplification versus distance.....	221
Figure 5.13 The Model3, (a) a sketch of the upper 3km of the regional model3, (b) horizontal amplification versus distance, (c) F0 of horizontal amplification versus distance, (d) vertical amplification versus distance, (e) F0 of vertical amplification versus distance.....	222

Figure 5.14 ABTX seismic station. (a) HVSR of the events shown in map (b) and the colors represent the events. (c) HVSR versus distance (km), (d) F0 versus distance (km). (e) HVSR versus back-azimuth (degrees), and (f) F0 versus back-azimuth (degrees)..... 223

Figure 5.15BGNE seismic station. (a) HVSR of the events shown in map (b) and the colors represent the events. (c) HVSR versus distance (km), (d) F0 versus distance (km). (e) HVSR versus back-azimuth (degrees), and (f) F0 versus backazimuth (degrees). 224

Figure 5.16 KCSC seismic station. (a) HVSR of the events shown in map (b) and the colors represent the events. (c) HVSR versus distance (km), (d) F0 versus distance (km). (e) HVSR versus back-azimuth (degrees), and (f) F0 versus backazimuth (degrees). 225

Figure 5.17 Variation of the incidence angle of P and S waves with depth and distance of the earthquakes using TauP software. (a-d) The incidence angle of the smallest ray parameter, and (e-h) is the incidence angle of the highest ray parameter. 226

Figure 5.18 (a) HVSR of local and regional events recorded in CUSSO. (b) HVSR of regional events. The black solid line is the average HVSR and the blue solid line is the weighed-average HVSR. Notice the shift in the fundamental frequency from 0.8 Hz to 0.2 Hz 227

ABSTRACT

This dissertation examines seismological data from regional earthquake sources in order to examine the seismological character of the crust and uppermost mantle in central and eastern United States. Firstly, site amplification of regional high-frequency Lg seismic phases is estimated using a Reverse-Two Station (RTS) method. RTS results show topography and sediment thickness are likely to affect amplification and both factors likely frequency-dependent. There is a negative correlation between the RTS-measured amplification and shallow shear-wave velocity. It appears that both regional topography (i.e., long-wavelength topography) and deeper subsurface seismic structures (basins and sediments) have a large impact on site amplification. Subsequently, Pn and Sn travel time tomography is used to estimate the uppermost mantle P-wave (Pn) velocity, S-wave (Sn) velocity, and the velocity ratio (V_{Pn}/V_{Sn}). In addition to velocity, effective attenuation of Sn phase (Q^{-1}_{Sn}) is also measured. The result shows regions of high velocity such as southern Georgia, eastern South Carolina and NMSZ and low Q_{Sn} values. The V_{Pn}/V_{Sn} ratio shows values higher than the average in regions such as the Mississippi Embayment, New England, and south Appalachian. V_{Pn}/V_{Sn} ratios are lower than the average in regions such as northwestern CEUS, South Georgia and eastern Texas. We estimated the uppermost mantle temperature by applying a constrained grid-search algorithm includes the observed V_{Sn} , V_{Pn} and Q_{Sn} with the calculated velocities of specific compositional models. The uppermost mantle temperature result, ~300-500 C, beneath the northern mid-continent, and the highest temperature, 1100 C, beneath New England

1 Chapter1: Introduction

This dissertation uses seismological data from regional earthquake sources in order to examine the seismological character of the crust and uppermost mantle in central and eastern United States. Specifically, the research investigates amplification and attenuation of seismic energy associated with different regional seismic phases, including Lg and Sn.

Prior seismological studies of the central and eastern United States (CEUS) have indicated that the lithosphere in this region to be colder and older than the lithosphere beneath the western U.S. (e.g., Bickford et al., 1986). These lithospheric characteristics allowed the seismic waves to propagate farther distances with higher amplitude and higher frequencies. This phenomenon requires different considerations for the earthquake hazard of the CEUS compared with the western U.S. (or other active plate boundary region). This is further explored herein using site response and further seismological characterization of the uppermost mantle in the CEUS.

Regional site response results from the interaction between the regional seismic waves and the subsurface geology. With the few numbers of recorded earthquakes and seismic stations, detailed seismic studies were limited. The relationship among distance, magnitude and site response was estimated using the stochastic (Hanks, 1979; Boore, 1983, 2003; Atkinson and Boore, 1995, 1997; Atkinson and Silva, 2000). Proxies, such as the time-averaged shear- wave velocity in the upper 30 meters (V_{s30m}), were applied in regions with few large earthquakes; however, deploying the USArray Transportable array (TA) between 2010-2013 provides us with the data required to test multiple theories in this vital region.

Investigation of the lithospheric structure also provides insight into its evolution. Physical and chemical characteristics of the lithosphere, along with the temperature variation, are important constraints for understanding of the deformation, strength, stress, and thickness of the uppermost mantle. Over the last decades the large-scale upper mantle has been well studied using several techniques (Sigloch, 2008, 2011; Obrebski et al., 2011; Porritt et al., 2014; Schmandt and Lin, 2014; Schaeffer and Lebedev, 2014; Yuan and Romanowicz, 2010; Yuan et al., 2011; Buehler & Shearer, 2017; Zhang et al., 2009). However, the detailed uppermost mantle seismic structure (Moho to the low velocity zone) has not been studied in the CEUS using both Sn and Pn regional seismic phases, simultaneously, which provides more information on the nature of the lithosphere than either phase, alone.

The scientific questions I am addressing in this dissertation are the following:

- (1) How does the subsurface geology affect the regional seismic waves?
- (2) What factors impact the interaction between the regional seismic waves and the subsurface geology?
- (3) How well do tectonic boundaries in the CEUS correlate with the observed seismic anomalies?
- (4) Does partial melt exist beneath CEUS?
- (5) Can a thermal and compositional model using the resulting geophysical parameters?

1.1 Outlines of the dissertation.

This dissertation is structured as follows:

- **Chapter 2** presents a general background of the main subjects discussed in this research: attenuation, intrinsic and scattering, site response, and regional seismic waves. In addition, I provide general geological, seismic, and geophysical background for the Central and Eastern United States. Next, I deliver a summary for the methods we applied with clarification examples.
- **Chapter 3** reports the investigation on the regional site response in central and eastern United States by applying non-conventional method such as Reverse-Two station method and compare our results with Horizontal to Vertical Spectral Ratio method (HVSR) and discussed the results based on the geological structure of the regions.
- **Chapter 4** presents my seismic structure model of the uppermost mantle and the temperature model beneath CEUS. I apply travel time tomography to estimate the uppermost mantle velocities of the Pn and Sn phases. Additionally, I measure the attenuation of the Sn phase. The combined seismic velocity structure and seismic attenuation allow modeling the temperature of the uppermost mantle.
- **Chapter 5** presents a site response focused on the midcontinent region of the Central U.S. using local and regional seismic phases.
- **Chapter 6** concludes the dissertation with a perspective of the broader scientific impact and directions for possible future inquiry.

1.2 References

- Buehler, J.S. and Shearer, P.M. (2017). Uppermost mantle seismic velocity structure beneath USArray, *J. Geophys. Res. Solid Earth* **122**, 436–48.
- Obrebski, M., Allen, R.M., Pollitz, F. and Hung, S.-H. (2011). Lithosphere–asthenosphere interaction beneath the western United States from the joint inversion of body-wave traveltimes and surface-wave phase velocities, *Geophys. J. Int.* **185**, 1003–21.
- Porritt, R.W., Allen, R.M. and Pollitz, F.F. (2014). Seismic imaging east of the Rocky Mountains with USArray, *Earth Planet. Sci. Lett.* **402**, 16–25.
- Schaeffer, A.J. and Lebedev, S. (2014). Imaging the North American continent using waveform inversion of global and USArray data, *Earth Planet. Sci. Lett.* **402**, 26–41.
- Schmandt, B. and Lin, F. (2014). P and S wave tomography of the mantle beneath the United States, *Geophys. Res. Lett.* **41**, 6342–49.
- Yuan, H. and Romanowicz, B. (2010). Lithospheric layering in the North American craton, *Nature* **466**, 1063–68.
- Yuan, H., Romanowicz, B., Fischer, K.M. and Abt, D. (2011). 3-D shear wave radially and azimuthally anisotropic velocity model of the North American upper mantle, *Geophys. J. Int.* **184**, 1237–60.
- Zhang, Q., Sandvol, E. and Liu, M. (2009). Lithospheric velocity structure of the New Madrid Seismic Zone: A joint teleseismic and local P tomographic study, *Geophys. Res. Lett.* **36**, 1–6

2 Chapter 2: Geological Background

The Central and Eastern United States (CEUS) was formed as a result of the collision and accretion events that took place from 1.9 to 1.7 Ga (Bickford et al., 1986). The region is dominated by the Appalachian-Ouachita orogenic belt (450–350 Ma) which separates the North America Craton from the Atlantic Coastal Plain to the east and the Gulf Coastal Plain to the south. In addition to preserved convergent boundaries, there are divergent belts such as the Mid Continental Rift system (MCR) (e.g. Hinze et al. 1970), the Reelfoot Rift (e.g. Ervin and McGinnis 1975) and the postulated East Continental Rift Complex (ECRC) (e.g. Stark, 1997). The Central United States is characterized generally as a platform, mantled by Paleozoic and Mesozoic sedimentary rocks, with limited tectonic activity since the Paleozoic. The sedimentary rocks range in thickness from zero meters in the region of the Ozark Dome to more than 3,000 meters in the region of the Denver Basin (MOSS 1936) with younger sediments restricted to river valleys and glacial deposits (Baquer and Mitchell 1998).

The core of the Appalachian-Ouachita orogenic belt is composed of Precambrian and Cambrian metamorphosed rocks with igneous intrusions. The crystalline core of the Appalachians is comprised of metamorphic plutonic rocks and underlain the Blue Ridge and Piedmont Plateau in the south while its northern part is composed of metamorphosed Proterozoic sedimentary and volcanic rocks.

The St. Francis Mountains, which consist of Precambrian igneous rock mountains surrounded by Paleozoic sedimentary rock, are one of the oldest igneous exposures in North America at 1.485 billion years old (Hildenbrand et al., 1996).

Quaternary and Pleistocene glaciation (2.58 to present) has affected large parts of the North American continent (Gradstein et al. 2004). The glacial deposits are a complex mixture of sediment types such as till and loess. They are often also comprised of silt, sand, and gravel in addition to clay. These glacial depositions cover most of the northern CEUS with variable thicknesses. Several different glacial periods occurred during the Pleistocene. The most recent period of glaciation (17,000-18,000) covered a large portion of North America extending south to the middle of Missouri and southern Illinois while the oldest glaciation period covered less land southwards (Fig. 1).

CEUS basins are mostly of Paleozoic and Mesozoic age and are filled with carbonate and evaporate rocks. Major basins include the Michigan basin, Illinois basin and the Appalachian basin, filled with evaporate rocks. The Michigan basin is about 250 kilometers wide and 5 kilometers deep. The rocks of the basin include Cambrian-Ordovician sandstones and carbonate rocks around the margins and at depth. A relatively thin veneer of Jurassic sediments is found at the center of the basin. The basement is made up of Precambrian rocks (Blakey and Ron, 2007). The Illinois basin is an elongated structure containing up to 4.5 km of sedimentary rock ranging from Cambrian to Pennsylvanian age. The basin extends approximately 400 miles northwest-southeast and 200 miles southwest-northeast. The basement rocks below the sedimentary rocks of the basin are Proterozoic granites and rhyolites of the Eastern Granite–Rhyolite Province, which date to 1.55 Ga (Van-Schmuss et al. 1996, 2007). Finally, the Appalachian basin was formed as a Paleozoic foreland depocenter extending 1730 km from the northeast to the southeast. The eastern part of the

Appalachian basin is comprised of the Valley and Ridge Province, an area featuring a series of large folds of sedimentary rock. These folds formed during the Alleghenian Orogeny of the Late Paleozoic.

West of the Valley and Ridge Province is the Appalachian Plateau, a region underlain by nearly flat-lying sedimentary rock consisting of a mixture of Cambrian, Ordovician, and Middle Silurian aged rock composed of shale, siltstone, and sandstone with an average thickness of approximately 6 km. Throughout the Appalachian Plateau there is a thick sequence of coal-bearing sedimentary rocks of Late Mississippian to Permian age. The deepest part of the Appalachian basin lies in eastern Pennsylvania, with sedimentary rock thicknesses up to 13 km. This sedimentary rock thickness decreases to a few thousands meter at the western margin of the basin (George and Fisher ed. 1970).

The Mississippi embayment is a large Mesozoic sag basin located above the Reelfoot Rift basin and the Black Warrior and Arkoma foreland basins (Coleman et al. 2012). Within the Mississippi embayment, sediments range from Jurassic to Quaternary age and have a maximum thickness of about 1000 m in the southern part of the basin. The Mississippi embayment is composed of gravel, sand, silt, clay, lignite, marl, chalk, and limestone. The Cretaceous, Tertiary, and Quaternary deposits include numerous aquifers, most of which contain fresh water at shallow to moderate depths (Gushing et al. 1968).

2.1 Seismicity of the CEUS

Although CEUS earthquakes are not the largest earthquakes in North America, they cause more wide spread damage than many other earthquakes in the western U.S. (Johnston, 1989). The seismicity source in the CEUS is intraplate seismicity and is still not well understood. For example, in 1811-1812, three of the largest earthquakes in the CEUS occurred in the New Madrid Seismic Zone (NMSZ). Paleoseismic studies have shown that clusters of events occurred in the NMSZ between 900 A. D. ± 100 years and 1450 A.D. ± 150 (Tuttle et al., 2005). To the north of NMSZ and along the southern Illinois–Indiana border, the Wabash Valley seismic zone (WVSZ) generated 9 November 1968 mb 5.5 earthquake. Other earthquakes include the 1987 mb 5.0 Olney, Illinois, (Hamburger and Rupp, 1988). Paleoseismological evidence points to several large ($M > 6$) events in the region over the past few thousand years (Obermeier, 1998; Obermeier et al., 1991). The eastern Tennessee seismic zone (ETSZ) is second to the NMSZ in the number of earthquakes in the CEUS, however, it did not generate earthquakes larger than M_w 4.8 in recent times (Powell et al., 1994). Paleoseismic studies show evidence for the occurrence of three prehistoric earthquakes ($M_w \geq 6$) in the ETSZ during the last 25,000 years (Warrell et al. 2017). In the South Carolina seismic zone the 1886 Charleston destructive 7.6 M_w was a particularly famous earthquake. Paleoseismic studies found at least five large prehistoric earthquakes ($> 5.5 M_w$) over the past 5,000 years (Amick and Gelinas, 1991). In more northern states, other earthquakes include the 5.2 M_l in the Blue Mountain Lake region and the Southern Quebec region had earthquakes up to magnitude 7 M_l in 1925, 1981 and 1982. The last big earthquake

to occur in CEUS was the Mineral Virginia earthquake in 2011 with magnitude Mw5.5, which was felt in Minnesota in the north and Florida in the south. Figure 1.2 shows the seismicity map of CEUS for events occurred between 1580 and 2015 and the main seismic zones in which they occurred.

The state of stress and principal stress directions are important keys to understanding the origin of the CEUS stress field and its variations. Recent stress inversion research shows that compression stress field dominates the entire CEUS eastern margin and extension stress field domains the southern and northern Great Plains. At a smaller scale, anomalies appear in central/southern Oklahoma, the New Madrid seismic zone, Eastern Tennessee and the southern Appalachians ((Levandowski et al., 2018). Regardless of the origin of these anomalies, they correlate with increasing earthquake frequency, therefore stress variations may focus intracontinental earthquakes. The current CEUS seismic hazard map shows these regions as substantial seismic hazard sources.

2.2 Regional Seismic waves

The regional seismic phases are the seismic waves propagating through the lithosphere (crust and uppermost mantle) within a regional distance (1° to 13°). There are four major high frequency phases in typical regional seismograms, ***Pn***, ***Sn***, ***Lg***, ***and Pg***. We will focus on the first three. The ***Pn*** is the first ***P*** arrival phase traveling within the uppermost mantle along the Moho discontinuity, the crust - mantle boundary with two crustal legs (Fig.). ***Pn*** is generally observed when the epicentral

distance is farther than the crossover distance, a distance where the head wave has the same travel time as the direct wave, approximately 200km. P_n phase, is a guided wave with a velocity window (7.8 - 8.1 km/s) (Buehler and Shearer, 2017; Zhang et al., 2009).

The S_n is similar to P_n , but it is produced by S -wave mainly traveling within the uppermost mantle beneath the Moho. It is a guided shear wave phase with frequency (1-4) Hz and with velocity window (4.3--4.7km/ s) (Kennett 1986) and may contain frequency components in excess of 20 Hz. It has been observed out to distances of 35 degrees (Huestis et al., 1973). S_n and P_n propagation efficiency is sensitive to the velocity gradient and attenuation in the mantle lid and hence to its properties; temperature, composition, and thickness (Beghoul et al., 1993; Ni and Barazangi, 1983).

L_g is a crustal guided wave that has been modeled both as higher mode Love and Rayleigh waves and as the superposition of multiply reflected S waves trapped in the crust (Bouchon, 1982; Kennett, 1986) and it has a group velocity window between 3.6 and 3.0 km/s in a frequency band of 0.5 to 5 Hz. In addition to the intrinsic and scattering characteristics of the crust through which it propagates, L_g is sensitive to the shape and lateral variations of the crustal wave guide (Bostock and Kennett, 1990; Kennett et al., 1986; Ni and Barazangi, 1983).

There are many factors that could affect the L_g phase: (1) Rapid changes in crustal thickness could attenuate or block L_g phases (Benz et al., 1997; Bostock and Kennett, 1990; Fan and Lay, 1998); (2) Thick sediments could have similar effects to the crustal thickness variation (Baumgardt and Der, 1997; Nuttli, 1980); (3) Regions

of thin crust, either severely thinned continental or oceanic crust, also prevent Lg propagation.

In their journey starting from the seismic source and continuing through the earth medium and toward the surface seismic waves interact with the medium through which they are traveling, either increasing or decreasing in velocity, losing energy or gaining energy.

The seismic records provide us with raw data that is important in estimating seismic properties such as seismic velocity and seismic attenuation. Estimating seismic characteristics is essential to predict the earth interior, the lateral and vertical heterogeneity. Seismic models, chemical models, and geothermal models provide us with reliable methods of predicting earth structure.

2.3 Attenuation:

The mechanisms governing the loss of seismic energy combines multiple processes including geometric spreading, scattering attenuation, and intrinsic attenuation.

$$Q_{total}^{-1} = Q_{in}^{-1} + Q_{Sc}^{-1} \quad (1.1)$$

where Q_{in}^{-1} is the intrinsic attenuation and Q_{Sc}^{-1} is the scattering attenuation.

Laboratory studies of attenuation mechanisms have improved our understating of the factors affecting attenuation. Laboratory studies indicate that temperature, pressure and composition are the three major parameters that constrain the mechanical properties of the Earth. In the upper mantle, grain boundary relaxation and high temperature background cause grain boundary damping of peridotite, the dominate rock in the upper mantle, which could be the origin of intrinsic attenuation (Jackson

and Anderson 1970; Kawase et al., 2014). Studying seismic attenuation using seismic wave records requires estimating seismic velocities and amplitude of various seismic waves. In this research, we focus on studying the regional seismic waves (Sn and Pn). Rheology of the lithosphere mantle in addition to the frequency and propagation path of the regional seismic waves affects the waves attenuation (Xie and Mitchell, 1990); therefore, estimating the Qsn can help us to image the thermal tectonic features within the uppermost mantle such as hot spots and slabs. Combining Qsn with seismic velocity can constrain the regional uppermost mantle tectonic models.

2.3.1 Scattering attenuation

Scattering attenuation is the redistribution of seismic energy in space and time as a result of the interaction of the seismic wavefield with different sizes of structural heterogeneities (Sato and Fehler 1998). This interaction generates incoherent signals with smaller amplitudes; however, the integrated energy is the same. Scattering attenuation is a function of frequencies. The parameters that govern the scattering process are the wavelength, heterogeneity, and propagation distance in the scattering medium. In region with high intrinsic attenuation the scattering effect may not be obvious, such as the western U.S. On the other hand, in Eastern U.S. the scattering mechanism becomes more effective because of the low intrinsic attenuation values

(Aki and Richards 2002).
$$Q_{sc}^{-1} = \frac{gV_0}{2\pi f}$$

(1.2) Where Q^{-1} is the scattering attenuation, g is the transport scattering coefficient, V is the velocity of the seismic waves, and f is the frequency.

2.3.2 *Intrinsic attenuation*

In order to fully understand the attenuation concept and its implications inside the earth, we should discuss the important concepts of elasticity and anelasticity. Elasticity is the resisting of permanent distortion and the ability to return to the original shape and size after removing the subjected forces. Anelasticity considers the condition when the medium does not rebound to the origin shape and size. Elastic properties and their variation in the earth are mainly controlled by the forces that hold the atoms in molecules together (interatomic forces), which will be affected by composition, pressure, water, melt, partial melt, crystalline structure, and temperature (Anderson et al. 1971; Karato and Spetzler 1990). Evidence for the deviation from the ideal elasticity includes velocity dispersion, e.g., seismic velocity depends on frequency, and seismic wave on attenuation.

The law of conservation of energy states that “the total energy of an isolated system remains constant, it is said to be conserved over time” (Richard Feynman 1970). In the elastic medium, the propagating energy is conserved; however, the earth is not fully elastic medium, therefore, portions of the seismic energy will be absorbed. Intrinsic attenuation is the absorption of seismic energy or the deviation from perfect elasticity background. Attenuation is quantified by the reciprocal of Quality Factor Q, where smaller Q results in high attenuation in equivalence way to the damped harmonic oscillator equation:

$$A(t) = A_0 e^{-\alpha_0 t / 2Q} \quad (1.3)$$

$$Q(f) = 2\pi \left(\frac{\text{total energy}}{\text{energy lost during one cycle}} \right) \quad (1.4)$$

$$Q_{in}^{-1}(f) = \frac{\Delta E}{2\pi E} = \frac{\Delta A}{\pi A}, (A = E^{0.5})$$

Where Q_{in}^{-1} is the intrinsic attenuation. Figure 1-4 shows example of Sn attenuation in the eastern U.S. by using two arrays of seismic records: a red north-south array and a green east- west array. Notice the Sn phase disappears (absorbed) near western Virginia.

2.4 Site Response

Site response studies mainly include the amplification and the fundamental frequency. Amplification, by definition, is the ratio of the ground motion between the surface and the rock basement at the same location. The maximum peak of the spectra ratio represents the amplification at a specific frequency, named the fundamental frequency (f_0).

The main phenomenon responsible for the amplification of ground motion is impedance contrast, the difference in the product of velocities and densities between the sediments and the underlying bedrock trapping seismic energy in the upper layer. Historically most urban settlements occur along river valleys often over soft surface deposits. Therefore, for a long time it has been known that earthquake damage is generally more over soft sediments than on firm bedrock outcrops.

2.4.1 *The causes of the amplification*

When the structure is horizontally layered (1-D structures), the trapped energy affects body waves travelling up and down the surface layers. When the surface sediments form a 2-D or 3-D structure (i.e., when lateral heterogeneities such as thickness variations are present), the surface waves will be trapped. The interference between these trapped waves leads to resonance patterns, the shape and the frequency of which are related to the geometrical and mechanical characteristics of the structure. While these resonance patterns are very simple in the case of 1-D media (vertical resonance of body waves), they become more complex in the case of 2-D and a fortiori 3-D structures because of the focusing and defocusing effects which will be added to the

impedance contrast effect. There is also very strong instrumental evidence that surface topography (convex and concave structures) considerably affects the amplitude and frequency content of ground motion (Geli et al. 1988; Faccioli 1991; Pedersen et al., 1994). This is evidenced by the sensitivity to the incident wavefield (wave type, incidence and azimuth angles) and weathered rocks found at the top of hills reinforces the topographic effect (Pedersen et al., 1994).

A well-known example of near-station focusing and defocusing effects is the amplification observed in the Santa Monica, California area during the Northridge earthquake of 1994. Gao et al., (1996) proposed that the late-arriving S phase amplification in Santa Monica was due to focusing from a lens-shaped structure at the bottom of the Los Angeles basin based on modelling of observed variations in seismic amplitude. This result was later supported by (Davis et al., 2000) who used a finite-difference method to model SH amplification in the Los Angeles basin resulting from focusing caused by the presence of subsurface structures at ~ 3 km depth. Using various sources, Davis et al. (2000) showed that the amplification values varied as a function of the azimuth, distance, and incidence angle. Impedance contrasts have been shown to influence ground motion even in the absence of attenuation and structural factors. This result was demonstrated by (Murphy and Mueller, 1971) in their simulation of body waves travelling through infinite horizontal layers with constant velocities.

Several modelling studies have been conducted to understand how various factors converge to affect the site response. For instance, (Faccenna et al., 2014) investigated the effects of basin structure on ground motion using finite-difference modeling of 3D long-period (> 2 s) ground motions for large (Mw 6.8) earthquakes,

where high frequency surface waves were generated by steep basin edges in the upper 1 km. They compared the motions resulting from an empty basin and the motions resulting from a basin filled with sediment ($625 \text{ m/s} < V_p < 5500 \text{ m/s}$) and asserted that the inclusion of sediment in the model yielded higher ground motion amplification. The highest amplification was found to occur at the center and along the basin edges. The studies discussed above make use of forward modeling to estimate site effects. Another effective approach is to isolate site effects in the frequency domain from observed records by defining the site response as the spectral ratio of the signal at a sedimentary site and a nearby bedrock site, assuming that the seismic signal recorded at the rock site represents an undisturbed input motion (Borcherdt 1970). While it would be preferable to define the site response as the ratio of the signal at the surface and at the base of the sediments, the required input motion data is often not available. Beresnev and Wen, (1996) were able to show that, for both weak motion and strong motion, the assumption made by Borcherdt (1970) is approximately correct. A third and particularly common approach to estimate site amplification is to measure average shear-wave velocity in the upper 30 m (V_{s30}) and use it as a proxy. For instance, Borcherdt (1992, 1994, 2004) used V_{s30} data from the western USA to create the National Earthquake Hazards Reduction Program (NEHRP) site classification system, which groups sites according to their amplification. Despite its common usage, there are several issues with estimating site effects with V_{s30} : (1) It is difficult to get accurate measurements of V_{s30} . While V_{s30} can be measured precisely using active or passive sources methods, it is often difficult and expensive. Instead, different proxies for V_{s30} , such as topographic slope (Wald and Allen 2007), are often used to estimate V_{s30} values from

the 3D Digital Elevation Model (DEM) as a slope of the topography; however, these methods can further increase the uncertainty in the classification process by introducing further bias,(2) several studies have shown that Vs30 measurements may only have a weak relationship to site amplification. For instance, Mucciarelli et al. (2006) only found a weak correlation between NEHRP classified Vs30 measurements calculated from boreholes in Italy site. Another study by Castellaro et al., (2008) reanalyzed the empirical approach used by Borchardt (1994) to create the NEHRP system with an orthogonal regression analysis rather than a standard regression analysis. The results substantially differed, further demonstrating that Vs30 is only a weak proxy to seismic amplification. This lack of correlation between observed Vs30 and site amplification has been attributed to the oversimplified assumption that amplification can be predicted using the average Vs30 alone (Wald and Mori, 2000). McNamara et al. (2015) observed variable HVSR peak frequencies and amplitudes in the eastern United States. They demonstrated that both of the thickness and the average S-wave velocity of the subsurface geologic material effect the fundamental (resonance) frequency of any site and they proposed to use the HVSR peak frequency to calibrate the Vs30 estimated from the DEM. They show a strong linear relationship between HVSR peak frequency and surface Vs30 measurements.

2.5 Temperature of the uppermost mantle:

Estimating the temperature of the uppermost mantle is an important step toward understanding lithospheric strength, thickness, and buoyancy. In addition, temperature variation could constrain the stress and deformation of the lithosphere

(Harris et al., 2004; Hyndman et al., 2009; Lowry and Pérez-Gussinyé, 2011). Several approaches are used to estimate temperature: (1) extrapolating surface heat flow measurements to depth (Artemieva and Mooney, 2001), (2) using elevation and/or isostasy (e.g., Hasterok and Chapman, 2007), (3) xenolith geothermometry (e.g., Artemieva, 2009); and (4) mapping seismic velocities (V_S , P_s) to temperature (Goes and Lee, 2002), however; xenolith samples are very sparse in CEUS, surface heat flow measurements are perturbed by surface hydrology and sensitive uncertain distribution of radiogenic heat production, P velocity is not sensitive for melt, and shear wave velocity is sensitive to melts and anelasticity in addition to temperature. The most important source of uncertainty in the process of estimating the temperature is the composition models assumed for the uppermost mantle.

The uppermost mantle composite is composed of peridotite, mostly Olivine, with lesser amounts of orthopyroxene, clinopyroxene and aluminous phase (garnet, spinel). A small amount of Eclogites and pyroxenites might result from special processes such as recycling oceanic crust into mantle and precipitation during the interaction of ascending magma with the lower crust. The initial uppermost mantle model, Primitive model or Pyrolite, has abundant aluminous phases. Transforming from primitive mantle to Lherzolite (enriched mantle) to Dunite (depleted mantle) occurs with decreasing CaO Al_2O_3 and increasing MgO and NiO because of Basalt extraction. The major characteristics of peridotite were summarized by McDonough and Rudnick 1994. In Orthopyroxenes (e.g. enstatite and ferrosilite) the CaO of Orthopyroxene vary as a function of temperature, while Na_2O and TiO reflect the bulk composition of peridotite. Clinopyroxenes (e.g. Diopside, Hednbergite) is a Cr

rich diopsides or Ti rich augites. Abundant amounts of TiO and Na₂O of clinopyroxene reflect the fertility of peridotites. Garnet (e.g., Pyrope, Almandine, and Grossular), an important element in estimating the temperature (Al) exchange between Orthopyroxene and Garnet is pressure depended and sensitive to temperature.

There are several mechanisms that have been proposed to explain the enriched upper mantle: (1) Melt of mantle peridotite on the thermal boundary because of the high thermal gradient; (2) small degrees of partial melt or fractionated vapor phase; (3) the effect of subducting oceanic crust; or (4) entrainment of material by adjacent convection layers. Metasomatism in a process introducing elements such as iron, titanium, and H₂O to the upper mantle lowers the solidus temperature. In addition, this process could introduce heat-producing elements such as potassium, uranium and thorium. The enrich sources of the metasomatism process include fluid, partial melt or subduction.

The Mg number ($Mg\# = 100 \times Mg / (Mg + Fe)$) is the ratio of the Mg and Fe end-members of mantle peridotite and is used as a proxy to indicate mantle composition. High Mg# correlates with increasing amounts of melt extraction because Fe preferentially enters the melt phase while Mg remains in the residuum during partial melting of mantle material. Low Mg# numbers correlate with a Fe content (reduction in Mg). Mg# ranges between 86-88 for fertile mantle to 93-94 for highly depleted mantle (Lee, 2003). Enriched mantle has lower seismic velocities compared to depleted mantle. The depleted mantle could be transformed into enriched mantle by infiltration resulted from different process such as passage of a mantle plume, rifting,

or upwelling, which could decrease the Mg# of the mantle and could result in negative velocity anomalies in various regions (Chen et al., 2014; Pollitz and Mooney, 2014).

The variation of VP and VS velocity with Fe-Mg substitution were introduced by Speziale et al., (2005). $\partial \ln VP / \partial X_{Fe}$ and $\partial \ln VS / \partial X_{Fe}$ range between -0.05 and -0.46 and between -0.08 and -0.74 respectively in the main mantle minerals and the ratio $\partial \ln VS / \partial \ln VP$ for Fe-Mg substitution range between 0.9 and 1.7, which suggests that the effect of this substitution is very different in different solid solutions systems.

In this research, we used the THERIAK-DOMINO algorithm to generate the composition models necessary to constrain the temperature. This algorithm calculates the stable mineral assemblage and phase compositions for a rock at specified pressure and temperature. The rock composition models of the uppermost mantle applied in this software are adapted from the literature (Figure 1.6).

2.6 Methods

Many seismic methods were applied in this research including Horizontal to vertical Spectral Ratio (HVSr), Two Station method, Reverse Two Station method, and Travel Time Tomography. We will introduce each of them in the next paragraphs.

2.6.1 HVSr Method

The seismic record is the final product of source, path and site effects; thus, the most effective approach to obtain site amplification is from the frequency domain of observed records. In order to directly measure the site response, one must record

the signal at the surface and base of the sediments; the site response can be defined as the ratio of these two signals. However, the input motion is not available for most measurements except for the borehole data. As an alternative method, Borchardt (1970) used the spectral ratio between the sedimentary site and the nearby bedrock reference site. The assumption that the seismic signal recorded at the rock site represents an undisturbed input motion was proved to be approximately correct by Beresnev & Wen, (1996) for both weak motion and strong motion. This method cannot easily be applied to the TA array since the geologic surficial information is not available for all the TA stations. To overcome the lack of seismic data and geologic information, the HVSR method was proposed. Nakamura (1989) mentioned that thick sedimentary basins, the peak of the Horizontal to Vertical Spectral Ratio (HVSR) of ambient seismic noise measurements correlates with the peak of the fundamental resonance frequency. Ambient noise is seismic noise dominated by short period waves <20 Hz, known as microseisms, which generally originated from the interaction of ocean waves and the continental shelves. Lermo and Chavez-Garcia (1993) proposed applying the Nakamura method on the shear wave part of weak-motion earthquake recordings. This application of the HVSR technique combines two techniques: the receiver function approach of Langston, (1979) using the H/V ratio to estimate the velocity structure model and the HVSR technique of Nakamura (1989, 1996). Whether the HVSR method measures the amplification of the ground motion or not has long been a source of debate. Zhao et al. (2006) and Sokolove et al. (2007) show that HVSR provides reliable estimates of site amplification at recording sites with low velocity near surface sediments. Parolai et al. (2007) has shown that the

HVSR and SSR methods provide similar results. Although the HVSR method provides stable results that correlate well with the surface geology, it has some limitations: the fundamental resonance frequency can underestimate the amplification factor and this method cannot be applied to rock sites because the amplification will be unity. Recently many studies used the HVSR method to estimate V_{s30m} and NEHRP soil class e.g. McNamara et al. (2015). In our work, we adapted J- SESAME (Site Effects assessment using AMbient Excitations) to analyze both the weak motion and the ambient noise following the steps:

- Breaking the seismic wave into windows from the arrival time of S-waves to end of group velocity 3.5km/s for weak motion. Choosing 50 sec of the ambient noise recorded before the first arrival time.
- Performing a Fast Fourier Transform (FFT) to each window after applying taper (5%).
- The horizontal spectrum was merged and divided by vertical spectrum.
- The ratio of each window was combined into an averaged spectrum.
- The output files contain H/V spectral ratio. The largest pick represents the amplification at a specific fundamental frequency.

$$A(f)_s = \frac{V(f)_s}{V(f)_b} \dots\dots\dots(1.5)$$

$$S(f)_E = \frac{H(f)_s}{H(f)_b} \dots\dots\dots(1.6)$$

$$S(f)_M = \frac{S(f)_E}{A(f)_s} = \frac{((H(f)_s)/(H(f)_b))}{((V(f)_s)/(V(f)_b))} = \frac{H(f)_s/V(f)_s}{H(f)_b/V(f)_b} \dots\dots\dots(1.7)$$

$$\frac{H(f)_b}{V(f)_b} = 1$$

$$S(f)_M = \frac{H(f)_s}{V(f)_s}$$

$$S(f)_M = \frac{\sqrt{(H(f)_{(NS)}^2 + H(f)_{(EW)}^2)} / 2}{V(f)_s} \dots\dots\dots(1.8)$$

Where Vs: amplitude spectrum of the vertical component of motion at the surface.

V_B: amplitude spectrum of the vertical component of motion at the base of the sediment layer, H_s: amplitude spectrum of the horizontal component of motion at the surface.

H_B: amplitude spectrum of the horizontal component of motion at the base of the sediment layer. S_E: estimate of site effect. A_s: amplitude effect of source

S_M: modified site effect function. S(f): the site effect on the earth surface.

H(f): horizontal spectral component. V(f): vertical spectral component

H(NS): horizontal north -south component (EW): horizontal east - west component.

2.6.2 *Travel time tomography*

The travel times for pn paths are described by eq 1.9,

.

$$T = T_e + T_s + \sum_{i=1}^n \Delta_i S_i \quad (1.9)$$

where a is the station delay, b is event delay, d_i is distance the ray travels in cell i , S_i is the slowness for cell i . The sum is calculated over all cells through which the ray

travels in the uppermost mantle.

$$\begin{aligned} \text{StationDelay} &= \int_{\text{sealevel}}^{\text{MohoDepth}} \sqrt{(S_c^2 - S^2)} dz \\ \text{EventDelay} &= \int_{\text{HypocenterDepth}}^{\text{MohoDepth}} \sqrt{(S_c^2 - S^2)} dz \end{aligned} ,$$

(1.10)

where S_c is crustal slowness as a function of depth. S is average mantle slowness (figure 1.8). The tomographic method used is following LSQR algorithm (Page and sauders 1982).

$$Ax=t \quad (1.11)$$

Where (t) is a vector of observed travel times. x is the parameter vector containing station delays, event delays and slowness. A is a matrix corresponding to the coefficients of the vector X .

$$AM^{-1}Mx = t \quad (1.12)$$

M is preconditioning matrix which does not change the least squares norm but has an effect on the convergence rate.

$$AM^{-1}z = t \quad (1.13)$$

M^{-1} in this case is a diagonal matrix that makes z dimensionless and scale z for the path density. For M^{-1} diagonal items, they are a square root of the number of the arrival at each station and event.

The solution was regularized by the Laplacian (second derivative) of slowness image to be small. The Laplacian is implemented as the weighted 2D infinite difference operator in the same manner as (lees & crosson 1989). The Laplacian regularization equations were applied directly to the slowness components of the preconditioned solution (z) rather than x. This will adjust for the ray density and smooth the results where the level of smoothing is controlled by the weight given to regularization equations.

2.6.3 Reverse -Two Station Method

The RTS method was first introduced by Chen et al (1987). It requires two stations and two events where an event is on either side of the station pair in a narrow azimuthal window. Two spectral ratios are combined to remove the common source and site terms. Bao et al., (2011) extended this method to estimate the Q values, site response, and source response. The ideal case for RTS is that both events are aligned with the inter-station path. It needs the four epicentral distances involved to be within a regional distance range (200-1500 km). A_{ai} , A_{aj} , A_{bi} , and A_{bj} denote spectral amplitudes of Lg recorded at stations i and j for events a and b, and d_{ai} , d_{aj} , d_{bi} , and d_{bj} are the corresponding distances:

$$\frac{A_{ai}}{A_{aj}} = \frac{S_a R_a I_i S_{Si} G_{ai}}{S_a R_a I_j S_{Sj} G_{aj}} \exp\left(\frac{\pi f d_{aj}}{v_j Q_j} - \frac{\pi f d_{ai}}{v_i Q_i}\right) \quad (1.14)$$

$$\frac{A_{bi}}{A_{bj}} = \frac{S_b R_b I_i S_{Si} G_{bi}}{S_b R_b I_j S_{Sj} G_{bj}} \exp\left(\frac{\pi f d_{bj}}{v_j Q_j} - \frac{\pi f d_{bi}}{v_i Q_i}\right) \quad (1.15)$$

We assume that the velocity structure is one-dimensional. The RTS allows the event locations to deviate from the inter-station great circle by two small angles ($\pm 15^\circ$).

G is the geometrical spreading of the wavefront, given by

$$G = \frac{1}{d_0} \left(\frac{d_0}{d} \right)^n, d \geq d_0 \quad \dots\dots\dots (1.16)$$

where d is the epicentral distance and d_0 is a critical distance (Street et al., 1975). For Lg, G can be simplified to

$$G = G_0 d^{-m}, \quad (1.17)$$

where G_0 is a constant (Pasyanos et al. 2009b). Here d is in length units and m is typically called the spreading exponent (Yang 2002). To solve for the relative site response, we multiply the two ratios in (1.14,15), obtaining (1.18) below:

$$\frac{A_{ai}A_{bi}}{A_{aj}A_{bj}} = \left(\frac{I_i S_{si}}{I_j S_{sj}} \right)^2 \left(\frac{G_{ai}G_{bi}}{G_{aj}G_{bj}} \right) \exp \left(\frac{\pi f d_{aj}}{v_j Q_j} - \frac{\pi f d_{ai}}{v_i Q_i} + \frac{\pi f d_{bj}}{v_j Q_j} - \frac{\pi f d_{bi}}{v_i Q_i} \right). \quad (1.18)$$

Assuming that the velocity structure is one-dimensional and the apparent Q values are identical along the path. If we then substitute (1.17) into (1.18),

$$\frac{A_{ai}A_{bi}}{A_{aj}A_{bj}} = \left(\frac{I_i S_{si}}{I_j S_{sj}} \right)^2 \left(\frac{G_{ai}G_{bi}}{G_{aj}G_{bj}} \right) \exp \left(\frac{\pi f (d_{aj} - d_{ai} + d_{bj} - d_{bi})}{vQ} \right) \quad (1.19)$$

$$\frac{A_{ai}A_{bi}}{A_{aj}A_{bj}} = \left(\frac{I_i S_{si}}{I_j S_{sj}} \right)^2 \left(\frac{d_{ai}d_{bi}}{d_{aj}d_{bj}} \right)^{-m} \exp \left(\frac{\pi f (d_{aj} - d_{ai} + d_{bj} - d_{bi})}{vQ} \right)$$

(1.20)

$$\frac{A_{ai}A_{bi}}{A_{aj}A_{bj}} = \left(\frac{I_i S_{Si}}{I_j S_{Sj}} \right)^2 \left(\frac{d_{ai}d_{bi}}{d_{aj}d_{bj}} \right)^{-m} \exp \left(\frac{(d_{aj} - d_{ai} + d_{bj} - d_{bi})}{d_{aj} - d_{ai} - d_{bj} + d_{bi}} \ln \left[\frac{A_{ai}A_{bj}}{A_{aj}A_{bi}} \left(\frac{d_{ai}d_{bj}}{d_{aj}d_{bi}} \right)^m \right] \right) \dots$$

(1.21)

$$\frac{A_{ai}A_{bi}}{A_{aj}A_{bj}} = \left(\frac{I_i S_{Si}}{I_j S_{Sj}} \right)^2 \left(\frac{d_{ai}d_{bi}}{d_{aj}d_{bj}} \right)^{-m} \exp \left(\ln \left[\frac{A_{ai}A_{bj}}{A_{aj}A_{bi}} \left(\frac{d_{ai}d_{bj}}{d_{aj}d_{bi}} \right)^m \right]^{\frac{(d_{aj} - d_{ai} + d_{bj} - d_{bi})}{d_{aj} - d_{ai} - d_{bj} + d_{bi}}} \right) \dots$$

(1.22)

we will obtain

$$\frac{A_{ai}A_{bi}}{A_{aj}A_{bj}} = \left(\frac{I_i}{I_j} \frac{S_{Si}}{S_{Sj}} \right)^2 \left(\frac{d_{ai}d_{bi}}{d_{aj}d_{bj}} \right)^{-m} \left[\left(\frac{A_{ai}A_{bj}}{A_{aj}A_{bi}} \right) \left(\frac{d_{ai}d_{bj}}{d_{aj}d_{bi}} \right)^m \right]^{\frac{d_{aj} - d_{ai} + d_{bj} - d_{bi}}{d_{aj} - d_{ai} - d_{bj} + d_{bi}}} \quad (1.23)$$

The ratio of the two site responses can then be expressed in logarithmic form

$$\frac{\ln S_{Si}}{\ln S_{Sj}} = \ln \frac{I_i}{I_j} + \frac{d_{aj} - d_{ai}}{d_{aj} + d_{bi} - d_{ai} - d_{aj}} \ln \frac{A_{ai}d_{ai}^m}{A_{aj}d_{aj}^m} + \frac{d_{bi} - d_{bj}}{d_{aj} + d_{bi} - d_{ai} - d_{bj}} \ln \frac{A_{bi}d_{bi}^m}{A_{bj}d_{bj}^m} \quad (1.24)$$

(1.24) can finally be written out as:

$$\ln S_{Si} - \ln S_{Sj} = \ln \frac{I_i}{I_j} + \frac{d_{aj} - d_{ai}}{d_{aj} + d_{bi} - d_{ai} - d_{aj}} \ln \frac{A_{ai}d_{ai}^m}{A_{aj}d_{aj}^m} + \frac{d_{bi} - d_{bj}}{d_{aj} + d_{bi} - d_{ai} - d_{bj}} \ln \frac{A_{bi}d_{bi}^m}{A_{bj}d_{bj}^m}$$

If we assume that the theoretical instrument response fully represents the real instrument response, all values on the right side of the equal sign in (1-25) are known and can be written as an inversion problem:

$$\mathbf{Gm} = \mathbf{d} \quad (1-26)$$

where \mathbf{m} is the vector of the logarithms of all site responses S_s , the matrix \mathbf{G} will be the stations,

and \mathbf{d} will consist of the term on the right side of the equal sign in (A11), which we have named RS (Relative Site response). A12 is expressed in matrix format below:

$$\begin{bmatrix} Ln(S_{Si}) \\ Ln(S_{Sj}) \\ \vdots \end{bmatrix} \begin{bmatrix} 1 & 0 & 0 & 0 & \dots\dots \\ 1 & 0 & -1 & 0 & \dots\dots \\ 0 & 1 & -1 & 0 & \dots\dots \\ 0 & 0 & 1 & -1 & \dots\dots \\ \vdots & \vdots & \vdots & \vdots & \dots\dots \end{bmatrix} = \begin{bmatrix} RS_{ij}^1 \\ RS_{ij}^2 \\ RS_{ij}^3 \\ \vdots \\ RS_{ij}^n \end{bmatrix} \dots\dots\dots(1-27)$$

This inversion problem can now be solved for the relative values of the two site responses S_{Si} and S_{Sj} . We first calculate the relative values of the site response S_s . We then choose a reference station, ideally with zero amplification, and run the LSQR algorithm to calculate the absolute values.

2.6.4 Modified Two -Station Method (TSM).

The TSM was introduced by Tsai and Aki (1969) and then modified by Xie and Mitchell (1990b). This method requires two recording stations aligned exactly with the source. We denote the two stations as stations i and j with the spectra A_i and A_j , respectively. The epicentral distances of station i and j are d_i and d_j , and inter-station distance is d_{ij} .

In the real situation, the perfect alignment geometry is not common. Therefore; a realistic geometry was accepted, the azimuths from the source to the two stations are

different by a small angle $\partial\theta$ (Xie et al., 2004). Systematic errors could be added to Q values resulted from the effect of attenuation out of the path and anisotropic source radiation pattern. These errors can be minimized if a threshold value limited to $\partial\theta_{\max} \pm 15^\circ$ (Xie et al. 2004; Der et al. 1984). Figure 1.12 shows an example of two spectra recorded in two stations L56A and Q58A, where the earthquake and the two stations are aligning together. The spectra of the Sn phase and noise spectra for this station pair shows frequency ranges between 1.5-4Hz. The spectral amplitude ratio of the two stations:

$$\frac{A_i}{A_j} = \frac{S R I_i S_{S_i} G_i}{S R I_j S_{S_j} G_j} \exp\left(\frac{\pi f d_j}{v_j Q_j} - \frac{\pi f d_i}{v_i Q_i}\right), \quad (1-28)$$

where subscripts i and j refer to values at stations i and j respectively. The assumptions we adapted in this method: (1) the velocity structure is one-dimensional, (2) apparent Q values are identical at stations i and j , (3) G was simplified to $G = d^{-m}$.

When this method was introduced by (Bao et al., 2011; Xie and Mitchell, 1990; Xie et al., 2004), the variation in S_s is assumed to be negligible. However, in this study, we have included S_s terms in the inversion code. Thus (1-7) is simplified as

$$\frac{A_i}{A_j} = \frac{S_{s_i} I_i d_i^{-m}}{S_{s_j} I_j d_j^{-m}} e^{\frac{\pi f}{v Q} (d_j - d_i)}. \quad (1-29)$$

Apparent attenuation ($1/Q$), inter-station (between i and j) value, as a function of frequency (f) can be derived as

$$\frac{1}{Q(f)} = \frac{v}{\pi f (d_j - d_i)} \ln\left(\frac{S_{s_i}(f) A_i(f) I_j(f) d_i^m}{S_{s_j}(f) A_j(f) I_i(f) d_j^m}\right), \quad (1-30)$$

$$\frac{1}{Q(f)} = \frac{v}{\pi f(d_j - d_i)} \left[\ln \left(\frac{S_{sj}(f)}{S_{si}(f)} \right) + \ln \left(\frac{A_i(f)I_j(f)d_i^m}{A_j(f)I_i(f)d_j^m} \right) \right] \quad (1-$$

31)

$$\frac{1}{Q(f)} - \frac{v}{\pi f(d_j - d_i)} \ln \left(\frac{S_{sj}(f)}{S_{si}(f)} \right) = \frac{v}{\pi f(d_j - d_i)} \ln \left(\frac{A_i(f)I_j(f)d_i^m}{A_j(f)I_i(f)d_j^m} \right) \quad (1-$$

32)

Two-dimensional tomography mapping the lateral variation of Q of regional phases was originally presented by Xie and Mitchell (1990). The study area was divided into a number of N_g grids with widths of W_{NS} degrees in a north-south direction and W_{EW} degrees in an east-west direction. The total N paths where the Q values are measured. The distance and Q along the n th path were denoted by Δ_n and Q_n , respectively. The unknown lateral variation of Q can be assumed to be a constant Q_m inside the m th grid. Denoting the length over which the n th path crosses the m th grid by Δ_{mn} and the total number of grids crossed by the n th path by M . The attenuation along the n th path can be rewritten as

$$\frac{1}{Q} = \exp \left(-f\pi \frac{\Delta_n}{Q_n v_n} \right) = \exp \left[-f\pi \sum_{m=1}^M \left(\frac{\Delta_{mn}}{Q_m v_m} \right) \right]. \quad (1.33)$$

Assuming a constant velocity along the n th path, (1-33) can further derived to

$$\frac{\Delta_n}{Q_n} = \sum_{m=1}^M \frac{\Delta_{mn}}{Q_m}. \quad (1.34)$$

The output of the TSM is note apparent Q but is Q with the site response terms of the two stations. We modified this step by applying (1.32) in (1.34). we find:

$$\frac{\Delta n}{Qn} = \sum_{m=1}^M \frac{\Delta mn}{Q_m} + \frac{v}{\pi f(d_j - d_i)} (\ln S_{Sj} - \ln S_{Si}) \quad (1.35)$$

(1.35) can be solved using an LSQR algorithm of Paige and Saunders (1982). This algorithm iteratively finds a least-squares solution to a set of linear equations of the $\mathbf{Gm}=\mathbf{d}$. \mathbf{m} is the vector of $1/Q_{mn}$'s and \mathbf{d} is the vector of $\Delta n/Q_n$. The matrix \mathbf{G} stores all the non-zero Δ_{mn} values and is a sparse matrix. Hearn and Ni (1994) applied a diagonal preconditioner matrix

$$m(i, i) = \sqrt{\sum \Delta_n \Delta_{mn}}. \quad (1.36)$$

This matrix yields a fast convergence rate for the algorithm. Meanwhile, a set of regularization equations, presented by Lees and Crosson, (1989) are implemented to smooth and stabilize the inversion. This method of Hearn and Ni, (1994) was to solve Pn velocity tomography.

2.6.5 Resolution tomographic model

A checker board test, a technique to estimate the model resolution, has been widely used in seismic velocity tomography and Griot et al., (1998); Ottemöller, (2002) adapted this technique into seismic attenuation tomography. High path coverage is critical in retrieving the checker board pattern and the structural size of the test. Many studies consider the checker board test capable of producing a qualitative spatial resolution and demonstrating the reliability of the results for real data. The synthetic data were computed for the same travel paths and parameters used in the inversion of real data. I used a checker board to evaluate the tomographic results in my studies (Q_{sn} , V_{sn} , and V_{pn}). Figure 1.14 is an example of a checkerboard of using Pn travel time

tomography using all the data set from ISC and TA in Central and Eastern United States.

2.7 Figures

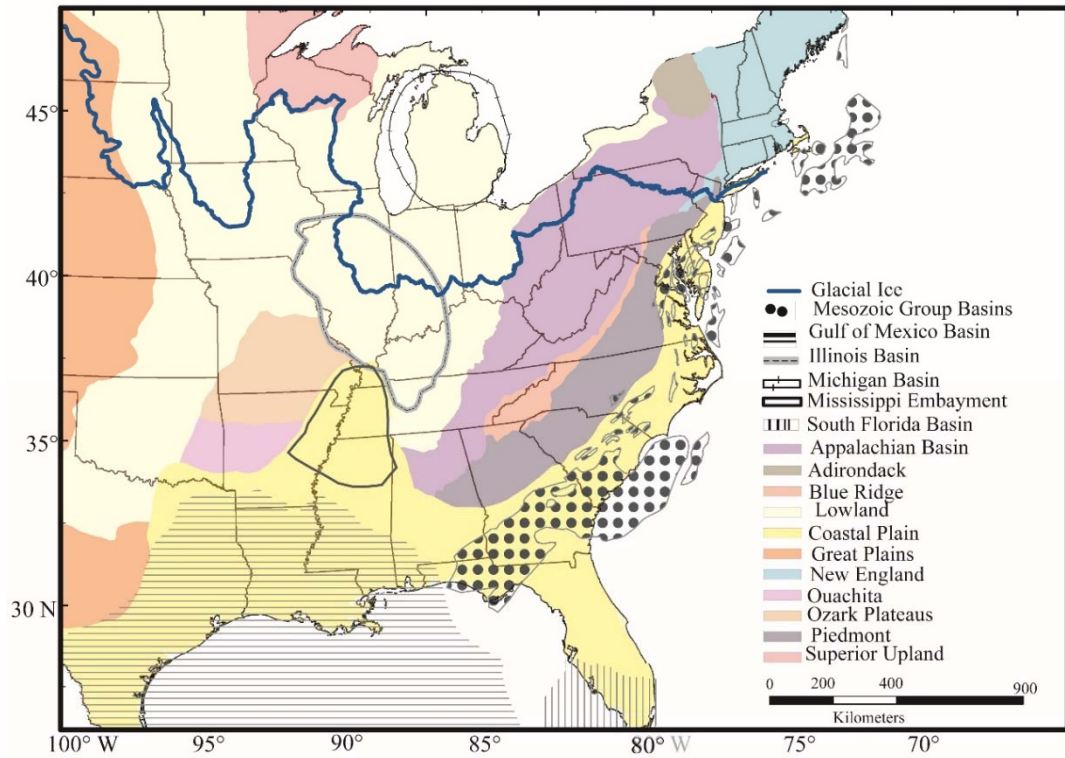
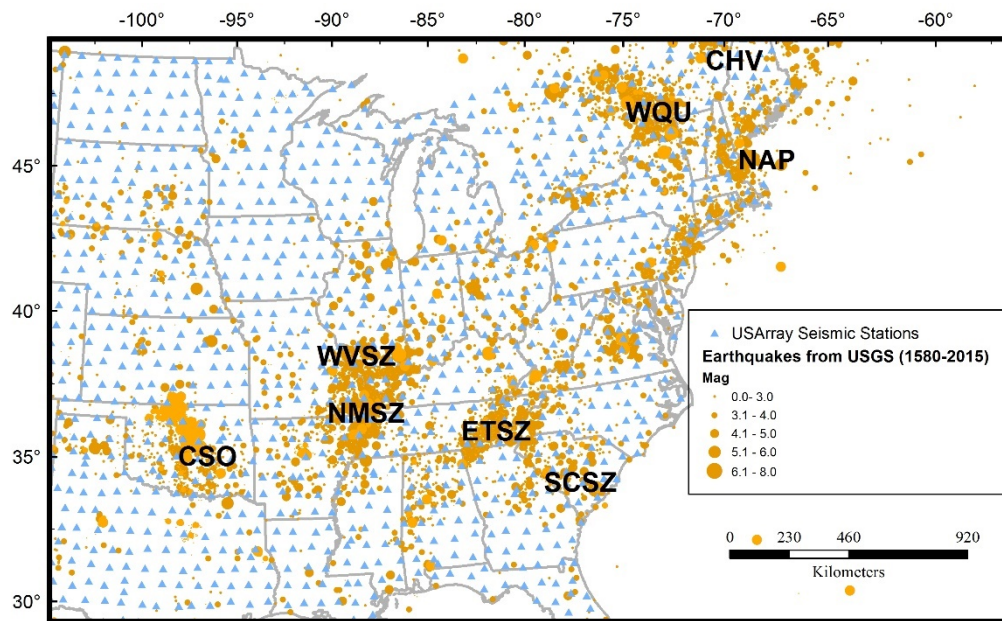


Figure 2.1. The study region with the main geological provinces, basins, and glaciation limits.



WVSZ:Wabash Valley Seismic Zone **SCSZ:South Carolina Seismic Zone** **NMSZ:New Madrid seismic Zone**
WQU:Western Quebec Seismic Zone **CSO:Central-South Oklahoma** **CHV:Charlevoix Seismic Zone**
ETSZ:East Tennessee Seismic Zone **NAP:Northern Appalachians Seismic Zone**

Figure 2.2 The seismicity map of CEUS. The orange circles are the size of the earthquakes recorded between 1980-2015 in addition to the historical events. The blue triangles are the USArray seismic stations.

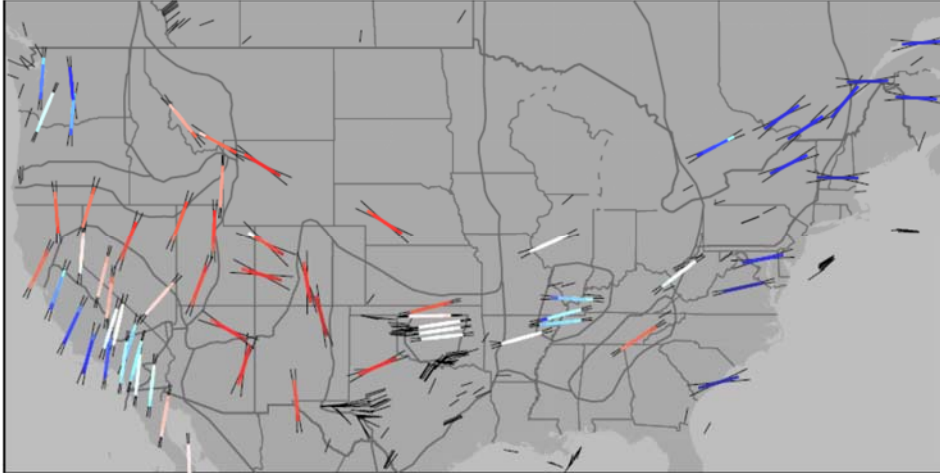


Figure 2.3 The bars are oriented parallel to σ_{Hmax} ; the thin lines span the 95% confidence interval. Each bar is divided into 5 segments, coloured as the 0.025, 0.16, 0.5, 0.84 and 0.975 quantiles of $A\phi$ (that is, ± 2 standard deviation range) (Levandowski *et al.*, 2018).

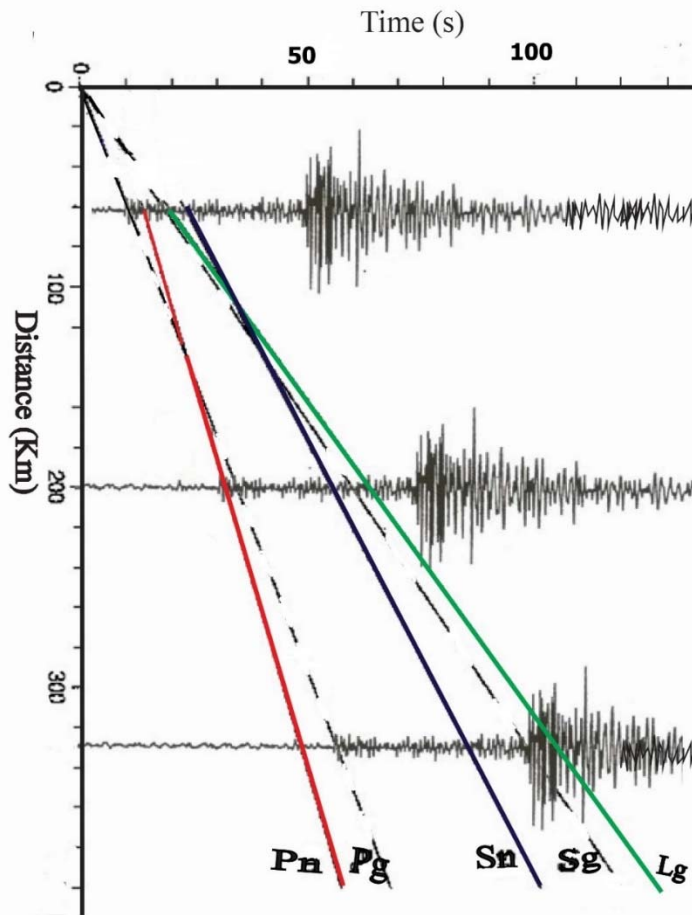


Figure 2.4 Regional seismic wave arrivals with time and distances. Pn, Sn and Lg are regional phases while Pg and Sg are local phases added as a reference (Borman P. (Ed.)2002).

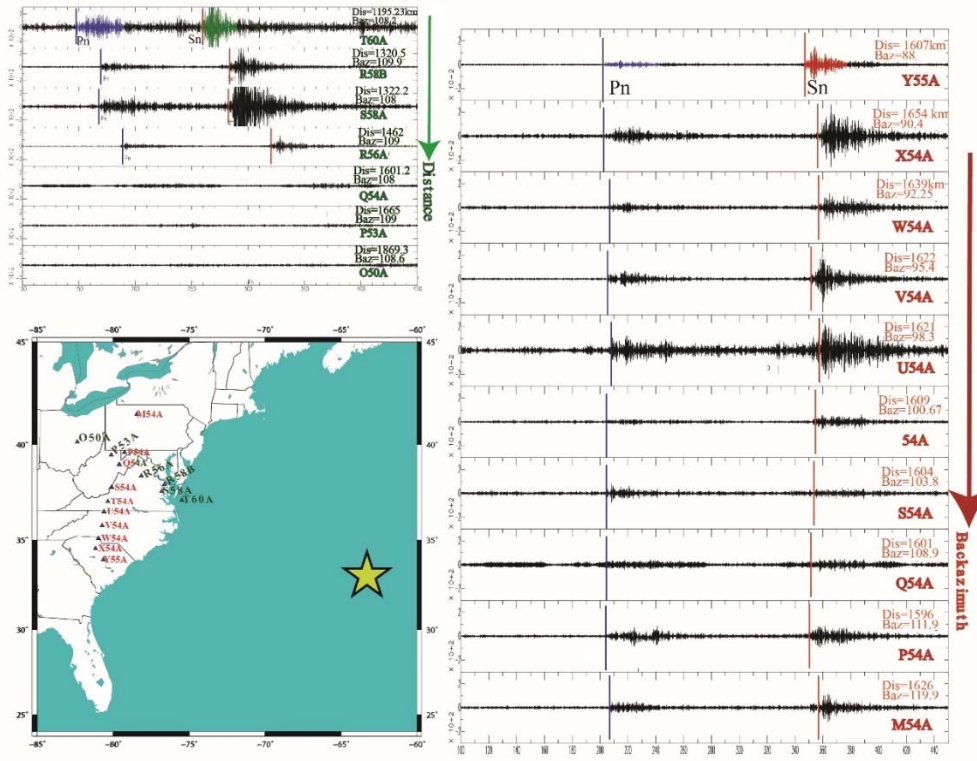


Figure 2.5. Example of Sn attenuation in eastern U.S.. Yellow star is the seismic events. The red array varies based on back-azimuth and the green array varies based on the distance from the events.

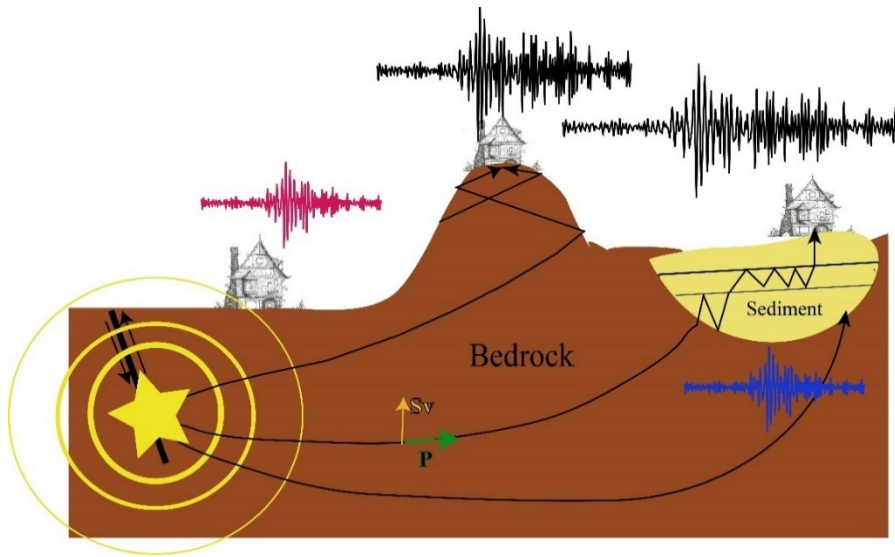


Figure 2.6. Sketch simplifies the local site effect on the seismic waves. Thick black line is the fault. Yellow star is the event.

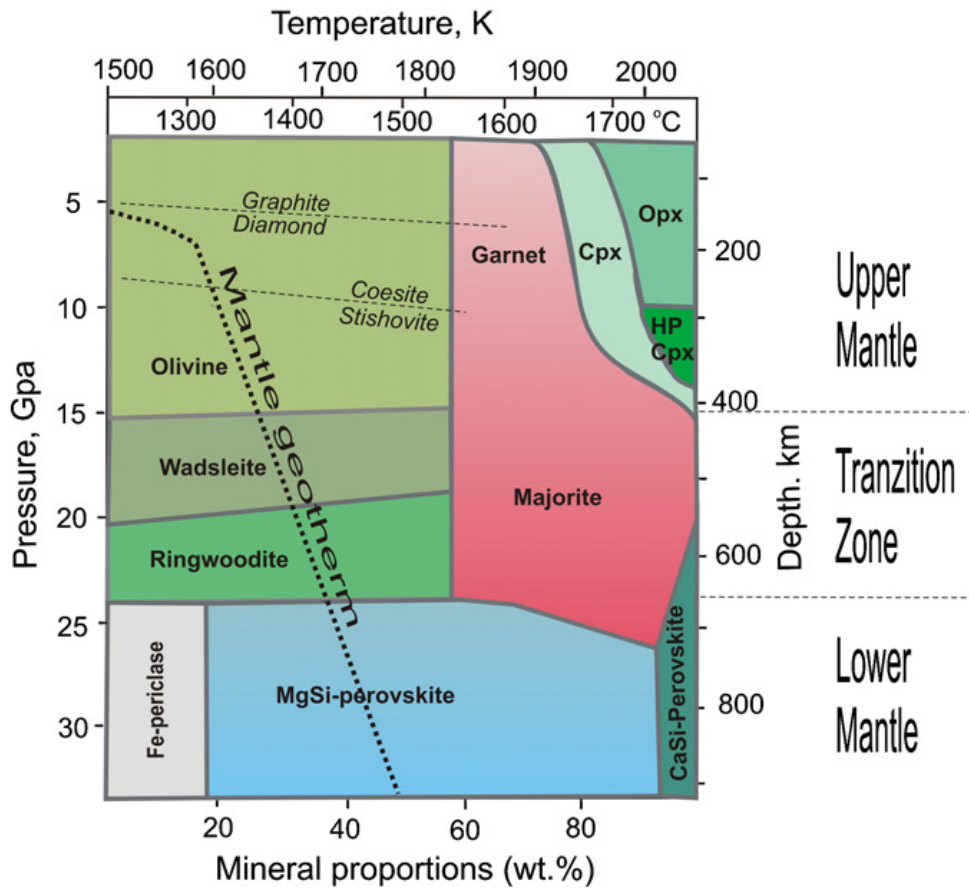


Figure 2.7. Mineral composition and phase transformations in the mantle after (Helfrich and Wood, 2001; Kennedy and Kennedy, 1976; Stixrude and Lithgow-Bertelloni, 2007)

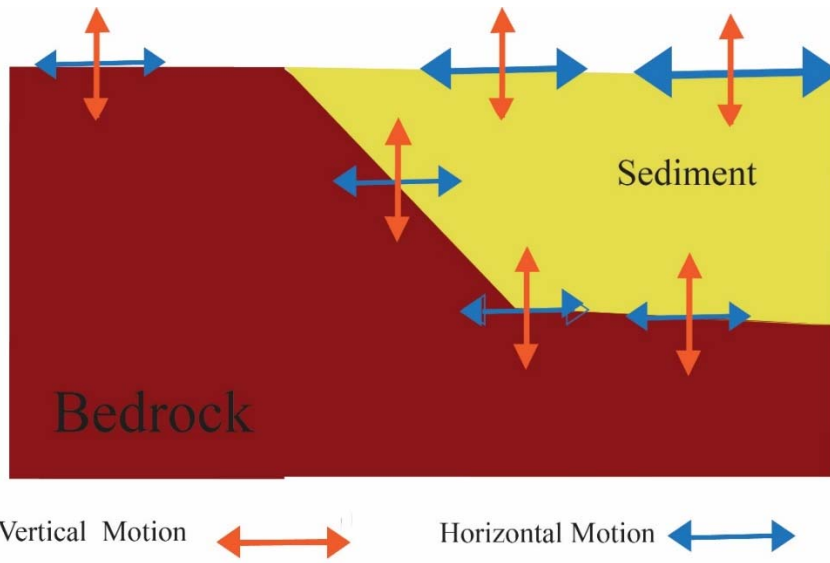


Figure 2.8. Sketch shows the horizontal and vertical motion in the bedrock and sediments.

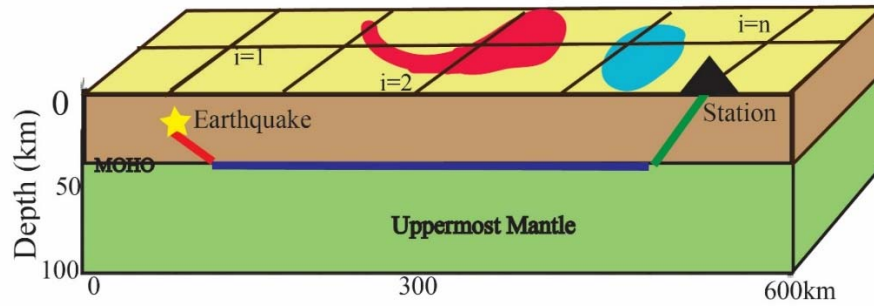


Figure 2.9. Sketch shows the S_n ray-path: two crustal arms and the uppermost mantle arm. This sketch shows tomographic cells as well

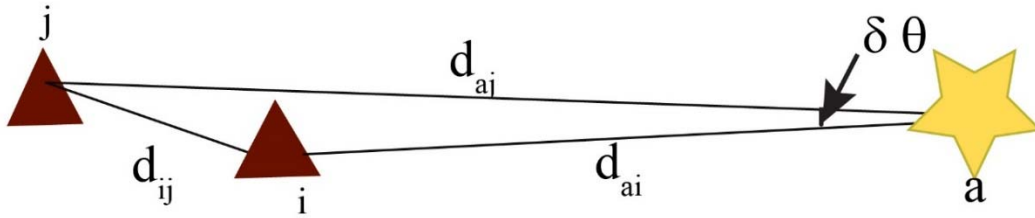


Figure 2.11. The geometry for the application of TSM for Q measurement.

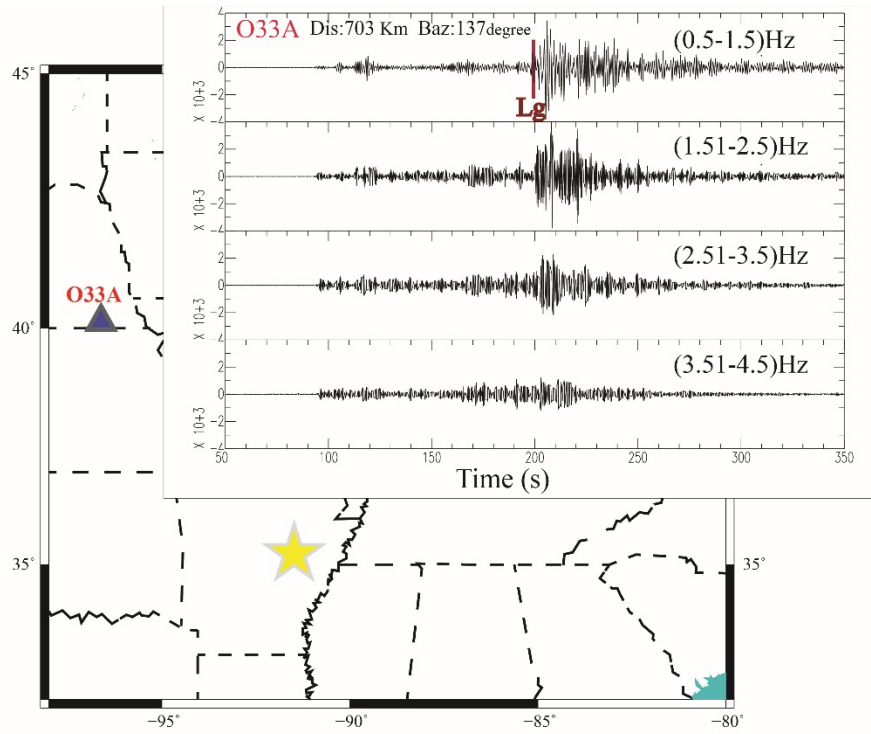


Figure 2.12. Example of Lg phase was recorded in O33A station and filtered with four filter bands.

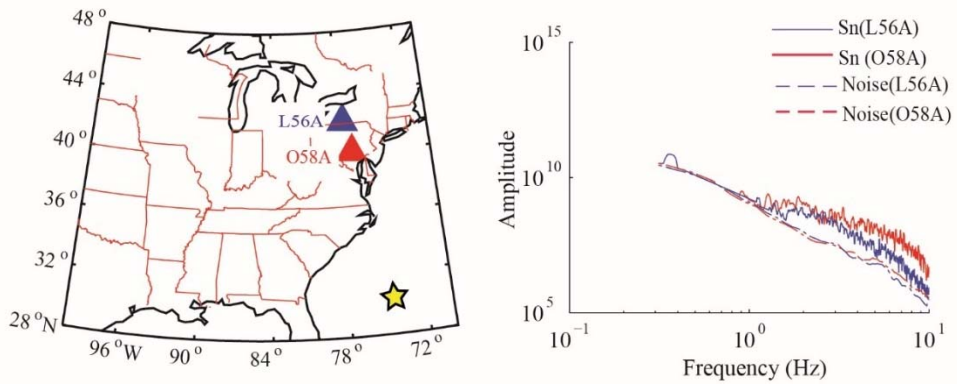


Figure 2.11. Example of TSM. (a) location of the event and the two stations L56A and Q58A. (b) the spectra of the Sn phases and noise

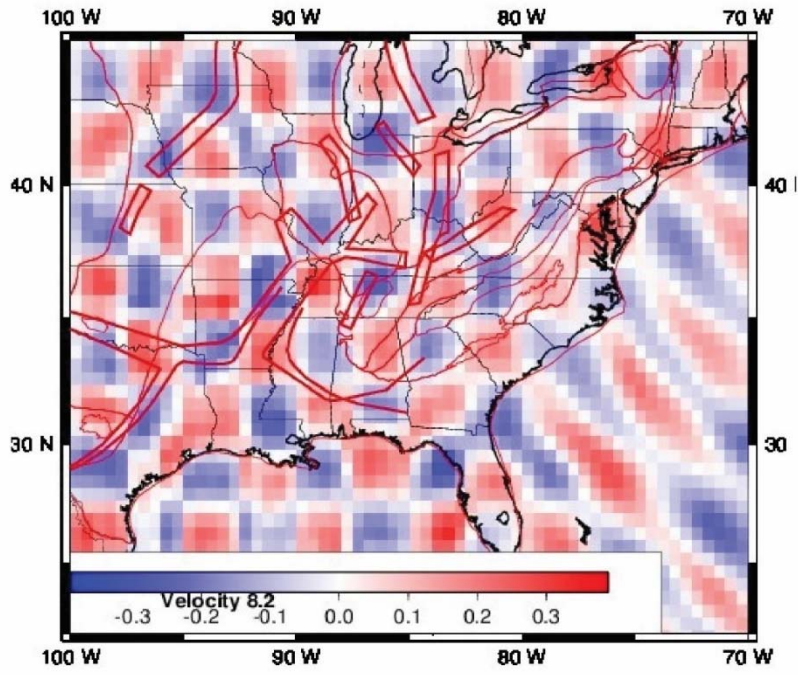


Figure 2.12 Checker board of Pn travel time tomography.

2.8 References

- Aki, K., and P.G. Richards (2002).
- Amick, D., and R. Gelinas (1991). The search for evidence of large prehistoric earthquakes along the Atlantic seaboard, *Science* (80-.). 251, 655–658.
- Anderson, D.L., C. Sammis, and T. Jordan (1971). Composition and evolution of the mantle and core, *Science* (80-.). **171**, 1103–1112.
- Artemieva, I.M. (2009). The continental lithosphere: Reconciling thermal, seismic, and petrologic data, *Lithos*.
- Artemieva, I.M., and W.D. Mooney (2001). Thermal thickness and evolution of Precambrian lithosphere: A global study, *J. Geophys. Res. Solid Earth* **106**, 16387–16414.
- Bao, X., E. Sandvol, J. Ni, T. Hearn, Y.J. Chen, and Y. Shen (2011). High resolution regional seismic attenuation tomography in eastern Tibetan Plateau and adjacent regions, *Geophys. Res. Lett.* **38**.
- Baumgardt, D.R., and Z. Der (1997). (PLT-TR-94-229, ENSCO, Inc., Springfield, VA).
- Beghoul, N., M. Barazangi, and B.L. Isacks (1993). Lithospheric structure of Tibet and western North America: Mechanisms of uplift and a comparative study, *J. Geophys. Res. Solid Earth* **98**, 1997–2016.
- Benz, H.M., A. Frankel, and D.M. Boore (1997). Regional Lg attenuation for the continental United States, *Bull. Seismol. Soc. Am.* **87**, 606–619.
- Beresnev, I.A., and K.L. Wen (1996). The accuracy of soil response estimates using soil-to-rock spectral ratios, *Bull. Seismol. Soc. Am.* **86**, 519–523.

- Bickford, M.E., W.R. Van, and I. Zietz (1986). Proterozoic history of the midcontinent region of North America, *Geology* **14**, 492–496.
- Borcherdt, R.D. (1970). Effects of local geology on ground motion near San Francisco Bay, *Bull. Seismol. Soc. Am.* **60**, 29–61.
- Bostock, M.G., and B.L.N. Kennett (1990). The effect of 3-D structure on Lg propagation patterns, *Geophys. J. Int.* **101**, 355–365.
- Bouchon, M. (1982). The complete synthesis of seismic crustal phases at regional distances, *J. Geophys. Res. Solid Earth* **87**, 1735–1741.
- Boundaries, S., and B.Y.B.L.N. Kennett (1986). Waves and structural boundaries by b. l. n. kennett, **76**, 1133–1141.
- Buehler, J.S., and P.M. Shearer (2017). Uppermost mantle seismic velocity structure beneath USArray, *J. Geophys. Res. Solid Earth* **122**, 436–448.
- Castellaro, S., F. Mulargia, and P.L. Rossi (2008). VS30: Proxy for seismic amplification?, *Seismol. Res. Lett.* **79**, 540–543.
- Chen, C., D. Zhao, and S. Wu (2014). Crust and upper mantle structure of the New Madrid Seismic Zone: Insight into intraplate earthquakes, *Phys. Earth Planet. Inter.* **230**, 1–14.
- Coleman, B.J.L., S.M. Cahan, and B. Sea (2012). Figure_1_CENOZOIC_final-new-kay - Figure_1_CENOZOIC.pdf, 2012.
- Daniel E. McNamara, W.J. Stephenson, J.K. Odum, and R.A. Williams (2015). Site Response in the eastern 1 U.S.: A comparison of Vs30 measurements with estimates from horizontal-to-vertical spectral ratios, *Geol. Soc. Am. Spec. Pap.* **67–79**.

- Davis, P.M., J.L. Rubinstein, K.H. Liu, S.S. Gao, and L. Knopoff (2000). Northridge earthquake caused by geologic focusing of seismic waves, *Science* (80-). **289**, 1746–1750.
- Ervin, C.P., and L.D. McGinnis (1975). Reelfoot rift: Reactivated precursor to the Mississippi embayment, *Geol. Soc. Am. Bull.* **86**, 1287–1295.
- Faccenna, C., T.W. Becker, M.S. Miller, E. Serpelloni, and S.D. Willett (2014). Isostasy, dynamic topography, and the elevation of the Apennines of Italy, *Earth Planet. Sci. Lett.* **407**, 163–174.
- Faccioli, E. (1991). Seismic amplification in the presence of geological and topographic irregularities,.
- Fan, G., and T. Lay (1998). Regionalized versus single-station wave-guide effects on seismic discriminants in Western China, *Bull. Seismol. Soc. Am.* **88**, 1260–1274.
- Gao, S., H. Liu, P.M. Davis, and L. Knopoff (1996). Localized amplification of seismic waves and correlation with damage due to the Northridge earthquake: evidence for focusing in Santa Monica, *Bull. Seismol. Soc. Am.* **86**, S209–S230.
- Geli, L., P.-Y. Bard, and B. Jullien (1988). The effect of topography on earthquake ground motion: a review and new results, *Bull. Seismol. Soc. Am.* **78**, 42–63.
- Goes, S., and S. Van Der Lee (2002). Thermal structure of the North American uppermost mantle inferred from seismic tomography, *J. Geophys. Res.* **107**, 2050.

- Griot, D., J. Montagner, and P. Tapponnier (1998). Phase velocity structure from Rayleigh and Love waves in Tibet and its neighboring regions, *J. Geophys. Res. Solid Earth* **103**, 21215–21232.
- Hamburger, M.W., and J.A. Rupp (1988). The June 1987 southeastern Illinois earthquake: Possible tectonism associated with the La Salle anticlinal belt, *Seismol. Res. Lett.* **59**, 151–157.
- Harris, N.B.W., M. Caddick, J. Kosler, S. Goswami, D. Vance, and A.G. Tindle (2004). The pressure–temperature–time path of migmatites from the Sikkim Himalaya, *J. Metamorph. Geol.* **22**, 249–264.
- Hasterok, D., and D.S. Chapman (2007). Continental thermal isostasy: 1. Methods and sensitivity, *J. Geophys. Res. Solid Earth* **112**.
- Hearn, T.M., and J.F. Ni (1994). Pn Velocities Beneath Continental Collision Zones: the Turkish-Iranian Plateau, *Geophys. J. Int.* **117**, 273–283.
- Helffrich, G.R., and B.J. Wood (2001). The Earth's mantle, *Nature* **412**, 501.
- Huestis, S., P. Molnar, and J. Oliver (1973). Regional Sn velocities and shear velocity in the upper mantle, *Bull. Seismol. Soc. Am.* **63**, 469–475.
- Hyndman, R.D., C.A. Currie, S. Mazzotti, and A. Frederiksen (2009). Temperature control of continental lithosphere elastic thickness, T_e vs V_s , *Earth Planet. Sci. Lett.* **277**, 539–548.
- Jackson, D.D., and D.L. Anderson (1970). Physical mechanisms of seismic-wave attenuation, *Rev. Geophys.* **8**, 1–63.

- Karato, S., and H.A. Spetzler (1990). Defect microdynamics in minerals and solid-state mechanisms of seismic wave attenuation and velocity dispersion in the mantle, *Rev. Geophys.* **28**, 399–421.
- Kawase, H., F. Nagashima, S. Matsushima, and F.J. Sánchez-Sesma (2014). Application of Horizontal-To- Vertical (H/V) Spectral Ratios for Both Microtremors and Earthquake Motions Based on the Diffuse Field Theory,.
- Kennedy, C.S., and G.C. Kennedy (1976). The equilibrium boundary between graphite and diamond, *J. Geophys. Res.* **81**, 2467–2470.
- Kennett, B. (1986). Lg waves and structural boundaries, *Bull. Seismol. Soc. Am.* **76**, 1133–1141.
- Kennett, G.A., F. Chaouloff, M. Marcou, and G. Curzon (1986). Female rats are more vulnerable than males in an animal model of depression: the possible role of serotonin, *Brain Res.* **382**, 416–421.
- Lees, J.M., and R.S. Crosson (1989). Tomographic inversion for three-dimensional velocity structure at Mount St. Helens using earthquake data, *J. Geophys. Res. Solid Earth* **94**, 5716–5728.
- Levandowski, W., R.B. Herrmann, R. Briggs, O. Boyd, and R. Gold (2018). An updated stress map of the continental United States reveals heterogeneous intraplate stress, *Nat. Geosci.* **11**, 433–437.
- Lowry, A.R., and M. Pérez-Gussinyé (2011). The role of crustal quartz in controlling Cordilleran deformation, *Nature* **471**, 353.
- MOSS, R.G. (1936). Buried pre-Cambrian surface in the United States, *Bull. Geol. Soc. Am.* **47**, 935–966.

- Murphy, J.R., and R.A. Mueller (1971). Seismic characteristics of underground nuclear detonations: Part II. Elastic energy and magnitude determinations, *Bull. Seismol. Soc. Am.* **61**, 1693–1704.
- Ni, J., and M. Barazangi (1983). High-frequency seismic wave propagation beneath the Indian Shield, Himalayan Arc, Tibetan Plateau and surrounding regions: high uppermost mantle velocities and efficient Sn propagation beneath Tibet, *Geophys. J. Int.* **72**, 665–689.
- Nuttli, O.W. (1980). The excitation and attenuation of seismic crustal phases in Iran, *Bull. Seismol. Soc. Am.* **70**, 469–485.
- Obermeier, S.F. (1998). Liquefaction evidence for strong earthquakes of Holocene and latest Pleistocene ages in the states of Indiana and Illinois, USA, *Eng. Geol.* **50**, 227–254.
- Obermeier, S.F., N.R. Bleuer, C.A. Munson, P.J. Munson, W.S. Martin, K.M. McWilliams, D.A. Tabaczynski, J.K. Odum, M. Rubin, and D.L. Eggert (1991). Evidence of strong earthquake shaking in the lower Wabash Valley from prehistoric liquefaction features, *Science (80-.)*. **251**, 1061–1063.
- Ottmöller, L. (2002). Lg wave Q tomography in Central America, *Geophys. J. Int.* **150**, 295–302.
- Pedersen, H., B. Le Brun, D. Hatzfeld, M. Campillo, and P.-Y. Bard (1994). Ground-motion amplitude across ridges, *Bull. Seismol. Soc. Am.* **84**, 1786–1800.
- Pollitz, F.F., and W.D. Mooney (2014). Seismic structure of the Central US crust and shallow upper mantle: Uniqueness of the Reelfoot Rift, *Earth Planet. Sci. Lett.* **402**, 157–166.

- Powell, C.A., G.A. Bollinger, M.C. Chapman, M.S. Sibol, A.C. Johnston, and R.L. Wheeler (1994). A seismotectonic model for the 300-kilometer-long eastern Tennessee seismic zone, *Science* (80-.). **264**, 686–688.
- Sato, H., and M. Fehler (1998). Scattering and attenuation of seismic waves in heterogeneous earth,.
- Stixrude, L., and C. Lithgow-Bertelloni (2007). Influence of phase transformations on lateral heterogeneity and dynamics in Earth's mantle, *Earth Planet. Sci. Lett.* **263**, 45–55.
- Tuttle, M.P., E.S. Schweig III, J. Campbell, P.M. Thomas, J.D. Sims, and R.H. Lafferty III (2005). Evidence for New Madrid earthquakes in AD 300 and 2350 BC, *Seismol. Res. Lett.* **76**, 489–501.
- Wald, D.J., and T.I. Allen (2007). Topographic slope as a proxy for seismic site conditions and amplification, *Bull. Seismol. Soc. Am.* **97**, 1379–1395.
- Warrell, K.F., R.T. Cox, R.D. Hatcher, J.D. Vaughn, and R. Counts (2017). Paleoseismic evidence for multiple $M_w \geq 6$ earthquakes in the eastern Tennessee seismic zone during the late quaternary, *Bull. Seismol. Soc. Am.* **107**, 1610–1624.
- Xie, J., and B.J. Mitchell (1990). A back-projection method for imaging large-scale lateral variations of Lg coda Q with application to continental Africa, *Geophys. J. Int.* **100**, 161–181.
- Xie, J., R. Gok, J. Ni, and Y. Aoki (2004). Lateral variations of crustal seismic attenuation along the INDEPTH profiles in Tibet from Lg Q inversion, *J. Geophys. Res. Solid Earth* **109**.

Zhang, Q., E. Sandvol, and M. Liu (2009). Lithospheric velocity structure of the New Madrid Seismic Zone: A joint teleseismic and local P tomographic study, *Geophys. Res. Lett.* **36**, 1–6.

3 Chapter 3: Investigation of the Regional Site Response in the Central and Eastern United States

Abstract

We have estimated the site amplification of regional high-frequency Lg seismic phases by a Reverse-Two Station (RTS) method using seismic events (Mw 4–6) recorded by Earthscope’s Transportable Array from 2010 to 2013. We compare regional site amplification estimates (horizontal and vertical) from the RTS technique with Horizontal-to-Vertical Spectral Ratio (HVSr) estimates derived from ambient noise and earthquake records. We compare the RTS results with (1) shallow shear-wave velocity estimates from near-surface (horizontal/vertical) ratios of the local body wave (initial P wave) method, and (2) high topography, basins and sediment thicknesses. Our RTS results show a strong positive correlation between regional site amplification and basins such as the Michigan basin, the Illinois basin, and the Mississippi embayment. In the case of the Illinois and Michigan basins, the higher the frequency, the higher the horizontal and vertical amplification. Waves passing through the Appalachian and Ozark plateaus are de-amplified on both vertical and horizontal ground components; however, the variation in amplification with frequency is larger for horizontal motion than vertical motion. In some regions, such as the western edge of the Appalachian basin and southern Illinois basin, vertical amplification decreases with frequency but horizontal amplification is essentially invariant with respect to frequency. Topography and sediment thickness are likely to

affect amplification and both factors likely frequency-dependent. There is a negative correlation between the RTS-measured amplification and shallow shear-wave velocity while HVSR shows a negative correlation only for low frequencies < 2.0 Hz. We conclude that regional ground motion amplification is clearly a function of more than one variable. In general, it appears that both regional topography (i.e., long-wavelength topography) and deeper subsurface seismic structures (basins and sediments) have a large impact on site amplification.

3.1 Introduction

Site response is a key component of seismic hazard analysis leading to pronounced fluctuations in ground motion even over relatively short distances (\sim 100s of meters; Imtiaz et al., 2015). Amplification of seismic waves can be thought of as the result of focusing and de-focusing of high frequency seismic waves (e.g., Gao et al., 1996; Davis et al., 2000; Nakamura, 2000; Mucciarelli and Gallipoli, 2001), and contrasts in elastic impedance (Murphy et al., 1971; Kramer, 1996). Impedance contrasts have been shown to influence ground motion even in the absence of attenuation and structural factors (e.g., Murphy et al., 1997; Davis et al., 2000). Many studies have been conducted to address how these factors combine to affect site response by simulating seismic records generated from different seismic velocity models, e.g., basins and mountains (Semblat et al., 2005; Pilz et al., 2011; Molnar et al., 2014; Maufroy et al., 2015).

Ground Motion Prediction Equations (GMPEs) were introduced to model the relationship among distance, magnitude and site response. In seismically active

regions with large numbers of seismic records, GMPEs can be found using regression analysis. In regions with few large earthquakes, such as the Central and Eastern U.S. (CEUS), stochastic methods are found to be effective in accurately simulating high-frequency ground motions (Hanks, 1979; Boore, 1983, 2003; Atkinson and Boore, 1995, 1997; Atkinson and Silva, 2000). A third approach to estimating site response is using proxies, such as the time-averaged shear-wave velocity in the upper 30 meters (V_{s30m}).

The spectral ratio approach to estimating site response defines the site response as a spectral ratio between a site deployed on sediments and a rock site. When the rock site is located close to the site of interest, or the rock and sediment sites are both located at one location (e.g. vertical seismic arrays), the method that is used is known as the Standard Spectral Ratio (SSR). The Horizontal-to-Vertical Spectral Ratio (HVSr) method using ambient noise or seismic data is found to be a convenient single site spectral-ratio method (Nakamura, 1989; Lermo and Chávez-García, 1993; Parolai et al., 2007). HVSr peak frequencies and amplitudes appear to be a function of both sediment thickness H and the time-averaged shear-wave velocity of the surface layer V_s (i.e. $f_0 = V_s/4H$, where f_0 is the theoretical resonance frequency in Hz; Haskell, 1960; Borchardt, 1970). Although HVSr results correlate with surface geology, it is not a reliable measurement of the amplification of seismic waves (Pilz et al., 2009; Massa et al., 2011). It may underestimate the amplification factor and cannot be applied to rock sites because the amplification will be unity.

A more common approach to estimating site amplification is to measure V_{s30m} and use it as a proxy for site amplification (Borchardt, 1992, 1994, 2004;

Petersen et al., 2008; Boore et al., 2014; Campbell and Bozorgnia, 2014). Low Vs30m values are associated with high amplification and high ground motion while high Vs30m values are associated with sites located on rock and having smaller ground motion. For site-specific applications, Vs30m can now be measured precisely using active or passive seismic methods which have become cost-effective in recent years. For regional applications, proxies such as topographic slope (Wald and Allen, 2007) from the 3D Digital Elevation Model (DEM) have been used. Using topographic slope as proxy introduces further bias and increases the uncertainty in the site classification process. Although many people have proposed Vs30m as a good proxy for site amplification (e.g., Hartzell et al., 2001; Boore et al., 2014), several other studies have shown that Vs30m measurements may not provide a good measure of site amplification (Wald and Mori, 2000; Mucciarelli and Gallipoli, 2006; Hassani and Atkinson, 2016). It may be that Vs30m derived site amplification may work for the western U.S. (e.g. Boore et al., 2014; Campbell and Bozorgnia, 2014; Chiou and Youngs, 2014) but does not work in CEUS (Hassani and Atkinson, 2016).

The Reverse Two-Station (RTS) method, often used to measure high-frequency wave attenuation (Chun et al., 1987), can also be used to estimate site response (Bao et al., 2011). This method requires a specific geometric condition where two seismic stations and two seismic events align along a great circle path within regional distances. The USArray Transportable Array (TA) provides us with the ability to apply this method in the CEUS due to its high density (70 km spacing between stations). One of the things that makes the RTS method unique and

important for this region is that it allows us to estimate the vertical and horizontal regional site amplification.

The Lg wave is a high-frequency guided wave that travels exclusively in the crust with a frequency band of 0.5 to 10 Hz and a group velocity of 3.0 to 3.6 km/s (Aki, 1980). This wave is observed at regional distances of 200 to 1500 km (Chun et al., 1987). The Lg phase has the largest amplitude for seismic records with paths entirely in the continental crust (Aki and Richards, 2002). The Lg phase is also sensitive to crustal velocity heterogeneity and it may be a good proxy for estimating bulk crustal attenuation of the crust.

CEUS earthquakes are not the largest earthquakes in North America, but they cause more widespread damage than earthquakes in the western U.S. (Johnston, 1989; Hough and Page, 2011). This is partly because Lg attenuation is less in the eastern U.S. than the western U.S. (Gallegos et al., 2014; McNamara et al., 2015; Chapman, 2015), which formed as a result of the collision and accretion of numerous terrains during events that took place from 1.9 to 1.7 Ga (Bickford et al., 1986).

The main geological features in the CEUS include the Appalachian-Ouachita orogenic belt (450–350 Ma), consisting of Precambrian and Cambrian metamorphosed rock with igneous intrusions; the coastal plain extending along the Atlantic Ocean and Gulf of Mexico; and the central United States, a platform mantled by Paleozoic and Mesozoic sedimentary rocks with limited tectonic activity since the Paleozoic (Moss, 1936; Baqer and Mitchell, 1998). Pleistocene glaciation (2.58 Ma to present) has affected large parts of the North American continent via the deposition of glacial sediments (Gradstein et al., 2004). CEUS basins are mostly of Paleozoic age

(e.g., the Illinois, Michigan, and Appalachian basins). The Appalachian basin is composed of two sedimentary Appalachians provinces: the Appalachian plateau and the Valley and Ridge (Fig. 1). The Mississippi embayment is a large Mesozoic basin associated with the Reelfoot Rift basin and the Black Warrior and Arkoma foreland basins (Coleman and Cahan, 2012). Within the Mississippi embayment, sediments have a maximum thickness of about 1000 m.

The goal of this paper is to use the RTS method to estimate Lg vertical and horizontal ground motion amplification in the CEUS. We will also use HVSR to compare with RTS estimates of site amplification. Finally, we will compare shallow shear-wave velocities (V_s) and our RTS site amplification estimates to determine how correlated these values are.

3.2 Data and Methods

The TA network consisted of 400 broadband portable seismometers with a station spacing of approximately 70 km. This network was continually moved eastward beginning on the west coast in 2004, with the typical deployment time being 18 months. By the end of its deployment in the contiguous United States, the TA network consisted of approximately 2000 stations, all of which recorded continuously.

Forty events were extracted from the continuous data recorded over the years 2010 to 2013. The earthquake data set consists of events with local magnitudes ranging between 4 to 6 M_l and epicentral distances ranging between 250 and 2000 km and a maximum hypocentral depth of 40 km. The minimum epicentral distance of 250

km guarantees that the Lg wave has formed while the maximum hypocentral depth of 40 km ensures that the event occurred in the crust. Most stations deployed at the edges of the CEUS have a limited number of regional seismic recordings compared with stations located in the central study region (see electronic supplement Figures S1 and S2). The arrival times of the phases were picked manually by Gallegos et al., (2014). The Lg windows were carefully picked to avoid Sn and Rayleigh wave contamination. Instrument responses were removed and transformed into the frequency domain using Fast Fourier Transform (FFT) and a 20% cosine taper window. Only spectra with a signal-to-noise ratio greater than 2.0 were used for further processing (Table S1, available in the electronic supplement).

3.2.1 HVSR Method

Nakamura (1989) suggested that for thick sedimentary basins, the peak of the HVSR of ambient seismic noise measurements correlates well with the peak of the fundamental resonance frequency F_0 , a particular frequency having the strongest effect within the seismic waves. Lermo and Chávez-García (1993) proposed applying the Nakamura method to the shear-wave portion of weak-motion earthquake recordings. This application of HVSR can be described using equation (1) below:

$$HVSR = \frac{H(f)_S}{V(f)_S} = \sqrt{\frac{(H(f)_N^2 + H(f)_E^2)}{2}}{V(f)_S}, \quad (1)$$

where HVSR is defined as the ratio of the horizontal amplitude spectra $H(f)_S$ and the vertical amplitude spectra $V(f)_S$ of ground motion at the ground surface. $H(f)_N$ and $H(f)_E$ are the north-south and east-west components, respectively. The key assumption in the HVSR method is that the vertical and horizontal motions recorded on bedrock are equal; however, this is often not the case (e.g., Woolery et al., 2016).

Whether or not the HVSR method measures the amplification of the ground motion has long been a source of debate. Carpenter et al. (2018) used borehole seismic records to show that the HVSR overestimates the low-frequency amplification near the fundamental frequency and they observed that HVSR from ambient noise recordings are not a good measure of the S-wave transfer function at borehole sites. Parolai et al. (2007) have shown that the HVSR and SSR methods provide similar results. In this study, we will consider HVSR maximum peak values < 2.0 as deamplification and HVSR maximum peaks > 2.0 as evidence of site amplification based on the SESAME guidelines for the clear peak (Bard et al., 2004).

J-SESAME (Site Effects assessment using AMbient Excitations) is a software package developed under the European research project SESAME. We use J-SESAME to analyze both earthquake records and ambient noise via the following steps:

- 1) We cut the seismic record into windows between the arrival time of S-waves and a group velocity of 3 km/s. This time window includes Sn and Lg regional phases. For the ambient noise analysis, a 50 sec window of ambient noise recorded before the P wave arrival time is selected.
- 2) A 5% cosine taper is applied to the windowed time series.
- 3) A FFT is applied to each window.
- 4) We smooth the three components using the method of Konno and Ohmachi (1998), as recommended in the J-SESAME guidelines (Bard et al., 2004).

- 5) We then merge the horizontal spectra using the geometric mean and divide it by the vertical spectrum.
- 6) The ratio of each window is combined into an averaged spectrum.
- 7) The output files contain the H/V spectral ratio. The largest peak of the spectral ratio occurs at the fundamental frequency F_0 .

The parameters used in this study are shown in Table 1.

3.2.2 *RTS Method*

The RTS method was first introduced by Chun et al. (1987) and was modified by Bao et al. (2011) to estimate the site response. The RTS geometry requires a station pair and an event pair, where each individual event is located on either side of the station pair in a narrow azimuthal window. Ideally, these event and station pairs will align along a great circle path; however, a more realistic requirement is to allow the source-to-station azimuths to vary up to $\pm 15^\circ$ in either direction. Each event is recorded by the station pair, resulting in an amplitude ratio for each event. We can define a seismic amplitude as

$$A(f) = S(f)R(f)I(f)S_s(f)G(d)e^{-\frac{\pi f d}{vQ(f)}}, \quad (2)$$

where A is the observed amplitude between the source and the receiver for a wave of frequency (f) recorded at epicentral distance d , R is the focal mechanism factor which is a function of path azimuth, I is the instrument response, S is the source excitation function, S_s is the site amplification response, v is the wave group velocity, Q is the attenuation quality factor, and G is the geometric spreading function, which defines the exponential decay with distance. To isolate the relative site response using the

RTS method, the amplitude ratios of a pair of events a and b recorded by stations i and j are multiplied, resulting in equation (3) below (see Appendix A):

$$\ln Ss_i - \ln Ss_j = \ln \frac{I_j}{I_i} + \frac{d_{aj} - d_{ai}}{d_{aj} + d_{bi} - d_{ai} - d_{bj}} \ln \frac{A_{ai} d_{ai}^m}{A_{aj} d_{aj}^m} + \frac{d_{bi} - d_{bj}}{d_{aj} + d_{bi} - d_{ai} - d_{bj}} \ln \frac{A_{bi} d_{bi}^m}{A_{bj} d_{bj}^m},$$

(3)

where the geometric spreading factor m is assumed to be 0.5 at distances greater than 2.5° (Yang, 2002).

If the site response for one station in the network is known, equation (3) can be used to solve for the absolute site response for all stations. Thus, a reference station or stations is required. An ideal reference station would have an HVSR value of 1.0 (rock site); however, in this study we selected reference stations with HVSR values ≤ 2.0 . Using the reference stations, we employ the LSQR algorithm (Paige and Saunders, 1982) to solve for the absolute site response terms based on relative site responses resulting from the RTS method. In order to apply LSQR, we pose equation (3) as an inverse problem $\mathbf{d}=\mathbf{G}\mathbf{m}$, where \mathbf{d} is a vector consisting of the terms on the right side of equation (3), \mathbf{G} is a sparse matrix denoting the station pair, and the model \mathbf{m} is defined as the logarithm of the site responses Ss of each station (see Appendix A). We consider a negative $\log(Ss)$ value as a deamplification of ground motion and a positive $\log(Ss)$ value as an amplification of ground motion with respect to the network average for the entire CEUS. We apply the RTS method to both vertical and horizontal (radial) components, resulting in vertical and horizontal amplifications.

3.3 Results

3.3.1 HVSR Method

We apply the HVSR method to earthquake seismic records (EQ_HVSR) and to ambient seismic noise preceding the main seismic events (NOISE_HVSR). We observe an F_0 of roughly 3.0 to 5.0 Hz along the Appalachians and low F_0 values of 0.5 to 1.5 Hz along the Coastal Plain, Mississippi embayment and Michigan basin (Figs. 2a and 2b). We find that F_0 has a negative correlation with sediment thickness and a positive correlation with topography. These correlations may be related to thin sediments and to the focusing of seismic waves that occurs at topographic crests (Massa et al., 2010; Pischiutta et al., 2010; Marzorati et al., 2011; Massa et al., 2014).

The HVSR results (Figs. 3a and 3b) show a correlation between the HVSR and major geologic features, such as the Mississippi Embayment in the south where HVSR generally has lower to medium values (1-3). We observed lower HVSR values (0-2) along the Appalachian Mountains and very high HVSR values (4-8) for the glaciated sediments in the northern CEUS.

The HVSR for earthquake seismic data and ambient noise were examined by comparing the two HVSR records from various stations across different geologic provinces. Figure 4 shows HVSR result for stations A28A and E38A, both located in the northern CEUS. At E38A we observe a high amplitude, narrow peak, while at A28A we see multiple peaks and a lower amplitude than E38A (Fig. 4a). The HVSR curves for stations Z35A and 244A, located in the Gulf Coastal Plain (Figs. 4c and 4d), show multiple peaks without a clear maximum peak. We note that most EQ_HVSR have higher amplitudes than NOISE_HVSR. The

EQ_HVSR/NOISE_HVSR ratio (Fig.S3) and the Probability Density Functions (PDFs) of EQ_HVSR and NOISE_HVSR (Fig.5a) show clearly how the two results differ. In order to specify the probability of an HVSR value falling within a particular range of values, we estimate the PDFs. The lack of overlap in the PDF's suggest that there is a systematic differences in the HVSR for noise and earthquake seismograms: PDFs of the HVSR results are shown: $(0.8 < \text{HVSR (EQ/Noise)} < 1.8) \sim 98\%$, suggesting that most of the EQ_HVSR values are higher than the NOISE_HVSR.; $(0.8 < F_0(\text{EQ/Noise}) < 1.2) \sim 92 \%$; $(F_0(\text{EQ/Noise}) = 1) \sim 45\%$, which clearly show that most of the F_0 values are similar for ambient noise and earthquake data. We also investigate the difference between EQ_HVSR and NOISE_HVSR in various frequency bands (Figs. 5b and 5c) and find that there are consistent differences in noise and earthquake F_0 values for $F_0 < 2.5$ Hz. For larger F_0 values, noise and earthquake derived estimates are essentially the same on average. We find that HVSR amplitude values derived from earthquake and noise data consistently differ (mostly EQ-HVSR > NOISE_HVSR) at all frequencies, particularly at $F_0 > 5$ Hz and $F_0 < 1.5$ Hz.

In the north-central U.S, the basement is mostly composed of high-grade metamorphic rocks overlain by a thin layer of poorly consolidated sediments (Reed and Bush, 2005). These sediments vary from glacial to non-glacial sediments and their thickness varies from 0 to 152 m (Fullerton et al., 2003); therefore, this region is valuable for studying the effect of very thin local sediments on site amplification. Figure 6 shows that in southeastern Wisconsin, seismic stations were located on outcrops of sedimentary rocks (dolostone) covered with thin layers of glacial till. In

northern Wisconsin, metamorphic rocks are covered with coarse glacial sediments. In southwestern Wisconsin, the bedrock is exposed or covered with Quaternary sediments. For stations located on glacial sediments and sedimentary rocks, HVSR amplitudes are found to range from 0.9 to 3.0. The HVSR amplitudes of stations located on glacial sediments and metamorphic rocks ranges from 3.8 to 8.0. For stations deployed on exposed bedrock, we find HVSR values ranging from 2.0 to 4.5. The fundamental frequency F_0 shows a negative correlation with sediment thickness in this region (Fig. S4). This example shows the variation in HVSR results based on the local surface geology. The glaciated sediments amplify HVSR values because of the high impedance contrast and F_0 increases with decreasing sediments thickness.

3.3.2 RTS Method

An important issue regarding our results is the stability of both the RTS and HVSR estimates. We tested the stability of our RTS site amplification model by choosing several different reference stations; this is necessary because the RTS method provides estimates of the relative site amplification and a reference station(s) is required to formulate an absolute site amplification model. We find that processing the RTS using various reference stations results in similar site amplification models. Thus, for simplicity we select a station (060A) with an HVSR value near 1.0 as our reference station (HVSR ~ 1.7 at $F_0 = 0.9$ Hz; Figure 7).

The site amplification is estimated over four frequency bands with central frequencies of 1.0, 2.0, 3.0, and 4.0 Hz, each with a bandwidth of 1 Hz. The frequency range of RTS method was found to be 0.5- 4.5 Hz because of a limited number of raypaths in this region (Gallegos et al., 2014). The RTS horizontal

amplification increases with increasing frequency while the vertical RTS amplification shows a weak negative trend with increasing frequency (Fig 8). For both the vertical and horizontal RTS results, we observe deamplification throughout most of the eastern Appalachian basin as well as in most of Kentucky and Missouri, while we observe strong amplification of Lg for stations in the Paleozoic basins (Michigan, Illinois) and the Mississippi embayment (Figs. 9 and 10) (see Figs. S5 and S6 in the electronic supplement); however, the range of site amplification differs between the horizontal and vertical RTS estimates. We compute the PDFs of the horizontal and vertical site amplifications for the frequency ranges defined above. We find that the vertical and horizontal amplification models tend to have similar PDFs at central frequency 4.0 Hz (Fig. S7). Figure 11 shows the horizontal to vertical ratio of RTS. The horizontal values are higher than the vertical values in the basins, while the vertical values are higher than the horizontal values for stations located in the mountains and plateaus. For the 2.0 Hz band, horizontal site amplification increased in northern Missouri, Indiana, Ohio, and eastern Wisconsin. For the 3.0 and 4.0 Hz bands, horizontal site amplification increased across Indiana, Ohio, Kansas, and Nebraska. For vertical amplification and frequencies ranging from 2.0 to 4.0 Hz, deamplification was observed in Kansas, Oklahoma, Indiana and Ohio (Fig.11).

To compare the vertical RTS, horizontal RTS and HVSR results, we must first discuss the contents of the time window used in the HVSR method, which includes both the Sn and Lg regional phases. The spectrum of this time window will be dominated by the Lg phase, which is much larger than Sn over continental paths. This time window, also used in the PEER 2014/17 - PEER NGA-East Database (Goulet et

al., 2014), is named SLg. Lg has previously been modeled as the superposition of S-wave reverberations within the continental crust (Bouchon, 1982; Storchak et al., 2003).

In the following section, we only discuss results from stations included in both analyses. All data sets are normalized by sorting the RTS and HVSR estimates into two groups: sites of deamplification and sites of amplification. We perform this sorting by defining RTS estimates < 1.0 and HVSR estimates < 2.0 as deamplified, while RTS estimates > 1.0 and HVSR estimates > 2.0 are classified as amplified. We now correlate the three normalized data sets. Figure 12 shows that at 1.0 Hz, the HVSR, horizontal RTS and vertical RTS have a positive correlation within the major basins. At 3.0 Hz, the horizontal RTS and HVSR show a positive correlation increasing towards the mountains/higher topography while the vertical RTS and HVSR show less correlation or a negative correlation for the same frequency band (see Figs. S8 and S9 for results at central frequencies of 2.0 Hz and 4.0 Hz, respectively).

3.4 Discussion

We observe a reasonably good correlation between topography and RTS site amplification. Large horizontal and vertical amplifications were observed for stations located in the basins; however, the vertical amplification values are less than the horizontal amplifications. In the mountains and Ozark plateau, the vertical RTS shows little to no amplification as compared with the horizontal RTS values, which shows a strong deamplification (Figs. 9 and 10). We found few positive site terms

(amplifications) within mountain belts, especially at higher frequencies (> 3.0 Hz). The RTS results in this study show a strong change in frequency dependence based on topography. For example, in basins such as the Illinois and Michigan basins, higher frequencies result in higher horizontal and vertical amplification. Yet in eastern Ohio and western Arkansas, vertical amplification decreases with increasing frequency, while horizontal amplification is essentially invariant.

Overall, the horizontal RTS to vertical RTS ratio (H/V) (Fig. 11) shows that horizontal amplification is larger for higher frequencies (3-4 Hz) in basins (e.g., Michigan, Illinois and the Mississippi embayment). H/V from the RTS method are observed to increase from the Appalachians towards the western edge of the Appalachian basin (e.g., eastern Ohio). The differential amplification between the Paleozoic basins, such as the Michigan, Illinois and Appalachian basins, can be explained by the thickness of the sediments in these regions (Figure S10). The Appalachian basin consists of a thick Paleozoic sediment and is much thicker (8-10 km) compared with other basins (2.5-4 km; Mooney et al., 2010).

The relationship between RTS amplification and sediment thickness is estimated using a linear regression over the four frequency bands defined in the prior section. The results at central frequencies of 1.0 Hz and 2.0 Hz can be seen in Figure 13 (results at central frequencies of 3.0 Hz and 4.0 Hz are shown in Figure S11), which shows a weak positive correlation between horizontal RTS and sediment thicknesses ≤ 4 km and a weak negative correlation with sediment thicknesses > 4 km. The vertical RTS trend is weaker than the horizontal RTS. The correlation between vertical and horizontal RTS amplifications and sediment thickness decreases

with increasing central frequency. We compute the p-value in order to determine the correlation between each frequency band and sediment thickness; the p-value is defined as the probability of obtaining a more extreme result than what was actually observed based on chance alone. P-values < 0.05 refer to a statistically significant model, indicating that the observed pattern is unlikely to be the result of a random process. For RTS amplifications measured in areas where sediment thicknesses are ≤ 4 km, our p-value results suggest that although there is large scatter in the data, as expressed by their small R^2 values, the weak trend we observe between the RTS results and sediment thickness is statistically significant. Thus, there are likely several other factors in addition to sediment thickness that have a significant impact on site terms in the CEUS. These factors may include the topographic wavelength and Moho depth in the CEUS as we will briefly describe below.

Based on how regional waves propagate, we would expect the relationship between the width of the topography and the seismic wavelength to be a very important factor in controlling site amplification. When the width and wavelengths are similar, amplification is likely to occur whereas when they differ significantly, deamplification or no amplification along the topographic slopes is observed (Massa et al., 2014). The Lg phase wavelength ranges between 0.5 and 35 km based on the frequency bands we applied. Further, because the Lg phase is sensitive to variations in crustal properties (Kennett, 1986), the depth to the Moho in the CEUS (Shen et al., 2016) may play a role in site amplification of the Lg phase. In the future, it will be important to combine modelling and observational studies of regional phase site

amplification and topography in order to fully understand the regional site response in the CEUS.

We now go on to compare our results with those of previous studies. Historic macroseismic data from NMSZ earthquakes (Hough, 2011) show a high intensity band along a narrow corridor running along the southern boundaries of Illinois, Ohio, Kentucky, and Indiana. We observe high RTS amplification values at central frequencies of 3 Hz and 4 Hz in the same area. Another high intensity corridor extends southeast toward South Carolina (Hough, 2011). Unfortunately, our RTS model does not have sufficient coverage in this part of the CEUS, although we do find large HVSR values in this region (Fig. S12).

Our results are generally consistent with Bao et al. (2011), who attributed site response variation in Tibet to changes in topography. Comparing the RTS results for the CEUS with the model determined by Bao et al. (2011) for Tibet shows the amplification range of the CEUS is smaller. Thus, the CEUS shows less amplification overall than the Tibetan plateau and its surrounding basins.

We have also used our RTS and HVSR estimates to evaluate how good of proxy shallow V_s is for site amplification. Ni et al. (2014) used seismic records from TA to model the H/V ratio of the initial portion of local P waves in order to estimate the shallow V_s for each station in the TA array. They found most of the fast, shallow velocities correspond to stations at relatively high elevations (e.g., the Appalachian Mountains and the Ozarks plateau) while slow shallow V_s correspond to basins (e.g., Mississippi embayment and Illinois basins). In Figure 14, we compare all of our measurements, including the vertical and horizontal RTS amplifications and the

HVSR values, to a published shallow V_s model (Ni et al., 2014) in the northern Mississippi Embayment. Shallow V_s correlates weakly with HVSR and correlates fairly with the vertical RTS amplification. For the horizontal RTS amplification, a strong correlation with the shallow V_s is observed although the two methods differ greatly in concept and were applied using different seismic phases. These similarities likely demonstrate that low V_s values correlate with high horizontal RTS amplification. Furthermore, note that in comparison with the horizontal RTS results, faster near-surface velocities (>1500 m/s) appear to reduce the strength of vertical RTS deamplification (Fig. 14d). (For further comparisons between V_s , F_0 , and HVSR see the electronic supplement Figs S13 and S14).

In order to generate quantitative models, the shallow V_s model from Ni et al. (2014; Fig. 15) is systematically compared with the RTS and HVSR results for all TA stations. First, we regroup the shallow shear-wave velocities into specific velocity ranges based on seismic site classifications defined in the International Building Code (IBC), which has been adopted by the National Earthquake Hazard Reduction Program (NEHRP) design provisions for new buildings. The sites were classified into six classes based on V_{s30m} (Table 2). We then use boxplots to show how HVSR and amplification RTS relate to shallow velocities.

In order to show the relationship between the F_0 and V_s , the boxplots show a very clear correlation between F_0 and shallow V_s values. Increasing velocity correlates well with increasing F_0 (Fig. 15b); however, we do not see a correlation between shallow V_s and HVSR amplitude for the 0.5-10 Hz frequency band (Fig. 15a). Using the same narrow frequency bands used to calculate RTS values, we again

compare HVSR and shear-wave velocity. From 0.5-1.5 Hz we see little correlation between HVSR and shear-wave velocity (Fig. 15c). From 1.5-2.5 Hz, there is a strong positive trend (Fig. 15d). Both the 2.5-3.5 Hz and the 3.5-4.5 Hz frequency bands show a weak positive trend (Fig. S16). A negative correlation between the shallow V_s and the horizontal and vertical RTS amplification values, respectively, can be seen at a central frequency of 1.0 Hz (Figs. 15e, g). Note that horizontal ground motions are deamplified for $V_s > 1500$ m/s (Fig. 15e). At higher frequencies (1.5-2.5Hz), a similar negative trend with V_s is observed for both horizontal and vertical RTS measurements (Figs. 15f, h and S17). Figure 16 shows a linear regression analysis for HVSR measurements as compared to shallow shear-wave velocity. We see that HVSR has a negative trend for the 0.5-1.5 Hz frequency band, with a reasonably large R^2 and significant p-values ($R^2=0.8$, $p=0.03$). Similarly, Figure 17 shows a regression analysis for all horizontal and vertical RTS amplification results as compared to shallow shear-wave velocity. We observe clear negative trends for all frequency bands, although this trend is relatively weak in some cases (e.g. Fig. 17h). Simulating high frequency wave ground motions shows that ground motion is strongly affected by the geometry of the basin and the mountains (Lee et al., 2008, 2009). More specifically the amplification of ground motions is mainly controlled by basin depth, shallow shear-wave speeds, and surface topography.

3.5 Conclusions

In this study, we have used the RTS method to estimate the site amplification of regional seismic waves in the CEUS. We find that regional amplification is a

multivariate function. It correlates with basins, high topography, sediment thickness and upper crustal seismic velocity structure. We estimated both horizontal and vertical regional amplification and our results show the following: the effect of topography is strongly frequency dependent, the horizontal and vertical ground motion strongly differ due to topographic effects, and the Lg phase is strongly amplified within shallow basins. The HVSR of ambient noise and the HVSR of earthquakes are similar with respect to the fundamental frequency; however, they increasingly differ in regions with more geological complexity. In particular, glacial sediments amplify regional high-frequency seismic waves. Based on these results, it is important to include regional seismic response with local site response in order to fully assess seismic hazard in the central and eastern United States.

3.6 Data and Resources

The data used in this study were collected from IRIS Data Management Center at www.iris.edu (last accessed January 2016). Some of the GIS data were downloaded from <http://www.ceus-ssc.com/Report/GIS.html> (last accessed December 2018). The Vs30m measurements were downloaded from the USGS website <https://earthquake.usgs.gov/data/vs30/us/> (last accessed December 2017). All figures were generated using Generic Mapping Tools (GMT) (www.soest.hawaii.edu/gmt, last accessed February 2018), Matlab (www.mathworks.com/products/matlab/, last accessed March 2018), A mapping package for Matlab (M-map, www.eoas.ubc.ca/~rich/map.html, last accessed January 2019). and Geographic Information System (GIS, www.esri.com, last accessed January 2019).

3.7 Acknowledgments

The authors are very grateful for Tom Pratt and anonymous reviewers for their constructive comments that improved the manuscript. The authors would also like to thank Muawia Barazangi and Francisco Gomez for their editorial help. This work was financially supported by U.S. Survey–National Earthquake Hazards Reduction Program (NEHRP) (Award GP14AP00036)

3.8 Tables

Table 1. The parameters used to process HVSR in J-SESAME.

Window length	50 seconds
Merging	Geometric (Bard et al., 2004)
Smoothing	Konno & Ohmachi (Konno and Ohmachi, 1998); Bard et al., 2004).
Bandwidth	40
Tapering	0.5%

Table 2. Definition of NEHRP Site Classifications in Terms of V_{s30m} .

Description	Site Class	Shear wave velocity (V_s)
Hard rock	A	>1500 (m/s)
Rock	B	760-1500 (m/s)
Soft rock	C	360-760 (m/s)

Stiff soil	D	180-360 (m/s)
Soft Clay	E	<180 (m/s)

3.9 Figures

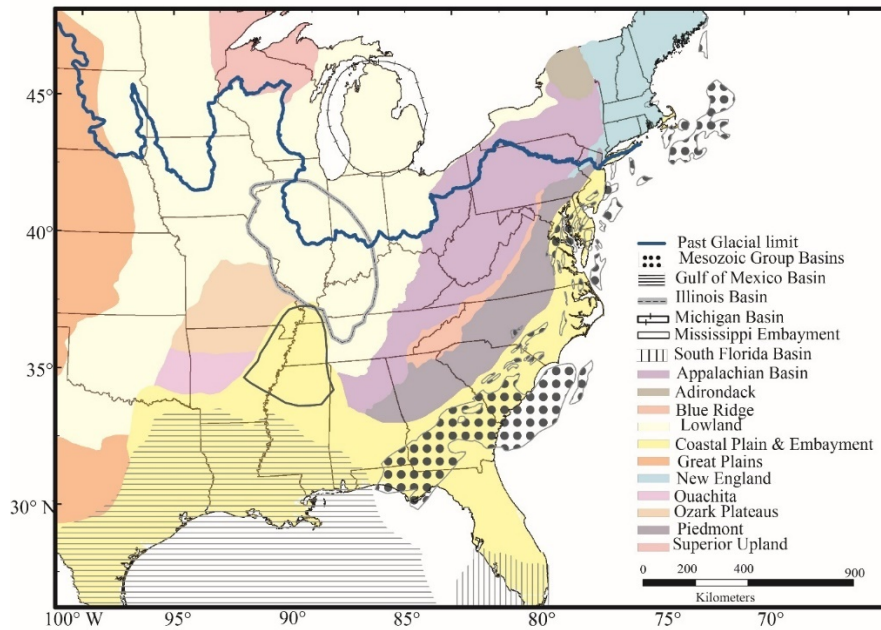


Figure 3.1. Map of the Central and Eastern U.S. (CEUS), including the main geologic provinces and the limits of continental glaciers from the last major ice ages.

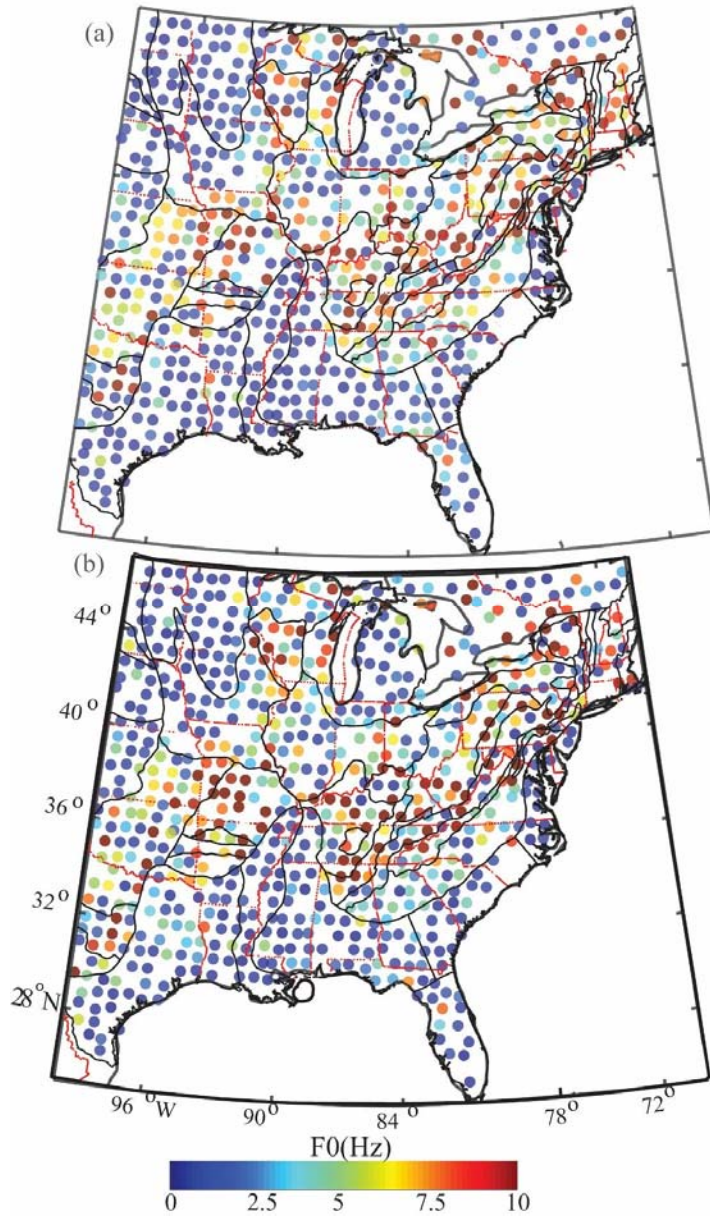


Figure 3.2. (a) The fundamental frequency (F_0) from ambient noise Noise_HVSR, (b) the fundamental frequency (F_0) from earthquake records EQ_HVSR. Note the high F_0 values in the Appalachians (red) and low F_0 values in the coastal plains (blue).

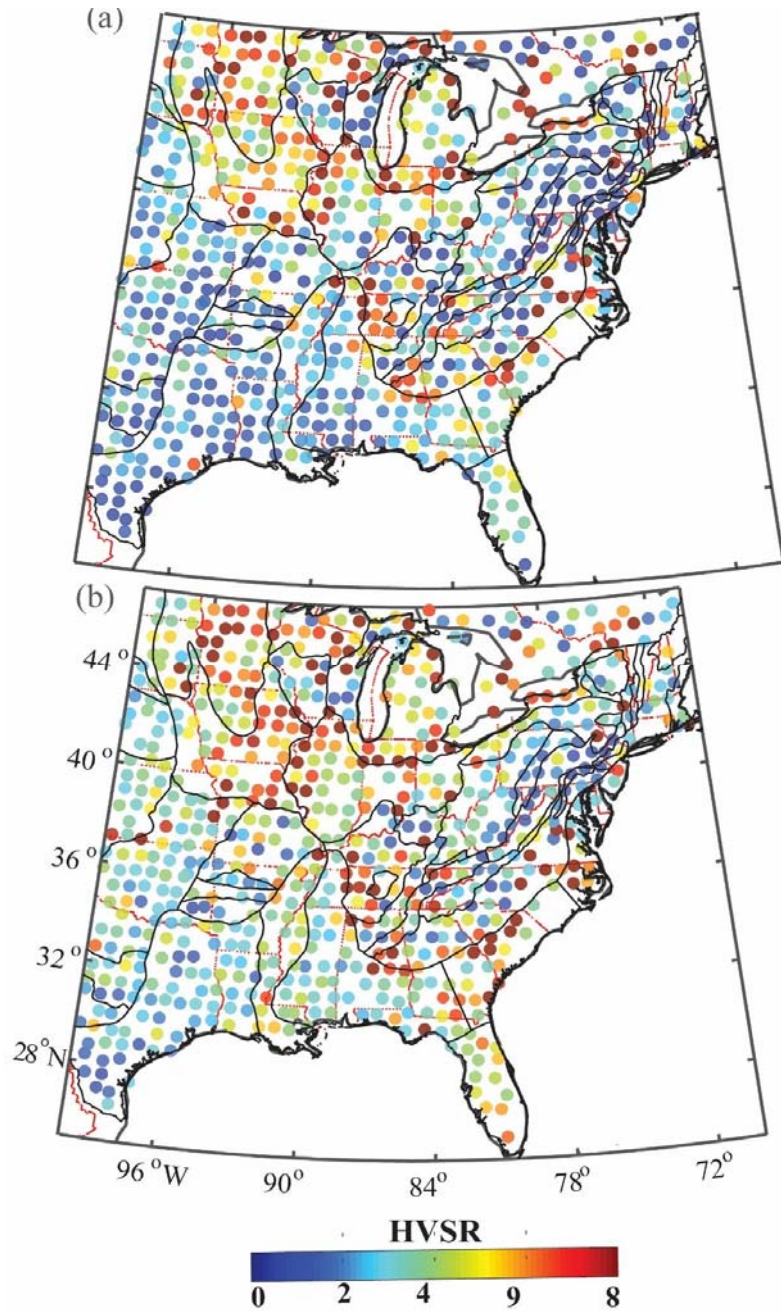


Figure 3.3. (a) The maximum peak HVSr values from ambient noise (Noise_HVSr), (b) The maximum peak HVSr values from earthquake records (EQ_HVSr). Note the high HVSr values (red) in regions covered in the past by glaciation.

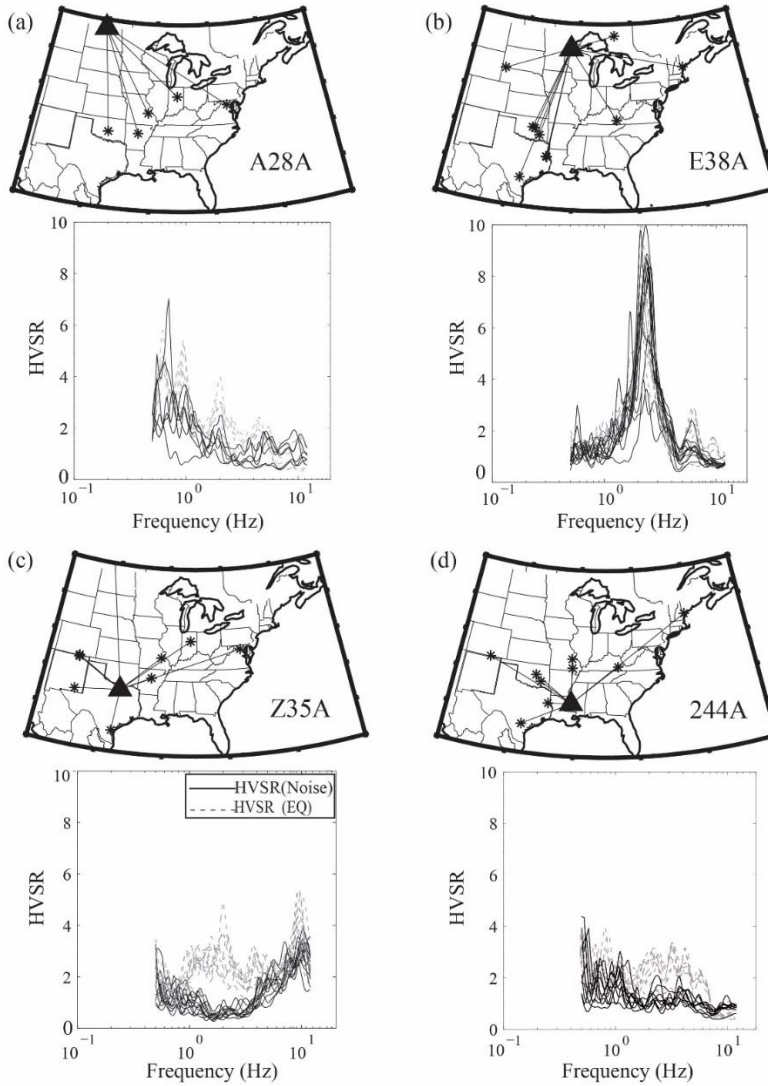


Figure 3.4. HVSR values recorded at four stations. Station (triangle) and event (star) locations are shown at the top of (a), (b), (c), and (d), respectively, with solid lines representing path. In the HVSR plots at bottom, all lines represent a horizontal to vertical spectral ratio recorded at a particular station, with dashed lines representing the HVSRs of earthquake records and solid lines representing the HVSRs of ambient noise. Note the difference in peak frequencies and amplitudes between the ambient noise and earthquake records.

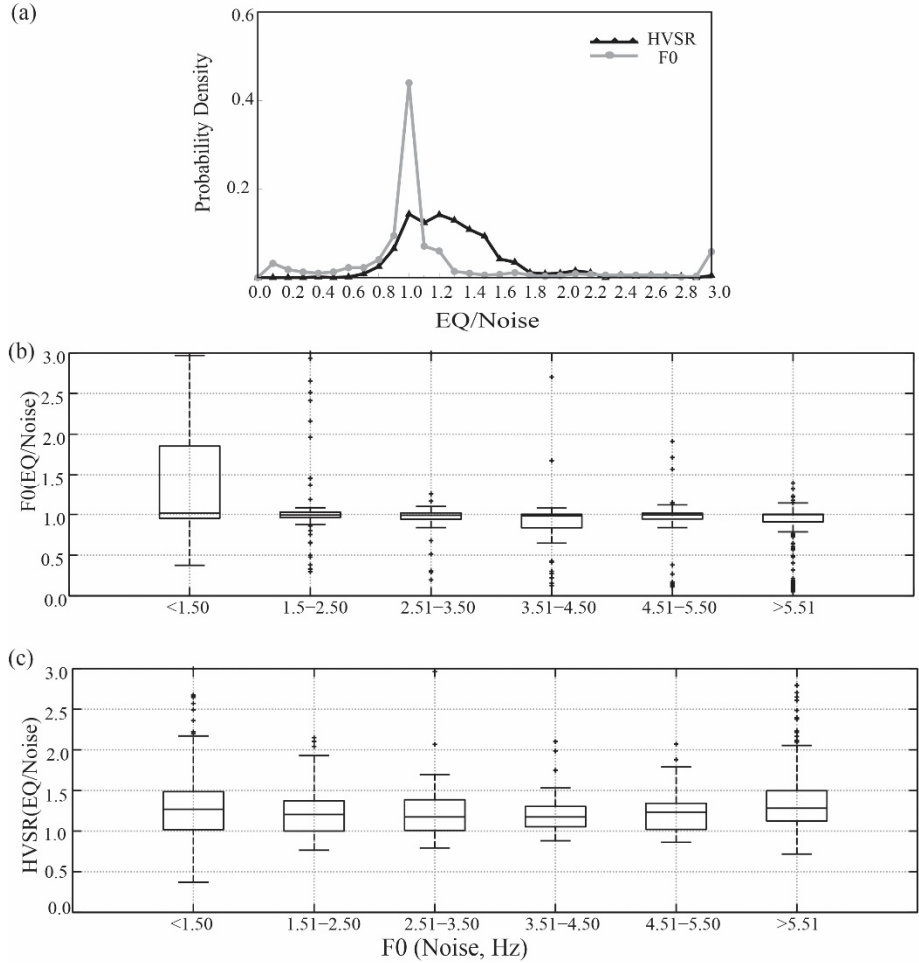


Figure 3.5. (a) The probability density of HVSr (EQ_HVSr/Noise_HVSr) and F_0 (EQ_HVSr/Noise_HVSr). The gray circles represent F_0 and the black triangles represent HVSr. (b) F_0 ratios versus frequency band 0.5-10Hz. (c) HVSr ratios versus frequency band 0.5-10Hz. $F_0 < 2.5$ Hz shows a high discrepancy between EQ_HVSr and Noise_HVSr for both F_0 and HVSr.

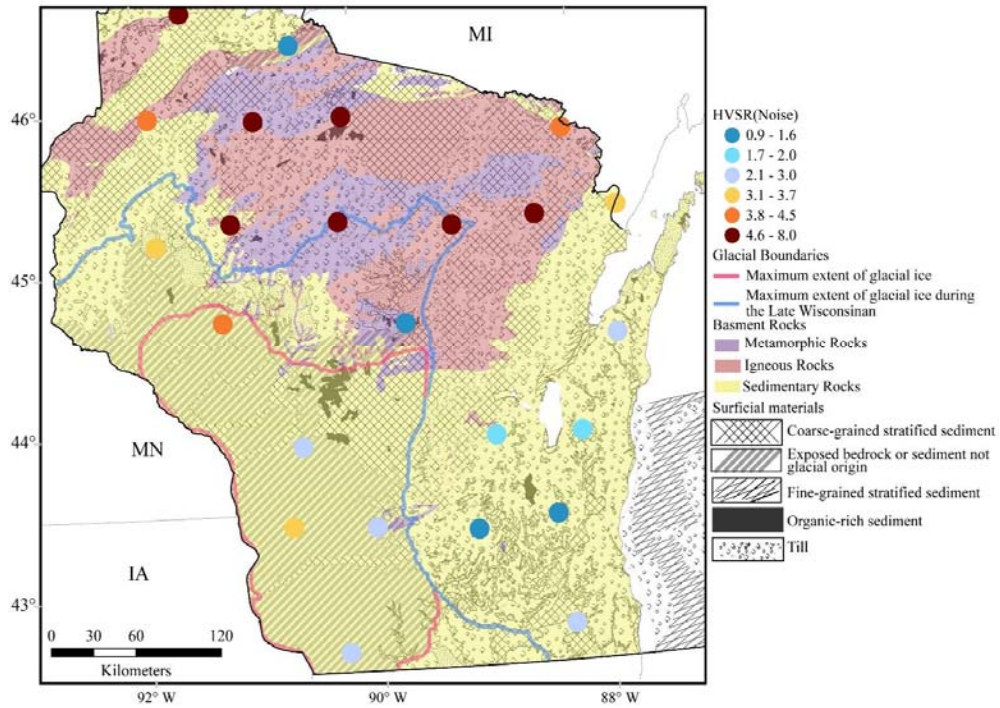


Figure 3.6. A simplified geologic map of Wisconsin and its subsurface geology. Note that the HVSR (Noise) is high in the north (metamorphic rocks) compared with the south (sedimentary rocks; see Fig. S4 for F_0 map).

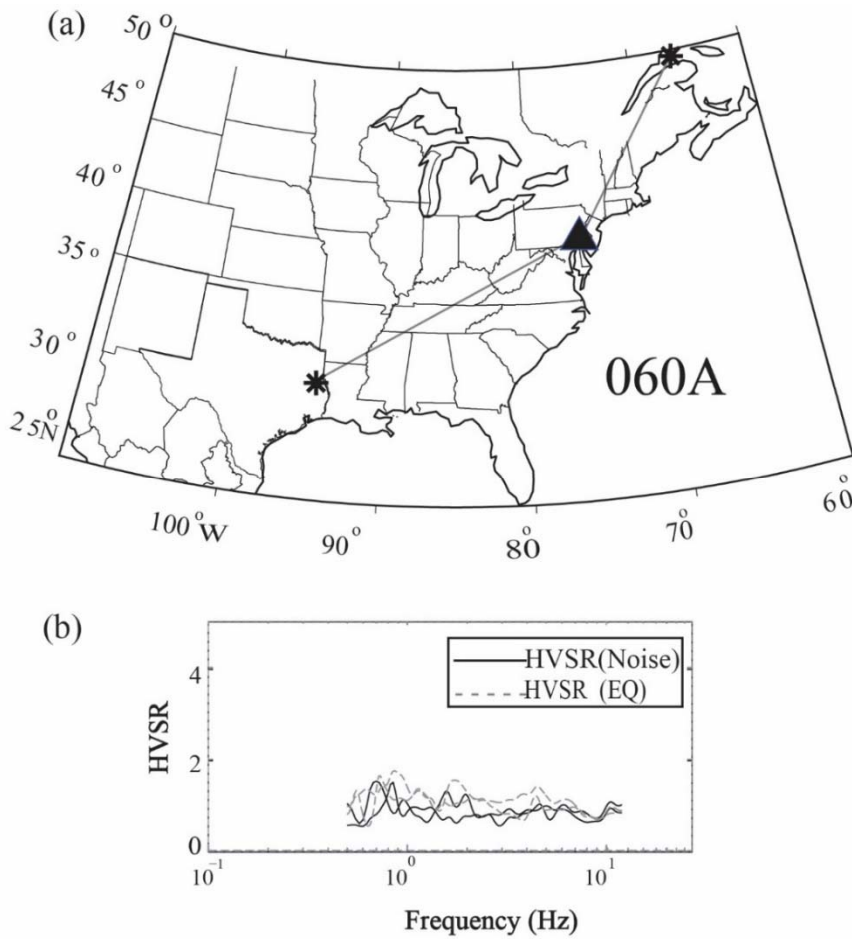


Figure 3.7.(a) Location of station 060A (triangle) and path and location of two recorded events (stars). (b) H/V spectra (dashed lines) of seismic events recorded at 060A (shown in a) and H/V spectra (solid lines) of ambient noise.

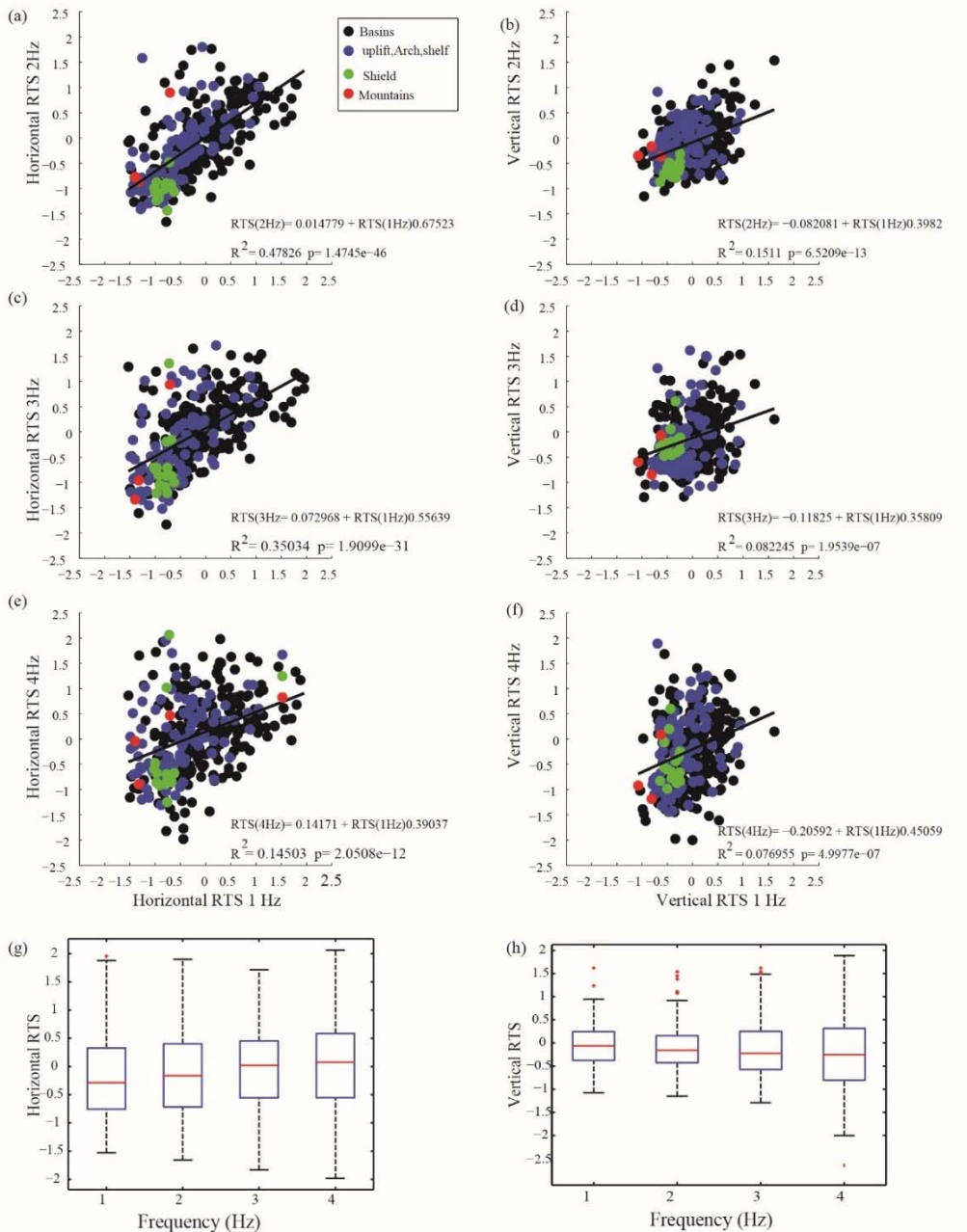


Figure 3.8. The vertical and horizontal RTS amplification of central frequency 1.0 Hz versus RTS amplification of the central frequencies: 2.0Hz, 3.0 Hz, 4.0 Hz. The color of the circles represents the topographic locations: black=basin, green= shield, red=mountain, and blue= uplift. (g) and (h) shows the horizontal and vertical RTS amplification versus four frequency bands using the boxplots.

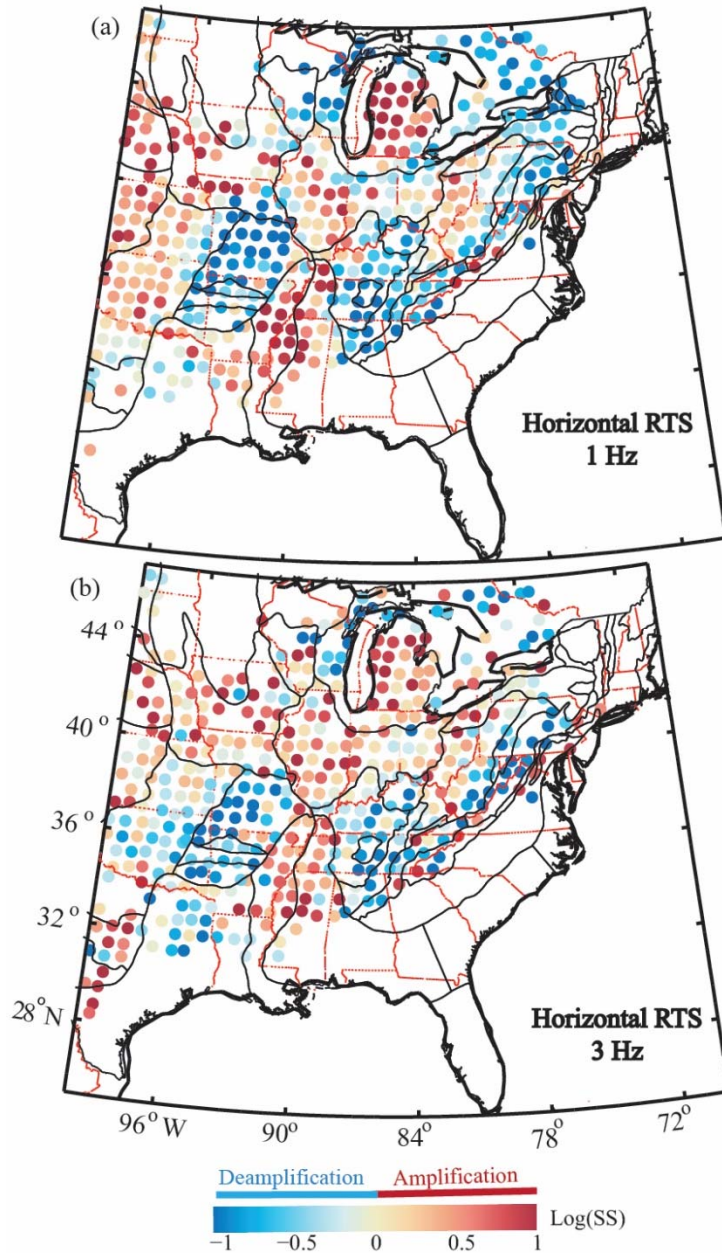


Figure 3.9. (a) Horizontal amplification values resulting from the RTS method at a central frequency of 1.0 Hz. (b) Horizontal amplification at a central frequency of 3.0 Hz. (see Fig. S5 for results at central frequencies of 2.0 and 4.0 Hz). Note that positive amplification (red) appears to correlate with basins.

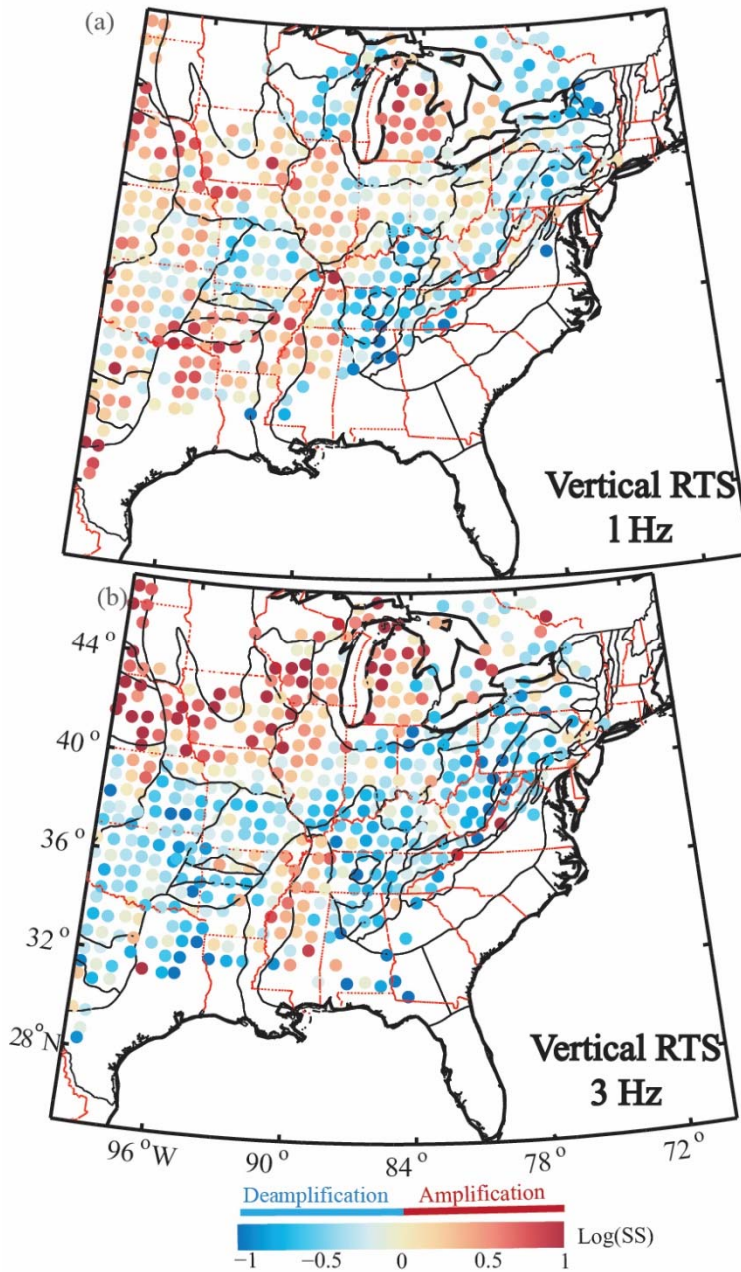


Figure 3.10. (a) Vertical amplification values resulting from the RTS method at a central frequency of 1.0 Hz. (b) Vertical amplification values resulting from the RTS method at a central frequency of 3.0 Hz. Note the positive amplification (red) in the basins (see Fig. S6 for results at central frequencies of 2.0 and 4.0 Hz).

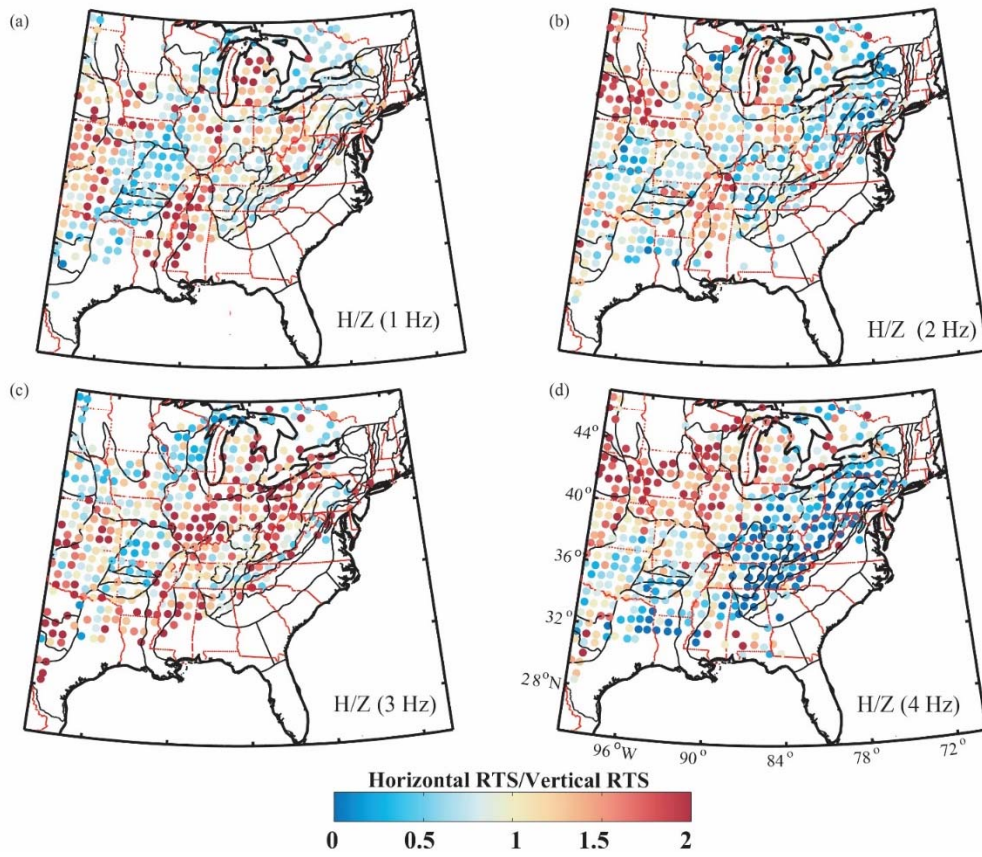


Figure 3.11. Horizontal to vertical ratio of amplification at central frequencies of 1.0, 2.0, 3.0 and 4.0 Hz. The H/Z ratio is high in the basins (red).

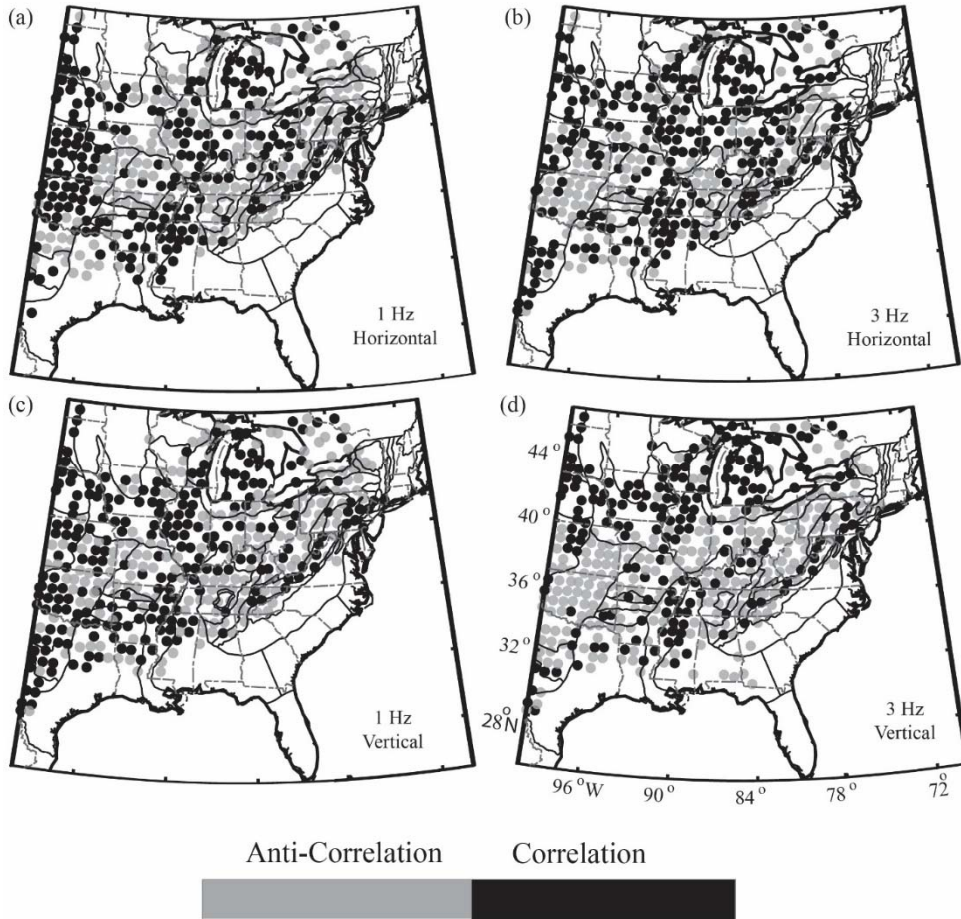


Figure 3.12. A comparison of HVSR and RTS results at central frequencies of 1.0 and 3.0 Hz. black circles represent positive correlations, while gray circles show no correlation. Correlation between HVSR and RTS is seen to increase in basins (Illinois and Michigan) at higher frequencies (see the electronic supplements figure S9).

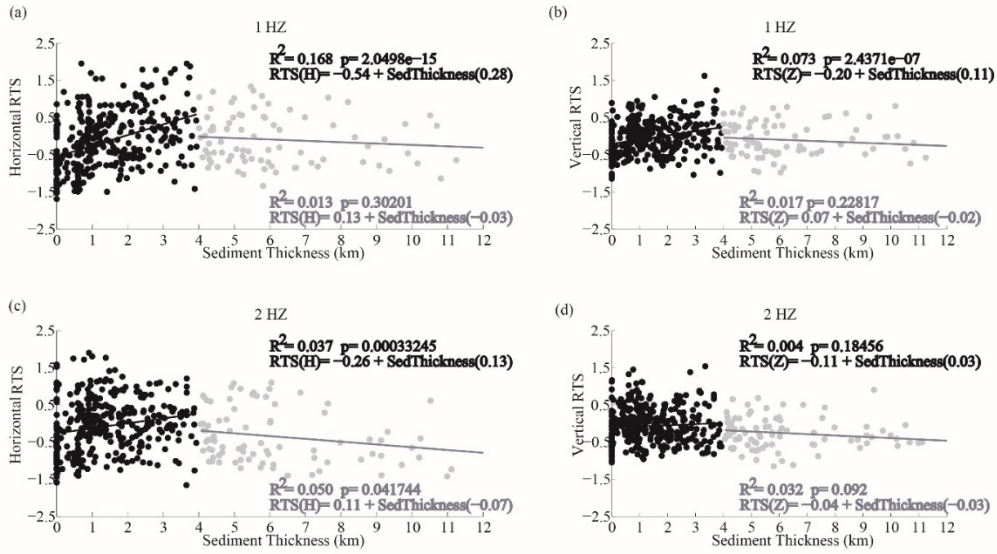


Figure 3.13. A comparison of sediment thickness and RTS results at central frequencies of 1.0 and 2.0 Hz. Black circles represent positive correlation while gray circles show a negative correlation. Note that a positive correlation occurs for sediment thicknesses ≤ 4 km while negative correlation is found for sediment thicknesses >4 km (see Fig. S11 for results at central frequencies of 3.0 and 4 Hz).

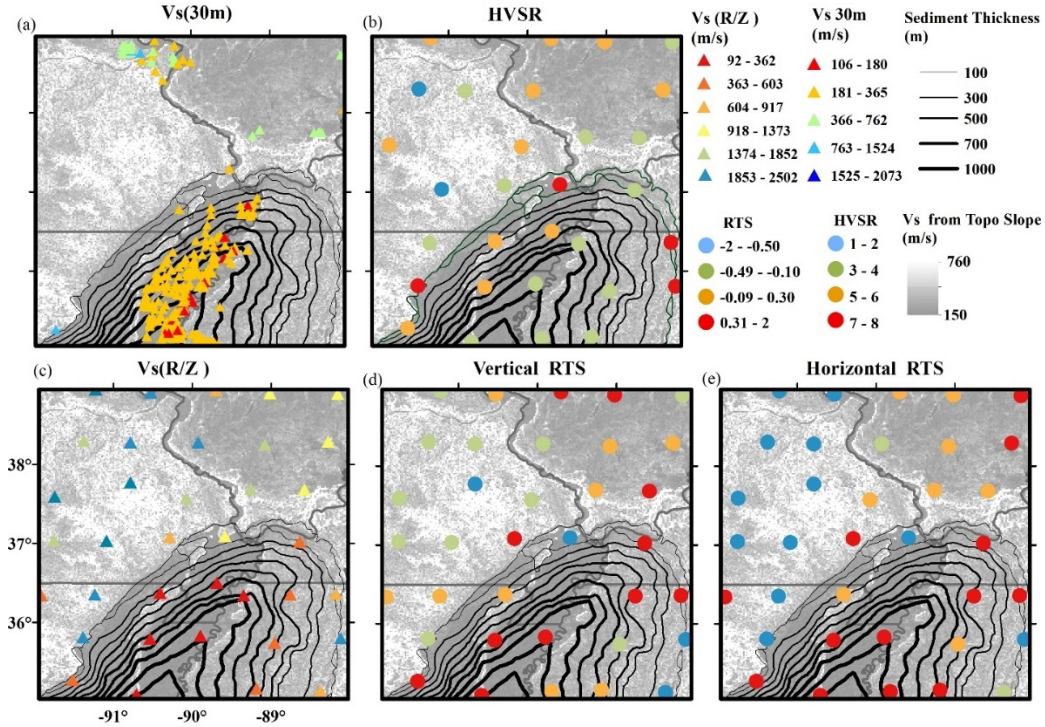


Figure 3.14. Maps representing V_s30m measurements in the northern Mississippi Embayment. In all maps, varying shades of gray represent V_s30m measurements based on topographic slope, with dark gray representing low V_s30m and light gray to white representing high V_s30m . Contours (in meters) represent sediment thickness values (Dart, 1992; Dart and Swolfs, 1998). In (a), triangles represent measured V_s30m , with warm colors representing low V_s30m and cool colors representing high V_s30m . (b) Circles represent HVSR values calculated in this study, with warm colors representing high HVSR and cool colors representing low HVSR. (c) $V_s(R/Z)$ is the shallow velocity model from Ni et al. (2014). (d) and (e) show the vertical and horizontal RTS site response values calculated in this study, respectively, with warm colors generally representing amplification and cool colors generally representing deamplification. Note the negative correlation between the (e) horizontal RTS and the

(c) $V_s(R/Z)$ (see Fig. S13 for comparisons between V_s30m , sediment thickness and the noise fundamental frequency F_0 , Fig. S14 for comparisons between V_s30m , sediment thickness, and the HVSR and F_0 of EQ/NOISE).

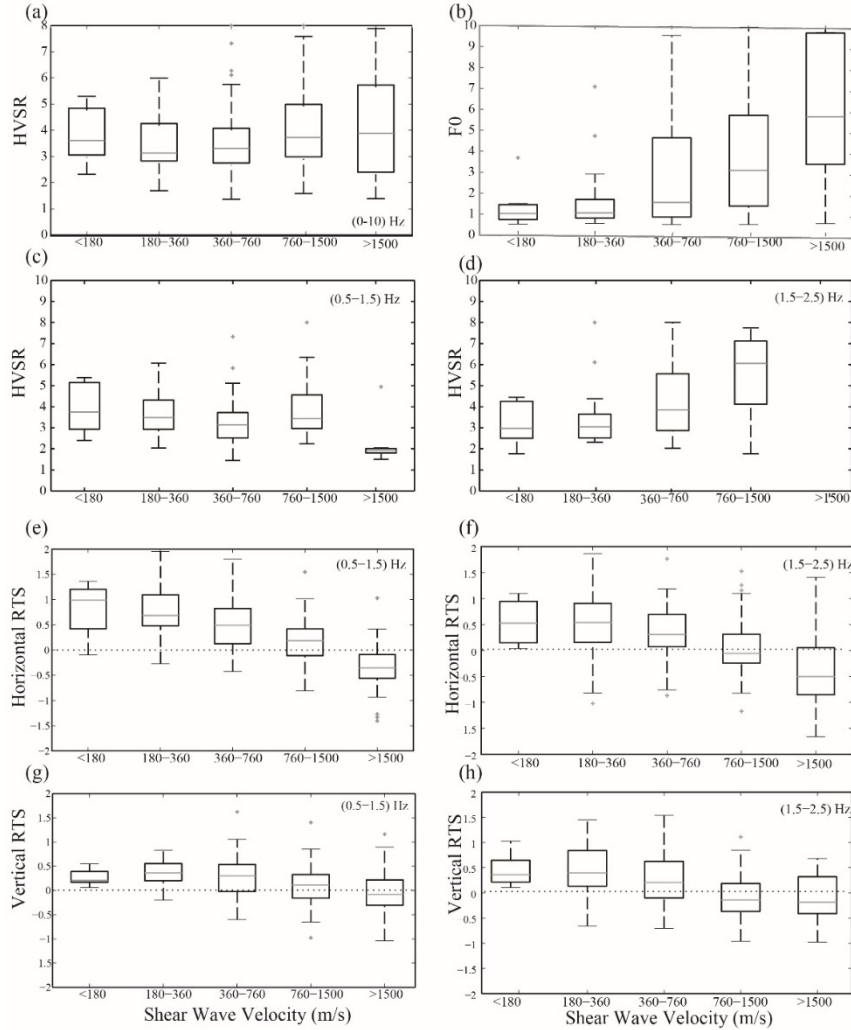


Figure 3.15. (a) Shallow V_s versus HVSR, (b) shallow V_s versus fundamental frequency F_0 , (c) Shallow V_s versus HVSR at a central frequency of 1.0 Hz (d), shallow V_s versus HVSR at a central frequency of 2.0 Hz, (e) shallow V_s versus horizontal RTS amplification at a central frequency of 1.0 Hz, (f) shallow V_s versus horizontal RTS amplification at a central frequency of 2.0 Hz, (g) shallow V_s versus vertical RTS amplification at a central frequency of 1.0 Hz, (h) shallow V_s versus vertical RTS amplification at a central frequency of 2.0 Hz (see Figs. S16 and S17 for shallow V_s versus all the frequency bands of HVSR and RTS).

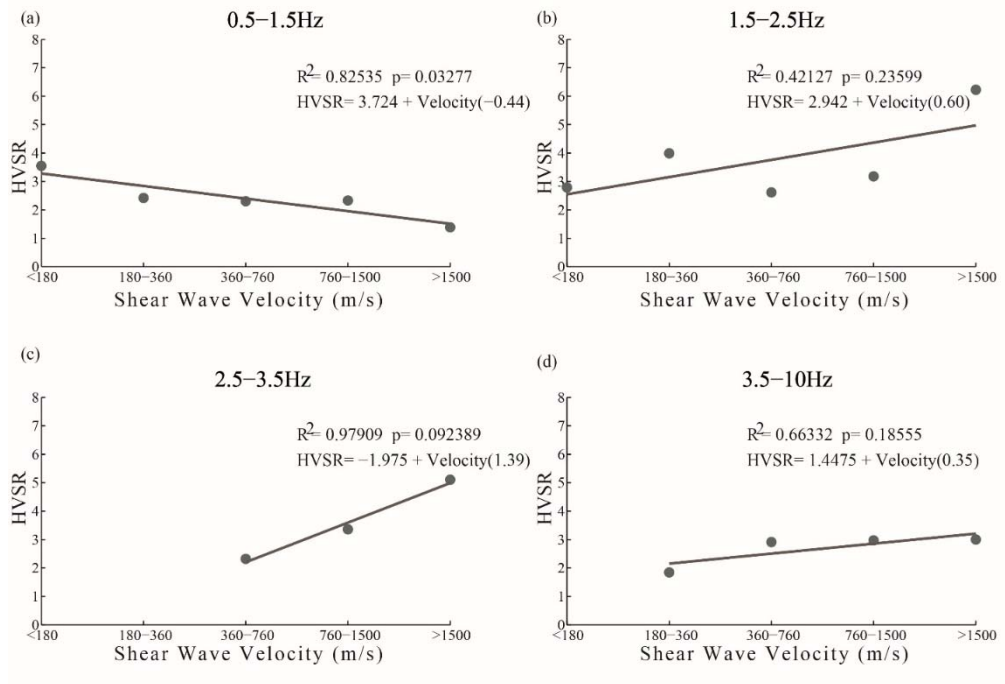


Figure 3.16. Shallow Vs versus HVSr at four frequency bands: (a) 0.5-1.5 Hz, (b) 1.5-2.5 Hz, (c) 2.5-3.5 Hz, and (d) 3.5-10 Hz. Note that HVSr has a negative trend with velocity for lower frequencies.

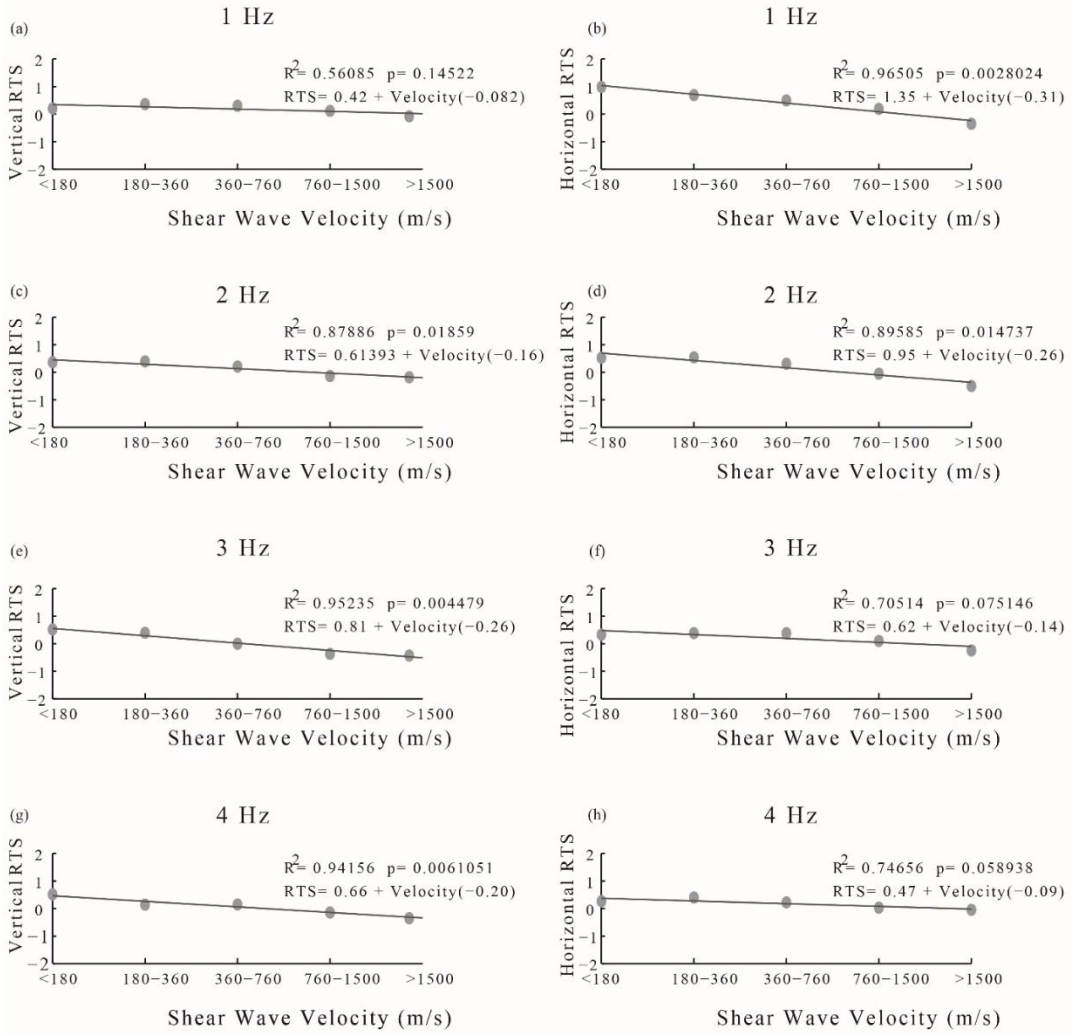
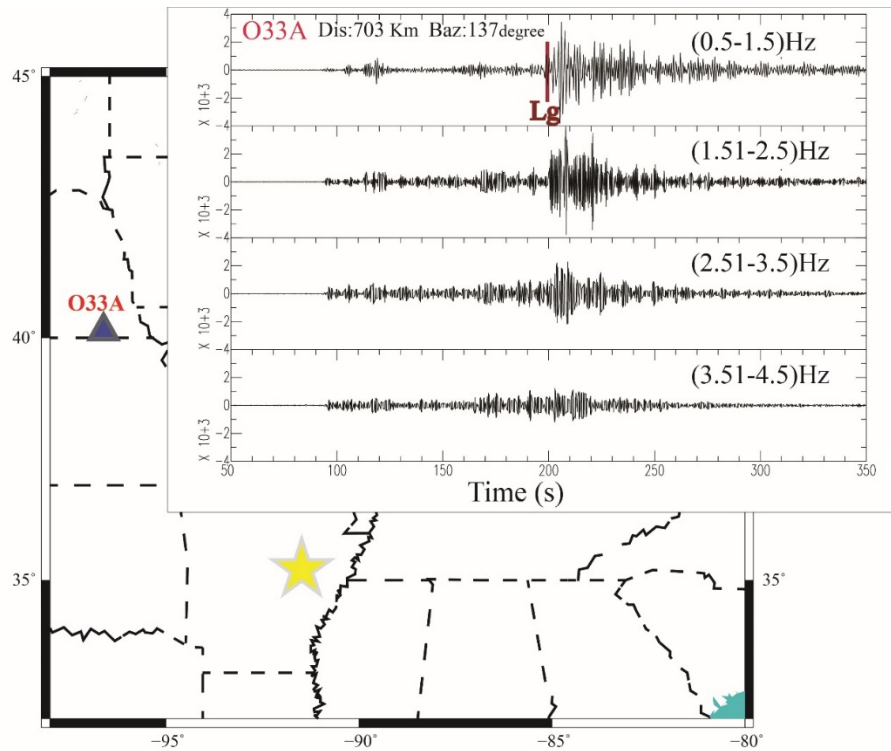
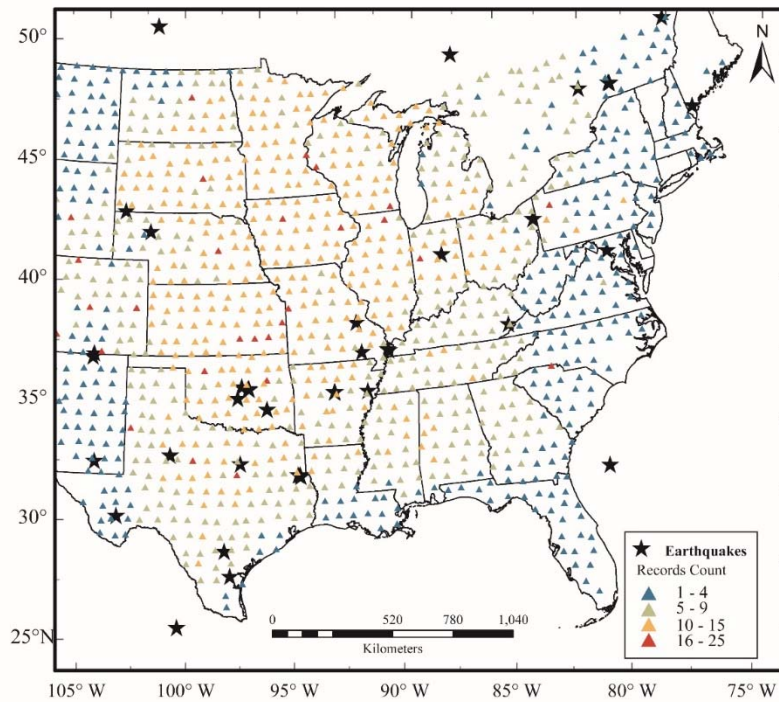


Figure 3.17. Shallow V_s versus horizontal RTS amplification and vertical RTS amplification at four frequency bands 1.0 Hz, 2.0Hz, 3.0Hz, and 4.0 Hz.

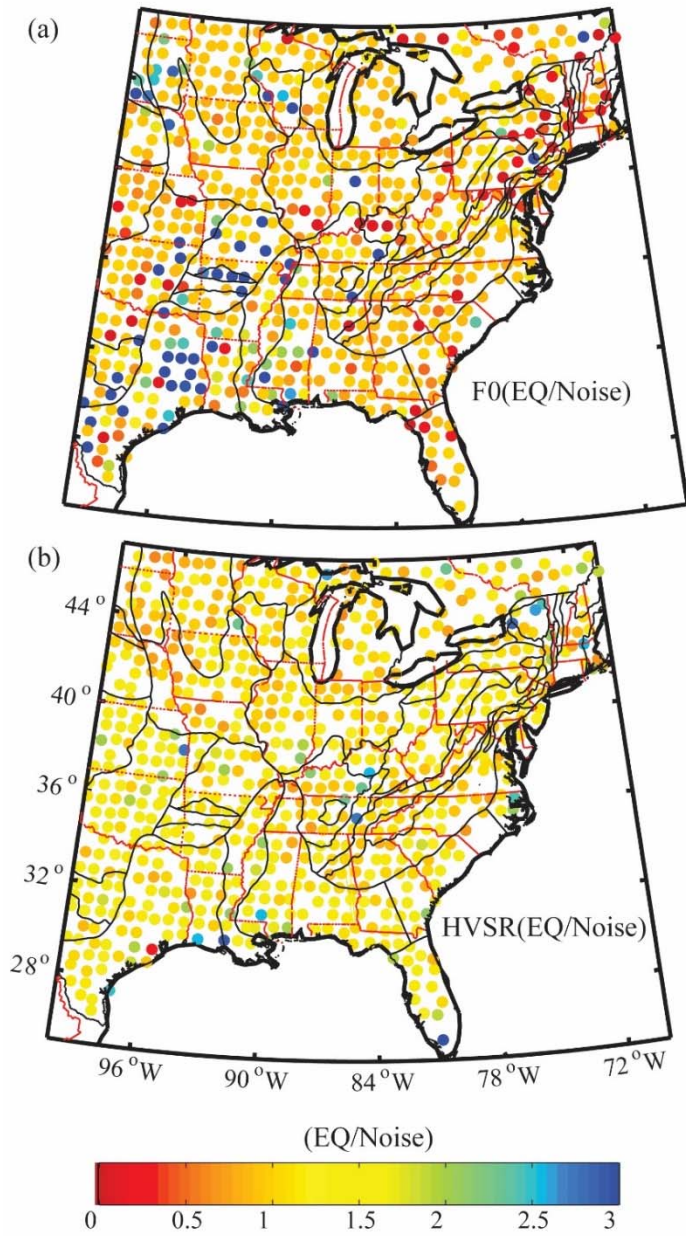
3.10 Supplementary figures:



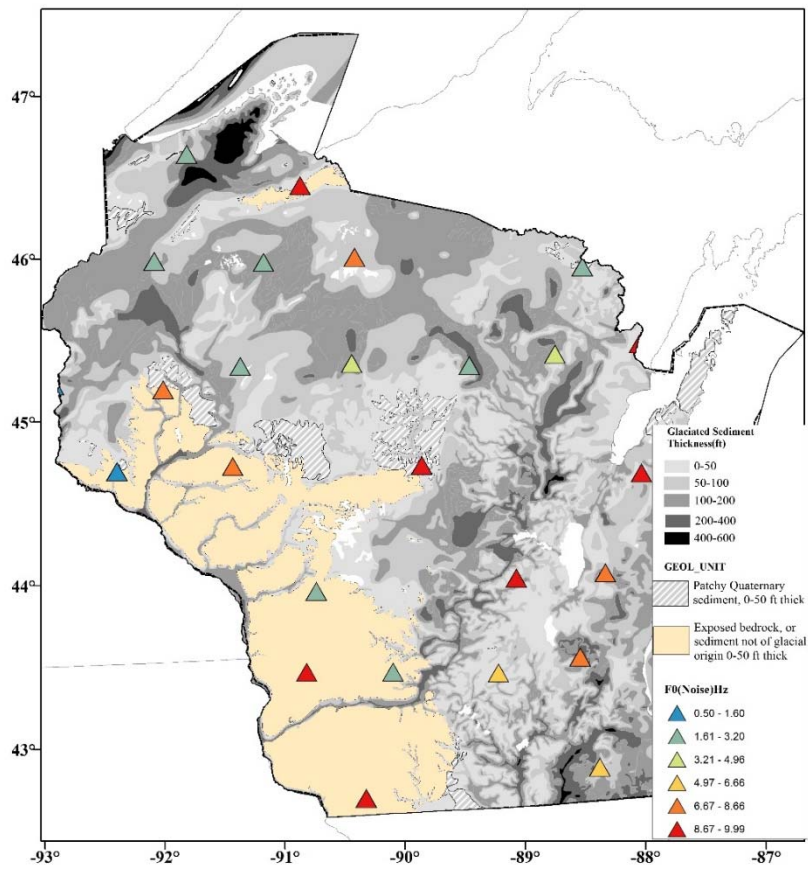
Supp. Figure 3.1. Example of seismic record with regional phases (Lg) for the four frequency bands we applied in this study. Blue triangle is TA station. Yellow star is an earthquake located in New Madrid Seismic Zone with magnitude Mw4.5.



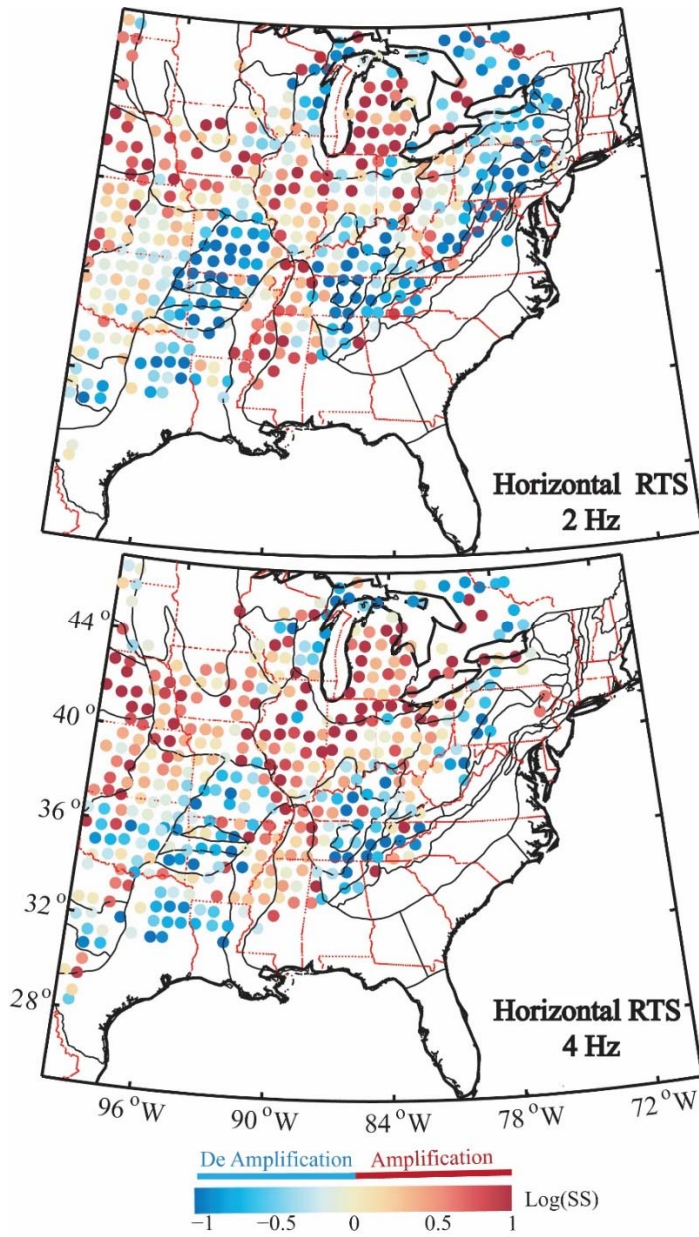
Supp. Figure 3.2. TA station distribution over the central and eastern United States. Colors represent the number of seismic recordings at each station. Earthquakes are shown as stars. Gray lines are state boundaries.



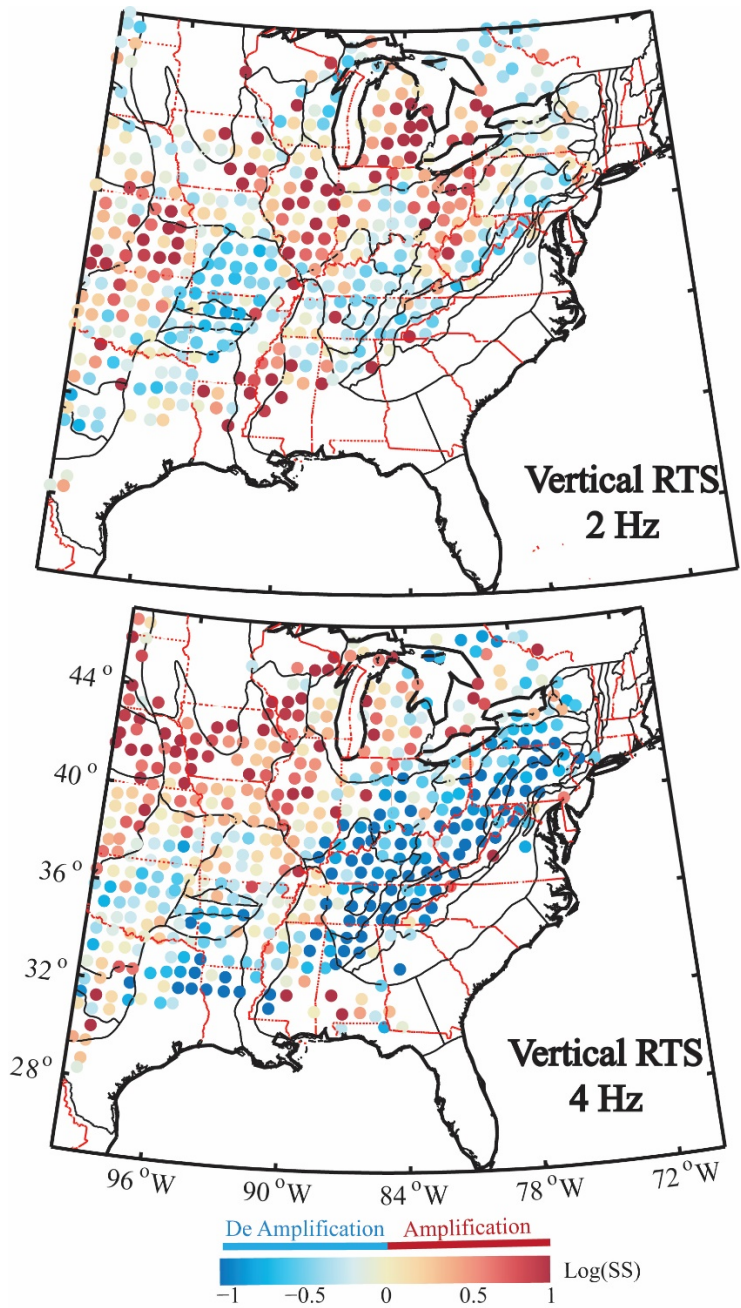
Supp. Figure 3.3. (a) The ratio of the fundamental frequency (F_0) of (EQ_HVSR/NOISE_HVSR), (b) the ratio HVSR amplitude of (EQ_HVSR/NOISE_HVSR).



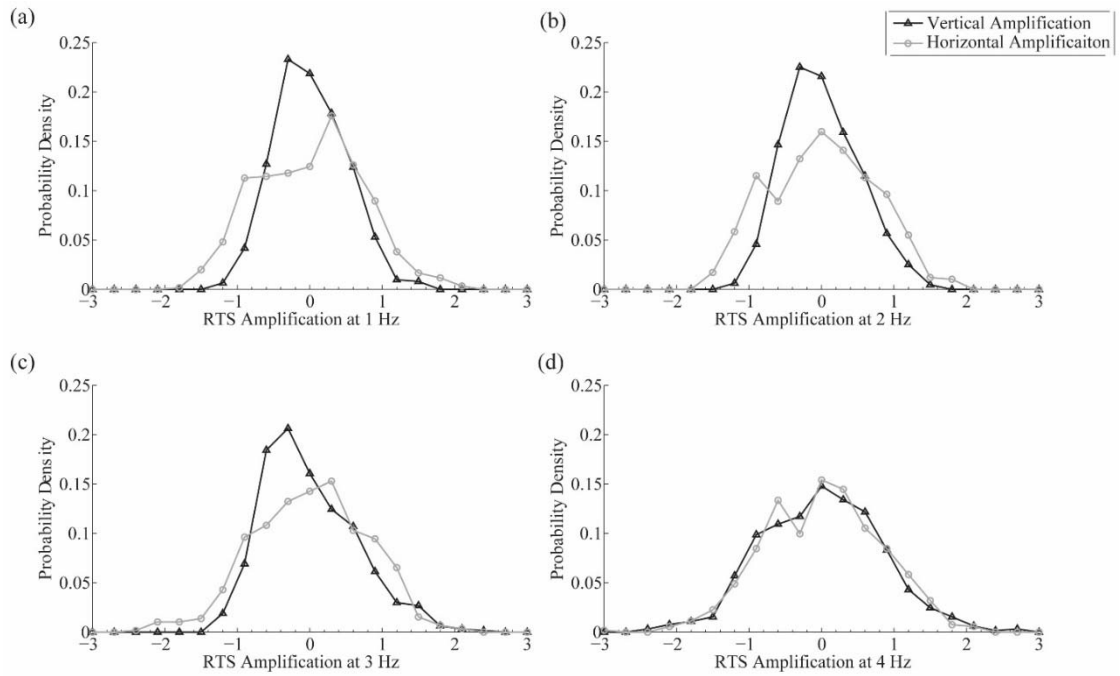
Supp. Figure 3.4. A simplified geologic map of Wisconsin and its subsurface geology. Note that the F0 (Noise) is higher for thin sediments.



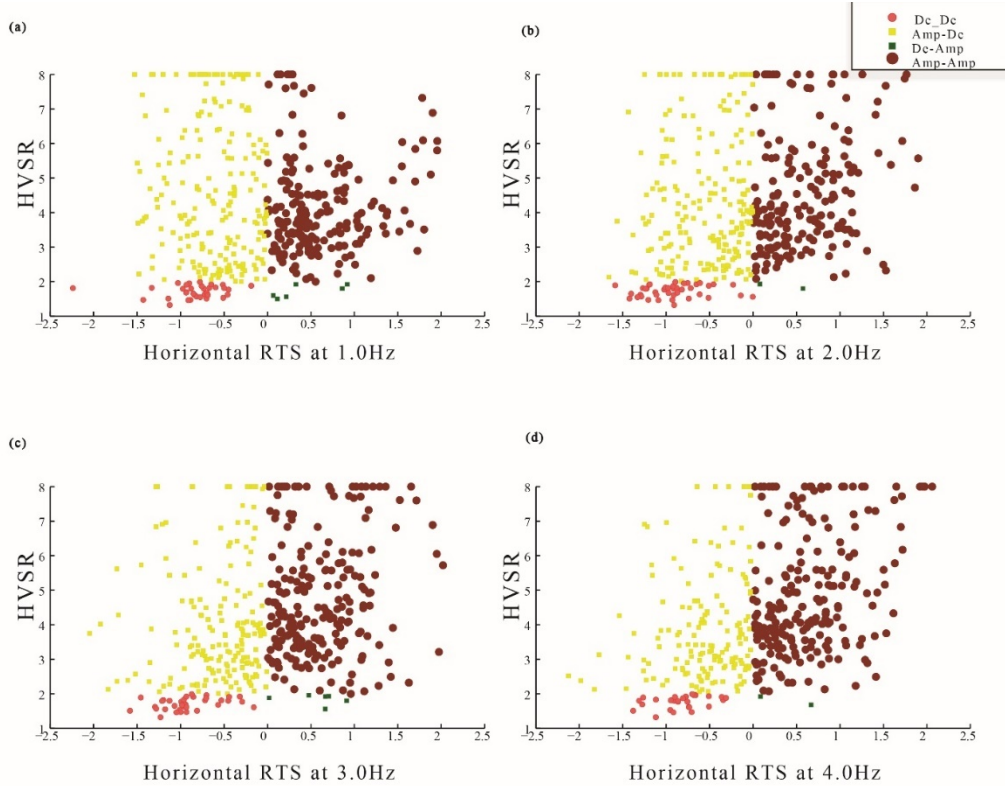
.Supp. Figure 3.5 (a) Horizontal amplification values resulting from the RTS method at a central frequency of 2 Hz, (b) Horizontal amplification values resulting from the RTS method at a central frequency of 4 Hz. Note the high amplification values in basins.



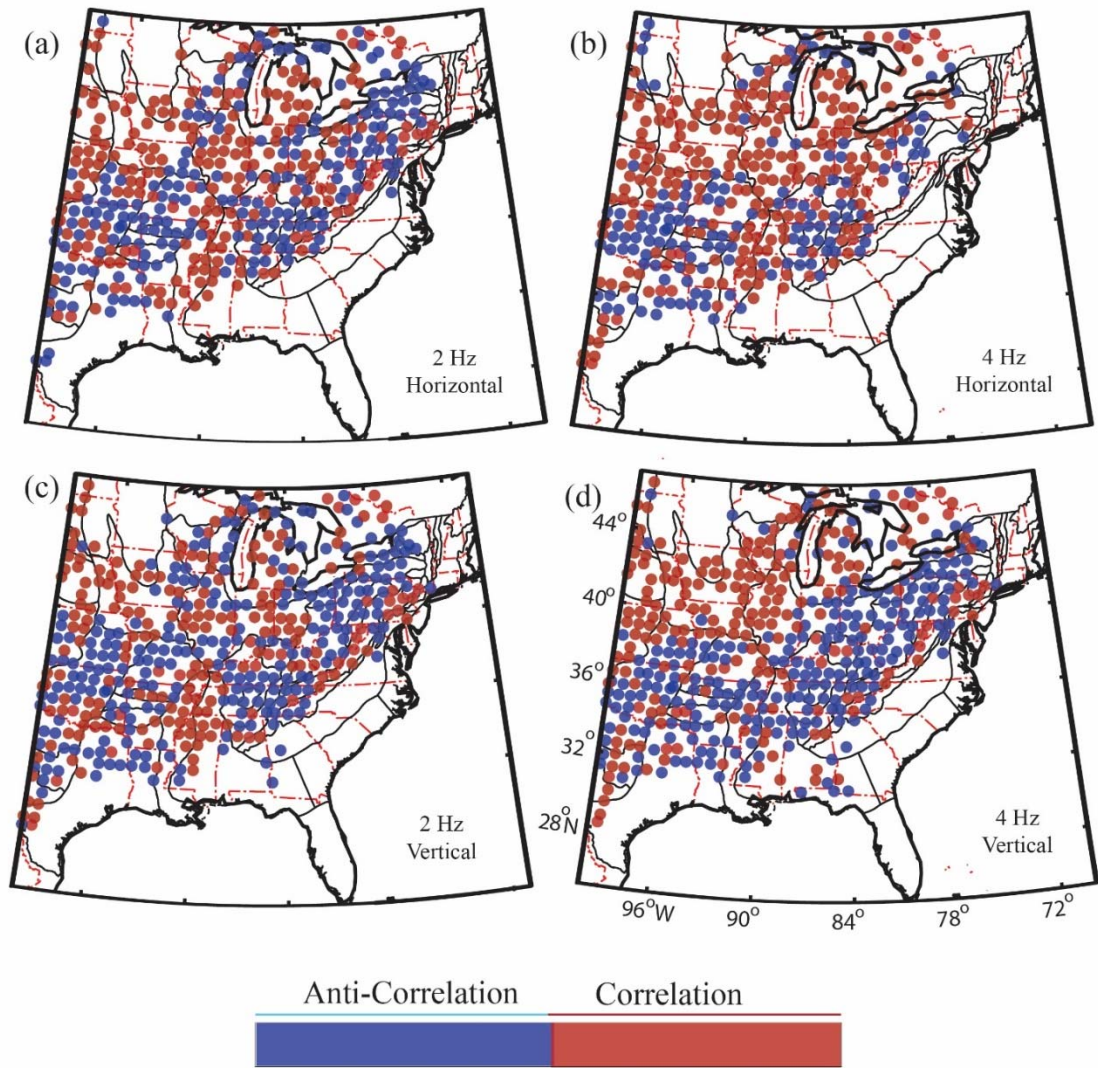
Supp. Figure 3.6 (a) Vertical amplification values resulting from the RTS method at a central frequency of 2 Hz, (b) Vertical amplification values resulting from the RTS method at a central frequency of 4 Hz.



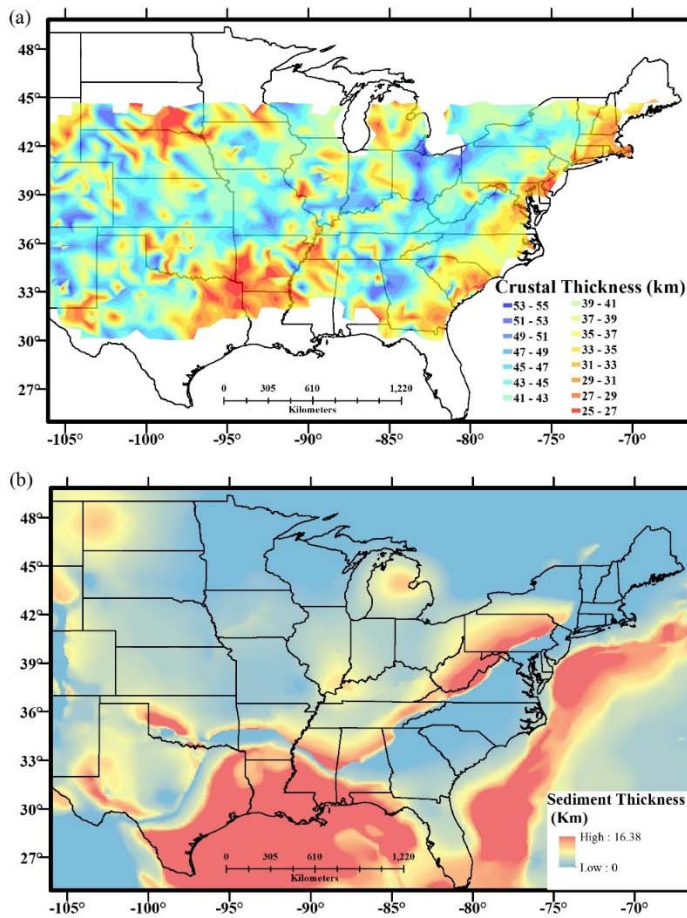
Supp. Figure 3.7. Probability density of the vertical and horizontal RTS amplification for each frequency. Note that with increasing frequency the vertical and horizontal amplification become increasingly similar.



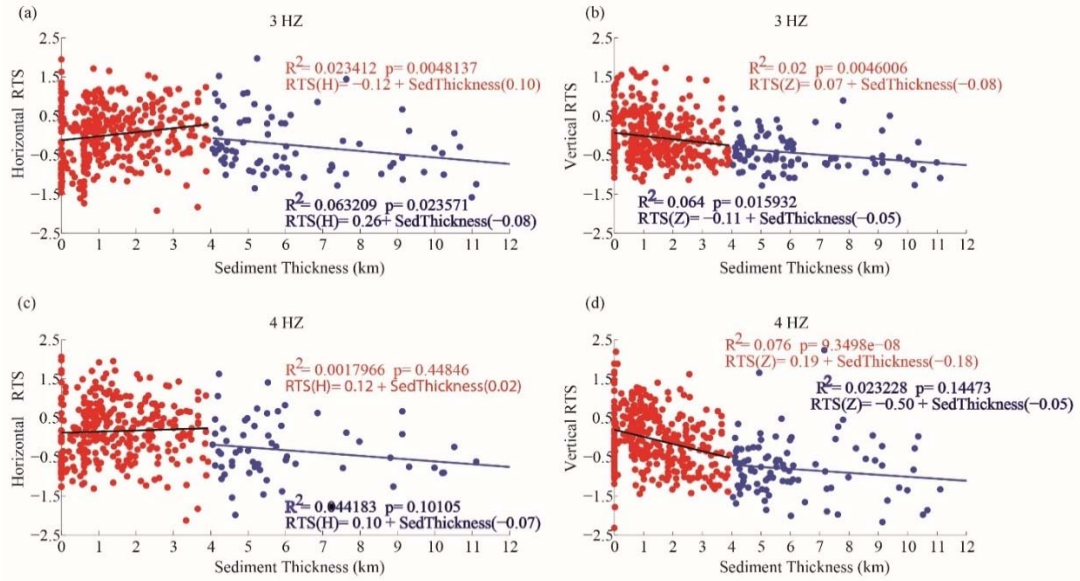
Supp. Figure 3.8. A comparison of the site amplification from the HVSR and RTS methods. Red circles represent positive (dark red and light red) correlations (De=Deamplification, Am= Amplification) while yellow and green squares show no correlation (anti-correlation).



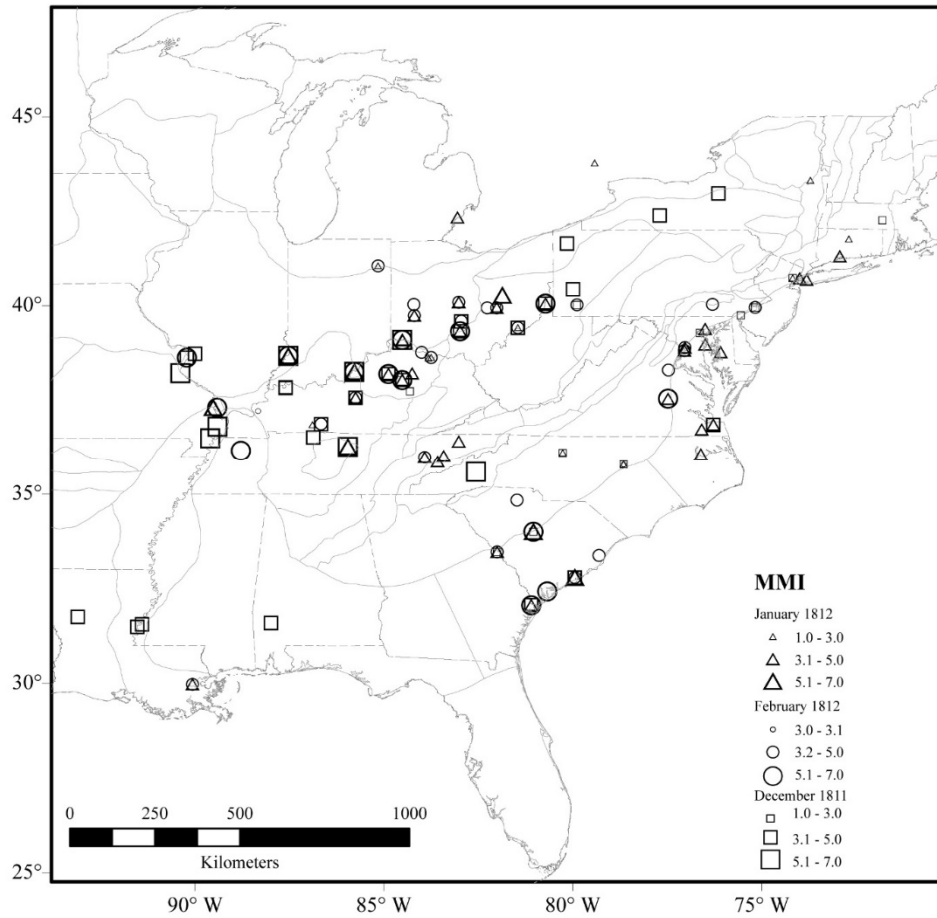
Supp. Figure 3.9. A comparison of the HVSR and RTS results for the central frequencies of 2 and 4 Hz. Dark circles represent positive correlations light circles show no correlation. Correlation between HVSR and RTS is seen to increase in basins (Illinois and Michigan) at higher frequencies.



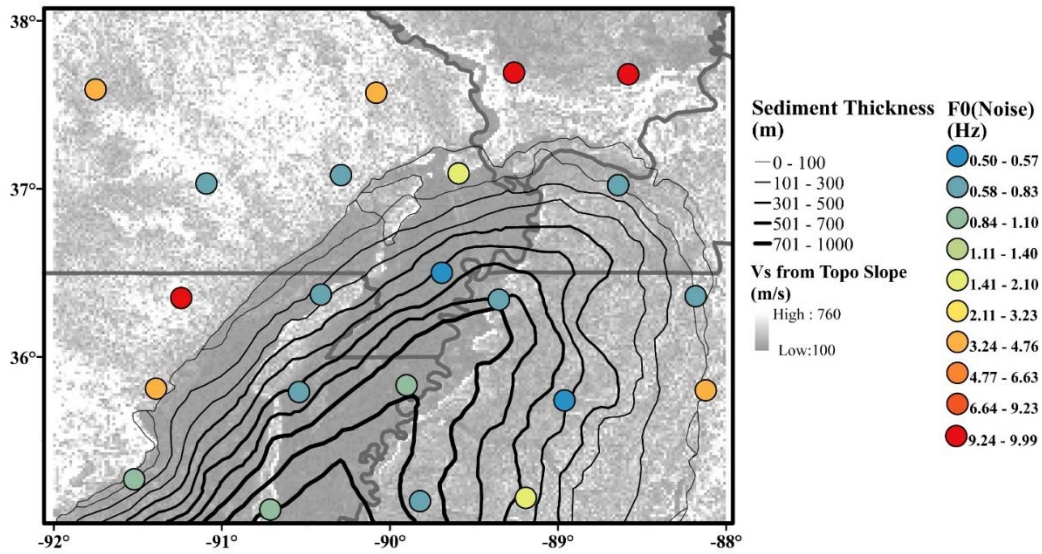
Supp. Figure 3.10. (a) Map of crustal thickness estimates for the contiguous United States from the EarthScope Automated Receiver Survey (EARS) dataset. (b) Sediment thickness (in km) in North America (Mooney and Kaban, 2010).



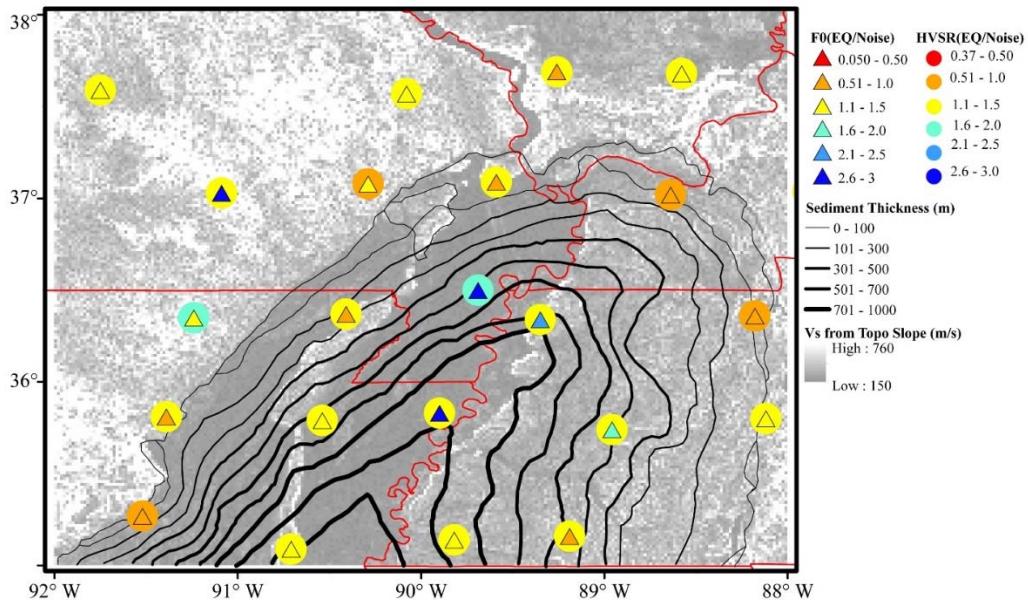
Supp. Figure 3.11. A comparison of sediment thickness and RTS results at central frequencies of 3.0 and 4.0 Hz. Red circles represent positive correlations for sediment thickness less than 4km while blue circles show a negative correlation for sediment thickness >4km.



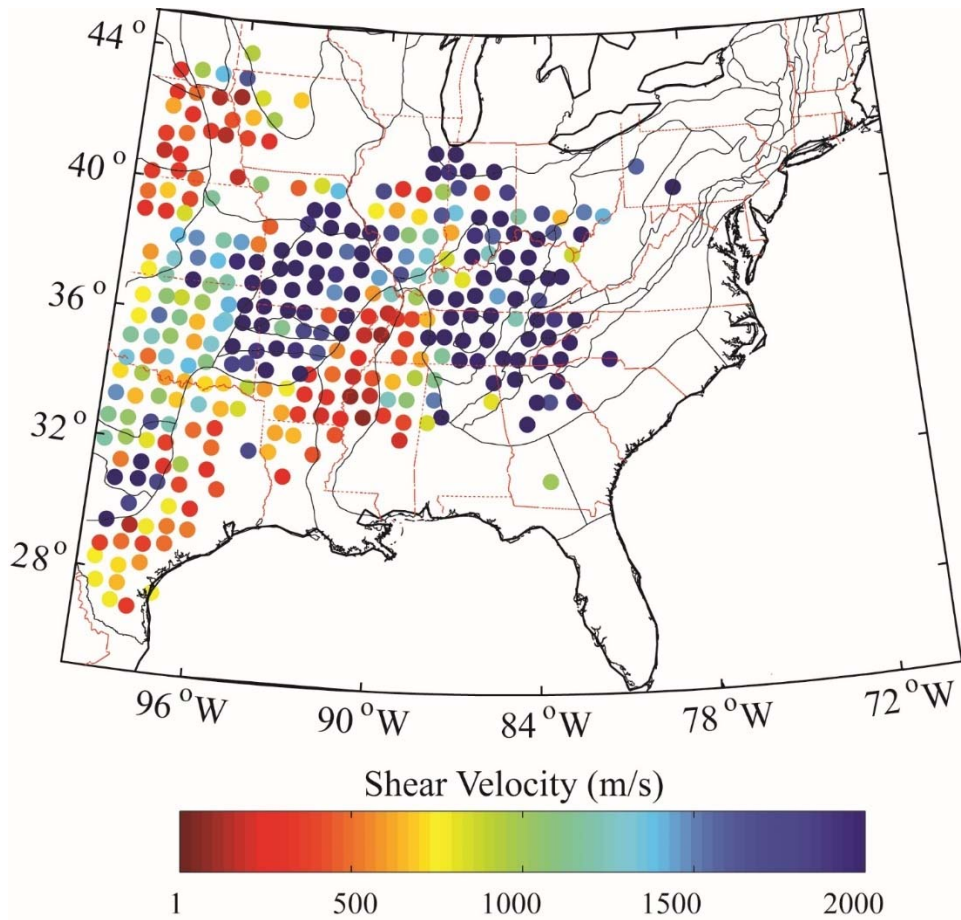
Supp. Figure 3.12. Intensity map for three historical earthquakes that took place in the New Madrid Seismic Zone in 1811 and 1812 (Hough and Page, 2011).



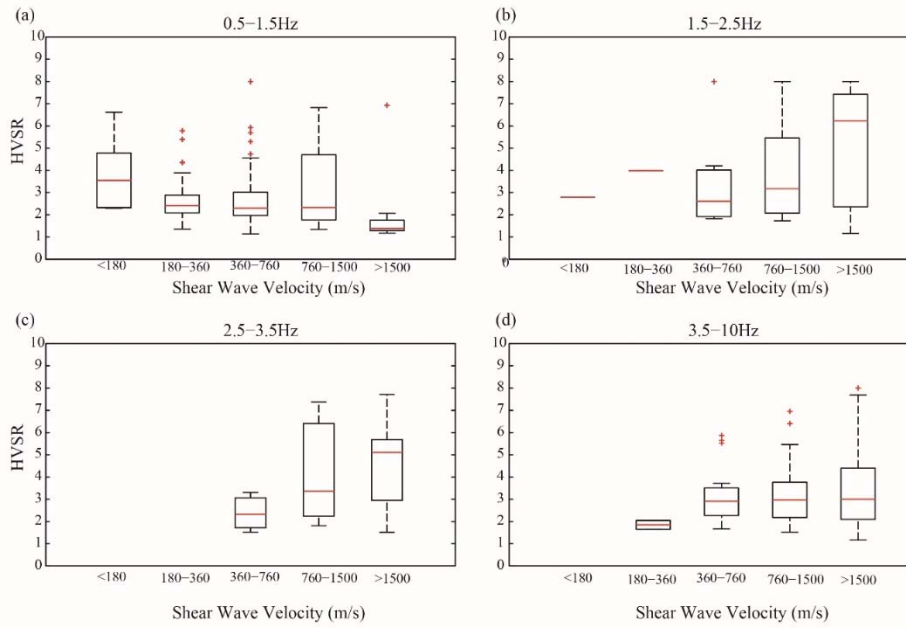
Supp. Figure 3.13. The gray and white colors represent Vs30 measurements based on the slope of the topographic map. The circles represent the fundamental frequency (F0). Contours (in meters) are sediment thickness from Dart (1992) and Dart and Swolfs (1998), modified from Langston et al. (2009).



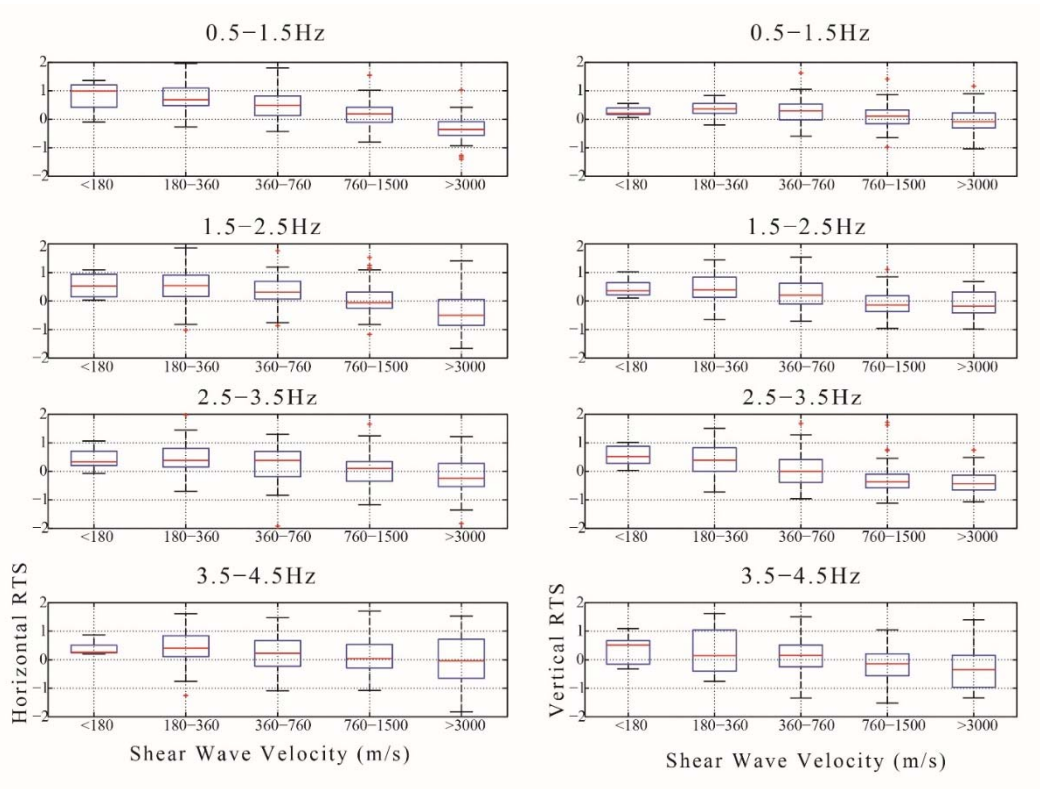
Supp. Figure 3.14. The gray and white colors represent Vs30 measurements based on the slope of the digital elevation model. The triangles represent the ratio of the fundamental frequency (F0) of (EQ_HVSR/NOISE_HVSR). The circles represent the ratio HVSR amplitude of (EQ_HVSR/NOISE_HVSR). Contours (in meters) are sediment thickness from Dart (1992) and Dart and Swolfs (1998), modified from Langston et al. (2009).



Supp. Figure 3.15. Shallow shear wave velocities from (horizontal/vertical) body waves Ni et al. (2014). Low shear wave velocities in Mississippi Embayment, high shear wave velocities in the Ozarks plateau and southern Appalachians.



Supp. Figure 3.16. (a) shear wave velocity versus HVSR at a central frequency of 1.0 Hz. (b) shear wave velocity versus HVSR at a central frequency of 2.0 Hz. (c) shear wave velocity versus HVSR at a central frequency of 3.0 Hz. (d) shear wave velocity versus HVSR for frequency range 3.5-10 Hz.



Supp. Figure 3.17. Shear wave velocity versus vertical and horizontal RTS amplification at four frequency bands 1.0 Hz, 2.0 Hz, 3.0 Hz, and 4.0 Hz.

3.11 References

- Aki, K. (1980). Attenuation of shear-waves in the lithosphere for frequencies from 0.05 to 25 Hz, *Phys. Earth Planet. Inter.* **21**, 50–60.
- Aki, K., and P. G. Richards (2002). *Quantitative Seismology*, Univ. Science Books, Sausalito, California.
- Atkinson, G.M., and W. Silva (2000). Stochastic modeling of California ground motions, *Bull. Seismol. Soc. Am.* **90**, 255–74.
- Bao, X., E. Sandvol, J. Ni, T. Hearn, Y. Chen, and Y. Shen (2011). High resolution regional seismic attenuation tomography in eastern Tibetan Plateau and adjacent regions, *Geophys. Res. Lett.* **38**, 16304.
- Baquer, S. and B.J. Mitchell (1998.). Regional Variation of Lg Coda Q in the Continental United States and its Relation to Crustal Structure and Evolution. *Pure. App. Geophys.* **2**, 613-638.
- Bard, P.-Y. (2004). Guidelines for the implementation of the h/v spectral ratio technique on ambient vibrations measurements, processing and interpretation sesame European research project wp12 – Deliverable D23.12 European Commission – Research General Directorate Project No. EVG1-CT-2000-00026 SESAME
- Bickford, M. E, W. R. Van Schmus, and I. Zietz (1986). Proterozoic history of the midcontinent region of North America, *Geology* **14**, 492-496.
- Boore, D.M. (1983). Strong-motion seismology, *Reviews of Geophysics*.

- Boore, D.M., J.F. Gibbs, W.B. Joyner, J.C. Tinsley, and D.J. Ponti (2003). Estimated ground motion from the 1994 Northridge, California, earthquake at the site of interstate 10 and La Cienega Boulevard bridge collapse, West Los Angeles, California, *Bull. Seismol. Soc. Am.* **93**, 2737–2751.
- Boore, D.M., and G.M. Atkinson (2008). Ground-motion prediction equations for the average horizontal component of PGA, PGV, an 5%-damped PSA at spectral periods between 0.01 s and 10.0 s, *Earthq. Spectra* **24**, 99-138
- Boore, D.M. (2014). What Do Data Used to Develop Ground-Motion Prediction Equations Tell Us About Motions Near Faults, *Pure. Appl. Geophys.* 171, 3023–43.
- Borcherdt, R.D. (1970). Effects of local geology on ground motion near San Francisco Bay, *Bull. Seismol. Soc. Am.* **60**, 29–61.
- Bouchon, M. (1982). The complete synthesis of seismic crustal phases at regional distances, *JGR. Solid Earth* **87**, 1735-1741.
- Campbell, K.W., and Y. Bozorgnia (2014). GA-West2 horizontal ground motion model for active tectonic domains, in (Model Development Group, EQECAT, Inc., Oakland, CA, United States).
- Carpenter, N.S., Z. Wang, E.W. Woolery, and M. Rong (2018). Estimating Site Response with Recordings from Deep Boreholes and HVSr: Examples from the Mississippi Embayment of the Central United States, *Bull. Seismol. Soc. Am.* **108**, 1199–1209.

- Chapman, M.C. (2015). Magnitude, recurrence interval, and near-source ground-motion modeling of the Mineral, Virginia, earthquake of 23 August 2011, *GSA Special Papers* **509**, 27–45.
- Chiou, B.S.-J., and R.R. Youngs (2014). Update of the Chiou and Youngs NGA model for the average horizontal component of peak ground motion and response spectra, *Earthq. Spectra* **30**, 1117–1153.
- Chun, K.Y., G.F. West, R.J. Kokoski and C. Samson (1987). A Novel Technique for Measuring Lg attenuation Results from Eastern Canada between 1 to 10 Hz, *Bull. Seismol. Soc. Am.* **77**, 398–419.
- Coleman, J.L., and S.M. Cahan (2012). Preliminary catalog of the sedimentary basins of the United States, U.S. Geological Survey Open-File Report, 27
- Dart, R.L., and H.S Swolfs (1998). Contour mapping of relic structures in the Precambrian basement of the Reelfoot rift, North American midcontinent, *Tectonics* **17**, 235-249.
- Davis, P.M., J.L. Rubinstein, S. Gao, L. Knopoff (2000). Northridge Earthquake Damage Caused by Geologic Focusing of Seismic Waves, *Science* **289**, 1746–1750.
- Fullerton, D.S., C.A. Bush, and J. N. Pennell (2003). Map of Surficial Deposits and Materials in the Eastern and Central United States (East of 102° West Longitude), 2789.
- Gallegos, A., N. Ranasinghe, J Ni, and E. Sandvol (2014). Lg attenuation in the central and eastern United States as revealed by the EarthScope Transportable Array, *Earth Planet. Sci. Lett.* **402**, 187–96.

- Gao, S., H. Liu, P.M. Davis, and L. Knopoff (1996). Localized Amplification of Seismic Waves and Correlation with Damage due to the Northridge Earthquake: Evidence for Focusing in Santa Monica, *Bull. Seismol. Soc. Am.* **86**, 209–30.
- Goulet, C.A., T. Kishida, T.D. Ancheta, C.H. Cramer, R.B. Darragh, W.J. Silva, Y.M. Hashash, J. Harmon, J.P. Stewart, K.E. Wooddell, and R.R. Youngs (2014). Pacific Earthquake Engineering Research Center.
- Gradstein, F., and J. Ogg (2004). Geologic time scale 2004—why, how, and where next!, *Lethaia* **37**, 175–181.
- Hanks, T.C. (1979). b values and $\omega - \gamma$ seismic source models: Implications for tectonic stress variations along active crustal fault zones and the estimation of high-frequency strong ground motion, *J. Geophys. Res.* **84**, 2235.
- Hartzell, S., D. Carver, and R.A. Williams (2001). Site response, shallow shear-wave velocity, and damage in Los Gatos, California, from the 1989 Loma Prieta earthquake, *Bull. Seismol. Soc. Am.* **91**, 468–78.
- Haskell, N. A (1960). Crust reflection of plane Sh waves, *Physics (College. Park. Md)* **65**, 15–18.
- Hassani, B., and G.M. Atkinson (2016). Site- Effects Model for Central and Eastern North America Based on Peak Frequency, *Bull. Seismol. Soc. Am.* **106**, 2197–2213.
- Hough, S.E. and M. Page (2011). Toward a consistent model for strain accrual and release for the New Madrid Seismic Zone, central United States, *J. Geophys. Res. Solid Earth* **116**, 1–17.

- Hough, S.E. (2012). Initial Assessment of the Intensity Distribution of the 2011 M w 5.8 Mineral, Virginia, Earthquake, *Seismol. Res. Lett.* **83**, 649–657.
- Intiaz, A., Cornou, C., Bard, P.-Y. and Zerva, A. (2015). Spatial coherence of seismic ground motion and geometric structure of the subsurface: an example in Argostoli, Greece, 9th *Colloq. Natl. AFPS* 2015 12.
- Johnston, C., and E.J. Mash (1989). A measure of parenting satisfaction and efficacy, *J. CLIN. CHILD. PSYCHOL.* **18**, 167–175.
- Kennett, B.L.N. (1986). Lg WAVES AND STRUCTURAL BOUNDARIES., *Bull. Seismol. Soc. Am.* **76**, 1133–1141.
- Konno, K., and T. Ohmachi (1998). Ground-Motion Characteristics Estimated from Spectral Ratio between Horizontal and Vertical Components of Microtremor, *Bull. Seismol. Soc. Am.* **88**, 228–41.
- Kramer, S. L. (1996). Geotechnical earthquake engineering. Pearson Education India.
- Lachet C., P.Y Bard, J.C. Gariel and K. Irikura (1995). Straight forward methods to detect non-linear response of the soil. Application to the recordings of the Kobe earthquake, *J. seismol.* **4**, 161-173.
- Lee, S.J., H.C. Chen, Q. Liu, D. Komatitsch, B.S. Huang, and J. Tromp (2008). Three-dimensional simulations of seismic-wave propagation in the Taipei Basin with realistic topography based upon the spectral-element method, *Bull. Seismol. Soc. Am.* **98**, 253–264.
- Lee, S.J., Y.C. Chan, D. Komatitsch, B.S. Huang, and J. Tromp (2009). Effects of realistic surface topography on seismic ground motion in the Yangminshan

- region of Taiwan based upon the spectral-element method and LiDAR DTM, *Bull. Seismol. Soc. Am.* **99**, 681–693.
- Lermo, J., and H.J. Chavez-Garcia (1993). Site effect evaluation using spectral ratios with only one station, *Bull. Seismol. Soc. Am.* **83**, 1574–1594.
- Massa, M., S. Lovati, E. D’Alema, G. Ferretti, and M. Bakavoli (2010). An experimental approach for estimating seismic amplification effects at the top of a ridge, and the implication for ground-motion predictions: The case of Narni, Central Italy, *Bull. Seismol. Soc. Am.* **100**, 3020–3034.
- Massa, M., S. Lovati, S. Marzorati, and P. Augliera (2011). Seismic Ground Motion Amplifications Estimated by Means of Spectral Ratio Techniques: Examples for Different Geological and Morphological Settings, *Earth and Environmental Sciences*.
- Massa, M., S. Barani, and S. Lovati (2014). Overview of topographic effects based on experimental observations: Meaning, causes and possible interpretations, *Geophys.J.Int.* **197**, 1537–1550.
- McNamara, D.E., W.J. Stephenson, J.K. Odum, and R.A. Williams (2015). Site response in the eastern United States: A comparison of Vs30 measurements with estimates from horizontal: vertical spectral ratios, *Geol. Soc. Am. Spec. Pap* **509**, 67-79.
- Marzorati, S., C. Ladina, E. Falcucci, S. Gori, M. Saroli, G. Ameri, and F. Galadini (2011). Site effects “on the rock”: The case of Castelvechio Subequo (L’Aquila, central Italy), *B.Earthq.Eng.* **9**, 841-868.

- Maufroy, E., E. Chaljub, F. Hollender, J. Kristek, P. Moczo, P. Klin, E. Priolo, A. Iwaki, T. Iwata, and V. Etienne (2015). Earthquake ground motion in the Mygdonian basin, Greece: The E2VP verification and validation of 3D numerical simulation up to 4 Hz, *Bull. Seismol. Soc. Am.* **105**, 1398–1418.
- Molnar, S., J.F. Cassidy, K.B. Olsen, S.E. Dosso, and J. He (2014). Earthquake ground motion and 3D Georgia basin amplification in southwest British Columbia: Shallow blind-thrust scenario earthquakes, *Bull. Seismol. Soc. Am.* **104**, 321-335.
- Mooney, W. D., and M.K. Kaban (2010). The North American upper mantle: Density, composition, and evolution, *J. Geophys. Res.* **115**, 1–24.
- MOSS, R.G. (1936). Buried pre-Cambrian surface in the United States, *Bull. Geol. Soc. Am.* **47**, 935–966.
- Mucciarelli, M., and M.R. Gallipoli (2001). A critical review of 10 years of microtremor HVSR technique, *Boll. Geof. Teor. Appl.* **42**, 255–66.
- Mucciarelli, M., and M.R. Gallipoli (2006). Comparison between Vs30 and other estimates of site amplification in Italy. In First European Conference on Earthquake Engineering and Seismology.
- Murphy, J.R., and A.H. Davis. (1971). Amplification of seismic body waves by low-velocity, *Bull. Seismol. Soc. Am.* **61**, 109–45.
- Murphy, J. B., J. D. Keppie, D. Davis, and T. E. Krogh (1997). Regional significance of new U-Pb age data for Neoproterozoic igneous units in Avalonian rocks of northern mainland Nova Scotia, Canada. *Geological Magazine* **134**, 113–120.

- Nakamura, Y. (1989). A method for dynamic characteristics estimation of subsurface using microtremor on the ground surface. *QR Railway Tech. Res. Inst.*, **30**, 25-33.
- Nakamura, Y. (2000). Clear identification of fundamental idea of Nakamura's technique and its applications. In Proceedings of the 12th world conference on earthquake engineering, New Zealand, Auckland.
- Ni, S., Z Li, and P. Somerville (2014). Estimating Subsurface Shear Velocity with Radial to Vertical Ratio of Local P Waves. *Seismol. Res. Lett.* **85**, 82–90.
- Paige, C.C., and M.A. Saunders (1982). Algorithm 583: LSQR: Sparse linear equations and least squares problems, *ACM Trans. Math. Softw.* **8**, 195–209.
- Parolai, S., M. Mucciarelli, M. R. Gallipoli, S. M. Richwalski, & , A. Strollo (2007). Comparison of empirical and numerical site responses at the Tito test site, Southern Italy. *Bull. Seism. Soc. Am.* **97**, 1413–1431.
- Petersen, M.D., A.D. Frankel, S.C. Harmsen, C.S. Mueller, K.M. Haller, R.L. Wheeler, R.L. Wesson, Y. Zeng, O.S. Boyd, D.M. Perkins, N. Luco, E.H. Field, C.J. Wills, and K.S. Rukstales (2008). Documentation for the 2008 Update of the United States National Seismic Hazard Maps, USGS
- Pilz, M., S. Parolai, F. Leyton, J. Campos, and J. Zschau (2009). A comparison of site response techniques using earthquake data and ambient seismic noise analysis in the large urban areas of Santiago de Chile, *Geophys. J. Int.* **178**, 713–728.
- Pilz, M., S. Parolai, M. Stupazzini, R. Paolucci, and J. Zschau (2011). Modelling basin effects on earthquake ground motion in the Santiago de Chile basin by a spectral element code, *Geophys. J. Int.* **187**, 929–945.

- Pischiutta, M., G. Cultrera, A. Caserta, L. Luzi, and A. Rovelli (2010). Topographic effects on the hill of Nocera Umbra, central Italy, *Geophysical Journal International*. **182**, 977–987.
- Reed, J., and C. Bush (2005). Generalized geologic map of the United States, Puerto Rico, and the US Virgin Islands. US Geol. Surv. National Atlas Small-Scale Collection, available at <http://pubs.Usgs.Gov/atlas/geologic/>.
- Semblat, J.F., M. Kham, E. Parara, P.-Y. Bard, K. Pitilakis, K. Makra, and D. Raptakis (2005). Seismic wave amplification: Basin geometry vs soil layering, *Soil. Dyn. Earthq.Eng.* **25**, 529–538.
- Shen, W., and M.H. Ritzwoller (2016). Crustal and uppermost mantle structure beneath the United States, *J.G.R.* **121**, 4306–4342.
- Storchak, D.A., J. Schweitzer, and P. Bormann (2003). The IASPEI standard seismic phase list, *Seismol. Res. Lett.* **74**, 761–772.
- Wald, L.A., and J. Mori (2000). Evaluation of Methods for Estimating Linear Site-Response Amplifications in the Los Angeles Region, *Bull. Seismol. Soc. Am.* **90**, S32–42.
- Wald, D.J., and T.I. Allen (2007). Topographic Slope as a Proxy for Seismic Site Conditions and Amplification, *Bull. Seismol. Soc. Am.* **97**, 1379–95.
- Woolery, E.W., Z. Wang, N. Seth Carpenter, R. Street, and C. Brengman (2016). The Central United States Seismic Observatory: Site Characterization, Instrumentation, and Recordings, *Seismol. Res. Lett.* **87**, 215–228.
- Yang, X. (2002). A numerical investigation of L g geometrical spreading, *Bull. Seismol. Soc. Am.* **92**, 3067–79.

4 Chapter 4: Uppermost Mantle Seismic Structure beneath Central and Eastern United States

Abstract

We constructed a detailed map of the uppermost mantle seismic structure (P and S velocity as well as S-wave attenuation) beneath the Central and Eastern U.S. (CEUS) using regional seismic waveforms and travel time arrivals recorded by the USArray and travel time arrivals from the International Seismic Center (ISC). We used a standard Pn and Sn travel time tomography algorithm with identical Pn and Sn travel time data sets to estimate the upper most mantle P-wave (Pn) velocity, S-wave (Sn) velocity, and the velocity ratio (V_{Pn}/V_{Sn}). Furthermore, we modified the Two Station Method in order to limit the contributions of site response and estimate the effective attenuation of Sn phase (Q^{-1}_{Sn}).

Lower Q values generally correspond with lower velocities both in terms of Pn and Sn-wave speeds (e.g., New England, Mississippi Embayment), however, some regions including southern Georgia, eastern South Carolina and NMSZ show high velocity and low Q_{Sn} values. This can be potentially explained by scattering attenuation of the Sn phase. The V_{Pn}/V_{Sn} ratio shows values higher than the average in regions such as the Mississippi Embayment, New England, and south Appalachian. V_{Pn}/V_{Sn} ratios are lower than the average in regions such as northwestern CEUS, South Georgia and eastern Texas. To estimate the uppermost mantle temperature, a constrained grid-search algorithm includes the observed V_{Sn} , V_{Pn} and Q_{Sn} with the

calculated velocities of specific compositional models is conducted. The uppermost mantle temperature result, ~300-500 C, beneath the northern mid-continent correlates with the depleted uppermost mantle, and the highest temperature, 1100 C, beneath New England correlates with phanerozoic enriched upper mantle. Although our temperature results appear to be well resolved, we found that V_{Pn} , V_{Sn} , and Q_{Sn} are not enough to constrain the detailed uppermost mantle composition model.

Our results highlight significant temperature heterogeneity in uppermost mantle across the CEUS and is consistent with there not being any melt within the uppermost mantle beneath the CEUS; therefore, we interpret all anomalies as being the result of either temperature and/or compositional variations.

4.1 Introduction

The Transportable Array (TA) provides a unique opportunity to map the seismic and thermal structure of the uppermost mantle beneath Central and Eastern United States (CEUS) in fine detail and at a high resolution. Over the last decades the large-scale upper mantle has been well studied using several techniques including multi-frequency body-wave tomography (Sigloch, 2008, 2011), joined surface wave and body waves tomography (Obrebski et al., 2011; Porritt et al., 2014; Schmandt and Lin, 2014) and long-period waveform tomographic modeling (Schaeffer and Lebedev, 2014; Yuan and Romanowicz, 2010; Yuan et al., 2011). The compressional velocity structure of the uppermost mantle was estimated using the Pn travel time tomography (e.g., Buehler & Shearer, 2017; Zhang et al., 2009). These studies show

major negative velocity anomaly beneath New England, and high velocity anomalies in northern mid-continent. However, the uppermost mantle seismic structure (Moho to the low velocity zone) has not been studied using both Sn and Pn regional seismic phases.

The Pn and Sn regional seismic phases are high frequency waves (0.5-8Hz) propagating in the lithospheric mantle with Pn velocity ~ 7.8 to 8.1 km/s, and Sn velocity ~ 3.8 to 4.7 km/s (Kennett, 1986). Due to their high frequency and propagation path, regional seismic phases are a valuable resource to map details of uppermost mantle V_P and V_S structure. The Sn regional seismic wave, a guided shear wave phase, not only can be used to estimate the uppermost mantle absolute shear velocity but also used to estimate the shear wave attenuation factor Q^{-1}_{sn} (Lü et al., 2014; Sun and Kennett, 2017).

The apparent attenuation (Q^{-1}) is composed function of both scattering attenuation and intrinsic (anelastic) attenuation, which is primarily the seismic energy loss due to anelasticity (Jin and Aki, 1988; Wennerberg, 1993). The attenuation of regional seismic waves is a function of lithospheric mantle velocity gradient, temperature, thickness, topography, as well as the presence of partial melt within the mantle lithosphere. Sn intrinsic attenuation and uppermost mantle shear wave velocity gradient, governs how efficiently the Sn phase propagates through the uppermost mantle (e.g., Molnar & Oliver, 1969, Ni & Barazangi, 1983; Beghoul et al., 1993; Molinaro et al., 2005). Sn waves propagate across stable regions, continental shields and platforms, efficiently while Sn paths crossing the mid-ocean ridge crests

or back arc basins, are inefficient or even blocked. Blocked seismic paths represent highly attenuated paths which could be due to a melt or high temperature (Molnar & Oliver, 1969).

Lateral variation in Pn velocity and Sn velocities are likely associated with temperature and compositional differences in the uppermost mantle (Goes & Lee, 2002; Perry et al., 2006; Schmandt & Lin, 2014); therefore, Correcting the calculated shear velocity for anelasticity is essential to accurately estimating the temperature and composition. Previous studies have solved this problem either by including the anelasticity as empirical synthetic Q values (Jackson et al., 2004; Shapiro & Ritzwoller, 2004) or P-wave velocities were only used in the temperature inversion (Schutt et al., 2018).

In this paper: (1) we estimate the Sn and Pn velocities using only Pn and Sn travel time ray path pairs. This allows us to calculate the V_p/V_s velocity ratios for the uppermost mantle since the resolution for both V_s and V_p should be nearly identical (Lü et al., 2014). The number of the seismic events, the epicenter distribution, and the quality of seismic data govern the ray- path coverage across CEUS (Lee, 2003; Niu et al., 2004); (2) we estimate Sn attenuation Q_{sn} after eliminating the site response; (3) we invert both velocities and attenuation values to temperature of the uppermost mantle. It is important to note that Pn and Sn travel time tomography yield absolute velocity estimates; therefore, it has the advantage over some of the other travel time tomography models in estimating mantle temperatures

The seismic structure of the uppermost mantle and its spatial variation provides us with important information about the mantle structure in the CEUS which can help to constrain the origin and evolution of the North American lithosphere. Resolving the detailed seismic structure beneath Proterozoic and Phanerozoic terranes may increase our understanding of lithospheric evolution, physical and chemical characteristics. Estimating temperature variation is an important step in understanding the strength, stress, thickness, and deformation of the uppermost mantle.

4.1.1 Geology, Geophysical, and Geochemical Background:

The North American continent was assembled in the Paleoproterozoic (2-1.8 Ga) by plate collisions of Archean continents and smaller Archean continental fragments (e.g., Hoffman et al., 1989; Whitmeyer & Karlstrom, 2007)(Fig.1). The U.S. is underlain by Archean, thick, compositionally depleted lithospheric mantle. The present shape of the North American continent resulted from processes of the late Permian collisional orogeny, and subsequent rifting along the Atlantic since the Cretaceous. During the Proterozoic, progressive series of juvenile volcanic arcs and oceanic terranes accreted along a southern plate margin and built the lithosphere of the continental United States. Early juvenile additions formed at the same time that the core was assembling (1.84-1.82 Ga). Following the major assembly of the core of North America (1.8 Ga), major accretionary provinces were added by arc-continent accretion with northeast-trending. The portion of North America's craton that lies within the central part of United States is almost entirely a cratonic platform with low topographic relief. The Coastal Plain, which extends from southern Texas to the northeast through the Mid-Atlantic States, was formed during the Jurassic and

Cretaceous during the opening of the Atlantic Ocean and Gulf of Mexico. Magmatic events have influenced the U.S. such as Proterozoic dykes that intruded into the Superior craton (Ernst and Bleeker, 2010) and Mesozoic magmatic activity in the northern east U.S. that caused a progression of kimberlite and alkaline igneous intrusions (Fig.1). The lithospheric thickness varies from thick 200-180km in the west to 80 km in the east, however; there is disagreement whether the negative gradient is the Lithosphere-Asthenosphere Boundary (LAB) or a Mid Lithospheric Discontinuity (Hansen et al., 2015; Lekić and Fischer, 2014; Levin et al., 2006; Wirth and Long, 2014; Yuan and Romanowicz, 2010)

The most well-resolved seismic velocity anomalies in the upper mantle beneath the CEUS are the positive anomaly in northwestern part of the CEUS (e.g., Goes & Lee, 2002; Grand, 1994), Reelfoot Rift (RFR) and the negative anomalies in the Eastern Grenville front (New England) and western Virginia (Pollitz and Mooney, 2014; Porter et al., 2016; Shen and Ritzwoller, 2016a). The Pn velocity gradient within the uppermost mantle increases with depth across most of the mid-continent and eastern Texas ($\sim 0.004 \text{ s}^{-1}$) while the Mississippi embayment shows negative gradient values (-0.001 s^{-1} ; Buehler & Shearer, 2017). The negative shear wave anomalies increase ($\sim 0.4 \text{ km/s}$) from 60km to 150km depth beneath New England, Virginia and Georgia (Clouzet et al., 2017) while Shen et al., (2016) found that most of CEUS have a positive shear wave gradient in the uppermost mantle except few regions show negative gradient including NMSZ and southern Arkansas ($\sim 0.2-0.3 \text{ km/s}$). The low Vs values are an indicator of partial melts or hydrous minerals while gentle velocity gradient could be an indicator of thermal boundary.

The results of a high- resolution 3D isotropic and radially anisotropic shear wave velocity model of the North American lithospheric mantle shows that the major tectonic Proterozoic sutures extend down to 100–150 km (Yuan and Levin, 2014). The magnetotelloric MT results from the upper mantle of the CEUS shows conductive anomalies, which may coincide with the proposed hot spot tracks in the CEUS, interpreted either as a partial melting or compositional effects (Yardley & Valley, 1997; Selway, 2014; Gribenko & Zhdanov, 2017). Mantle plumes migrate through the lithospheric mantle, resulting in compositional changes. The plume could be a source of water that would facilitate mineral transformations and metasomatism of a mantle peridotites. The thermal anomaly is unlikely for hotspot with ages $\sim >75$ Myr (Van Arsdale and Cox, 2007; Chu et al., 2013).

S_n , P_n velocity and Q_{sn} variations are sensitive to the composition, temperature, and existing melt/partial melt in the upper mantle. The relationships between velocity, composition and temperature were studied in previous work (e.g., Lee, 2003; Schutt & Leshner, 2006; Wagner et al., 2008). The upper mantle is dominantly composed of peridotite, a rock with a high percentage of Olivine, along with pyroxenites, eclogites, and amphibolites (Bodinier et al., 1987; Kelemen et al., 1992). These presence of none-peridotitic rocks are important in predicting the tectonic history of the upper mantle. These inclusions could be an indication of an asthenospheric upwelling, subductions, or a slab remnant.

4.2 Data and Methods

4.2.1 *Sn attenuation*

Regional seismic records from the EarthScope Transportable Array network (TA) of earthquake 4-6Mw, were used to estimate Sn attenuation. In total we have 19,831 Sn wave arrivals with epicentral distances smaller than 2,000 km recorded between 2010 and October 2013. We picked the Sn phase manually based on three types of Sn phases: efficient, inefficient, and blocked. Manually picked Sn travel time windows prevent including seismic energy propagating below the uppermost mantle, which could contaminate our data. Blocked Sn ray-paths are not included in the model, which could have the potential to bias our Sn Q model upward.

The Reverse two station method provides a reliable approach to estimate Q_{Sn} because it eliminates the local site effect, however, we do not have enough ray paths fill the geometric requirement for this method (TSM) (Bao et al., 2011). To overcome this limitation, we modified the Two Station Method and we named the Modified Two Stations Method (MTSM) in order to estimate the site effect and remove it from the TSM results. The result is a measure of effective Sn attenuation (Q effective) which includes the anelastic and scattering attenuation.

The TSM was presented by Tsai and Aki (1969) and improved by (Cong et al., 1996; Xie and Mitchell, 1990). The ideal situation for applying this method requires two recording stations aligned exactly with the source. We denote the two stations as stations i and j with the spectra A_i and A_j , respectively. The epicentral distances of station i and j are d_i and d_j , and inter-station distance is d_{ij} . S_{si} and S_{sj} are

the site responses, and I_i and I_j denote the instrument responses at stations i and j , respectively. This method has two assumptions: the one-dimensional velocity structure, and the identical (the inter-station) apparent Q values at stations i and j . The apparent $1/Q$ value as a function of frequency can be written as

$$\frac{1}{Q(f)} = \frac{v}{\pi f(d_j - d_i)} \ln \left(\frac{A_i(f) S_{sj}(f) I_j(f) d_i^m}{A_j(f) S_{si}(f) I_i(f) d_j^m} \right) \quad (3.1).$$

We moved the relative site response term to the left-hand side of the (Eq. 1) to be included in the solution instead of neglecting the ratio (Eq. 2;3).

$$\frac{1}{Q(f)} = \frac{v}{\pi f(d_j - d_i)} \left[\ln \left(\frac{S_{sj}(f)}{S_{si}(f)} \right) + \ln \left(\frac{A_i(f) I_j(f) d_i^m}{A_j(f) I_i(f) d_j^m} \right) \right] \quad (3.2)$$

$$\frac{1}{Q(f)} - \frac{v}{\pi f(d_j - d_i)} \ln \left(\frac{S_{sj}(f)}{S_{si}(f)} \right) = \frac{v}{\pi f(d_j - d_i)} \ln \left(\frac{A_i(f) I_j(f) d_i^m}{A_j(f) I_i(f) d_j^m} \right) \quad (3.3)$$

4.2.2 Q Tomography

In general, tomographic inversions apply least squares algorithms such as LSQR (Paige and Saunders, 1982) Eq. (4). The left hand side is the data matrix d that consists of the TSM Q values. On the right-hand side, the G matrix is a sparse matrix containing the values of Δ_{mn} and the model space m is defined as $1/Q_m$ for the m th cell and the inversion problem will be written as ($d=Gm$).

$$\frac{\Delta n}{Qn} = \sum_{m=1}^M \frac{\Delta mn}{Q_m}$$

(3.4).

To overcome one of the of relative site response, we modified the tomographic code to estimate the site effects of each station and calculate the Q independent of site response. We include two site response terms, one for each station (Eq. 5; 6).

$$\frac{\Delta n}{Qn} = \sum_{m=1}^M \frac{\Delta mn}{Q_m} + \frac{v}{\pi f(d_j - d_i)} (\ln S_{Sj} - \ln S_{Si}) \quad (3.5).$$

$$\begin{pmatrix} \frac{\Delta n}{Qn_1} \\ \frac{\Delta n}{Qn_2} \\ \cdot \\ \cdot \\ \frac{\Delta n}{Qn_i} \end{pmatrix} = \begin{pmatrix} \Delta m_1 n_1 & \Delta m_2 n_1 & \cdot & \cdot & 1 & -1 \\ \Delta m_1 n_2 & \Delta m_2 n_2 & \cdot & 1 & \cdot & -1 \\ \Delta m_1 n_3 & \Delta m_2 n_3 & 1 & \cdot & -1 & \cdot \\ \Delta m_1 n_3 & \Delta m_2 n_3 & -1 & \cdot & \cdot & 1 \\ \dots & & & & & \\ \Delta m_1 n_i \dots \dots \Delta m_M n_i \end{pmatrix} \begin{pmatrix} \frac{1}{Q_{m1}} \\ \frac{1}{Q_{m2}} \\ \cdot \\ \cdot \\ \ln S_{Sj} \\ \ln S_{Si} \end{pmatrix} \quad (6)$$

where Q_n is the attenuation factor Q along the path n. Q_m is variation of the Q across the cell m. \square is the length of path n over cell m, total number of cells is M. S_{Sj} is the site response of the far station, S_{Si} is the site response of the nearest station.

We applied the modified tomographic code in order to calculate the raypath based Q values that are independent of the site effect. Simulations using checkerboard

models (Fig. 2) were used to test the efficiency of MTSM in reducing the site effects on the Q values. The checkerboard with 30% Perturbation shows that MTSM is efficient in improving ray-path based Q values and reducing the effect of changes in localized site amplification.

4.2.3 Travel Time Tomography

In order to measure uppermost V_{Pn} and V_{Sn} , we use a standard approach to Pn travel time tomography. We used P_n and S_n phase data recorded at USArray transportable array stations between April 2004 and July 2017. P_n phases were routinely picked at the Array Network Facility. Often it is hard to pick S_n arrivals automatically without checking manually. The arrival time data was downloaded from (<http://anf.ucsd.edu/tools/events/download.php>); 206,000 P_n picks from 12,000 events. In addition to TA data, over 60,000 P_n travel times from the International Seismological Centre between 1970-2014 were added to the data set and processed. Ray coverage is densest in the central United States and sparser in the northwest, south, and south eastern part of the United States (see the electronic supplements Fig. S1a). The epicentral distances of the travel times used in this study is 4-16 degree for S_n and P_n. We increased the minimum epicentral distance to avoid contamination from L_g, and P_g, S_g first arrivals. To further improve the data quality, we used the following criteria: The minimum number of event and stations used in the processing is 6, (i.e. each event should be recorded at least in 6 stations and each station has to record at least 6 events). The travel time residuals to fitted line is ± 6 for both P_n and S_n while residuals greater than ± 6 range were discarded; the depth of the seismic events is less than 40 (see electronic supplements Figure S2). The linear least squares

method of Hearn (1996) was applied to estimate the velocity in the uppermost mantle, the station time delay and the source time delay. The travel times can be written as (Eq.7):

$$\begin{aligned}
 T &= E_j + R_i + \Delta_{ji}S \\
 \Delta_{ji}S &= \sum_{k=1}^n \Delta_k S_k \quad \dots (3.7) \\
 R_j &= \int_{sealevel}^{MohoDepth} \sqrt{(S_c^2 - S^2)} dh \\
 E_i &= \int_{HypocenterDepth}^{MohoDepth} \sqrt{(S_c^2 - S^2)} dh
 \end{aligned}$$

where E_j and R_i are the source and station delay terms, respectively, Δ is the great circle distance between the source and the receiver, S is the slowness in the uppermost mantle, and k is the uppermost mantle cell along the Δ_{ji} , S_c is the crustal slowness as function of depth dh . In this equation we assume there is no vertical velocity gradient beneath the Moho.

4.2.4 Resolution models

We used the Checkerboard synthetic model approach to estimate the resolution and the reliability of the inversion method for both the travel time tomography and Q_{Sn} attenuation. First, we generated a synthetic data set. We used the same processing parameters (e.g., Laplacian Damping, weights, number of inversion iterations, ray-paths, station and event locations) that we used in the inversion of the actual data set. We then tested different synthetic anomaly sizes (e.g., (2.5×2.5) and (5×5)). The lateral resolution is recoverable over most of the continental area for the

5×5 cell, except for Florida, however, for 2.5×2.5 cell size the resolution across northern CEUS, south CEUS and east coast is relatively poor (a collection of checkerboard maps of different cell sizes is shown in the electronic supplements Figure S3). In addition, the uncertainty in seismic models was determined by bootstrap algorithm (Tichelaar and Ruff, 1989), which repeated the whole inversion ~100 times. The standard deviation (std) of bootstrap uncertainty considers as an indicator for the reliability and stability of our results. Figures 3b,4b,5b are the standard deviation (std) bootstrapped V_{Pn} , V_{Sn} , and the ratio V_{Pn}/V_{Sn} , respectively.

4.3 Results

We have formulated V_{Pn} , V_{Sn} , (V_{Pn}/V_{Sn}) and Sn attenuation models of the Central and Eastern United States (Figures 3,4, and 5). The recorded earthquakes were principally located within specific seismic zones such as the New Madrid Seismic Zone (NMSZ), St. Lawrence Rift System (SLRS) and Charlevoix Seismic zone (Anglin and Buchbinder, 1981); therefore, large regions such as the southern and southwestern CEUS, have relatively poor ray coverage. Figure S1a shows the ray path coverage colored based on the length of the ray path (in degree) and figure S1b shows the depth that the ray paths propagate through (40 -120 km).

The mean value of the Pn velocity is 8.2 km/s and the maximum positive perturbation is 0.35 km/s while the maximum negative perturbation is 0.2 km/s (Fig. 3). Using all Pn phases without taking into account the Sn data set, we find an average velocity of 8.2 km/s (in electronic supplements figure S4), which is similar to (Buehler and Shearer, 2017) who found a mean Pn velocity of 8.1 and maximum

perturbation of 0.5, however, they inverted a larger data set of Pn ray-paths and generated a Pn tomography model for all United states where the low Pn velocities in the western U.S. lowers the average. Negative anomalies were observed beneath the northeastern CEUS, along the east coast (e.g., eastern Virginia, eastern North Carolina), and the northern part of the Reelfoot rift. Positive anomalies were observed beneath southern South Carolina and NMSZ.

Our average S_n velocity is 4.65, the maximum positive perturbation is 0.45 km/s and the maximum negative perturbation is 0.33km/s (Fig.4). Similar to our results, (Shen and Ritzwoller, 2016a) find average values of 4.4 km/s and 0.4 km/s perturbation at 70 km depth for a model covering the entire U.S. If we look at the eastern US portion of their model, the average is higher, ~4.5Km/s. Clouzet et al. (2018) found that at 60 km depth the average velocity is 4.63 km/s and the perturbation is 0.2 km /s along the U.S. eastern coast. Figure 4 shows negative anomalies beneath the entire east coast, mid-continent (e.g., following a north/south trend perpendicular to the Reelfoot rift), and a few negative anomalies beneath southern Mid-Continent Rift (MCR). Positive anomalies were observed beneath the southern portions of South Carolina, and south-Georgia.

We find a mean value of the V_{Pn}/V_{Sn} ratio of, 1.76 which is essentially as the global average. The maximum V_{Pn}/V_{Sn} ratio perturbation is ~0.08 (Fig. 5). V_{Pn}/V_{Sn} ratio correlates strongly with the V_{Sn} because V_{Sn} perturbation range is wider than the range of V_{Pn} perturbation. The average regional velocity ratio observed beneath eastern China is 1.8 and the maximum perturbation is 0.1 (Sun and Kennett, 2016)

higher than our results. Their results of the regional velocity ratio and velocity anomalies were interpreted as upwelling hot material and sudden changes in the uppermost mantle composition.

Q_{S_n} is typically a function of frequency. We generated Q_{S_n} for three non-overlapping frequency bands: 1.0, 2.0, and 3.0 Hz. Figure 6 shows regions of significantly attenuated 1 Hz S_n along the east coast and the Mississippi Embayment. We observed a strong correlation between Reelfoot Rift (RFR) and a low Q_{S_n} (200-500). Throughout the entire craton we find a relatively large Q_{S_n} (~500). In southeastern U.S., we find a strong frequency dependence of Q_{S_n} . (Figure S5) and a weak correlation with the negative S_n and P_n velocity anomalies, which might be evidence of attenuation via scattering of the S_n wave front. A strong correlation between S_n attenuation and negative velocity anomalies of P_n and S_n were observed along the U.S. east coast and Mississippi Embayment. Comparing our S_n attenuation model with Rayleigh wave attenuation model for 40s, we find a very good correlation along the eastern coast, NMSZ, and northern mid-continent (Bao et al., 2016).

4.4 Discussion

We have generated models of V_{P_n} , V_{S_n} , and Q_{S_n} variations in the uppermost mantle beneath CEUS. We primarily observe positive anomalies (in terms of V_{P_n} , V_{S_n} , and Q_{S_n}) in the north Central U.S. and negative anomalies correlating with the Reelfoot rift zone, Mississippi embayment, and New England. We have systematically compared our observations to other seismic results and methodologies.

4.4.1 Northern Mid-Continent

Large positive velocity anomalies are observed in the northwestern CEUS (+8.3-8.5/4.66-4.9). These positive anomalies appear in number of previous studies (e.g. Chen et al., 2016; Pollitz & Mooney, 2014). They likely represent the deep cratonic roots of the Superior craton. The ray-paths in this region are relatively long, therefore they sample greater depths than other regions ($> \sim 100$ km). We observe a few small negative anomalies close to the eastern boundary of the (Mid-Continent Rift)MCR and they are similar to anomalies in (Shen and Ritzwoller, 2016b) ~ 4.6 km/s while the surrounding region is 4.8km/s. The V_{Pn}/V_{Sn} velocity ratio in this region shows two anomalies with higher values than the global average (1.82-1.85). The LAB is deep in this region (> 250 km); therefore, a possible partial cause of much of the variability in seismic structure could be compositional heterogeneity (e.g. depleted mantle having higher velocities). A possible enriched mantle remnant could result from rejuvenation processes beneath the MCR and the surrounding boundaries (Nicholson et al., 1997; Paces and Bell, 1989). It is worth noting that we have explored if we could determine whether different compositional models could better explain the V_{Pn} and V_{Sn} models and found that we cannot uniquely determine an optimal compositional model. Some insight can be obtained from examining Kimberlites from Kansas which provide some information on the lithospheric composition of terranes near the MCR where xenoliths are compositionally fertile lherzolites which could reflect melt-metasomatism beneath this region (Griffin et al., 2004)

4.4.2 *East Coast:*

Our Pn and Sn results show low Vs and Vp values of ~ 4.2 km/s and 7.9 km/s, beneath New England. The ray-paths for the east coast are relatively short (< 8 degree); thus, the depth they sample is relatively shallow (e.g., ~ 60 km). The attenuation model shows a low Q anomaly that correlates well with low Sn velocity anomalies (200-400 Q_{Sn}). Our results correlate well with Savage et al. (2017), who found low velocity anomalies (~ 4.2 km/s) under New England at a depth of 75 km. Our results also correlate well with Buehler & Shearer, (2017) where both models have Pn velocities of 7.9 km/s. The negative anomalies in this region could be related to the Great Meteor hot spot (Crough, 1981; Heaman & Kjarsgaard, 2000; Li & Stephens, 2003; Mooney et al., 1983). The kimberlite resulting from volcanism along the seamount off shore in the Atlantic Ocean may be associated with the Meteor hot spot; however, other theories attribute these anomalies to delamination that occurred after the Appalachian Orogeny (e.g., Levin et al., 2000; Nelson, 1992). A hypothesized active upwelling magma was suggested after observation of variation in the strength of seismic anisotropy (Levin et al., 2017). Absence of volcanism or uplift in this region support this theory, however, our results cannot be used to distinguish between these two end member models.

For the Appalachian region of West Virginia, our results show slightly lower than average Pn and Sn velocities (~ 8.0 and ~ 4.5 km/s respectively), with slightly different locations for each of the anomalies. The differences in the anomalies location could be attributed to the low resolution and the high uncertainty of the bootstrap results of both V_{Sn} and P_{Sn} in this region. Buehler and Shearer (2017)

observed negative Pn anomalies ~ 7.9 km/s similar to our result; (Savage et al., 2017) find low shear velocities in west Virginia at 50 km, which extends to the east with increasing depth. Shen et al. (2014) show low shear velocity at a depth of 70 km while the low shear wave velocities at 200 km was observed by Schmandt and Lin (2014) and Clouzet et al. (2018). Volcanism occurred along the eastern margin of North America in western Virginia During the middle Eocene (Mazza et al., 2014; Tso and Surber, 2006). Upwelling asthenosphere has been proposed to explain the volcanism in this region given the observed chemistry of the basaltic rocks. One of the theories for the origin of this young volcanism involves the delamination of an eclogitic keel from the base of the crust (Mazza et al., 2014). Another model involves a small-scale upwelling associated with asthenospheric flow at the continental margin. Murphy and Egbert (2017) observed high anomalies beneath the eastern Appalachian Mountains extending to 200 km depth, which is consistent with a thick lithosphere ($\sim > 200$ km). The differences in lithospheric thickness between the Proterozoic terrains in the Appalachians could generate upwelling currents at the edge of a lithospheric keel which could increase the temperature and/or generate metasomatism in this region.

4.4.3 Central U.S.

Many studies have imaged the lithospheric structure in this region specially beneath the Reelfoot Rift (RFR). Our result for both Sn and Pn shows velocities (8.3 km/s, 4.7 km/s) that are higher than the global average. This result correlates well with the Pn tomographic model reported by previous works (Buehler & Shearer, 2017; Li et al., 2007; Zhang et al., 2009). Our V_{Sn} result agrees with

shear-wave velocities (~ 4.8 km/s) from (Chen et al., 2018). Most likely, the positive anomalies extend from the lower crust (Chen et al., 2016) into the upper most mantle, which underlain by low velocity zone between 75-150 km (Chen et al., 2018). For the northeastern arm of the Reelfoot rift (NE-RFR), which is the Southern Indiana Arm (Braile et al., 1984); Nelson, 1991) and it is the least developed part in RFR (Nelson, 1990), we found negative P_n and S_n anomalies: $S_n \sim 4.3$ km/s, and $P_n \sim 8.1$ km/s, which is similar to negative anomalies ~ 4.4 km/s found by (Chen et al., 2016). Below the Central Illinois basin we find low $V_{S_n} \sim 4.2$ km/s and V_{P_n} anomalies, which mostly correlates with $V_s \sim 4.4$ at 40-60 km (Chen et al., 2016) and correlates also with Bedle and van der Lee, (2006) who found 200 ms delay at 60 km depth and the delay decrease to 0 ms at 100 km. This upper most mantle negative anomalies could be the result of metasomatism as a result of a remnant rift structures that formed prior to the Reelfoot Rift (Marshak and Paulsen, 1996; Chen et al., 2016). The S_n attenuation map shows low Q_{S_n} (300-400) values along all the Mississippi Embayment and beneath the Reelfoot rift. The complex structure of this region makes it possible that scattering attenuation plays a role in attenuating the S_n phase in addition to the intrinsic attenuation.

The V_{P_n}/V_{S_n} ratio shows a higher value than the average V_{P_n}/V_{S_n} of ~ 1.76 beneath NMSZ and a lower than the average southern the RFR. V_{P_n}/V_{S_n} ratio variations in this region could be evidence of pronounced compositional variation, which could suggest a combination of composition -temperature effect in this region. There are a number of pieces of evidence that support the compositional-temperature effect: (1) high density anomalies of ~ 0.016 g/cm³ at 100 km, reducing to ~ 0.008

g/cm³ at 200km depth (Kaban et al., 2014); (2) Arkansas xenolith sample depleted down to ~130 km; (3) At larger depth ~(150-250km), low-velocity anomaly dipping to the SW (Nyamwandha and Powell, 2016) which could be the LAB (Gao et al., 2008). Many hypotheses could explain these observations e.g.; A flat part of the Farallon slab lies in the transition zone beneath the central U.S (Sigloch and Mihalynuk, 2013) and could generate ascending fluids which could generate metasomatic process in surrounded regions (Tommasi, 1998; Savage, 1999); A thinned lithosphere, which resulted from rifting (Braile et al., 1986; Catchings, 1999; Nelson & Zhang, 1991; Stephenson, 2012); The hypothesized cretaceous hotspot (100Ma), proposed to have resulted in the intrusion of ultramafic and alkali rocks (Cox & Van Arsdale, 1997; Cox & Van Arsdale, 2002); Edge driven convection is another possible hypothesis (Benoit et al., 2013; Gao and Liu, 2014).

4.4.4 Southern CEUS

The ray-path coverage for this region is not enough to generate high resolution V_{Pn} and V_{Sn} models ; however, we found an interesting positive anomaly in eastern Texas. The observed positive anomaly is larger in V_s than in V_p , generating a smaller V_p/V_s ratio. A high velocity anomaly was observed in the same region at 70 km depth by Evanzia et al., (2014). In southern South Carolina and western Georgia, our results show high velocity anomalies and low V_p/V_s ratio, which agree with Wagner et al.(2018) who show positive shear wave anomalies (0.2-0.4 km /s) for depths between 60 km and 90 km. Kaban et al., (2014) shows a large density anomalies at 100 km in addition to the positive velocity anomaly. We suggest that this anomaly is related to the presence of eclogite. Eclogite generates fast seismic velocities and

positive density anomalies (Hacker, 1996). The V_p/V_s ratio for eclogite was calculated to be between 1.68-1.81 (Anderson, 1989; Worthington, 2013), which is within our range of V_p/V_s . In the southern CEUS, the high S_n attenuation result do not correlate with negative velocity anomalies, as we expect. Furthermore, Q_{S_n} shows a strong frequency dependence. Geologically, this region is complex and composed of assemblages of different lithospheric terranes (Oceanic and continental platelets) that could cause strong lateral heterogeneity that could attenuate S_n via scattering; therefore, we suggest that the low Q_{S_n} could be due to scattering attenuation. This mechanism could be similar to what has been observed in northeast China where a big jump in the Moho and LAB upward was observed (Guo et al., 2014; Tilmann et al., 2003).

4.5 Temperature Implications

Lateral variations in regional seismic velocities and the attenuation anomalies in the uppermost mantle can be attributed, at least in part, to temperature variations; however, compositional variations, and partial melt may also contribute in generating seismic anomalies. When estimating mantle temperatures using seismic wave speeds, one often assumes that velocity heterogeneity be attributed entirely to differences in temperature. Compositional variation and the potential for partial melt must also be considered (Cammarano et al., 2003; Schutt and Leshner, 2006; Stixrude and Lithgow-Bertelloni, 2005). Jackson & Faul, (2010) shows ~ 0.1 km/s of the total velocity variation would correspond with changes in temperature of up to 150°C ; 1% melt may reduce the observed seismic velocities by 2.5% (Hammond & Humphreys,

2000; Kreutzmann et al., 2004; Kreutzmann et al., 2004). It is important to note that we do not observe any evidence for partial melt across the entire CEUS based on our Q_{Sn} measurements. The effect of water has been addressed in many papers; Takei, (2017) suggested that water effects on seismic waves are relatively minor and attributed the low velocity and higher attenuation above the subducted slab to prevailing oxygen fugacity and the presence of melt while the anomalies in the rift zones to only melt. In addition, a small percent of water could react with other elements to generate stable minerals in the uppermost mantle (e.g., phlogopite).

4.5.1 Temperature Model

Using our models of seismic velocity and attenuation, we estimate temperature while accounting for the compositional effect by designing a grid search with multiple compositional models (Table 1) using the following approach:

1) The Theriak-Domino algorithm is used to generate mineral stability fields as a function of (P, T) based on a literature review (de Capitani and Brown, 1987; Holland and Powell, 1998; Horn et al., 2000; Kelsey, 2008; McDonough and Sun, 1995; Workman and Hart, 2005)

2) Abers & Hacker, (2016) Matlab code is used to calculate the elastic seismic velocities as a function of (P, T).

3) The effect of anelasticity is added by including the Q_{Sn} measurement. We use the following expression to correct for the shear quality factor Q_{Sn} and thereby anelastic contributions to the isotropic (anharmonic) P and S wave velocities (e.g., Anderson, 1989; Jackson, 2000). The compressional quality factor is obtained from

$$Q_P^{-1} = (4V_S^2/3V_P^2) Q_S^{-1} \dots\dots\dots (8).$$

The assumption that Q_{Sn} is weakly frequency dependent will impose an error in estimating the temperature because we have found a strong frequency dependence of Q_{Sn} in specific regions such as northern Florida and the coastal plain. Also, the frequency dependence of attenuation in the lithospheric mantle has been observed by a number of studies (e.g., Dalton, 2017; Jackson & Faul, 2010). Anelastic shear-wave velocities V_{S_corr} can be calculated from:

$$V_{s_corr}(P, T, C) = v_{s_calculated}(P, T, C) \left(1 - \frac{2Q_s}{\tan\left(a \frac{\pi}{2}\right)} \right) \dots\dots\dots(3.9),$$

(Anderson, 1989; Jackson et al., 1992,2002), which (\square) has been determined experimentally to be between 0.15–0.25 (Jackson et al., 1992,200); $v_{s_calculated}$ is an isotropic anharmonic shear-wave velocity as a function of temperature (T) and composition (C). Anelastic P-wave velocities V_{P_corr} is obtained by simply using (Eq. 8,9). The Q_s value in this formula represent the anelastic attenuation, however, we will use the effective Q_{Sn} which is a function of both scattering and anelastic attenuation (see the flow chart in Figure 7).

4.5.2 Model resolution:

We constructed the temperature and compositional models by taking the mean of 50 bootstrap iterations in order to estimate the standard errors and thus the models' stability. For temperature, the standard deviation (std) of the bootstrap result shows high uncertainty along the northeastern model edge (Figure 8) where we also see strong frequency dependence to Q_{Sn} . For the composition model, we find a much

higher standard deviation that is spread across the entire study region. Figure 8 shows that the mean of all bootstrap iterations for each point in the model. The uncertainties in the temperature model can be related to many factors: variations in the compositional model choices could result in temperature differences of up to 200°C (e.g., (Lee, 2003); the uppermost mantle of CEUS is found to be anisotropic (e.g., Yuan et al., 2011; Buehler & Shearer, 2017), however, we did not consider anisotropy in our models. Another important factor is that the value of a in (Eq. 9), where $a=0.1-0.3$ for frequency ≤ 1 Hz and a low frequency-dependence of the upper mantle (Jackson, 1993, 2000); therefore, the value of a is not the same for uppermost mantle with higher Q_{S_n} frequency dependence.

4.5.3 Results and discussion of the temperature model

Figure 9 shows three temperature models: (a) the temperature model using only the P_n velocity model which corrected for attenuation (estimated Q_{P_n}); (b) the temperature model resulted from inverting the S_n velocity corrected for attenuation Q_{S_n} ; (c) the temperature model result from inverting both S_n and P_n together, and both were corrected for attenuation. We find that the uppermost mantle temperature increases from the P_n model to S_n model while the S_n - P_n velocity model gives an average of the P_n and S_n temperature models. Our temperature model using both V_{P_n} and V_{S_n} shows that most of the uppermost mantle beneath the CEUS is 600-300C, except for a few higher values that reach up to $\sim 1100^\circ\text{C}$. Temperatures correlate well with upper mantle body wave tomography (e.g., Schmandt and Humphreys, 2011), and temperatures $>800^\circ\text{C}$ are largely confined to the NMSZ and western Virginia. Temperatures $>1100^\circ\text{C}$ are found in western New England. The highest temperature

limit in our grid search algorithm is 1300 ° C; however, the maximum temperature of our model (T_{SnPn}) is 1100° C. It is important to note that the temperature estimations depend on the compositional models we applied in the grid search algorithm (Table 1). Temperatures <600°C occur along a trend from under the Central Plains, through Kansas and Texas. Mean temperatures is 511°C with a standard deviation of 166°C. It is worth noting that none of our temperatures approach the dry solidus of mantle rocks which is consistent with our Q_{Sn} measurements.

The lowest estimated temperature in our model is 300° C, which is lower than previous studies such as (Goes and Lee, 2002; Hansen et al., 2015; Tesauro et al., 2014); however, the lowest temperature at Moho beneath western U.S. was estimated to be around 200° C (Schutt et al., 2018b). Lodders & Fegley, (1998) estimated the upper most mantle lowest temperature to be approximately 200 ° C. The 300° C in our model is consistent for all the compositional models applied in the grid search algorithm (Table 1) and the (std) of bootstrap shows very low values (0-30, Fig.8a), which could be an indicator for a cold uppermost mantle in this region.

Comparing the three temperature models, the highest temperature in the T_{Sn} model is ~1200° C, which is higher than the highest temperatures in T_{Pn} model ~1000° C and T_{PnSn} ~1100°. The temperature differences between the models likely result from the effects of anelasticity which is more pronounced on shear wave velocity. Our temperature results strongly imply that there is no evidence of melt in this region since the highest temperature is less than the adiabatic temperature.

Although this is what we expect to see given the lack of active volcanism in the CEUS, many other temperature models have temperatures exceeding 1300° C.

A comparison of our T_{Pn} and T_{Sn} values with Goes and Lee (2002) shows that we have lower values for both models (T_{Sn} and T_{Pn}). Goes and Lee, (2002) inverted shear wave velocity model, with vertical resolution of approximately 50km, and a P velocity model with a vertical resolution between 50-100 km, and standard Q values from the experimental parameters of synthetic Forsterite (Sobolev et al.,1996). In our model, the Q_{Sn} values are measured using the Modified Two Station method (MTSM)) and we assume that the bulk of Q_{Sn} value is a result of intrinsic attenuation. We recognize this is not a correct across the entire CEUS and thus overestimated temperatures in regions such as the southeastern U.S. Finally, Goes' model has many unreliable regions where both T_s and T_p temperatures are very different from each other while our models are much more consistent. Our results for the unreliable regions in Goes & Lee (2002) model show low temperatures (300-500C) beneath mid-continent, higher temperature (800C) beneath Illinois basin, and high temperature (900-1100C) beneath the northeastern U.S.

We have also compared our shear wave (V_{Sn}) temperature model with Hansen et al.(2015), who estimated the uppermost mantle temperature at 83 km from the surface wave tomography model of Pollitz and Mooney(2014) and used an Olivine anelasticity model (Jackson & Faul, 2010). The similarity between two models was observed for the cold uppermost mantle beneath the NMSZ, cold uppermost mantle beneath northern mid-continent, the hot uppermost mantle beneath the southern

border of Reelfoot rift and Illinois basin; however, our T_{sn} temperature model shows higher temperature variation than the Hansen et al. (2014) model. The two models differ in southern part of the Gulf coastal plain where Hanson et al, (2014) model shows higher temperatures than our model because our temperature models do not have enough resolution in this region. The basic difference between the two models is the anelasticity. While Hansen et al., (2015) empirical anelastic model is grain size dependent and assumed a constant mantle grain size of 0.1mm for simplicity, our model is used calculated Q_{Sn} resulted from MTSM. Comparing our temperature model T_{sn} with Tesauro et al., (2014) temperature model at depth 100km resulted from inverting the regional tomography model (Bedle and Van Der Lee, 2009), we find the two models correlate in New England, South Virginia and in southern RFR with higher temperatures (900-1200C), and in northern mid-continent with low temperature (300-500C) while the two models do not correlate in Illinois Basin where our model shows higher temperatures 900-1200C and beneath NMSZ where our model shows lower temperature (300-600C), which could be attributed to the fact that Sn and Pn samples the shallow uppermost mantle which is different from Tesauro's model. Furthermore, we have higher ray-paths density in this regions which makes our results is robust.

We did not find a fair correlation between the major tectonic boundaries and the temperature, V_{Sn} , V_{Pn} , and Q_{Sn} anomalies. In addition, we find our thermal structures are compatible with surface heat flow measurements (Blackwell et al., 2011). The high temperature of uppermost mantle (900-1100C) correlates well with the high surface heat flow beneath Mississippi embayment (70-90mW/m²), New

England (60-80 mW/m²) and western Illinois basin (60-70 mW/m²). In addition, the low heat flow in cratonic regions (20-40 mW/m²) correlates with low temperature regions of our model (300-500C) (Figure S6).

Hydrous minerals are likely present in the uppermost mantle and would bias our temperature estimations. For example, hydrated phlogopite can lead to significantly overestimated temperature results because %2 Phlogopite could generate ~0.25 km/s and ~0.15 km/s anomalies for V_{Pn} and V_{Sn} , respectively (figures S7, S8, and S9; table2). Furthermore, some of our low Q_{Sn} regions may be the result of strong lateral heterogeneity in uppermost mantle shear wave velocities not high intrinsic attenuation. This is suggested by the very strong frequency dependence of the Q_{Sn} along the southeastern part of the U.S. coastal plain.

Gao and Liu (2014) mapped the discontinuities (d410 and d660) using radial receiver functions and suggested the temperature of the mantle transition zone (MTZ). comparing comparison of our uppermost mantle temperatures with Gao and Liu(2014) d410, show a very good correlation although these results come from very different methods. Variation of the mantle transition zone thickness (MTZ) across CEUS provided some evidence of remnant segments of the Farallon slab beneath the central U.S.. In addition to the d410 and d660, Upper mantle discontinuities can affect the temperature of the uppermost mantle based on its depth and type (chemical or thermal discontinuity (LAB)). Beneath the northern mid-continent, Chen et al.,(2018) proposed a thermally controlled Lithosphere Asthenosphere Boundary (LAB) ~250km and a seismic compositional discontinuity 87 ± 6 km, which imply

cold lithosphere in this region which is consistent with our temperature model. In the northeast US, Kind et al. (2012) find a negative discontinuity between 60 km to 80 km and Liu and Gao (2018) shows a discontinuity at depth $\sim 76 \pm 5$ km. This discontinuity was interpreted as the LAB and is observed in parts of the CEUS where we estimated the highest uppermost mantle temperatures (1100°C). Thinning of the lithosphere in this region could be the result of lithosphere–plume interaction, which could generate lithospheric basal erosion beneath the northeastern U.S. and lead to large uppermost mantle temperatures (Eaton and Frederiksen, 2007). In the Reelfoot Rift, the discontinuity at 80 km depth could be a compositional boundary while thermal LAB lies at a comparable depth to the surrounding area (i.e. >150 km) but shallower than in cratonic regions. As a result, the high temperature values observed in eastern RFR could be attributed to both composition and temperature anomalies. Our high temperature values resulted from inversion the corrected negative velocity anomalies into temperature. However, these negative anomalies could be a result of metasomatism triggered by existing segments of Farallon slab in the transition zone. In addition, it is worth noting that the RFR is tectonically and geologically is complex; therefore, this region could scatter the regional seismic waves which could lead to an overestimate of the uppermost temperatures.

4.6 Conclusions

In this paper we estimate the uppermost mantle seismic velocity from V_{Pn} and V_{Sn} using the travel time tomography for earthquakes recorded by TA and ISC stations. The S_n attenuation of the uppermost mantle (Q^{-1}_{Sn}) is estimated by applying

the modified Two Station Method on TA seismic records to isolate site amplification from path attenuation. Our travel time tomography results show negative Pn and Sn velocity anomalies beneath New England, and Illinois basin; positive anomalies beneath northern mid-continent, and New Madrid Seismic zone. Sn attenuation results show high attenuated Sn regions beneath Mississippi Embayment, and New England. Inverting the regional velocities (Pn and Sn) with including the anelasticity effect enable us to explore the potential of using seismic parameters to image the thermal and compositional structure. Our velocity and attenuation results do not show evidence for any uppermost mantle partial melt beneath the entire CEUS.

Temperature anomalies are strongly compatible with high surface heat flow. In order to obtain acceptable fits in the inversion, the upper most mantle most likely was affected by metasomatism especially in the cratonic region in northern mid-continent (near the MCR), which could have resulted in the formation of seismically slow minerals such as amphibole, phlogopite and carbonate. Temperature along with the metasomatism in the shallow uppermost mantle may explain the anomalies of the regional seismic waves in regions such as the Reelfoot Rift and New England. Joint temperature -composition inversions could not generate stable uppermost mantle compositional models which could imply that seismic alone is not sufficient to constrain the composition of the uppermost mantle. In the future, we will include the density in the grid search in addition to the velocities and anelasticity in order to better constrain the uppermost composition.

4.7 Tables

P (2Gpa)	Ol		Opx		Cpx		Grt		
	Fo	Fa	En	fs	di	hed	Py	alm	gr
1	90	9.993	0.001	0.001	0.001	0.001	0.001	0.001	0.001
2	49.3564	7.1436	0.7096	0.0904	27.1166	2.6834	2.7905	5.1708	4.9388
3	48.0026	8.5974	5.5295	0.0705	22.57	0.33	2.9192	11.2661	0.7146
4	48.257	8.643	5.5644	0.3356	22.1133	1.1867	9.2199	2.7661	1.914
5	47.5115	9.3885	5.821	0.379	24.2451	1.5549	8.1995	1.7364	1.9641
6	48.3795	7.7205	10.6887	1.2113	15.4845	0.4155	9.9471	3.6957	2.2573
7	47.833	8.567	11.5486	0.5514	15.3748	0.6252	10.3165	2.872	2.1115
8	47.833	8.567	11.5061	0.6939	16.0173	2.0827	8.9005	2.4778	1.8217

Table 1. The compositional models applied in the grid search algorithm (Olivine, Orthopyroxene, Clinopyroxene, and Garnet). They are generated by Theriak-Domino (de Capitani and Brown 1987; Holland and Powell 1998; Kelsey 2008).

4.8 Figures

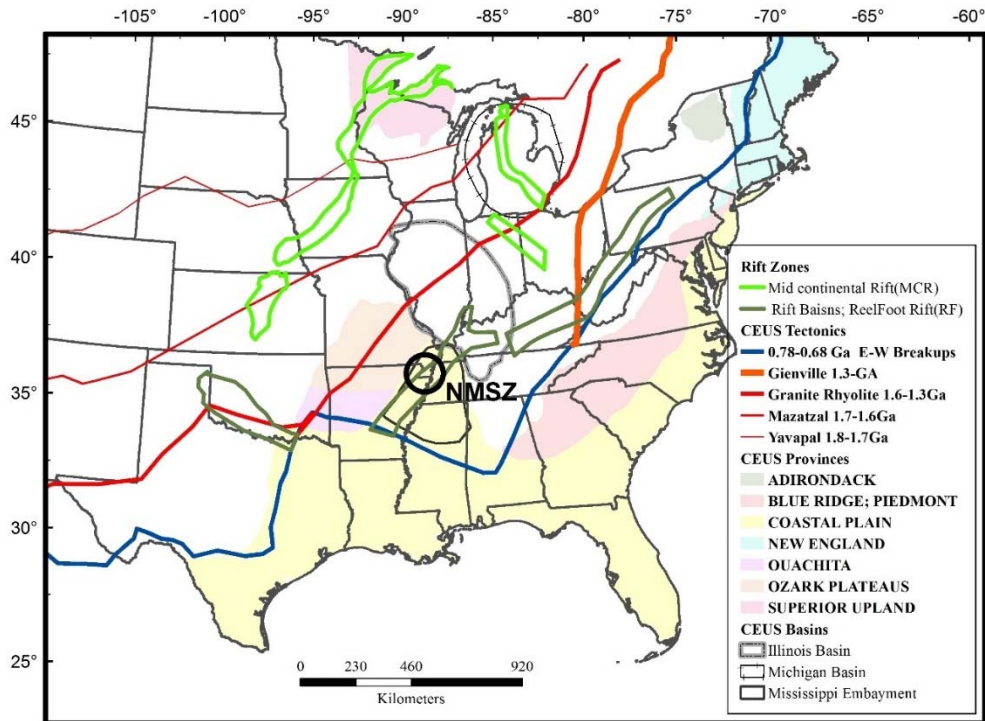


Figure 4.1 Central and Eastern U.S. crustal and physiographic provinces. Dashed red lines represent the crustal provinces. Green lines represent the rift zones (Whitmeyer & Karlstrom, 2007). NMSZ is New Madrid Seismic Zone.

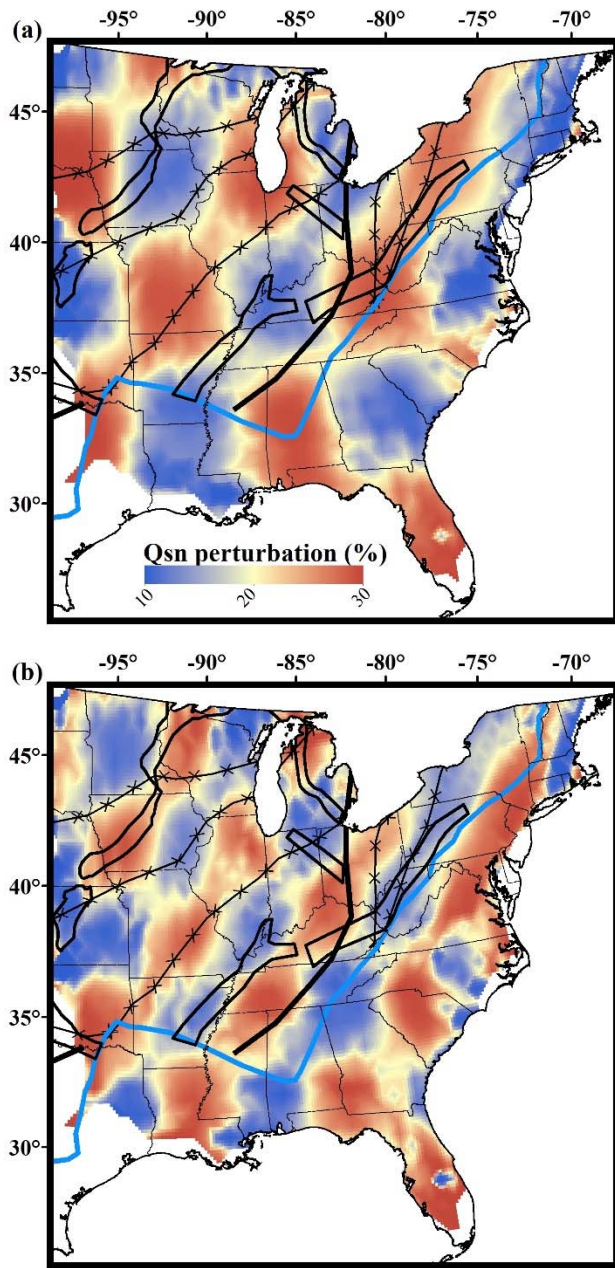


Figure 4.2. Checkerboard test of QSn resulted from the modified tomographic code. Synthetic data was generated with 30% perturbations.

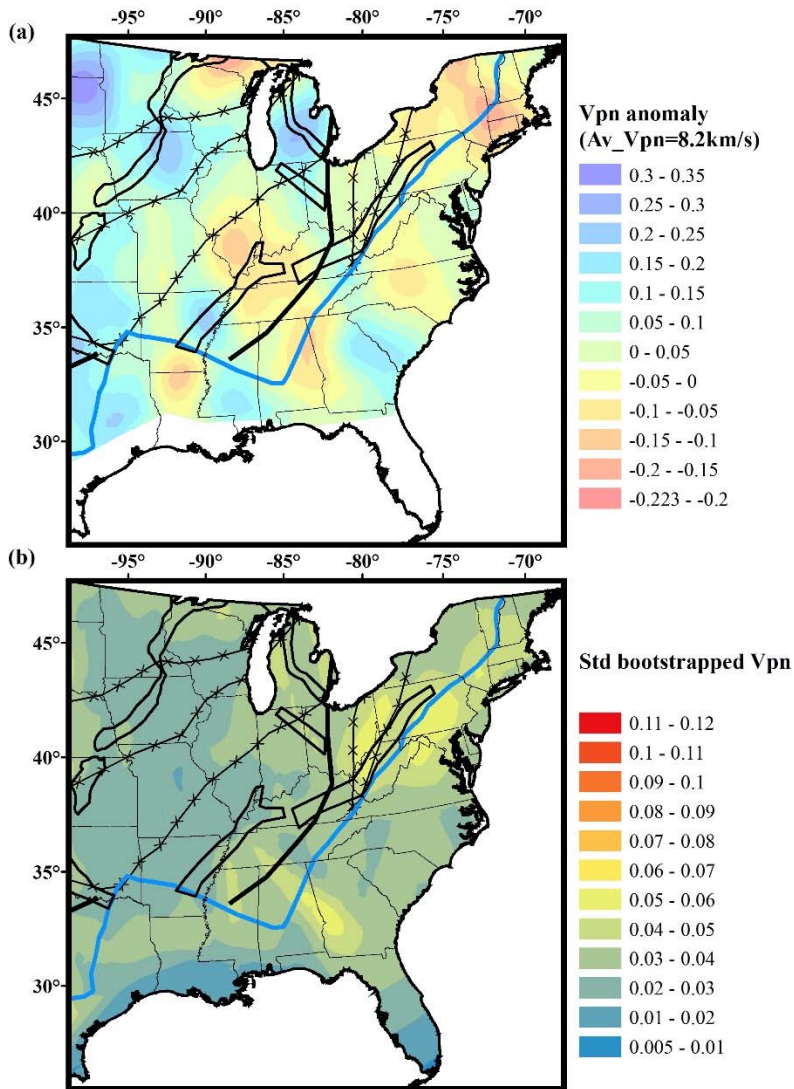


Figure 4.3(a) Lateral variations in Pn wave velocity beneath the continental United States. Notice the negative anomaly in northern Reelfoot Rift (RFR), Illinois basin, beneath New England and the positive anomaly beneath north western CEUS, South Carolina and NMSZ

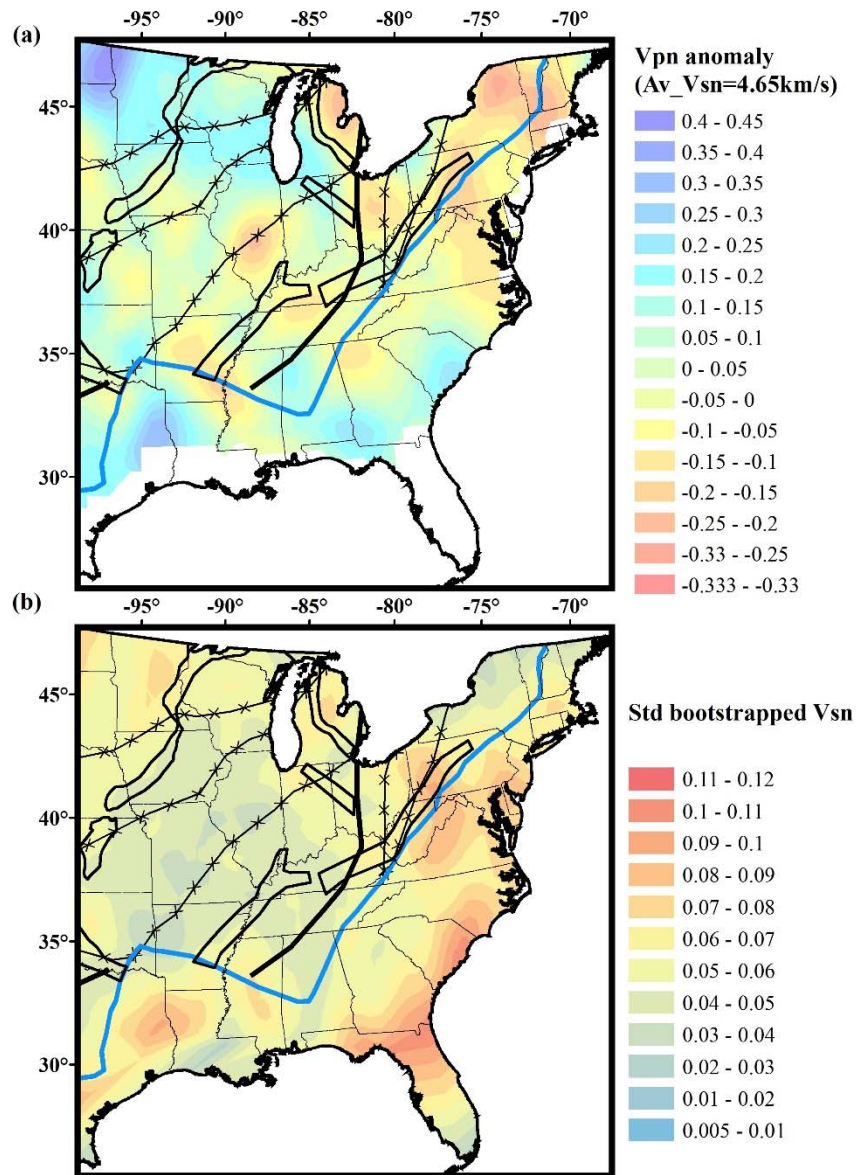


Figure 4.4 (a) Lateral variations in Sn wave velocity beneath central and eastern continental United States, Notice the negative anomaly beneath Illinois basin and southern Reelfoot Rift (RFR), and notice the positive anomaly beneath NMSZ and South Caroli

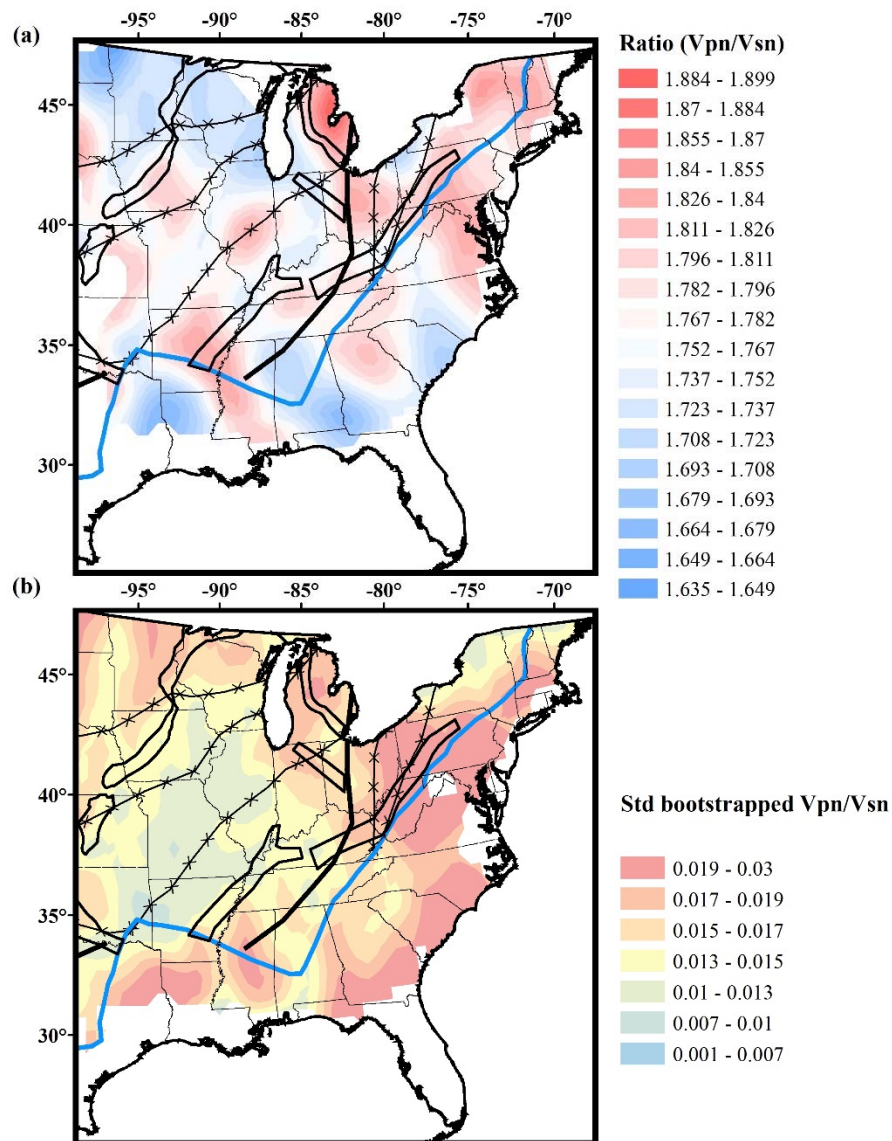


Figure 4.5 (a) Lateral variations of the velocity ratio (V_{pn}/V_{sn}) beneath the continental United States. Notice the low V_{pn}/V_{sn} ratio beneath NMSZ and the high V_{pn}/V_{sn} ratio beneath southern the Appalachian (Northern Georgia) and center Illinois. (b) Lateral standard deviation of the bootstrapped ratio.

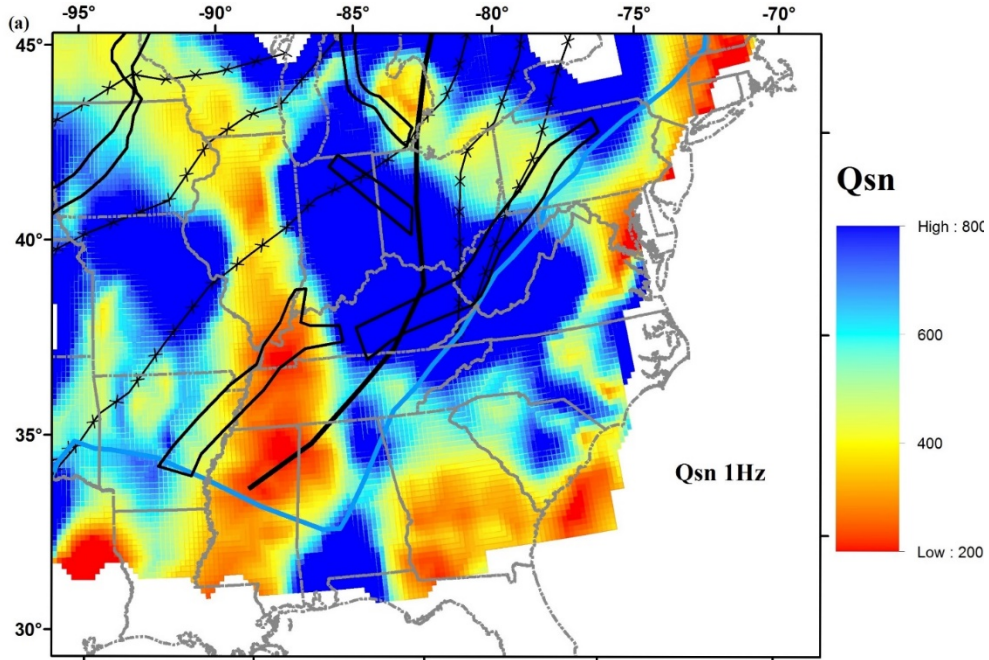


Figure 4.6. Lateral variations in Sn attenuation (attenuation = $Q-1$) for frequency 1 Hz beneath the CEUS. Notice the low Q beneath New England, Mississippi embayment, and central and southern Georgia

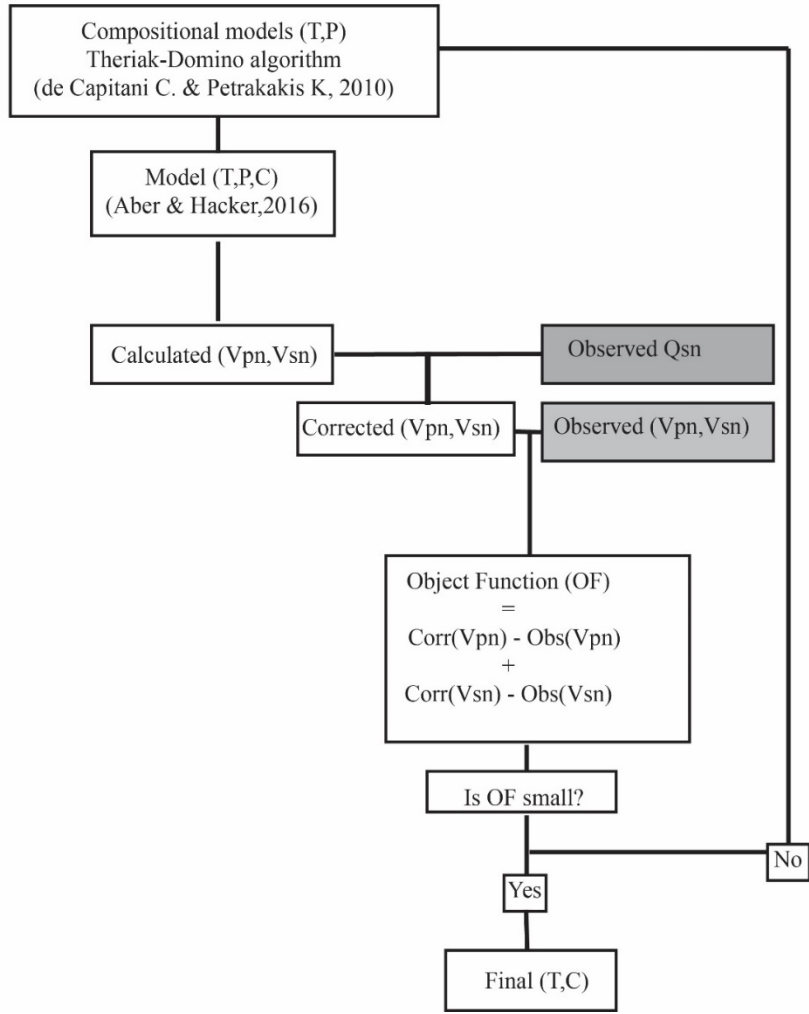


Figure 4.7 Flow chart represents the grid search algorithm applied to estimating the temperature of the uppermost mantle.

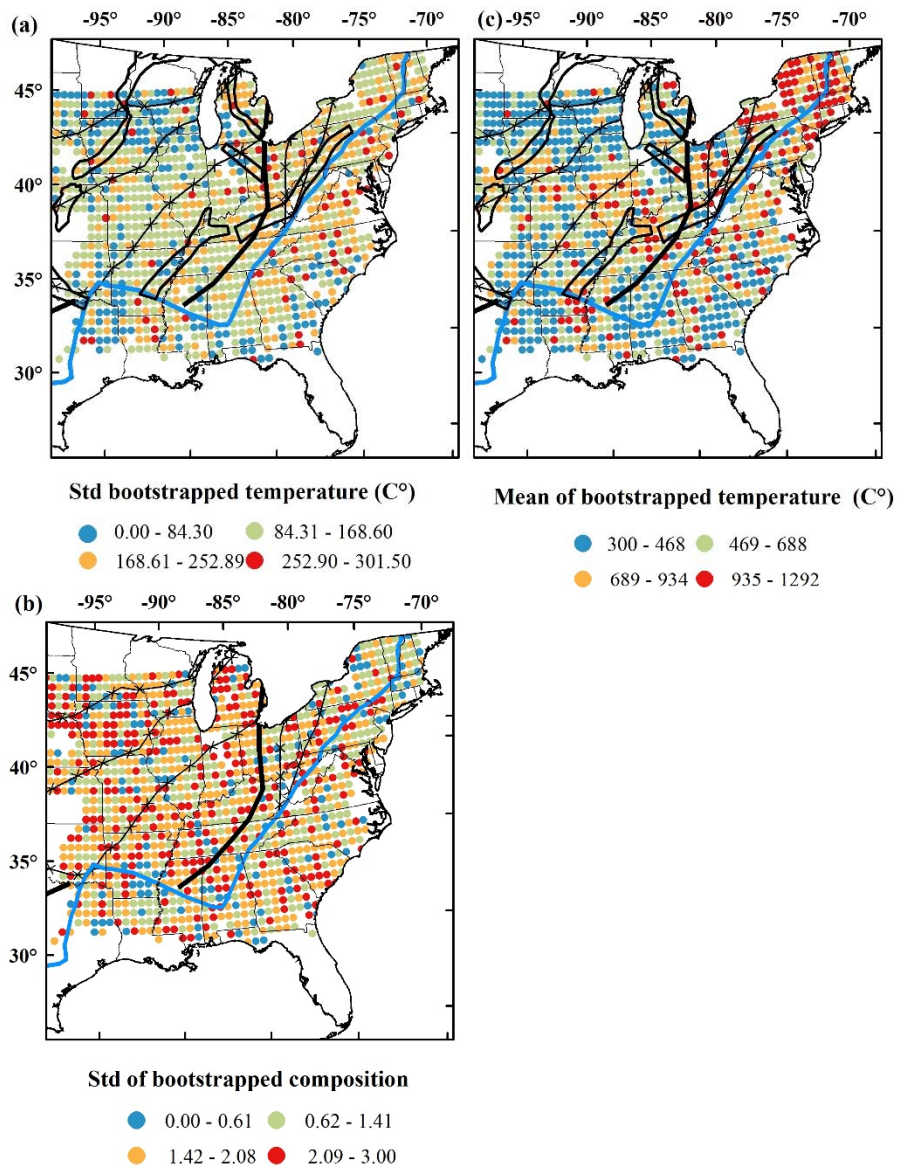


Figure 4.8. (a) the standard deviation (std) of the bootstrap result of the (TPnSn) temperature model. (b) the mean of the bootstrap result (TPnSn) of the temperature model. (c) the standard deviation (std) of the bootstrap result of the composition model.

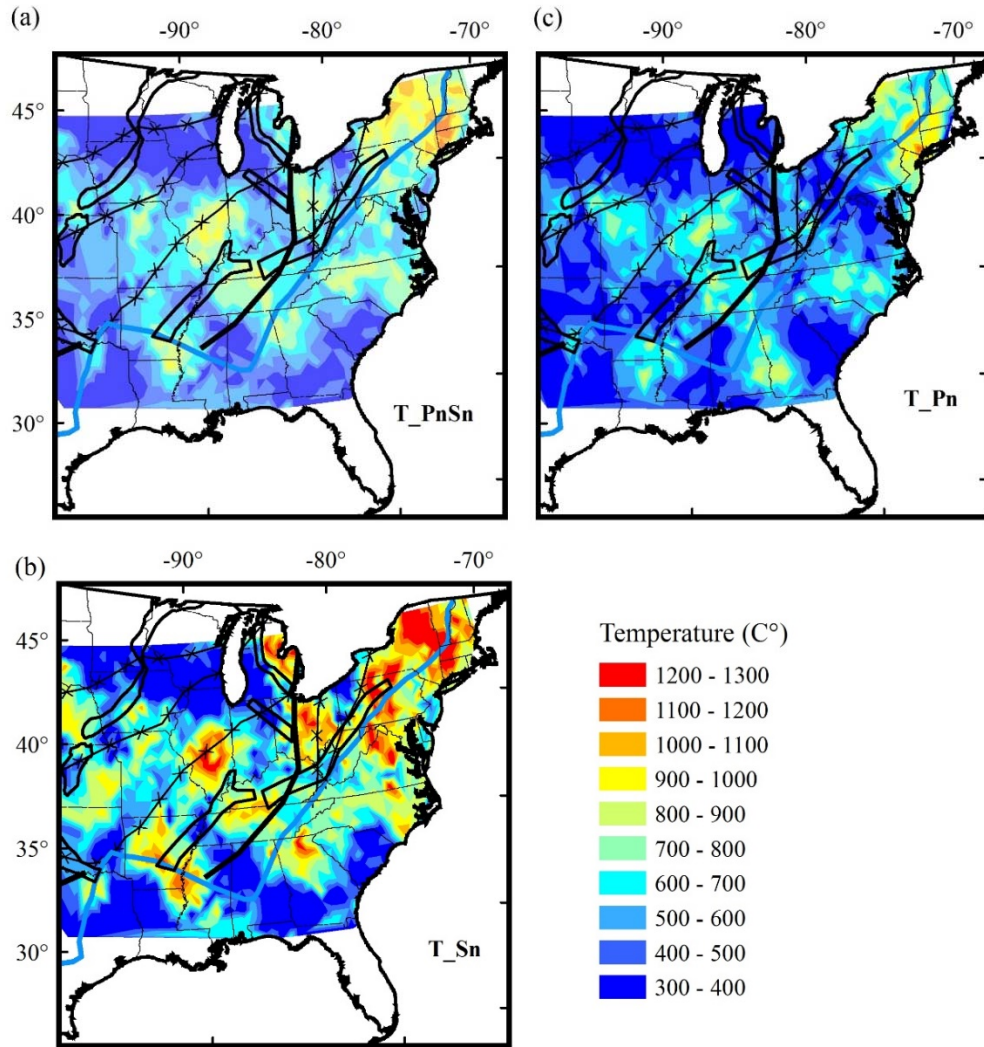
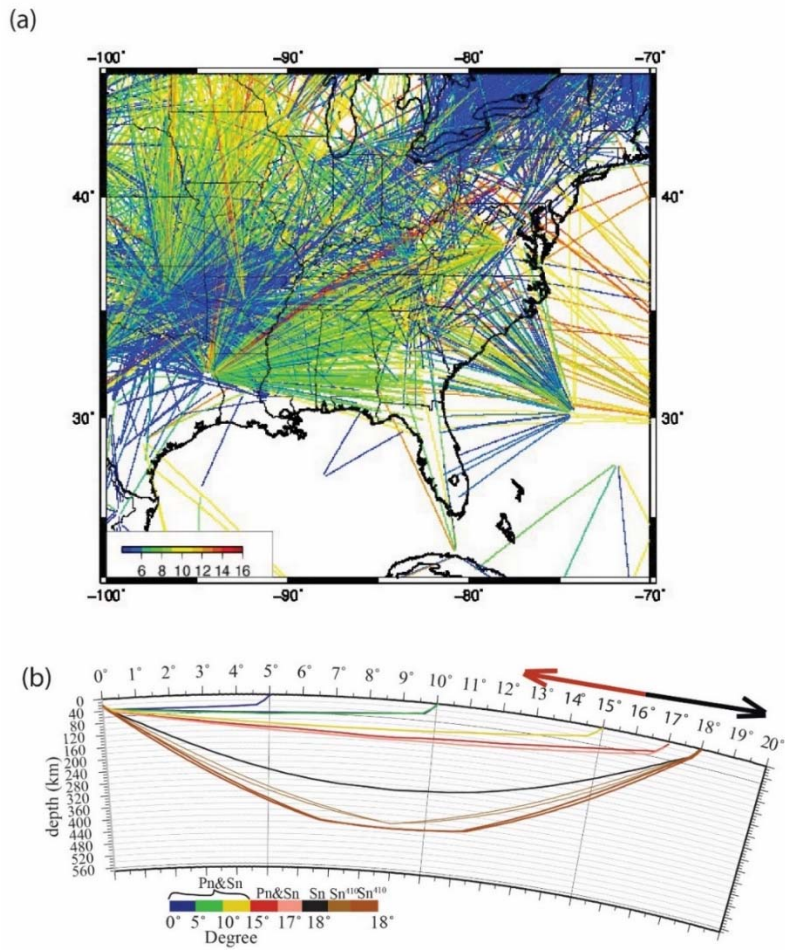


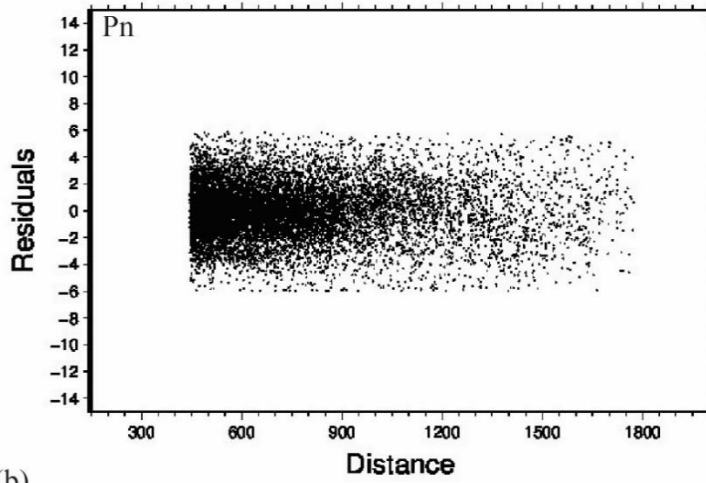
Figure 4.9. Upper most mantle temperature variation beneath CEUS for (a) Temperature resulted from inverting both Sn and Pn velocity, (b) Temperature resulted from inverting Sn velocity, (c) Temperature resulted from inverting Pn velocity. Notice the high temperature.

4.9 Supplementary Figures

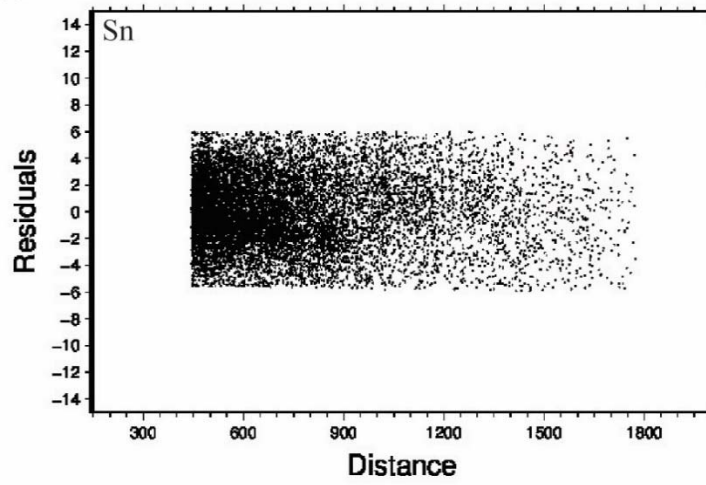


Supp. Figure 4.1 . (a) The ray-paths used in the Pn and Sn travel time tomography. The color represents the length of the ray-path in degree. Notice that New England and Reelfoot Rift zone were covered with short ray-paths and northern western CEUS were covered with long ray-paths.

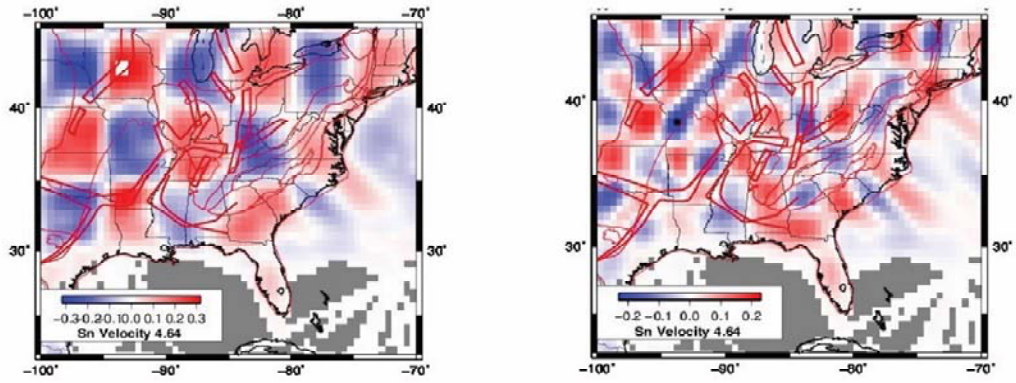
(a)



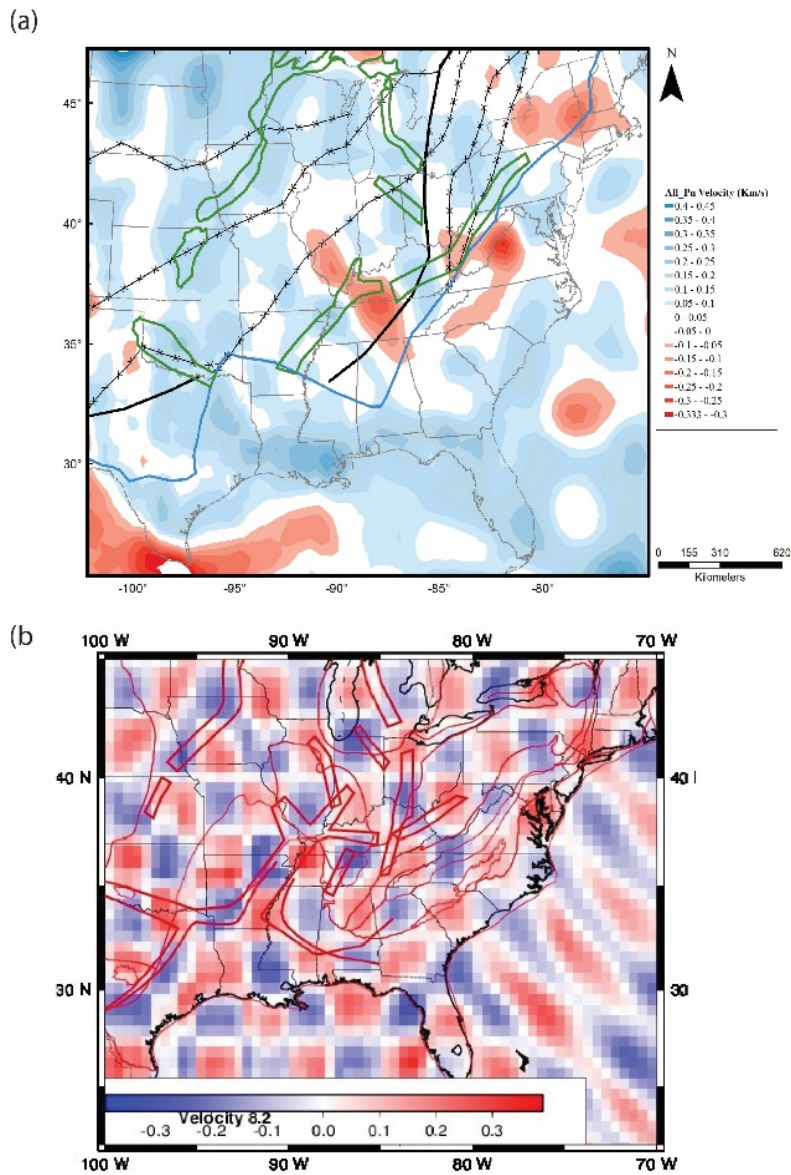
(b)



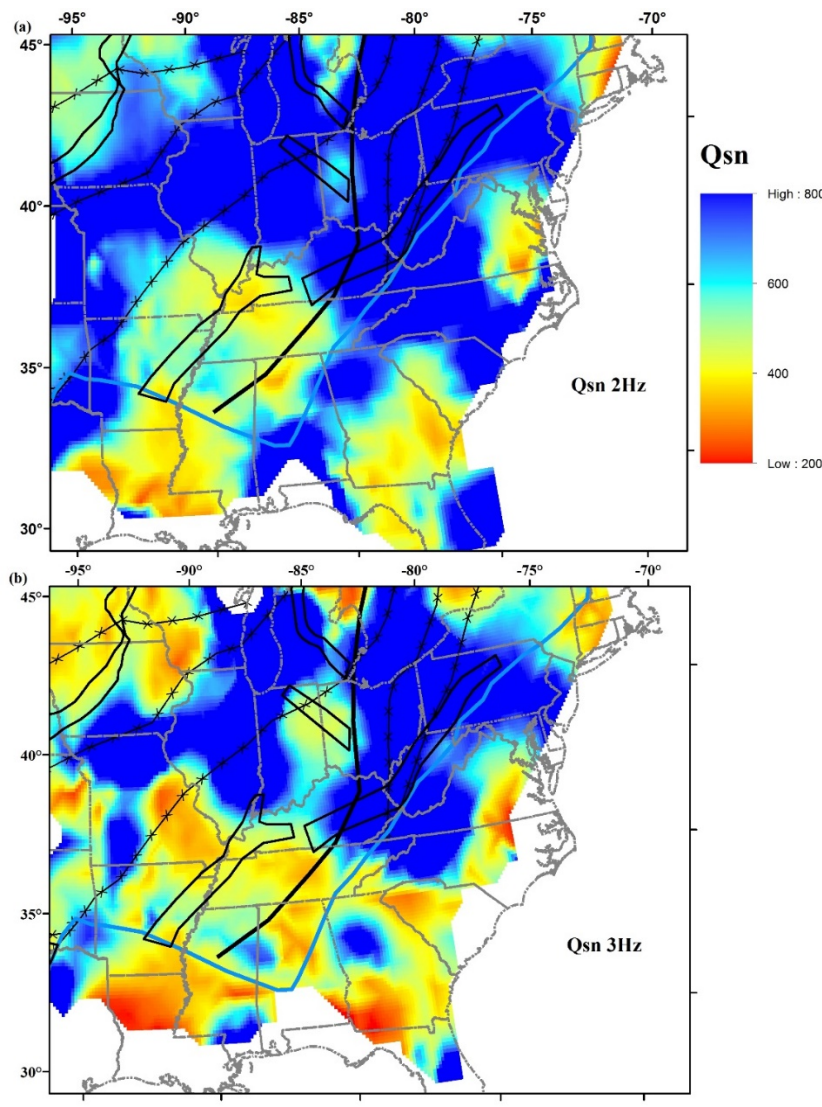
Supp. Figure 4.2 (a) Residuals plot of all available Pn wave picks within epicentral distance smaller than 18 degree. (b) Residuals plot of all available Sn wave picks within epicentral distance smaller than 18 degree



Supp. Figure 4.3. (a) Checkerboard test of V_{sn} and V_{pn} with $\pm 0.3\%$.

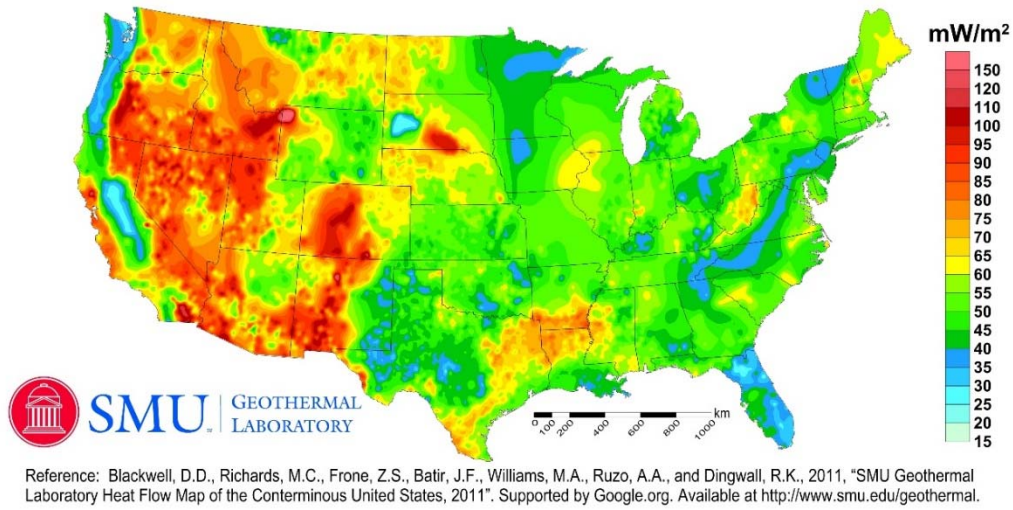


Supp.Figure 4.4(a) lateral variation of Pn velocity using all the Pn ray-paths, (b) the checkerboard of Vpn with $\pm 0.3\%$.

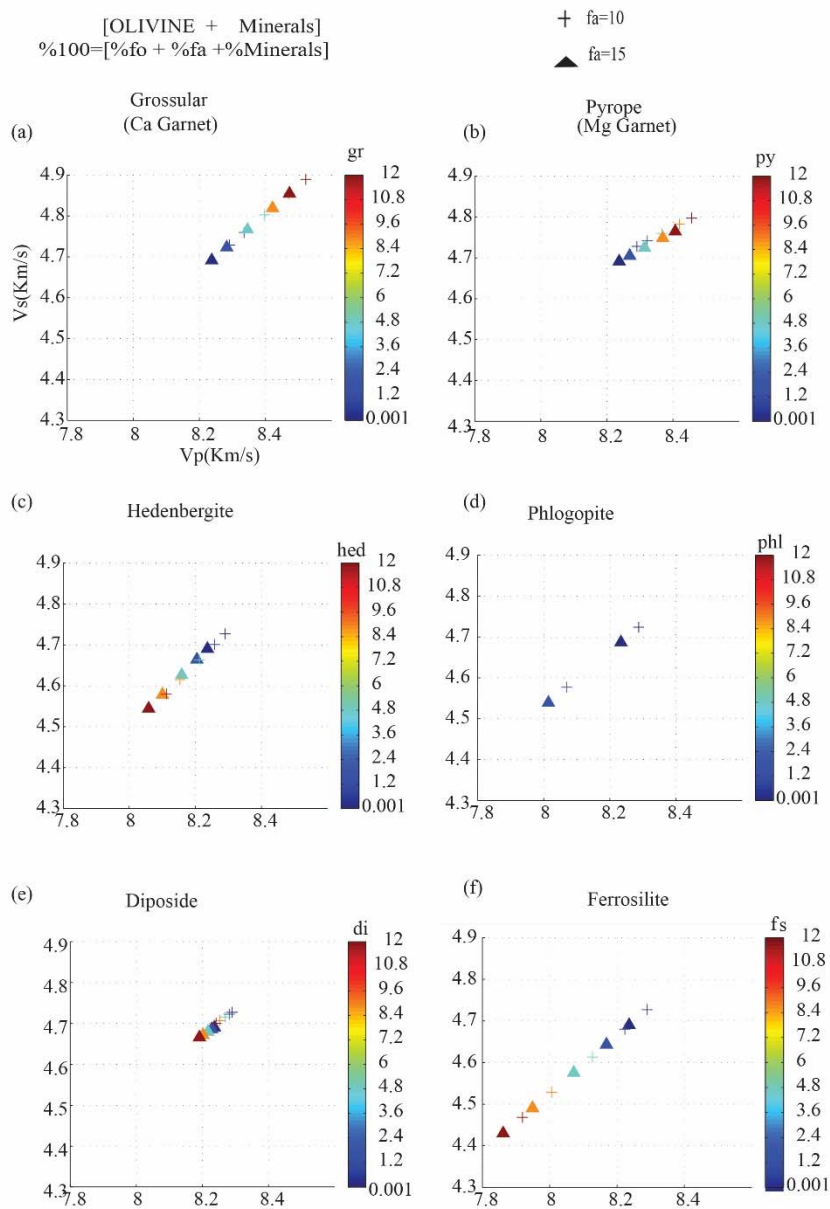


Supp. Figure 4.5 Lateral variations in Sn attenuation (attenuation = $Q-1$) beneath the continental United States, (a) for 2 Hz and (b) for 3 Hz.

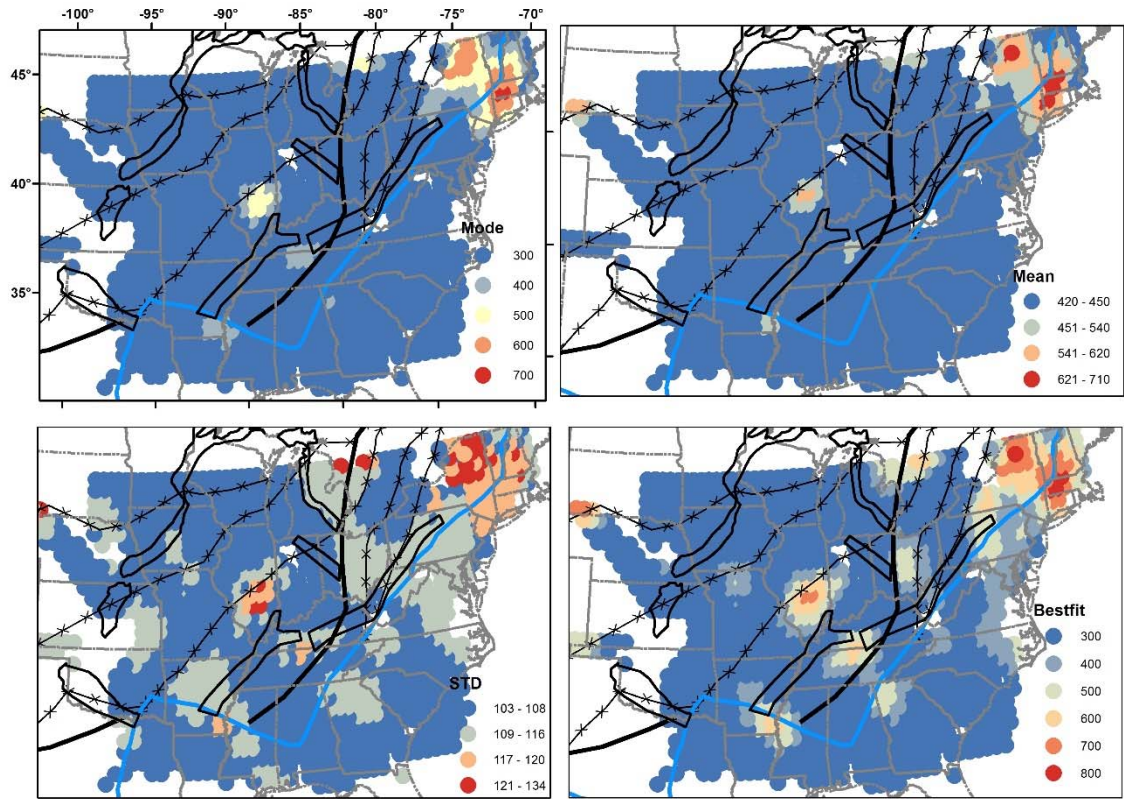
SMU Geothermal Laboratory Heat Flow Map of the Conterminous United States, 2011



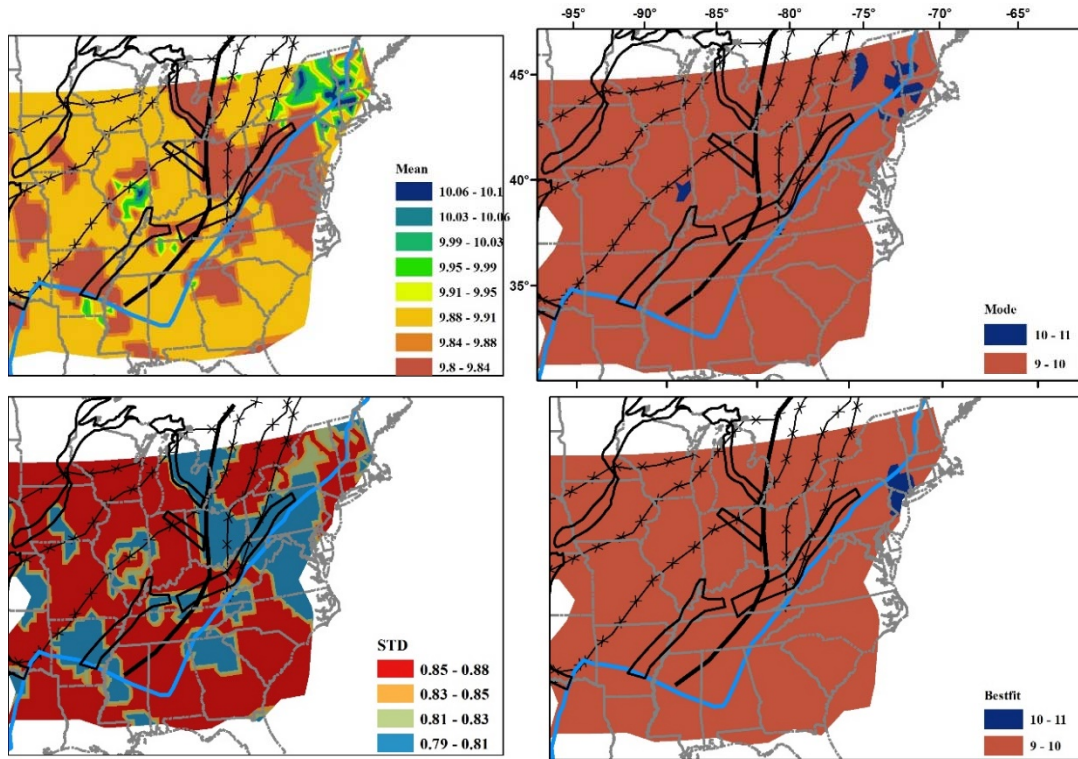
Supp.Figure 4.6 . Heat flow map of U.S. (Blackwell et al., 2011).



Supp. Figure 4.7 The velocity variation of Di, Fs, gr, and hed minerals were calculated for two compositions: the star represents Fa = 10, and the Triangle Fa = 15. Each mineral was calculated for 0.001, 2, 5, 9 and, 12%.



Supp. Figure 4.8. Uppermost mantle temperature variation beneath CEUS from enriched models (Table S1).



Supp.Figure 4.9 . Uppermost mantle compositional variation beneath CEUS resulted from enriched models (Table S1).

Model#	Fo%	Fa%	Py%	Alm%	Or%	Phl%	En%	Di%	Rut%
9	65	7.3	3.95	2	3.4	0.05	5.6	12.2	0.5
10	65	7.3	3.5	2	3.4	0.5	5.6	12.2	0.5
11	65	7.3	3.0	2	3.4	1	5.6	12.2	0.5

Supp_Table S1. Compositional models with phlogopite (enriched models from Theriak-Domino, de Capitani and Brown 1987; Holland and Powell 1998; Kelsey 2008).

4.10 References

- Abers, G.A., and B.R. Hacker (2016). A MATLAB toolbox and Excel workbook for calculating the densities, seismic wave speeds, and major element composition of minerals and rocks at pressure and temperature, *Geochemistry, Geophys. Geosystems* **17**, 616–624.
- Anderson, D.L. (1989a). Where on earth is the crust?, *Phys. Today* **42**, 38–46.
- Anderson, D.L. (1989b). (Oxford, U. K.: Blackwell).
- Anglin, F., and G. Buchbinder (1981). Microseismicity in the mid-St. Lawrence Valley Charlevoix zone, Quebec, *Bull. Seismol. Soc. Am.* **71**, 1553–1560.
- Bao, X., E. Sandvol, E. Zor, S. Sakin, R. Mohamad, R. Gök, R. Mellors, T. Godoladze, G. Yetirmishli, and N. Türkelli (2011). Pg attenuation tomography within the Northern Middle East, *Bull. Seismol. Soc. Am.* **101**, 1496–1506.
- Bao, X., C.A. Dalton, G. Jin, J.B. Gaherty, and Y. Shen (2016). Imaging Rayleigh wave attenuation with USArray, *Geophys. J. Int.* **206**, 241–259.
- Bedle, H., and S. Van Der Lee (2009). S velocity variations beneath North America, *J. Geophys. Res. Solid Earth* **114**.
- Beghoul, N., M. Barazangi, and B.L. Isacks (1993). Lithospheric structure of Tibet and western North America: Mechanisms of uplift and a comparative study, *J. Geophys. Res. Solid Earth* **98**, 1997–2016.

- Benoit, M.H., M.D. Long, and S.D. King (2013). Anomalously thin transition zone and apparently isotropic upper mantle beneath Bermuda: Evidence for upwelling, *Geochemistry, Geophys. Geosystems* **14**, 4282–4291.
- Blackwell, D., M. Richards, Z. Frone, A. Ruzo, R. Dingwall, and M. Williams (2011). Temperature-At-Depth Maps For the Conterminous US and Geothermal Resource Estimat, *GRC Trans.* **35**.
- BODINIER, J.-L., Ja. PABRIES, J.-P. LORAND, and J. DOSTAL (1987). Geochemistry of amphibole pyroxenite veins from the Lherz and Freychinède ultramafic bodies, *Bull. Miner.* **110**, 345–358.
- Boore, D.M., and J.J. Bommer (2005). Processing of strong-motion accelerograms: Needs, options and consequences, *Soil Dyn. Earthq. Eng.* **25**, 93–115.
- Braile, L.W., W.J. Hinze, J.L. Sexton, G.R. Keller, and E.G. Lidiak (1984). Tectonic development of the New Madrid seismic zone, *US Geol. Surv. Open File Rep.* **84**, 204–233.
- Braile, L.W., W.J. Hinze, G.R. Keller, E.G. Lidiak, and J.L. Sexton (1986). Tectonic development of the New Madrid rift complex, Mississippi embayment, North America, *Tectonophysics* **131**, 1–21.
- Buehler, J.S., and P.M. Shearer (2017). Uppermost mantle seismic velocity structure beneath USArray, *J. Geophys. Res. Solid Earth* **122**, 436–448.
- Cammarano, F., S. Goes, P. Vacher, and D. Giardini (2003). Inferring upper-mantle temperatures from seismic velocities, *Phys. Earth Planet. Inter.* **138**, 197–222.

- de Capitani, C., and T.H. Brown (1987). The computation of chemical equilibrium in complex systems containing non-ideal solutions, *Geochim. Cosmochim. Acta* **51**, 2639–2652.
- Catchings, R.D. (1999). Regional Vp, Vs, Vp/Vs, and Poisson's ratios across earthquake source zones from Memphis, Tennessee, to St. Louis, Missouri, *Bull. Seismol. Soc. Am.* **89**, 1591–1605.
- Chen, C., C.A. Hersh Gilbert, and X.Y. Michael W. Hamburger, Timothy Larson, Stephen Marshak, Gary L. Pavlis (2016). Shear velocity structure beneath the central United States: implications for the origin of the Illinois Basin and intraplate seismicity, *Geochemistry, Geophys. Geosystems* **17**, 1020–1041.
- Chen, C., H. Gilbert, K.M. Fischer, C.L. Andronicos, G.L. Pavlis, M.W. Hamburger, S. Marshak, T. Larson, and X. Yang (2018). Lithospheric discontinuities beneath the U.S. Midcontinent – signatures of Proterozoic terrane accretion and failed rifting, *Earth Planet. Sci. Lett.* **481**, 223–235.
- Clouzet, P., Y. Masson, and B. Romanowicz (2018). Box Tomography: first application to the imaging of upper-mantle shear velocity and radial anisotropy structure beneath the North American continent, *Geophys. J. Int.* **213**, 1849–1875.
- Cong, L.L., J.K. Xie, and B.J. Mitchell (1996). Excitation and propagation of L(g) from earthquakes in central Asia with implications for explosion/earthquake discrimination, *J. Geophys. Res. Earth* **101**, 27779–27789.

- Cox, R.T., and R.B. Van Arsdale (1997). Hotspot origin of the Mississippi embayment and its possible impact on contemporary seismicity, *Eng. Geol.* **46**, 201–216.
- Cox, R.T., and R.B. Van Arsdale (2002). The Mississippi Embayment, North America: A first order continental structure generated by the Cretaceous superplume mantle event, *J. Geodyn.* **34**, 163–176.
- Crough, S.T. (1981). Mesozoic hotspot epeirogeny in eastern North America, *Geology* **9**, 2–6.
- Dalton, C. (2017). How seismic lose energy, *Science (80-.)*. **358**, 1536–1537.
- Ernst, R., and W. Bleeker (2010). Large igneous provinces (LIPs), giant dyke swarms, and mantle plumes: significance for breakup events within Canada and adjacent regions from 2.5 Ga to the Present, *Can. J. Earth Sci.* **47**, 695–739.
- Evanzia, D., J. Pulliam, R. Ainsworth, H. Gurrola, and K. Pratt (2014). Seismic Vp & Vs tomography of Texas & Oklahoma with a focus on the Gulf Coast margin, *Earth Planet. Sci. Lett.* **402**, 148–156.
- Gao, S.S., and K.H. Liu (2014). Mantle transition zone discontinuities beneath the contiguous United States, *J. Geophys. Res. Solid Earth* **119**, 6452–6468.
- Gao, S.S., K.H. Liu, R.J. Stern, G.R. Keller, J.P. Hogan, J. Pulliam, and E.Y. Anthony (2008). Characteristics of mantle fabrics beneath the south-central

- United States: Constraints from shear-wave splitting measurements, *Geosphere* **4**, 411.
- Goes, S., and S. Van Der Lee (2002). Thermal structure of the North American uppermost mantle inferred from seismic tomography, *J. Geophys. Res.* **107**, 2050.
- Grand, S.P. (1994). Mantle shear structure beneath the Americas and surrounding oceans, *J. Geophys. Res. Solid Earth* **99**, 11591–11621.
- Gribenko, A. V., and M.S. Zhdanov (2017). 3-D Inversion of the MT EarthScope Data, Collected Over the East Central United States, *Geophys. Res. Lett.* **44**, 11,800-11,807.
- Griffin, W.L., S.Y. O'Reilly, B.J. Doyle, N.J. Pearson, H. Coopersmith, K. Kivi, V. Malkovets, and N. Pokhilenko (2004). Lithosphere mapping beneath the North American plate, *Lithos* **77**, 873–922.
- Guo, Z., Y. Cao, X. Wang, Y. John Chen, J. Ning, W. He, Y. Tang, and Y. Feng (2014). Crust and upper mantle structures beneath Northeast China from receiver function studies, *Earthq. Sci.* **27**, 265–275.
- Hacker, B.R. (1996). Eclogite Formation and the Rheology, Buoyancy, Seismicity, and H₂O Content of Oceanic Crust, *Geophys. Monogr. Geophys. UNION* **96**, 337–346.

- Hammond, W.C., and E.D. Humphreys (2000). Upper mantle seismic wave velocity: Effects of realistic partial melt geometries, *J. Geophys. Res. Solid Earth* **105**, 10975–10986.
- Hansen, S.M., K. Dueker, and B. Schmandt (2015). Thermal classification of lithospheric discontinuities beneath USArray, *Earth Planet. Sci. Lett.* **431**, 36–47.
- Heaman, L.M., and B.A. Kjarsgaard (2000). Timing of eastern North American kimberlite magmatism: continental extension of the Great Meteor hotspot track?, *Earth Planet. Sci. Lett.* **178**, 253–268.
- Hearn, T.M. (1996). Anisotropic Pn tomography in the western United States, *J. Geophys. Res. B Solid Earth* **101**, 8403–8414.
- Hoffman, P.F., A.W. Bally, and A.R. Palmer (1989). Precambrian geology and tectonic history of North America, *Geol. North Am. Overv.* 447–512.
- Holland, T.J.B., and R. Powell (1998). An internally consistent thermodynamic data set for phases of petrological interest, *J. Metamorph. Geol.* **16**, 309–343.
- Horn, I., R.L. Rudnick, and W.F. McDonough (2000). Precise elemental and isotope ratio determination by simultaneous solution nebulization and laser ablation-ICP-MS: application to U-Pb geochronology (vol 164, pg 283, 2000), *Chem. Geol.* **167**, 403-+.

- Jackson, I. (2000). Laboratory measurement of seismic wave dispersion and attenuation: recent progress, *Washingt. DC Am. Geophys. Union Geophys. Monogr. Ser.* **117**, 265–289.
- Jackson, I., and U.H. Faul (2010). Grainsize-sensitive viscoelastic relaxation in olivine: Towards a robust laboratory-based model for seismological application, *Phys. Earth Planet. Inter.* **183**, 151–163.
- Jackson, J., K. Priestley, M. Allen, and M. Berberian (2002). Active tectonics of the South Caspian Basin, *Earth* 214–245.
- Jackson, J.M., J. Zhang, and J.D. Bass (2004). Sound velocities and elasticity of aluminous MgSiO₃ perovskite: Implications for aluminum heterogeneity in Earth's lower mantle, *Geophys. Res. Lett.* **31**.
- Kaban, M.K., M. Tesauro, W.D. Mooney, and S.A.P.L. Cloetingh (2014). Density, temperature, and composition of the North American lithosphere-New insights from a joint analysis of seismic, gravity, and mineral physics data: 1. Density structure of the crust and upper mantle, *Geochemistry, Geophys. Geosystems* **15**, 4781–4807.
- Kelemen, P.B., H.J.B. Dick, and J.E. Quick (1992). Formation of harzburgite by pervasive melt/rock reaction in the upper mantle, *Nature* **358**, 635.
- Kelsey, D.E. (2008). On ultrahigh-temperature crustal metamorphism, *Gondwana Res.* **13**, 1–29.

- Kennett, B. (1986). Lg waves and structural boundaries, *Bull. Seismol. Soc. Am.* **76**, 1133–1141.
- Kind, R., X. Yuan, and P. Kumar (2012). Seismic receiver functions and the lithosphere-asthenosphere boundary, *Tectonophysics* **536–537**, 25–43.
- Kreutzmann, A., H. Schmeling, A. Junge, T. Ruedas, G. Marquart, and I.T. Bjarnason (2004). Temperature and melting of a ridge-centred plume with application to Iceland. Part II: Predictions for electromagnetic and seismic observables, *Geophys. J. Int.* **159**, 1097–1111.
- Lee, C.-T.A. (2003). Compositional variation of density and seismic velocities in natural peridotites at STP conditions: Implications for seismic imaging of compositional heterogeneities in the upper mantle, *J. Geophys. Res. Solid Earth* **108**.
- Lekić, V., and K.M. Fischer (2014). Contrasting lithospheric signatures across the western United States revealed by Sp receiver functions, *Earth Planet. Sci. Lett.* **402**, 90–98.
- Levin, V., J. Park, M.T. Brandon, and W. Menke (2000). Thinning of the upper mantle during late Paleozoic appalachian orogenesis, *Geology* **28**, 239–242.
- Levin, V., A. Henza, J. Park, and A. Rodgers (2006). Texture of mantle lithosphere along the Dead Sea Rift: Recently imposed or inherited?, *Phys. Earth Planet. Inter.* **158**, 174–189.

- Levin, V., A. Servali, J. Van Tongeren, W. Menke, and F. Darbyshire (2017). Crust-mantle boundary in eastern North America, from the (oldest) craton to the (youngest) rift, *Spec. Pap. Geol. Soc. Am.* **526**, 107–131.
- Li, N., and M. Stephens (2003). Modeling linkage disequilibrium and identifying recombination hotspots using single-nucleotide polymorphism data, *Genetics* **165**, 2213–2233.
- Li, Q., M. Liu, Q. Zhang, and E. Sandvol (2007). Stress evolution and seismicity in the central-eastern United States: Insights from geodynamic modeling, *Spec. Pap. Geol. Soc. Am.* **425**, 149–166.
- Liu, L., and S.S. Gao (2018). Lithospheric layering beneath the contiguous United States constrained by S-to-P receiver functions, *Earth Planet. Sci. Lett.* **495**, 79–86.
- Lodders, K., and B. Fegley (1998). (Oxford University Press on Demand).
- Lü, Y., Z. Zhang, S. Pei, E. Sandvol, T. Xu, and X. Liang (2014). 2.5-Dimensional tomography of uppermost mantle beneath Sichuan-Yunnan and surrounding regions, *Tectonophysics* **627**, 193–204.
- Mazza, S.E., E. Gazel, E.A. Johnson, M.J. Kunk, R. McAleer, J.A. Spotila, M. Bizimis, and D.S. Coleman (2014). Volcanoes of the passive margin: The youngest magmatic event in eastern North America, *Geology* **42**, 483–486.
- McDonough, W.F., and S.-S. Sun (1995). The composition of the Earth, *Chem. Geol.* **120**, 223–253.

- Molinaro, M., H. Zeyen, and X. Laurencin (2005). Lithospheric structure beneath the south-eastern Zagros Mountains, Iran: recent slab break-off?, *Terra Nov.* **17**, 1–6.
- Molnar, P., and J. Oliver (1969). Lateral variations of attenuation in the upper mantle and discontinuities in the lithosphere, *J. Geophys. Res.* **74**, 2648–2682.
- Mooney, W.D., M.C. Andrews, A. Ginzburg, D.A. Peters, and R.M. Hamilton (1983). Crustal structure of the northern mississippi embayment and a comparison with other continental rift zones, *Dev. Geotecton.* **19**, 327–348.
- Murphy, B.S., and G.D. Egbert (2017). Electrical conductivity structure of southeastern North America: Implications for lithospheric architecture and Appalachian topographic rejuvenation, *Earth Planet. Sci. Lett.* **462**, 66–75.
- Nelson, K.D. (1992). Are crustal thickness variations in old mountain belts like the Appalachians a consequence of lithospheric delamination?, *Geology* **20**, 498–502.
- Nelson, W.J. (1991). Structural Styles of the Illinois Basin, *Am. Assoc. Pet. Geol. Memoir* **51**, 209–243.
- Nelson, K.D., and J. Zhang (1991). A COCORP deep reflection profile across the buried Reelfoot rift, south-central United States, *Tectonophysics* **197**, 271–293.
- Ni, J., and M. Barazangi (1983). High-frequency seismic wave propagation beneath the Indian Shield, Himalayan Arc, Tibetan Plateau and surrounding regions:

high uppermost mantle velocities and efficient Sn propagation beneath Tibet, *Geophys. J. Int.* **72**, 665–689.

Nicholson, S.W., K.J. Schulz, S.B. Shirey, and J.C. Green (1997). Rift-wide correlation of 1.1 Ga Midcontinent rift system basalts: implications for multiple mantle sources during rift development, *Can. J. Earth Sci.* **34**, 504–520.

Niu, F., A. Levander, C.M. Cooper, C.T.A. Lee, A. Lenardic, and D.E. James (2004). Seismic constraints on the depth and composition of the mantle keel beneath the Kaapvaal craton, *Earth Planet. Sci. Lett.*

Nyamwandha, C.A., and C.A. Powell (2016). Seismic anisotropy beneath the Mississippi Embayment and the New Madrid Seismic Zone: A study of shear wave splitting, *J. Geophys. Res. Solid Earth* **121**, 8239–8253.

Obrebski, M., R.M. Allen, F. Pollitz, and S.-H. Hung (2011). Lithosphere–asthenosphere interaction beneath the western United States from the joint inversion of body-wave traveltimes and surface-wave phase velocities, *Geophys. J. Int.* **185**, 1003–1021.

Paces, J.B., and K. Bell (1989). Non-depleted sub-continental mantle beneath the Superior Province of the Canadian Shield: Nd-Sr isotopic and trace element evidence from Midcontinent Rift basalts, *Geochim. Cosmochim. Acta* **53**, 2023–2035.

- Paige, C.C., and M.A. Saunders (1982). LSQR: An Algorithm for Sparse Linear Equations and Sparse Least Squares, *ACM Trans. Math. Softw.* **8**, 43–71.
- Perry, H.K.C., C. Jaupart, J.-C. Mareschal, and N.M. Shapiro (2006). Upper mantle velocity-temperature conversion and composition determined from seismic refraction and heat flow, *J. Geophys. Res.* **111**, 1–14.
- Pollitz, F.F., and W.D. Mooney (2014). Seismic structure of the Central US crust and shallow upper mantle: Uniqueness of the Reelfoot Rift, *Earth Planet. Sci. Lett.* **402**, 157–166.
- Porritt, R.W., R.M. Allen, and F.F. Pollitz (2014). Seismic imaging east of the Rocky Mountains with USArray, *Earth Planet. Sci. Lett.* **402**, 16–25.
- Porter, R., Y. Liu, and W.E. Holt (2016). Lithospheric records of orogeny within the continental U.S., *Geophys. Res. Lett.* **43**, 144–153.
- Savage, M.K. (1999). Seismic anisotropy and mantle deformation: what have we learned from shear wave splitting?, *Rev. Geophys.* **37**, 65–106.
- Savage, B., B.M. Covellone, and Y. Shen (2017). Wave speed structure of the eastern North American margin, *Earth Planet. Sci. Lett.* **459**, 394–405.
- Schaeffer, A.J., and S. Lebedev (2014). Imaging the North American continent using waveform inversion of global and USArray data, *Earth Planet. Sci. Lett.* **402**, 26–41.
- Schmandt, B., and E. Humphreys (2011). Seismically imaged relict slab from the 55 Ma Siletzia accretion to the northwest United States, *Geology* **39**, 175–178.

- Schmandt, B., and F. Lin (2014). P and S wave tomography of the mantle beneath the United States, *Geophys. Res. Lett.* 6342–6349.
- Schutt, D.L., and C.E. Lesher (2006). Effects of melt depletion on the density and seismic velocity of garnet and spinel lherzolite, *J. Geophys. Res. Solid Earth* **111**.
- Schutt, D.L., A.R. Lowry, and J.S. Buehler (2018a). Moho temperature and mobility of lower crust in the western United States, *Geology* **46**, 219–222.
- Schutt, D.L., A.R. Lowry, and J.S. Buehler (2018b). Moho temperature and mobility of lower crust in the western United States, *Geology* **46**, 219–222.
- Selway, K. (2014). On the causes of electrical conductivity anomalies in tectonically stable lithosphere, *Surv. Geophys.* **35**, 219–257.
- Shapiro, N.M., and M.H. Ritzwoller (2004). Inferring surface heat flux distributions guided by a global seismic model: particular application to Antarctica, *Earth Planet. Sci. Lett.* **223**, 213–224.
- Shen, W., and M.H. Ritzwoller (2016a). Crustal and uppermost mantle structure beneath the United States, *J. Geophys. Res. Solid Earth* **121**, 4306–4342.
- Shen, W., and M.H. Ritzwoller (2016b). Crustal and uppermost mantle structure beneath the United States, *J. Geophys. Res. Solid Earth* **121**, 4325–4344.
- Sigloch, K. (2008). (Princeton University).
- Sigloch, K. (2011). Mantle provinces under North America from multifrequency P wave tomography, *Geochemistry, Geophys. Geosystems* **12**.

- Sigloch, K., and M.G. Mihalynuk (2013). Intra-oceanic subduction shaped the assembly of Cordilleran North America, *Nature* **496**, 50.
- Stephenson, W.J. (2012). Origin of the Blytheville Arch, and long-term displacement on the New Madrid seismic zone, central United States, *Recent Adv. North Am. Paleoseismology Neotectonics East Rockies* **493**, 1.
- Stixrude, L., and C. Lithgow-Bertelloni (2005). Mineralogy and elasticity of the oceanic upper mantle: Origin of the low-velocity zone, *J. Geophys. Res. Solid Earth* **110**.
- Sun, W., and B.L.N. Kennett (2016). Uppermost mantle structure beneath eastern China and its surroundings from Pn and Sn tomography, *Geophys. Res. Lett.* **43**, 3143–3149.
- Sun, W., and B.L.N. Kennett (2017). Uppermost mantle structure beneath eastern China and its surroundings from Pn and Sn tomography,.
- Tesauro, M., M.K. Kaban, W.D. Mooney, and S. Cloetingh (2014). NACr14: A 3D model for the crustal structure of the North American Continent, *Tectonophysics* **631**, 65–86.
- Tesauro, M., M.K. Kaban, and W.D. Mooney (2015). Variations of the lithospheric strength and elastic thickness in North America, *Geochemistry, Geophys. Geosystems*.

- Tichelaar, B.W., and L.J. Ruff (1989). How good are our best models? Jackknifing, bootstrapping, and earthquake depth, *Eos, Trans. Am. Geophys. Union* **70**, 593–606.
- Tilmann, F., J. Ni, T. Hearn, Y.S. Ma, R. Rapine, R. Kind, J. Mechie, J. Saul, S. Haines, S. Klemperer, et al. (2003). Seismic imaging of the downwelling Indian lithosphere beneath central Tibet, *Science* (80-.). **300**, 1424–1427.
- Tommasi, A. (1998). Forward modeling of the development of seismic anisotropy in the upper mantle, *Earth Planet. Sci. Lett.* **160**, 1–13.
- Tsai, Y.-B., and K. Aki (1969). Simultaneous determination of the seismic moment and attenuation of seismic surface waves, *Bull. Seismol. Soc. Am.* **59**, 275–287.
- Tso, J.L., and J.D. Surber (2006). Eocene igneous rocks near Monterey, Virginia; a field study, *Virginia Miner.* **49**, 9–24.
- Wagner, L.S., M.L. Anderson, J.M. Jackson, S.L. Beck, and G. Zandt (2008). Seismic evidence for orthopyroxene enrichment in the continental lithosphere, *Geology* **36**, 935–938.
- Wagner, L.S., K.M. Fischer, R. Hawman, E. Hopper, and D. Howell (2018). The relative roles of inheritance and long-term passive margin lithospheric evolution on the modern structure and tectonic activity in the southeastern United States, *Geosphere* **14**, 1385–1410.

- Whitmeyer, S.J., and K.E. Karlstrom (2007). Tectonic model for the Proterozoic growth of North America,.
- Wirth, E.A., and M.D. Long (2014). A contrast in anisotropy across mid-lithospheric discontinuities beneath the central United States-A relic of craton formation, *Geology* **42**, 851–854.
- Workman, R.K., and S.R. Hart (2005). Major and trace element composition of the depleted MORB mantle (DMM), *Earth Planet. Sci. Lett.* **231**, 53–72.
- Worthington, P.F. (2013). Protocols for the improved application of core permeability data in integrated reservoir studies. (Gaffney, Cline and Associates (Consultants) Pte. Ltd, Singapore), p.
- Xie, J., and B.J. Mitchell (1990). A back-projection method for imaging large-scale lateral variations of Lg coda Q with application to continental Africa, *Geophys. J. Int.* **100**, 161–181.
- Yardley, B.W.D., and J.W. Valley (1997). The petrologic case for a dry lower crust, *J. Geophys. Res. Solid Earth* **102**, 12173–12185.
- Yuan, H., and V. Levin (2014). Stratified seismic anisotropy and the lithosphere-asthenosphere boundary beneath eastern North America, *J. Geophys. Res.* **119**, 3096–3114.
- Yuan, H., and B. Romanowicz (2010). Lithospheric layering in the North American craton, *Nature* **466**, 1063–1068.

Yuan, H., B. Romanowicz, K.M. Fischer, and D. Abt (2011). 3-D shear wave radially and azimuthally anisotropic velocity model of the North American upper mantle, *Geophys. J. Int.* **184**, 1237–1260.

Zhang, Q., E. Sandvol, and M. Liu (2009). Lithospheric velocity structure of the New Madrid Seismic Zone: A joint teleseismic and local P tomographic study, *Geophys. Res. Lett.* **36**, 1–6.

5 Chapter 5: Investigation of Local & Regional Site Response in the Central U.S.

Abstract:

We attempted to better understand the difference in site response from seismic waves travelling at local and regional distances. We have used the Horizontal to Vertical Spectral Ratio (HVSr) and the ratio of surface ground motion to ground motion recorded at 30 m and 270 m depth (Transfer Function TF30m, TF270m) of seismic records of the CUSSO vertical array located in southwestern Kentucky. We conduct local and regional 2D numerical simulations using SpecFem2D. Our results emphasize the effect of deep-geologic structures (basins) on site response due to focusing and defocusing effects. Deep structure could affect local and regional seismic waves differently because the crustal heterogeneity leads to attenuation effects (scattering and anelasticity) along the propagation paths. The 2D regional modeling shows that ground motion amplification increases toward the far end of deep basins while it is homogenous across shallow basins. We also found that in order to account for seismic waves propagating in all directions in complex geological regions, we needed to apply a weighted-average algorithm

5.1 Introduction

Seismic hazard from earthquakes at regional distances cannot be neglected in the central United States because of the low attenuation of regional seismic waves in this region (Gallegos et al., 2017). Earthquakes in the central U.S. are located in major seismic zones such as the New Madrid Seismic Zone (NMSZ) in the mid-continent and the St. Lawrence seismic zone in the northeast. The intensity map of historic seismic events in the mid-continent ($M \sim 7-7.5$) shows that earthquakes can be felt as far away as New York (Hough and Page, 2011). The 2011 M_w 5.8 Mineral, Virginia earthquake is a modern example of regional seismic waves being felt at regional distances such as Minnesota and Florida. Regional seismic waves have caused damage in Mexico City (Furumura and Kennett, 1998). In addition, large earthquakes around the world have triggered landslides hundreds of miles away from the epicenter (Meunier et al., 2008; Zhang et al., 2013). The destruction from earthquakes over regional distances can, in part, be attributed to site effects, which is the amplification of the ground motion at specific frequencies (Motazedian et al., 2011; Yilar et al., 2017); therefore, studying how factors affecting site response is essential to understanding seismic hazards. A site effect is defined as the effect of unconsolidated rock (i.e., sediment) on seismic waves, specifically vertically incident shear waves; however, surface waves can also be amplified at specific frequencies, which could pose a significant threat to tall buildings (Kawase and Aki, 1989; Joyner, 2000; Bowden & Tsai, 2017). It is necessary therefore, to consider all kinds of seismic waves in hazard studies.

The Lg wave is a high-frequency guided wave traveling in the crust with a frequency band of 0.5 to 10 Hz and a group velocity of 3.0 to 3.6 km/s (Aki and Richards, 2002). Lg most likely forms as a superposition of S-wave reverberations and Sv to P and P to Sv conversions within the continental crustal waveguide (e.g., Bouchon, 1982; Storchak et al., 2003) or it may be the sum of higher mode surface waves (e.g., Knopoff et al., 1973; Oliver and Ewing, 1958). Lg is observed at regional distances of 200 to 1500 km (Chun et al., 1987) and it has the largest amplitude for regional seismic records with paths entirely in the continental crust (Boore, 2003). In addition, Lg waves can generally be considered guided waves and thus do not have a distinct ray path such as do body waves. In the Central and Eastern U.S. Gallegos et al. (2014) show high attenuation of Lg in thick sediments and high heat flow regions, e.g., the Mississippi embayment and the Gulf coastal plain.

Previous studies focused on studying local site effects using direct shear waves because the horizontal ground motion of shear waves is critical for buildings. Salinas et al. (2014) compared HVSRs from different phases and seismic events with epicentre distances within a hundred kilometre and found that averaging over multiple events could reduce the variance in the measurements. Sedaghati et al. (2018) compared the HVSR of coda waves, surface waves, and shear waves of seismic records in the northern Mississippi embayment. No prior studies have compared the behaviour of regional and local seismic waves.

In this paper, we focus on investigating the site response of regional seismic waves versus local seismic waves. We choose the Central United States Seismic Observatory (CUSO), a vertical array, for several reasons (figure 1): (1) it is located in the mid-

continent adjacent to the NMSZ and records small earthquakes daily in addition to regional earthquakes; (2) CUSSO is located in the northern Mississippi embayment with a well-known sediment thickness of 600 m; (3) the sediment lithology of the location has been well studied (Woolery et al., 2016); and (4) CUSSO is a vertical array which allows us to track the seismic waves propagation through shallow layers. CUSSO gives us the opportunity to understand local site response with two approaches: using observed earthquake data and conducting parametric simulations.

Historically, seismic site effect studies used methods that depend on the specific locations of seismic stations. A common practice is to compare the seismic records of a site with a reference station, preferably one in a deep borehole (Steidl et al., 1996). Other site response studies have used the surface seismic stations installed on outcropping bedrock as a reference and they assume a non-amplified (amplification equal to 1) site as a reference site. Steidl et al. (1996) has shown that whether reference sites are installed on an outcropping bedrock or in a borehole, they often have amplifications that are not equal to 1; therefore, comparing seismic waves recorded at each layer could give us insight into how amplification varies with depth. In seismology, bedrock is defined as a rock with shear-wave velocity of 3000-3500 m/sec (Kobayashi and Nagahashi, 1976) while in earthquake engineering, it is defined as a rock with shear-wave velocity >700 m/sec (Ohsaki, 1979). In this paper, we adapted the engineering bedrock definition for the rock layer underneath the sediments while the rock underlain the engineering bedrock and it has a shear-velocity >3500 m/s is the crystalline rock, which is mostly igneous and metamorphic **rocks**.

Numerical modelling of seismic wave propagation in sedimentary basins has shown that site response is a combination of many factors: attenuation, basin geometry, impedance contrast between sediments and bedrock, and ray parameter (e.g., Kham et al., 2006; Myers et al., 2007; Narayan & Kumar, 2012; Satoh et al., 1995). Therefore, simulating different scenarios of ground motion is necessary to understand both local and regional site response.

SpecFem combines high order Finite Element Method (FEM, Komatitsch et al., 2002) with Spectral Element Method (SEM) to simulate seismic wave propagation, including variations in seismic wave speed, density, and anelasticity, and topography in various environments (Tromp et al., 2008). 3D regional models (500 to 1000 km) are computationally expensive, especially with low velocity layers. Makra & Chavez-Garcia (2016) compared simulations of ground motion for 2D and 3D models of the Mygdonian basin in northern Greece. They found that although 2D modelling typically over-estimates the site effect, the differences between the 2D and 3D simulation were small. Here, we use 2D waveform simulation software SpecFEM2D to generate local and regional basin site response models. SpecFem 2D was used to model the Taipei basin (Lee et al., 2008), which is a relatively small (20 km x 20 km) and shallow basin (750 m depth).

5.2 Geological and Geophysical background of CUSSO

The CUSSO station is a vertical array in the central United States that is deployed within the Mississippi Embayment sediment and terminates at 10 meters into Paleozoic rock. It is located in the northern Mississippi embayment in Sassafas Ridge,

Kentucky. The Mississippi embayment is characterized by a south-plunging synclinal trough (Figure 1). The top of Paleozoic bedrock is at 585 m depth. The Mississippi embayment is located in the Eastern Granite-Rhyolite Tectonic province, which is split into the eastern and southern sections that formed between 1470 -1370 Ma. Primarily, it consists of granite and rhyolite formed by extension via rifting. This embayment is a graben system consisting of three major divisions: the Reelfoot rift; the Rough Creek Graben; and the Rome Trough. The northern part of the embayment forms the Reelfoot rift, which is a northeast-trending basement depression extending from the cratonic margin in the south to the Eastern Granite-Rhyolite Province in the north. The CUSSO velocity model shows that the lower boundary of layer 1 correlates with the top of the basal Quaternary gravel, and the lower boundaries of layers 2, 4, 5, 6, and 7 are interpreted as the basal boundaries for the Jackson, Claiborne, Wilcox, Porters Creek clay, and Clayton–McNairy formations, respectively. The Moho depth around the New Madrid Seismic Zone (NMSZ) ranges from 40 to 45 km and thins toward the southwest and northeast (32-38 km) with higher thickness in central Tennessee (45-50 km). The early Cambrian/late Proterozoic upper crust hosts most of the seismicity (Chiu and Sudama, 1992; Csontos and Van Arsdale, 2008; Dunn et al., 2010; Luo et al., 2009; Wheeler, 1997). The USGS North American compilation of seismic properties shows that the Precambrian depth is at 3-5 km in the NMSZ and increases towards the northeast and southwest (8-9 km) and decreases to 1 km in central Tennessee and to 0 km toward the northeast (St. Francois Mountains, Missouri). Woolery et al. (2016) find a small horizontal amplification of ~1.5 between the bedrock at 526 m depth and the ground surface. At the subsurface layer between 30 m and the

ground surface, frequencies are de-amplified below 1 Hz, while for frequencies above 1 Hz, the amplification occurs at three dominant spectral peaks: 2, 5.5, and 11 Hz. They compared H/H to H/V and showed that at lower frequencies <1 Hz, H/V consistently exhibited larger amplification than H/H, whereas at higher frequencies (>1.1 Hz) H/H was consistently larger than H/V. Carpenter et al. (2018) show that the horizontal amplification is maximum at frequency 1.3 Hz with an amplitude between 5-15. and that the frequencies of the theoretical site response peaks were consistent with the observed peaks. In addition, they found that HVSR can replace the S-wave transfer functions for low-frequency analyses ($f <$ fifth peak frequency).

5.3 Observed Seismic Records

5.3.1 Data analysis

We used seismic records from local and regional events for magnitudes between 3 and 5.7 Mw, focal depths between 1-40 km, and hypocentral distances between 30-1200 km. We divided the data set into two groups based on distance: local events for distances between 30-300 km, and regional events for distances between 300-1000 km. Three component acceleration seismic records (V, EW, NS) at three interfaces were used: at the surface, at 30 m depth, and at 258 m depth (Fig. 2). We baseline-corrected all records by removing the mean and linear trend, and then deconvolved the instrument responses and integrated to generate seismic velocity records. We selected short windows that isolated the shear waves: for local events we used a width of 5 seconds in order to avoid surface wave contamination, and for regional events, the width of the window is between the S wave- arrival and group velocity of 3 km/s. Each selected

window is cosine-tapered at 5%. We calculate the amplitude spectrum for each window. We calculated the transfer function (TF) of horizontal ground motion (TFh30m and TFh270m) and vertical ground motion (TFv30m and TFv270m). The transfer function is the ratio of the ground motion of the earth surface to the ground motion recorded at 30 m and 270 m depth interfaces in the frequency domain. We also calculated the horizontal amplification, vertical amplification, and horizontal to vertical ground motion amplification (H/V). We calculated horizontal to vertical spectral ratios (HVSRs) from ground motion records at the free surface using the J-Sesame code (Bard et al., 2004) based on the criteria in Table 1. Unfortunately, the available ground motion amplification and transfer function TF of the same events are limited and they do not vary widely in magnitude or location; however, we use them for comparison with TFs30 and TF270m.

For the observed data we will discuss two effects: magnitude and azimuthal effect.

5.3.2 Magnitude effect

The effect of the earthquake magnitudes on the seismic site response was explored using events with different sizes. The size of the earthquakes does not affect the amplitude of the transfer function of the horizontal motion (TFhs) for $F < 5$ hz, but it does for the transfer function of the vertical motion (TFvs). For local events ($D = 20$ to 150 km, $Mag = 2.7$ to 3.6), figure 3 shows consistent TFhs and less consistent TFvs, particularly at 1 to 2 Hz. The HVSR shows that spectra shape varies in relation to earthquake magnitude. We compared TF30m and TF270m with horizontal and vertical amplification at CUSSO. Figures 3 shows that the variation in fundamental frequency and spectral amplitudes are less for CUSSO horizontal amplification than

TFh30m and TFh270m; however, the shape of the spectra is highly variable (figure 3). The magnitude effect primarily appears at low frequencies because small earthquakes are incapable of generating low frequency signals. Local and small magnitude earthquakes show higher variation in the amplification and fundamental frequency values; therefore, we have concentrated on frequencies less than 1 Hz in order to focus on the first order spectral features.

5.3.3 Azimuthal effect

For earthquakes with magnitude 2.2-2.8 M and distances 20-50 km, consistent TFh30m and TFh270m were observed, while the TFv30m and TFv270m show less consistent amplitude spectra. We observe that for local events, the azimuthal effect on horizontal amplification is minor while there is a noticeable effect on vertical amplification (Fig. 3). For regional earthquakes (magnitudes between 3.7 and 4.7 and distances between 500 and 650 km), the results of both frequency and amplitude are more consistent than for local results. The HVSR also shows a great deal of variability in amplitude and frequency; F0 varies between 1.3 and 2 Hz and amplitude varies between 2-10. Most regional events are located west of CUSSO, which generates a gap in our understanding of the regional azimuthal site effect characteristics.

In order to understand the origin of the features in the observed data we used numerical simulations and the known lithology for CUSSO.

5.4 Synthetic data

The 2D SPECFEM package was used to model the local and regional site response. SPECFEM combines the boundary composition flexibility of the FEM with the spectral

accuracy of pseudo-spectral methods where the free surface and main internal discontinuities of the earth have been considered (Komatitsch and Tromp, 1999). The anelastic effects on seismic waves were incorporated into SPECFEM using a series of standard linear solids and seismic wave simulations, using parallel computing (Savage, 2010). SPECFEM requires earthquake source characteristics, mesh design, and boundary conditions. Low velocity layers and thin layers have a critical effect on the propagation of high frequency seismic waves. To maintain high frequency ground motion records, the element size of the low-velocity layer should be smaller than the element size of the deeper high-velocity layer. Absorbing boundary conditions (Stacey, 1988) are applied to the sides and bottom of the model to prevent reflections (Table S3 shows the element size for each layer in our models from bottom layer to top layer).

5.4.1 Local Model

The local model consists of four sediment layers, a bedrock, and a crystalline rock (Figure 6). The virtual seismometers are located on the layer interfaces (figure 6). The local model is 24 km east-west and 15 km depth. The grid size inside the basin is about 60 m horizontally and 30 m vertically. A small vertical grid size is chosen to better describe the boundary between sediment and bedrock, and bigger mesh is used for sediments at the edge of the basin to reduce the computational cost. The mesh contains 777,254 spectral elements that are decomposed into 180 slices for parallel computing. Because a polynomial of degree $N = 4$ is used in SEM to simulate the wavefield, each spectral element contains $(N + 1) = 5$ Gauss–Lobatto–Legendre (GLL) points (Komatitsch et al., 2004). A normal fault source with strike 0° , dip 90° , rake 0° and focal depth of 5.0 km with size 3.21×17 kN.m is adapted as an earthquake scenario.

A Gaussian source time function is used with $F_0 = 10$ Hz, a time step of 0.35 ms, and the maximum resolved frequency is <3.0 Hz but for a local model with 150 m/s the resolved frequency is ~ 2 Hz.

5.4.2 Velocity effects

To track the velocity effect on the site response, we vary the velocity values of the upper five layers as follows (Fig.7) and we summarize the results in table (2). In this result we show how each velocity value changes the HVSR, horizontal amplification, and vertical amplification results.

5.4.3 Simplified Local Model ($f < 13$ Hz)

We used a three-layer model in order to simulate high frequency seismic waves ≤ 13 Hz. We tested the effect of flat layers, dipping layers towards the east, and dipping layers towards the west (Figure 8). We then used these synthetic high frequency seismograms. The results of the simulations show that dipping layers increase the vertical amplification of frequencies less than 3 Hz and decrease the horizontal amplification for the same frequency range. The F_0 of H/V increased from 1 Hz for flat bedrock to 3 Hz for a dipping bedrock layer. Additionally, the effect of bedrock thickness (e.g., the Paleozoic layer below the sediment and above the crystalline layer) was tested and the result was that the fundamental frequency shifted slightly to higher frequencies and the amplitude was increased while for frequencies higher than F_0 , the amplitudes were decreased. Dipping bedrock layers shift the fundamental frequency to 3 Hz and increase the amplification for $F > 3$ Hz. For the model with layers dipping toward the west, the amplification was higher than for layers dipping toward the east.

5.4.4 Regional models:

Figure 9 shows the regional model ($X = 500$ km, $Y = 60$ km) (sediment, basin geometry, and the earthquake). The rectangular shaped basin is adapted to eliminate the effect of sediment thickness variation and to focus on the effect of the seismic waves themselves. The regional model consists of a sediment layer, a bedrock layer, and a crystalline rock layer. An array of 40 virtual seismometers was located on the surface and another array was located on the sediment-bedrock interface (figure 9). A normal fault source with strike 0° , dip 90° , rake 0° , focal depth of 10.0 km, and size 5.21×17 kN.m was used to simulate an earthquake scenario. A Gaussian source time function ($f_0 = 1.1$) was used that constrains, in our model, source response frequency between 0.05 Hz to 3.0 Hz.

5.4.5 Basin effects:

We compared three models: a thin basin (600 m) with impedance contrast 0.3, a thick basin (1200 m) with impedance contrast 0.3, and a thin model (600 m) with impedance contrast 0.4. For the thin basin model, stations within the basin show horizontal amplification of the ground motion at frequencies between 0.4 and 1 Hz. The vertical ground motion does not show any amplification, but it shows changes in the spectral shape where most of the energy was focused around 0.7 Hz. The horizontal amplification calculated along the basin show similar fundamental frequencies (F_0) (Fig.10). By changing the basement velocity, we observe similar spectra shape, but the amplitude is higher and F_0 was shifted toward higher frequency because of the high impedance contrast that traps and focuses the energy at higher frequencies. For the thick basin model, we observe that spectra become more complex; the amplification

increases toward the far end of the basin, F0 shows little variation, the H/V_F0 and HVSR_F0 are similar and have two peaks, 0.3 and 0.7 Hz.

5.5 Discussion

Our results show consistent TFhs compared to TFv. The consistent shape of the TFs spectra decreases from TF30m to TF270m; however, it increases for bedrock-surface amplification. The HVSR shows variation in the frequency of the maximum peaks (F0) and amplitudes based on the event size, back-azimuth, and hypocenter distance: (1) TFh30m and TF270m show very weak correlation between amplification and distance (local vs. regional), (2) the earthquake magnitude influences the ground motion amplitude, primarily at lower frequencies < 1 Hz, (3) the sediment velocity affects the amplification and the fundamental frequency while the bedrock velocities affect the ground motion amplitude, which agrees with prior studies (e.g., Pavel et al., 2017). The relationship between the distance and HVSRs generated at CUSSO show variation in the linear trend between regional and local distances. For local distances (< 300), the HVSR gradient is very weak positive while the regional gradient is negative; however, F0 shows constant values for all distances. The regression analysis shows a clear trend between the regional events and HVSR.

For the USArray seismic stations located near CUSSO, we find Lg phases that are highly attenuated (Q Lg phase is 200; Gallegos et al., 2014), and Lg horizontal motion is amplified in the frequency band 0.5-4.5 Hz, while the Lg vertical amplification varies as a function of frequency: for $f < 2.5$ Hz, Lg is amplified, and for $f > 2.5$ Hz, Lg is de-

amplified (Yassminh et al., 2019). Specifically, across the NMSZ for earthquakes distance less than 500 km, the horizontal and vertical QLg were estimated to be 390 and 410 for $f > 3$ Hz, respectively (Bisrat et al., 2014; Langston, 2003; Nazemi et al., 2017; Pezeshk et al., 2018). For high frequency body waves (P and S), site amplification is more significant than path-based attenuation in the Mississippi embayment. The calculated Poisson ratio of NME sediment is 0.44, which is independent of the sediment thickness and is similar to the observed Poisson ratio (Woolery et al., 2016). As a result, the NMSZ region shows greater local-wave attenuation than regional-wave attenuation, and the Q_s/Q_p ratio is higher for the local waves, which will have greater effect on site response. For $f < 2$ Hz, Q values were not determined because higher frequency surface waves contaminate the shear waves and the Lg group velocity window (Nazemi et al., 2017). Our HVSR at ground surface shows high amplitudes at 0.3., 0.7-0.8, and 1.2 Hz. Wang et al., (2018) and Carpenter et al., 2018) shows high HVSR amplitude using S waves windows at 0.3, 0.8,1.2 Hz; using ambient noise 0.3, and 0.8 Hz; using transfer function of S_h at 0.35,0.8 Hz. Sedaghati et al., (2018) show HVSR of several seismic phases with peaks at 0.3, 0.9, and 1.3 Hz, though the maximum amplitudes vary based on the type of the seismic waves which is similar to our results that shows the maximum peak varies within the high amplitude peaks based on the magnitude and which seismic waves we use in the analysis.

In order to test the effect of geology on HVSR (amplitude and frequency), we compared our CUSSO result with other stations located in different geological locations; ABTX (Fig 14), BGNE (Fig 15), and KMSC (Fig 16). ABTX is located in the edge of the

Edwards Plateau the Northern Central Plains where the Permian rocks (limestone, dolomite or gypsum) are covered by alluvium of Quaternary age (Chairman et al., 1954). Station KMSC is located in the southeastern Appalachian Mountains. BGNE is located on Terrace Plains, and is underlain by Illinoian and Pleistocene terrace deposits (Pabian et al., 2003; Pabian & Diffendal Jr, 1991). Stations located on thick and complex sediments show differences in trends between local and regional site responses. Generally, local amplification decays with distance faster than regional amplification. For stations located on thin sediment layer or rock, the HVSR is more consistent between both local and regional seismic records. For example, for KCSC and ABTX stations, which are located on mountain and platform, respectively, the HVSR has a constant trend with distance and does not show a change in slope between regional and local distances. We found that F_0 is mostly constant with respect to epicentral distance and back-azimuth. CUSSO events have a maximum distance equal to 900 km while other stations maximum distances are 1400 and 2000 km, which could be caused by the attenuation mechanisms beneath CUSSO.

The Northern Mississippi Embayment (NME), where CUSSO is located, is a complex Paleozoic basin filled with 600 meters of unlithified sediments and underlain by metamorphic rocks. In such complex basins, focusing and defocusing are the two most important processes localizing the ground motion at specific frequencies. Increasing the velocity contrast between the basin sediments and bedrock increases the focusing-defocusing effects. Local shear waves transmit into the sediment with incident angles varying based on the depth and the hypocentral distance (Fig. 17) (e.g., distance 20-200 km based on TauP ; Aki and Richards, 2002; Crotwell et al., 1999; David von

Seggern, 2010). Increasing the impedance contrast strongly decreases the critical angle resulting in trapped shear waves within the sediment layer (Shearer, 1999). Basin boundaries, curved-dipping interfaces with a high velocity contrast, have a noticeable effect on the incidence of the seismic waves. Our simulations (Fig. 8) show that the slope of the basin-edge increases the high frequency amplification and increases F_0 . In addition, the slope of the basin-edge has an effect on the ground motion. Therefore, the location of the source with regard to the basin imposes a variation in the site response (azimuthal effect). Complex seismic velocity structures such as deep basins filled with sediments could redirect the seismic waves through the deep sediment and basins edges. We are unable to fully characterize these effects since we are only using a 2D model. For simple structures, the impedance contrast is the main cause of site response while focusing and defocusing effects will be added to the impedance contrasts to generate complex site effects. Site response simulation results show that the deep structure influences the high frequency waves consistent with prior studies e.g. Kawase et al., (2018).

Unlike direct local shear waves, Lg waves propagate efficiently through most of the CEUS crust and do not follow a specific ray-path. Lg waves propagate horizontally within the crust and reach distances of 2000 km. Waves slow when they propagate in basins, and thus Lg waves could amplify similarly to the surface waves amplification (Bowden and Tsai, 2017). The large impedance contrast at the basin edge traps the seismic waves propagating both vertically and laterally, which results in constructive and destructive interference and changes the frequency content of the seismic waves; however, the Lg waves could be subjected to higher scattering than local phases due to

the effect of sediments, non-unique Lg ray-path, local heterogeneities, fractures, and/or irregular topography (Aki and Chouet, 1975; Ducellier et al., 2013; Frankel and Wennerberg, 1987; Tsai and Aki, 1969). The heterogeneity along the propagation path redistributes the energy of seismic waves via scattering and anelasticity. The NW-SE heterogeneous crustal structure in NMSZ (Bisrat et al., 2014) most likely triggers the attenuating mechanisms in the crust. We compared regional seismic waves propagating from eastern CUSSO with regional seismic waves propagating from other directions (Fig.18b). Earthquakes located in eastern CUSSO with easterly back-azimuths and smaller magnitudes than the rest of the regional events have higher HVSR amplitudes at lower frequencies. Our results emphasize the effect of the attenuation along the propagation path on site responses. As a special case, in CUSSO the attenuation effect appeared as an azimuthal effect.

The HVSR method depends on averaging over many spectral ratios (Sesame, 2004). For CUSSO, there is a gap in the azimuthal coverage especially for regional events, which biases the HVSR result. To overcome this bias, we applied a weighted averaged algorithm. In this algorithm we weighted HVSRs based on the location (distance and back-azimuth) and number of events. Figure 18 shows the result of the average HVSR and the weighted average HVSR. The major difference is the peak at 0.8 Hz because it mostly appears in larger regional events, which in our case have a higher weight:

$$W - HVSR = \frac{\sum_{i=1}^n (w_i \times HVSR_i)}{\sum_{i=1}^n w_i} \quad (4.1)$$

where w_i is the weight assigned to each HVSR to compensate for over or under sampling of specific distance and back-azimuth. We applied the design weight $=1/\text{sampling fraction}$, where the sampling fraction in CUSSO's case is the over-sampling amount for a given distance and back-azimuth (table 2). This approach of weighting the HVSR before averaging them to generate the W-HVSR depends strongly on the geologic structure of the seismic station.

In the NMSZ region, one of the factors that may cause inconsistent HVSR is water saturation. The degree of saturation may have substantial influence on vertical-motion amplification, both amplitude and frequency content, which suggests that we may need to carefully consider the condition of saturation in the NMSZ region. Even a slight decrease from full saturation of the overlying sediment may cause large differences in the amplitudes of ground motion in both the horizontal and vertical components and the amplitude ratios between the two components at the ground surface. The effect of saturation on the site response is based on incidence angle variation (Whiteley et al. 2018; Yang, 2001; Yang & Sato, 2000).

Our results agree with Kawase et al. (2014, 2011), who introduce diffuse-field theory as an explanation for the H/V ratio and emphasize the scattering mechanism in site response, and suggest that averaging HVSR of earthquakes with crustal source depth and regional distance is sufficient to predict the site response.

We compared our 2D simulated site response results with the observed data of Fehr et al., (2019). We found agreement on some points: (1) the F0 and the amplification increase with decreasing sediment thickness; (2) focusing and defocusing processes

have an important effect on site response in thin sediment layer; and (3) the impact of the impedance contrast overcomes basin edge effects.

We calculated the 1D site response model following the method of Kramer S.L. (1996). The 1D model does not account for the bedrock thickness and topography. We compared our results for the 2D and the 1D synthetic site response results for frequency > 1 regarding only the frequency. Greater differences between 1 D and 2D were observed for regional models than for local models (Figure S2). For local models, the sediment in the bottom of the model results in considerable differences between the 1D and 2D models, which could be the effect of the focusing and defocusing that the 1D model does not account for. We recommend adapting 2D ground motion modelling using FEM or SpecFEM to measure the site response. 2D modeling accounts for the deep earth layers, in addition to being convenient and computationally inexpensive. The limitation of the 2D modeling is that it does not account for the azimuthal effect that was observed in the CUSSO spectra and shows a clear trend between the back-azimuth and regional distances.

5.6 Conclusions

In this study, we have investigated the local and regional site response in the Central U.S. Recorded seismic data of the CUSSO vertical array were analyzed and the site response was calculated. We simulated local and regional amplification and fundamental frequency of a 2D model with point-source radiation.

We found that simple geologic structure shows consistent results between regional and local site responses while complex geologic structures (basins) show differences. We

found that the basin site response is a combination of basin geometry, sediments, distance and azimuth between the seismic source and seismic stations. Additionally, the scattering mechanisms resulting from the crustal heterogeneity, thickness variation, and sediments have primary effects on the regional seismic waves and on characterizing the site response. In complex geologic regions, in order to account for regional seismic phases which are affected by the deep seismic velocity structure, we recommend the weighted-average algorithm.

5.7 Tables

Table 1. The parameters used to process HVSR in J-SESAME.

Window length	50 seconds
Merging	Geometric (Bard et al., 2004)
Smoothing	Konno & Ohmachi (Konno and Ohmachi, 1998); sesame, 2004).
Bandwidth	40
Tapering	0.5%

Table 2. The 2D simulation results of the local models.

	First model			Second model				Third model			Fourth model			Fifth model		
	(0-30m)			(30 m - 270 m)				(270-520m)			(520-580m)			(580-5000m)		
Velocity (m/s)	150	350	500	350	450	600	800	700	900	1100	1100	1400	2000	2500	3500	4000
HVSR -F0	1.2	1	0.9	2.5	0.8	1	2.5	1.5	1	1	1.7	1.7	1.7	1.7	1	2.7
HVSR -amp	20	4	4	9	4.5	4	9	30	4	3	3	7	4	200	4	150
Horizontal F0	1.2	1	1	0.7	0.7	1	1.2	1.6	1	1.2	1.7	1.7	1.7	1.7	1	1.7
Horizontal Amplification	40	10	10	15	190	10	20	200	10	19	30	15	10	30	9	10
Vertical_F0	1.8	1.2	1.2	0.7	1	1.2	1.5	0.7	1.2	1.8	1.7	1.5	1.5	0.7	1.2	1
Vertical Amplification	10	10	8	7	0.8	10	6	5	10	25	28	8	7	4	10	0.5

Table 3. The weighted criteria of CUSSO seismic records.

Class	Criteria	Weight
Local	30>distance>300	1
Regional	300<distance<1000	$\frac{\text{Local event count}}{\text{Regional event count}}$
West	Back-azimuth<180	1
East	5>Back-azimuth>180	$\frac{\text{Western event count}}{\text{Eastern event count}}$
Local & West		1+1
Local & East		1+ $\frac{\text{Western event count}}{\text{Eastern event count}}$
Regional & West		$\frac{\text{Local event count}}{\text{Regional event count}}$ +1
Regional & East		$\frac{\text{Local event count}}{\text{Regional event count}}$ + $\frac{\text{Western event count}}{\text{Eastern event count}}$

5.8 Figures

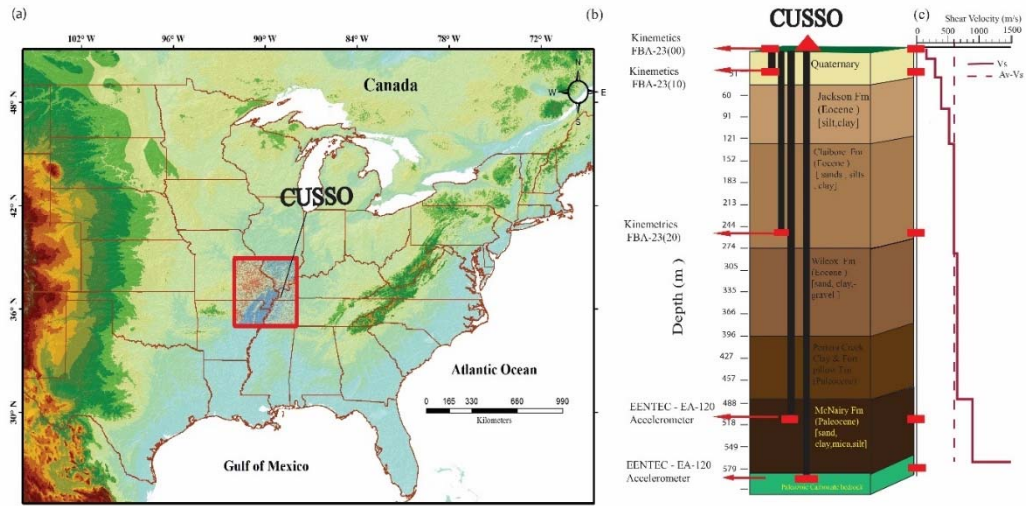


Figure 5.1 CUSSO location and geological units beneath CUSSO.

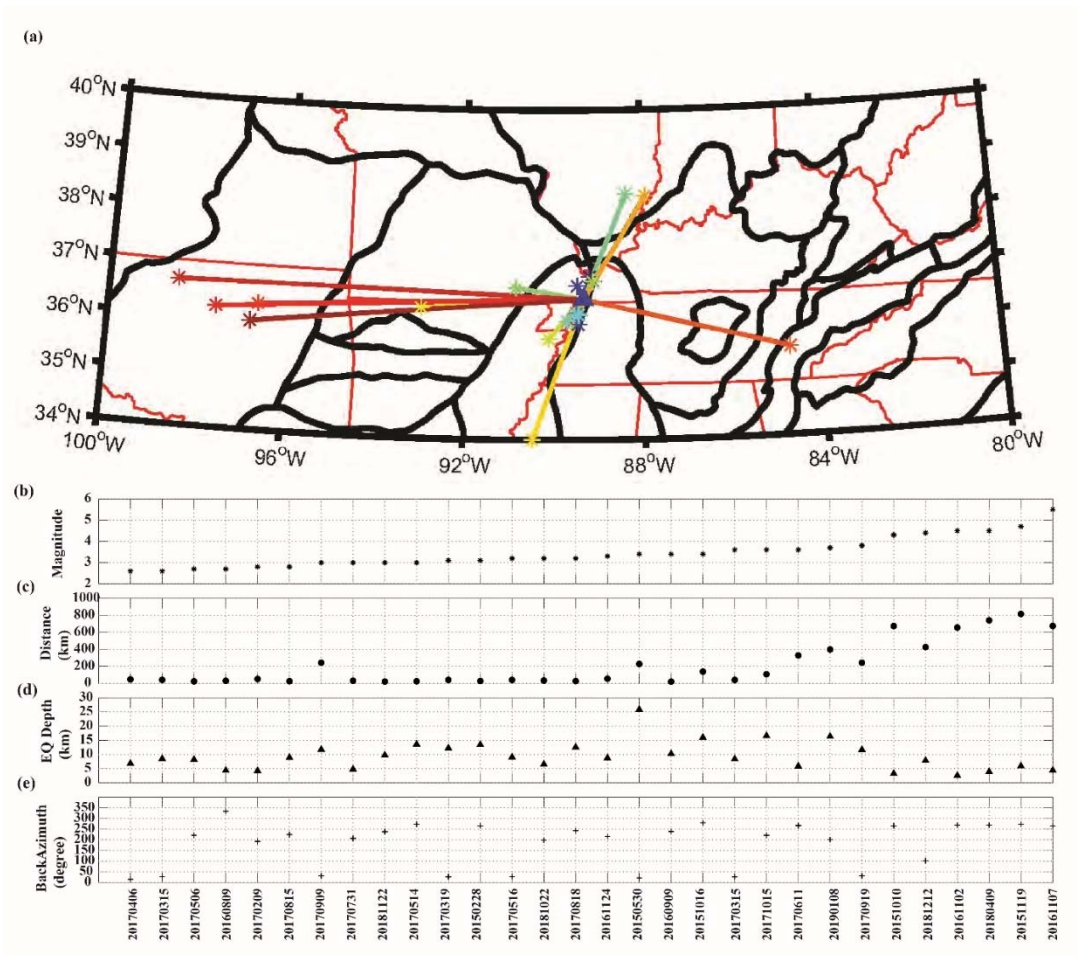


Figure 5.2 (a) The map shows locations of the analyzed earthquakes (stars), CUSSO (triangle), and the geological units surrounding the CUSSO. Graphs indicate attributes of the earthquakes used: (b) magnitude, (c) distance, (d) depth, and (e) back-azimuth

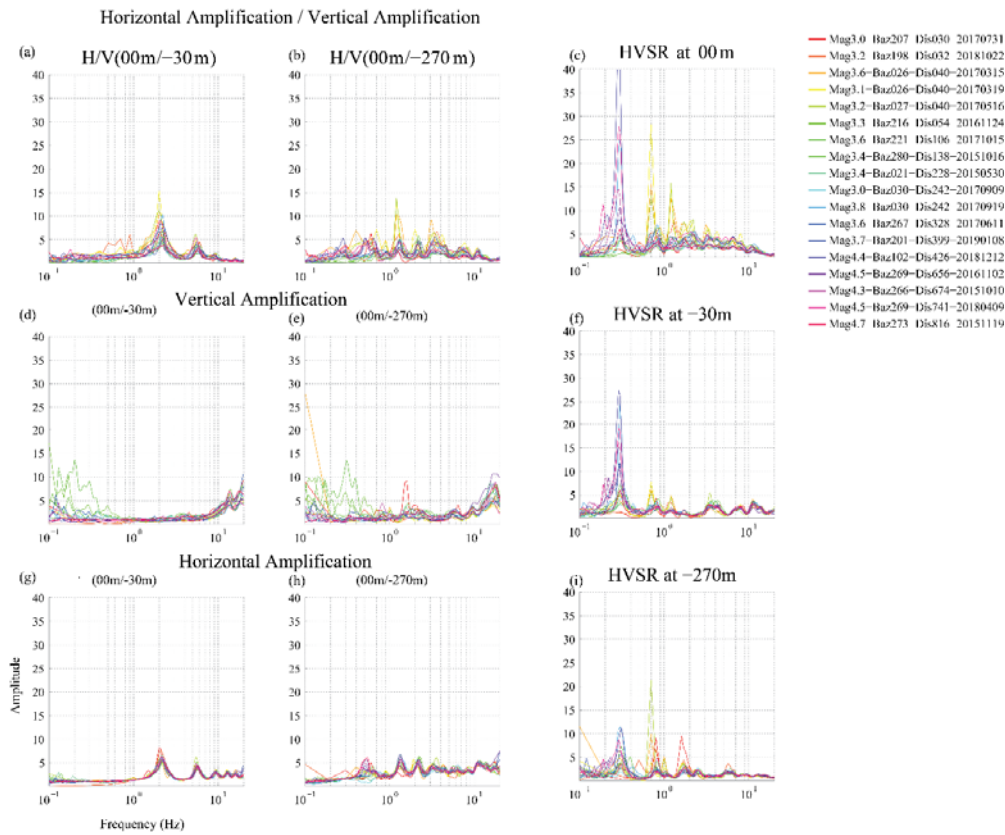


Figure 5.3 (a) The horizontal to vertical ratio of Tf30m, (b) the horizontal to vertical ratio of TF270m, (d) the vertical TF of the upper 30m, (e) the vertical TF of the upper 270m, (g) the horizontal TF of the upper 30m, and (g) the horizontal TF of Upper 270m, (c,f,i) the HVSR at the earth surface, at depth 30m and at 270m, respectively.

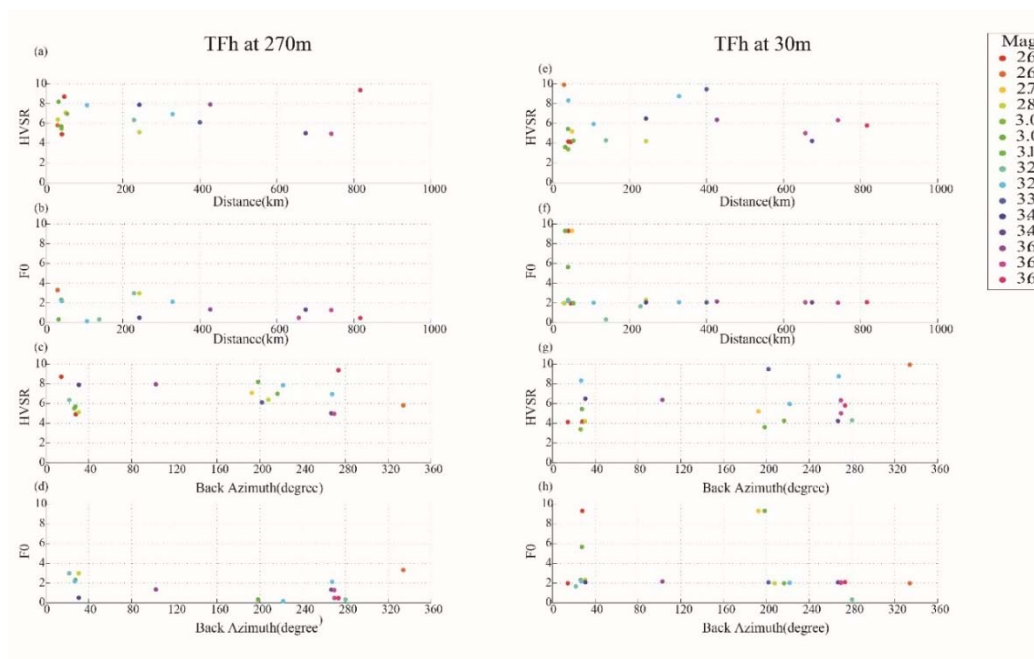


Figure 5.4(a-b) Variation of the amplitude of the TF270 and the F0 with distance. (c-d) Variation of the amplitude of TF270m and F0 with the back-azimuth. (e-f) The amplitude of the TF30m and the F0 versus the distances in km. (g-h) Amplitude of TF30m and F0.

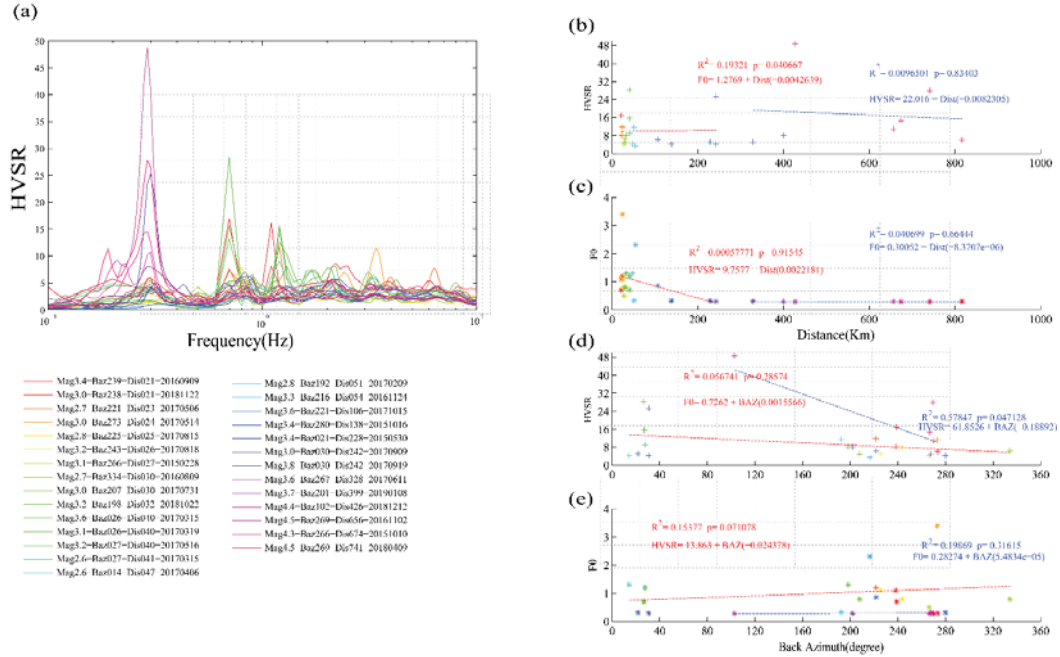


Figure 5.5(a) HVSR of the events where each line represents an event and the solid black line represents the averaged HVSR. (b) The maximum amplitude of HVSR versus the distance (km), (c) F0 versus the distance (km). (d) The maximum amplitude HVSR versus the back azimuth.

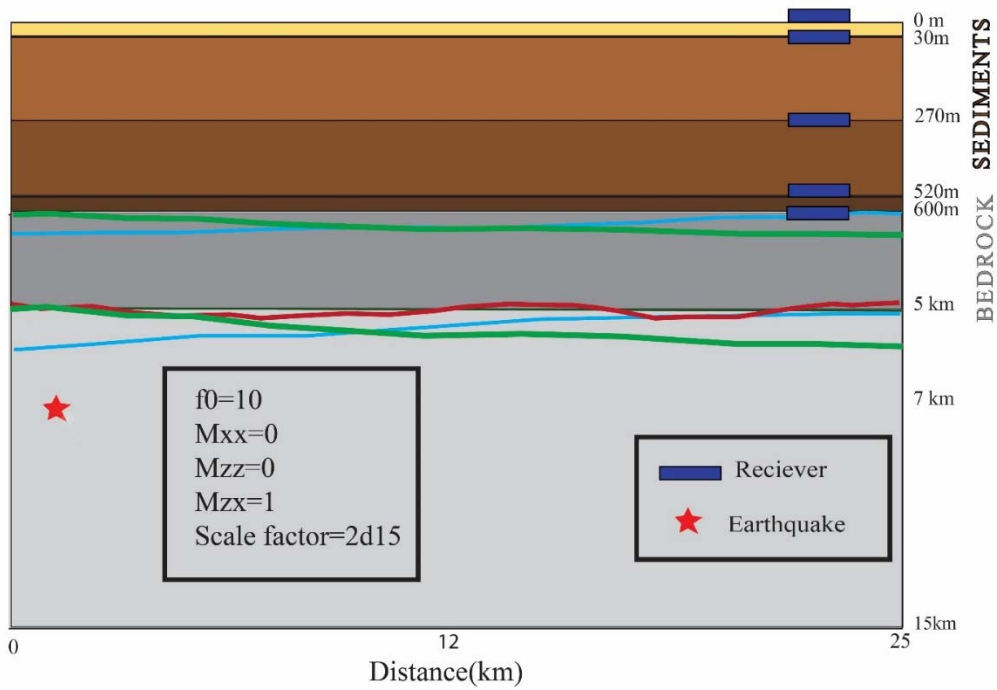


Figure 5.6 A sketch of the local model. The red star represents the earthquake location, blue squares are the vertical array of virtual seismometers, blue and green lines represent the dipping bedrock models, and the red line represent the wavy bedrock model.

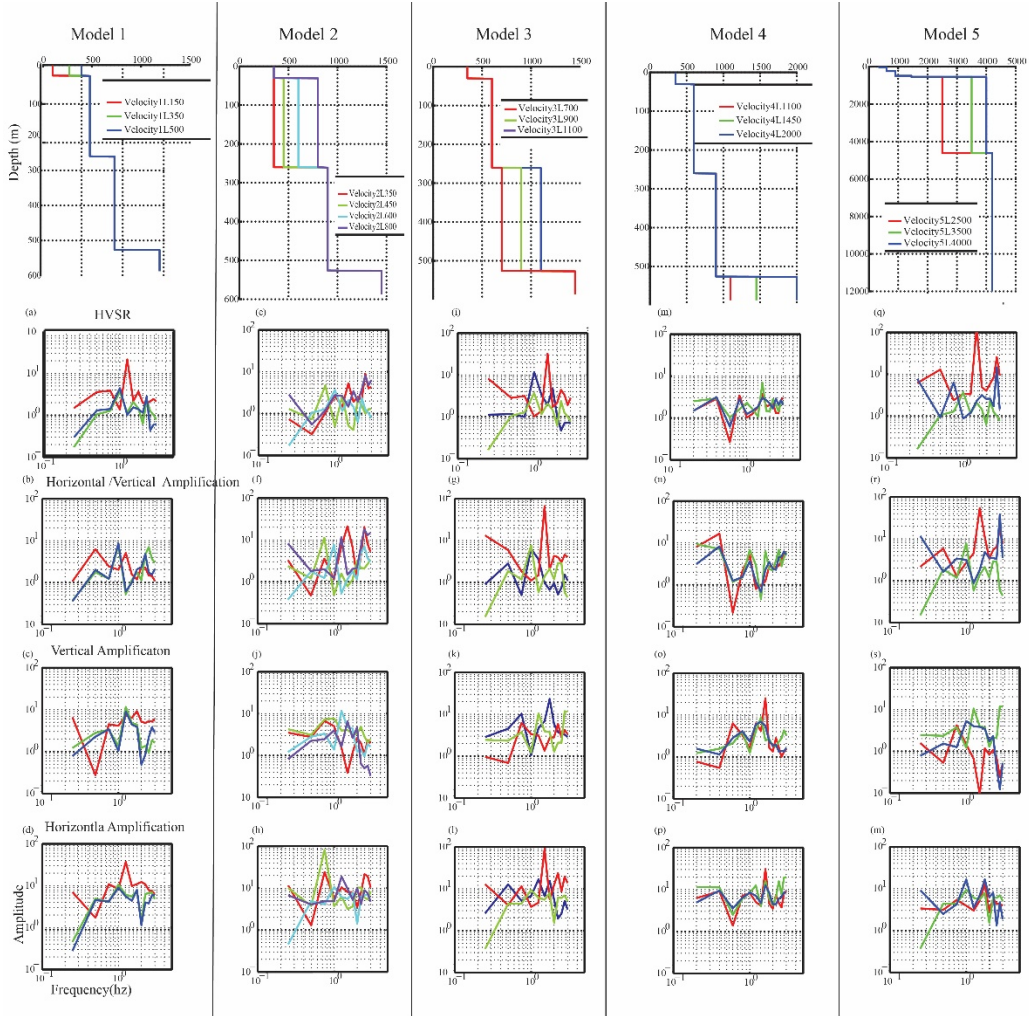


Figure 5.7. (a) Results of the 2D simulation models. (b) first model, (c) second model, (d) third model, (e) fourth model and (f) fifth model.

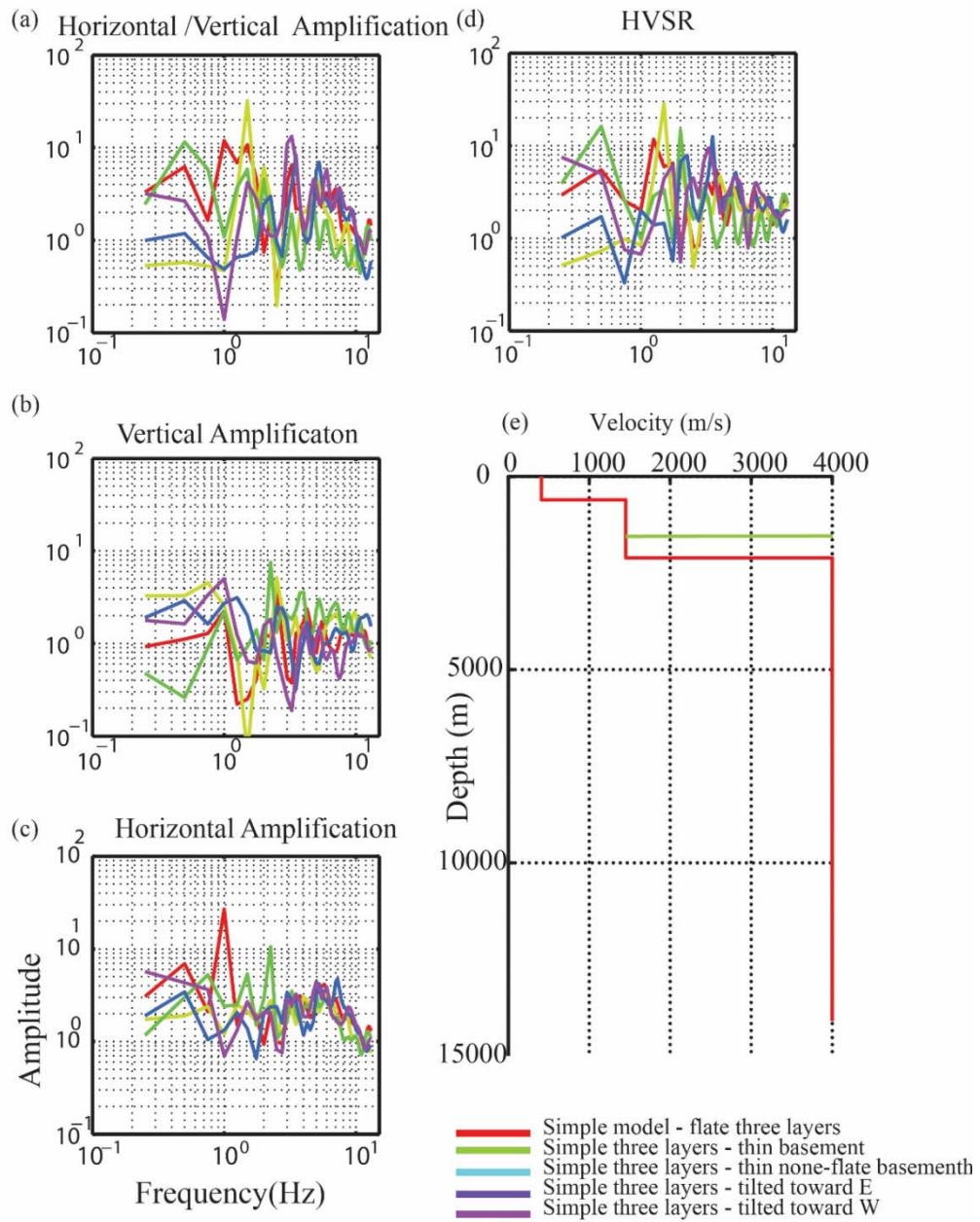


Figure 5.8 Simplified local models (three-layer local model). (a) The horizontal amplification to vertical amplification ratio, (b) vertical amplification, (c) horizontal amplification, (d) HVSR at the earth surface, and (e) velocity models.

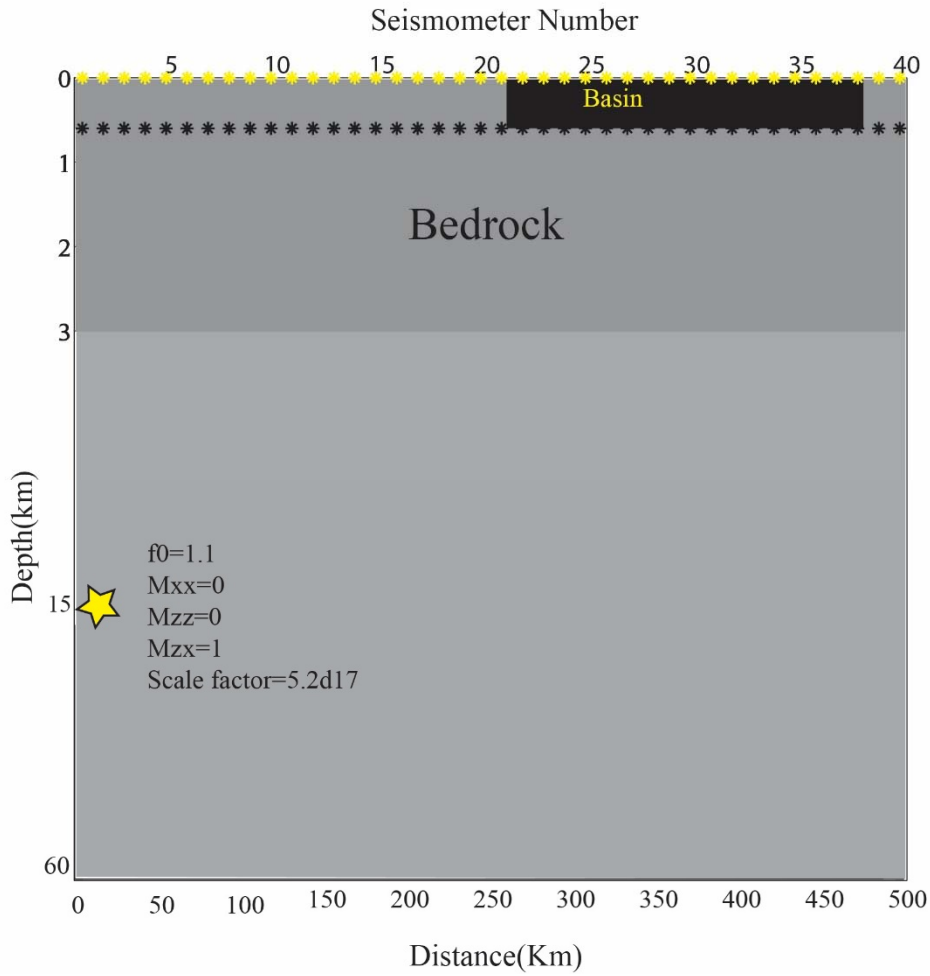


Figure 5.9 The regional model sketch conducted to test the basin effect on regional seismic waves, where the yellow star represents the earthquake location. Points are the two arrays of virtual seismometers, yellow is the surface array and the black is the bedrock

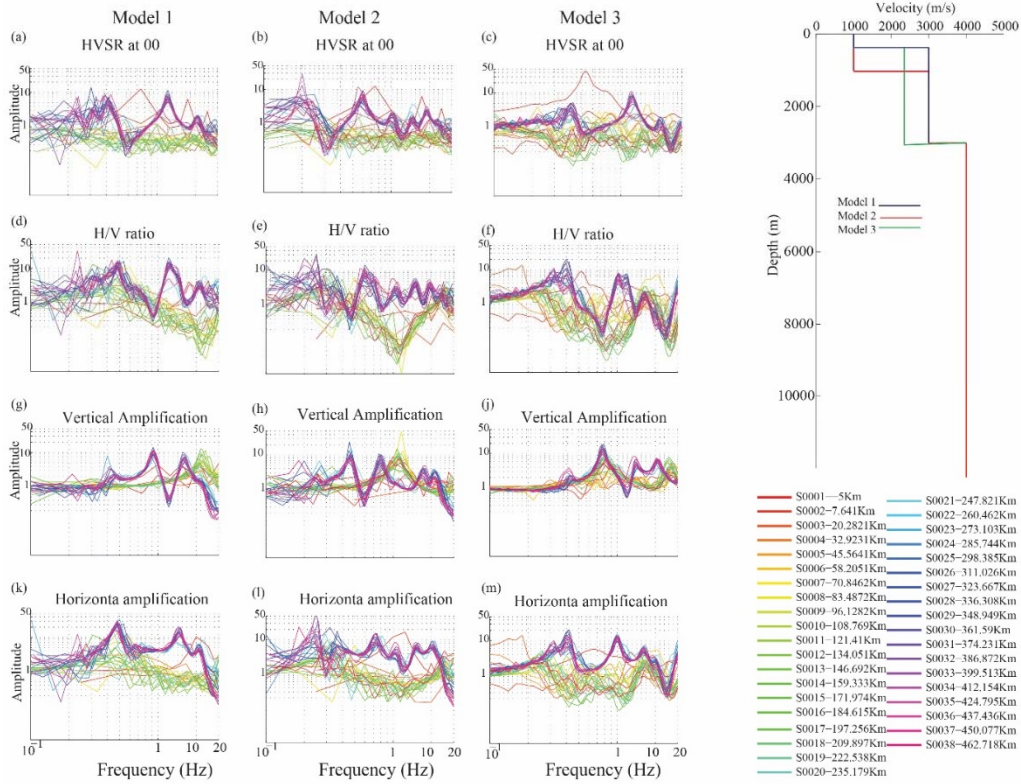


Figure 5.10 The three regional models: model1, model2, and model3; (a-c) shows the HVSR, (d-f) vertical amplification / horizontal amplification ratio, (g-h) vertical amplification (j-k) show the horizontal amplification, and (m) the velocity models simulated.

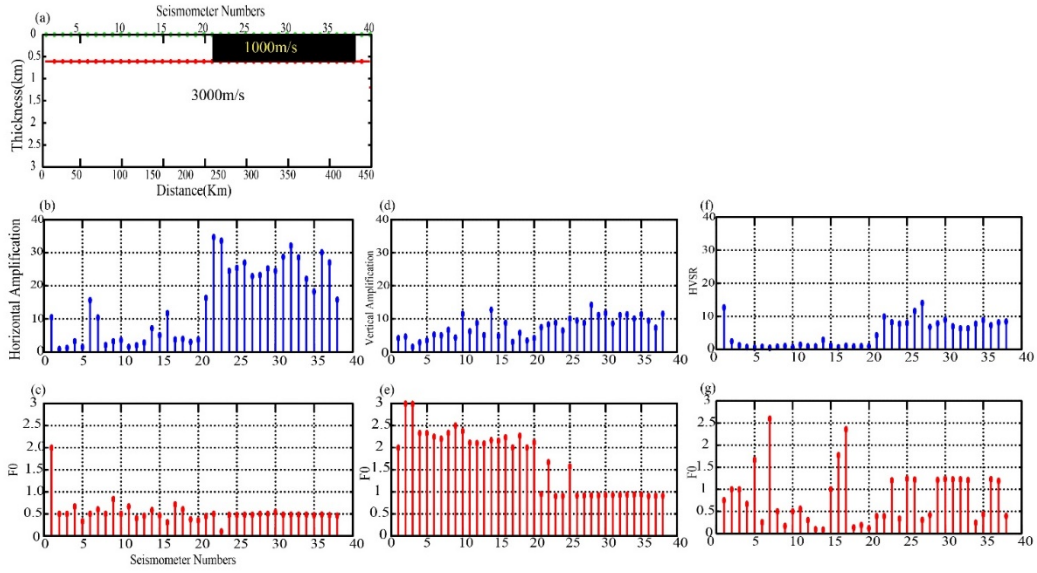


Figure 5.11 The Model1, (a) sketch of the upper 3km of the regional model1, (b) horizontal amplification versus distance, (c) F0 of horizontal amplification versus distance, (d) vertical amplification versus distance, (e) F0 of vertical amplification versus distance

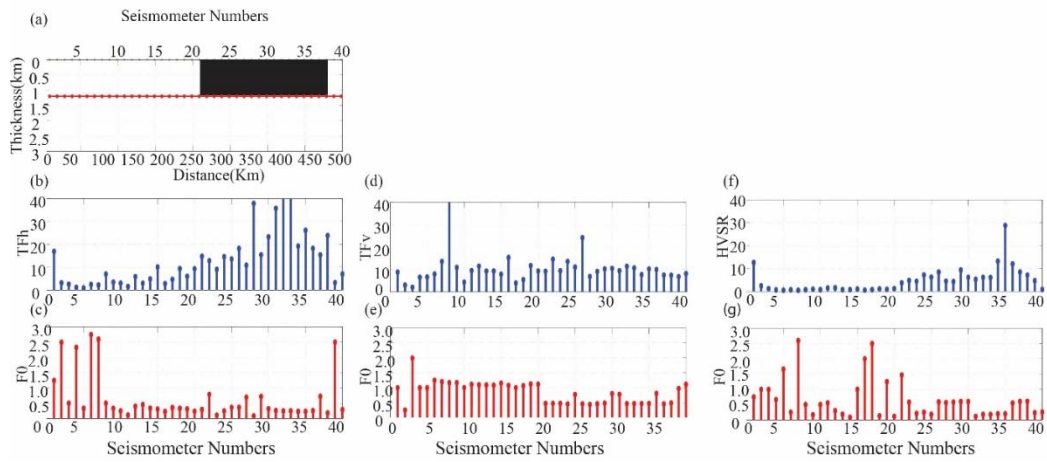


Figure 5.12 The Model2, (a) a sketch of the upper 3km of the regional model2, (b) horizontal amplification versus distance, (c) F0 of horizontal amplification versus distance, (d) vertical amplification versus distance, (e) F0 of vertical amplification versus distance.

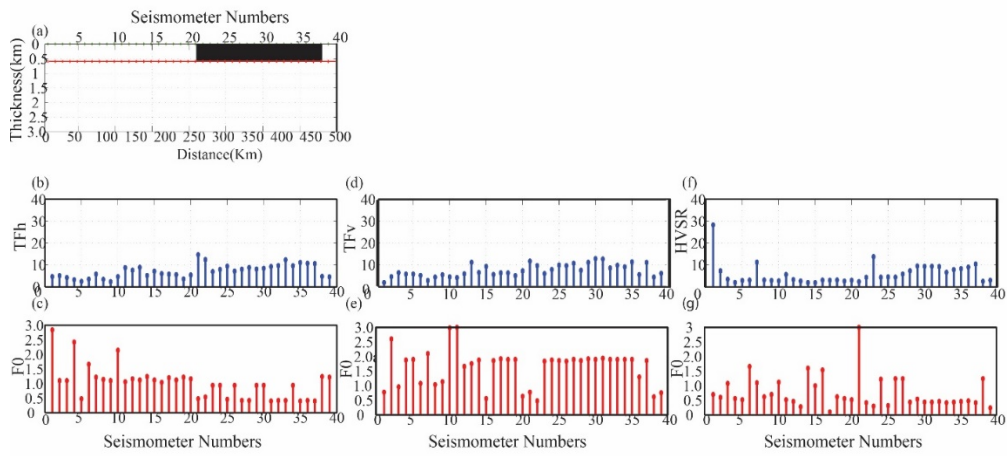


Figure 5.13 The Model3, (a) a sketch of the upper 3km of the regional model3, (b) horizontal amplification versus distance, (c) F0 of horizontal amplification versus distance, (d) vertical amplification versus distance, (e) F0 of vertical amplification versus distance.

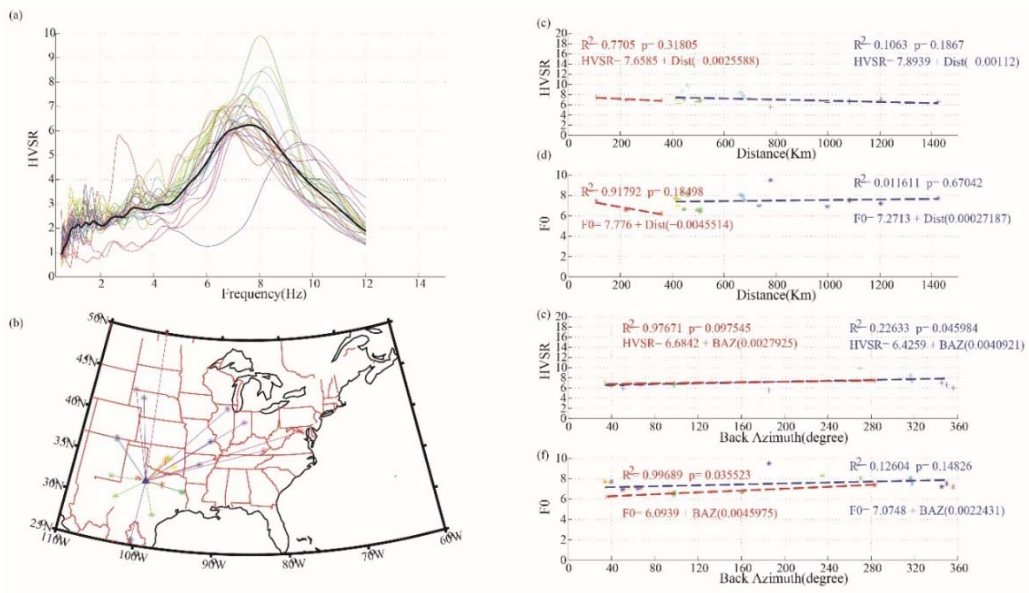


Figure 5.14 ABTX seismic station. (a) HVSR of the events shown in map (b) and the colors represent the events. (c) HVSR versus distance (km), (d) F0 versus distance (km). (e) HVSR versus back-azimuth (degrees), and (f) F0 versus back-azimuth (degrees).

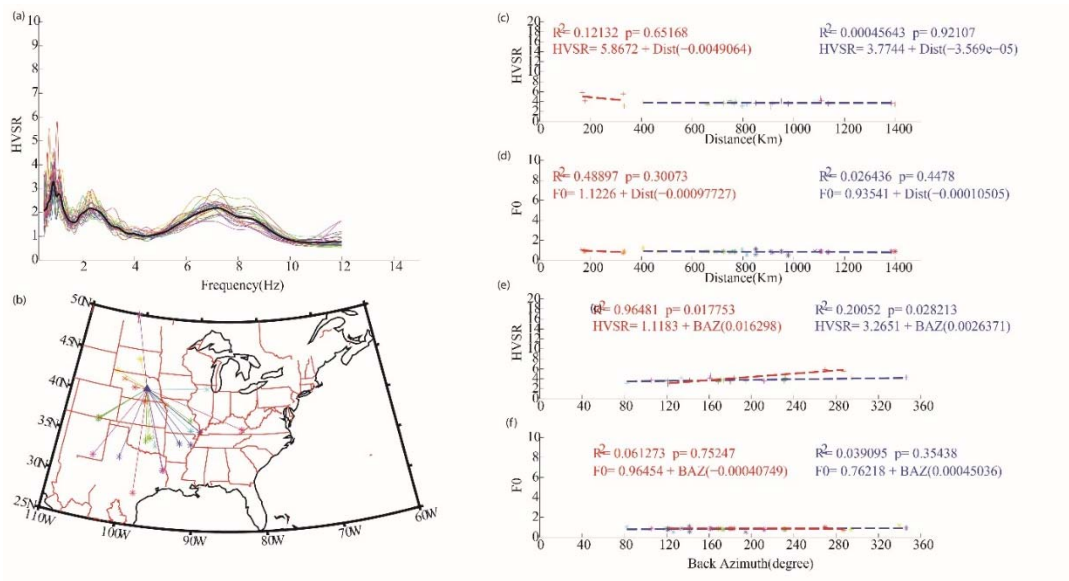


Figure 5.15BGNE seismic station. (a) HVSR of the events shown in map (b) and the colors represent the events. (c) HVSR versus distance (km), (d) F0 versus distance (km). (e) HVSR versus back-azimuth (degrees), and (f) F0 versus backazimuth (degrees).

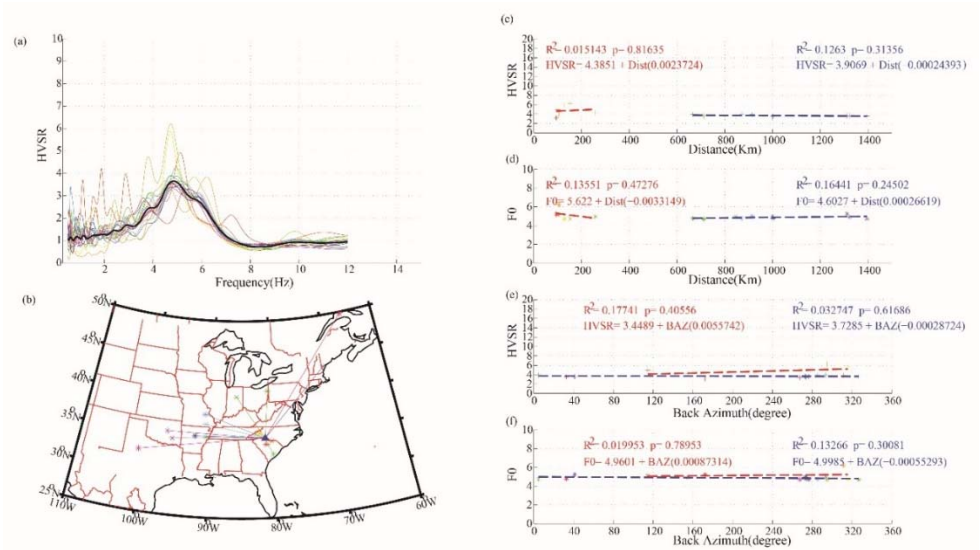


Figure 5.16 KCSC seismic station. (a) HVSR of the events shown in map (b) and the colors represent the events. (c) HVSR versus distance (km), (d) F0 versus distance (km). (e) HVSR versus back-azimuth (degrees), and (f) F0 versus backazimuth (degrees).

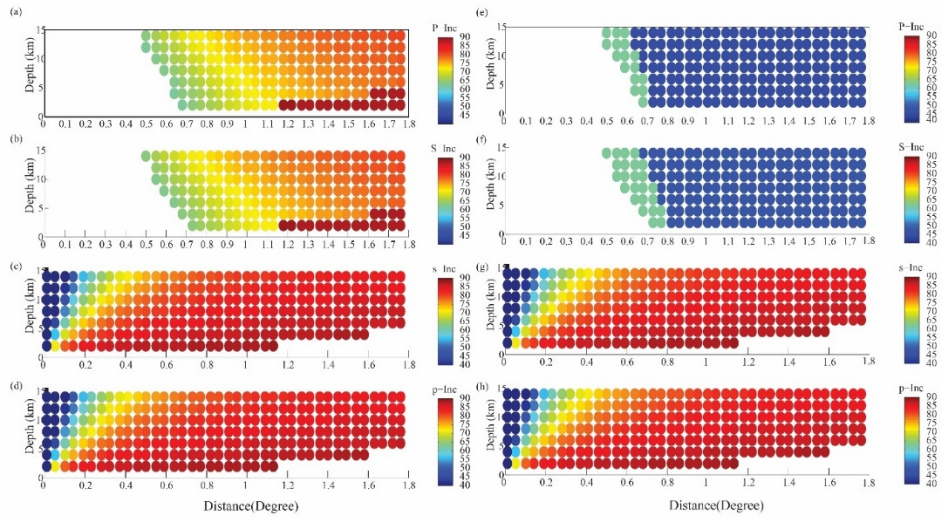


Figure 5.17 Variation of the incidence angle of P and S waves with depth and distance of the earthquakes using TauP software. (a-d) The incidence angle of the smallest ray parameter, and (e-h) is the incidence angle of the highest ray parameter.

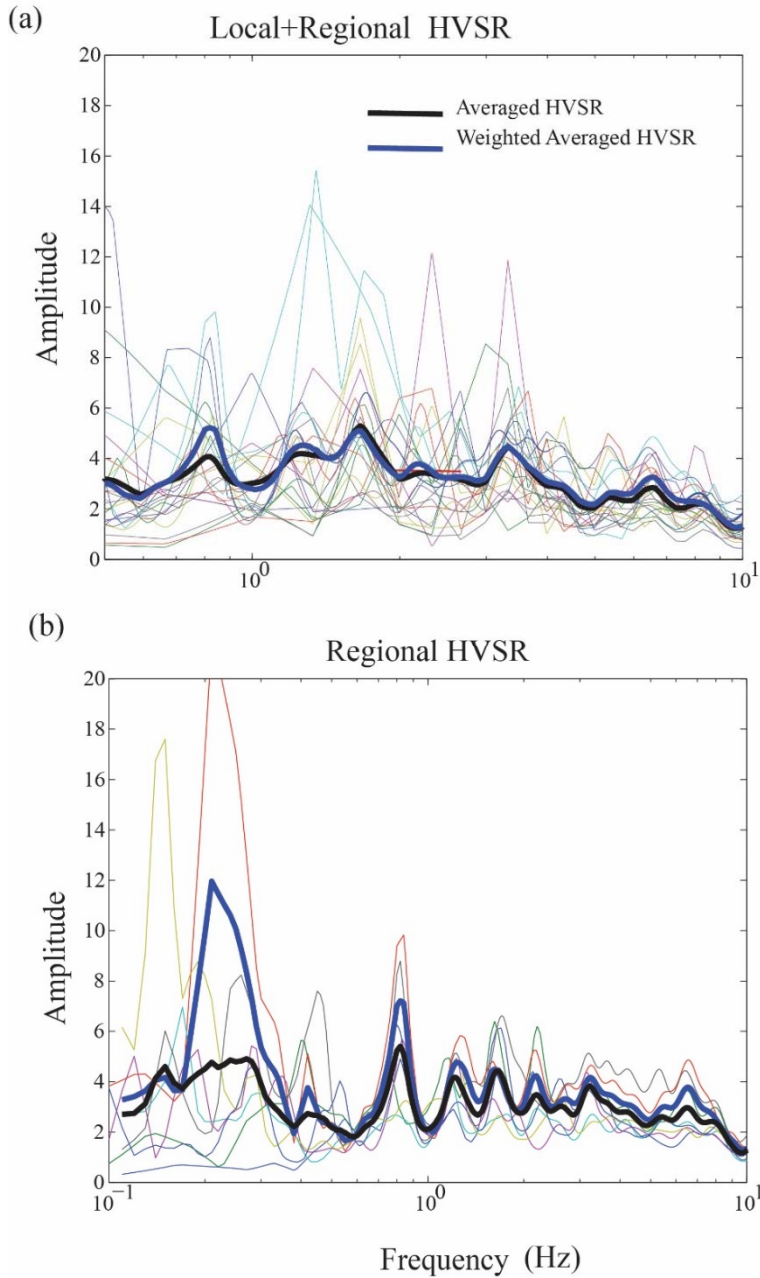
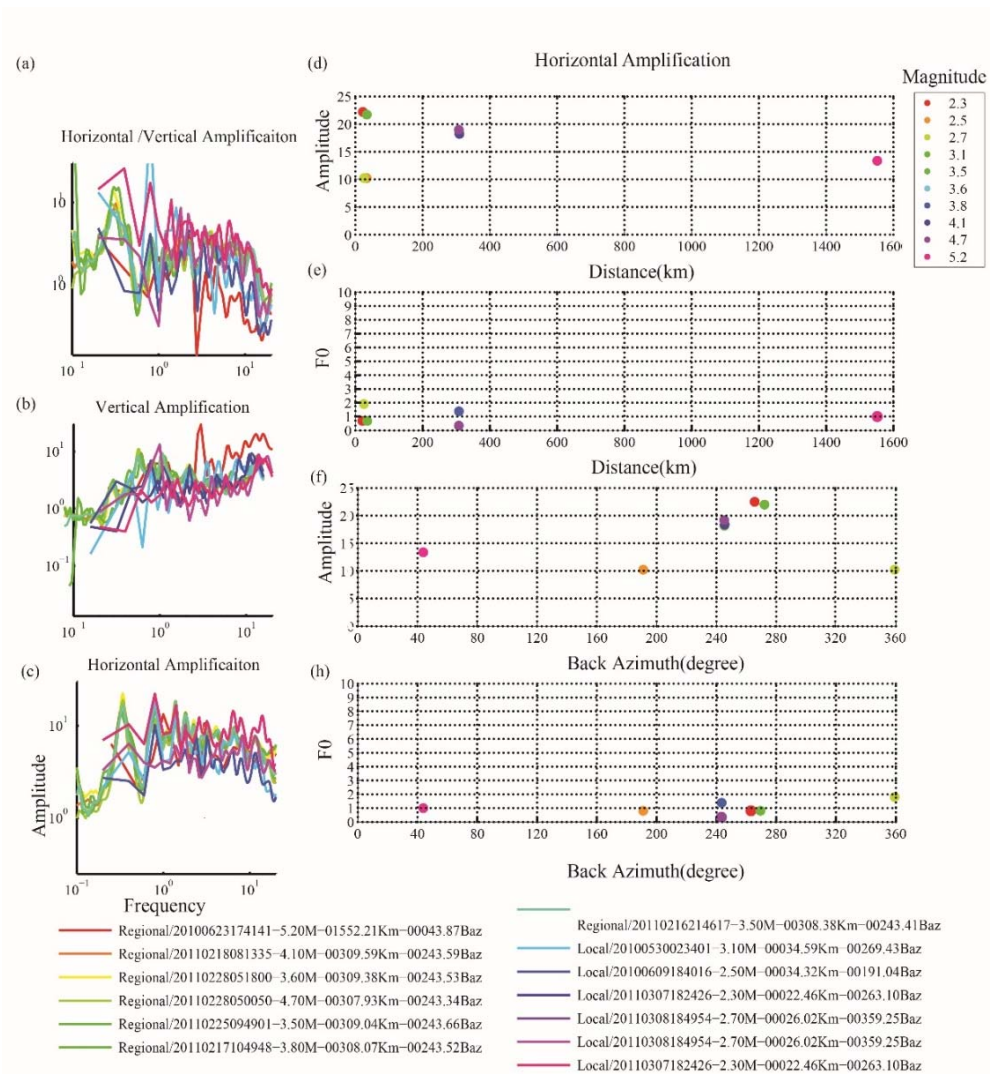
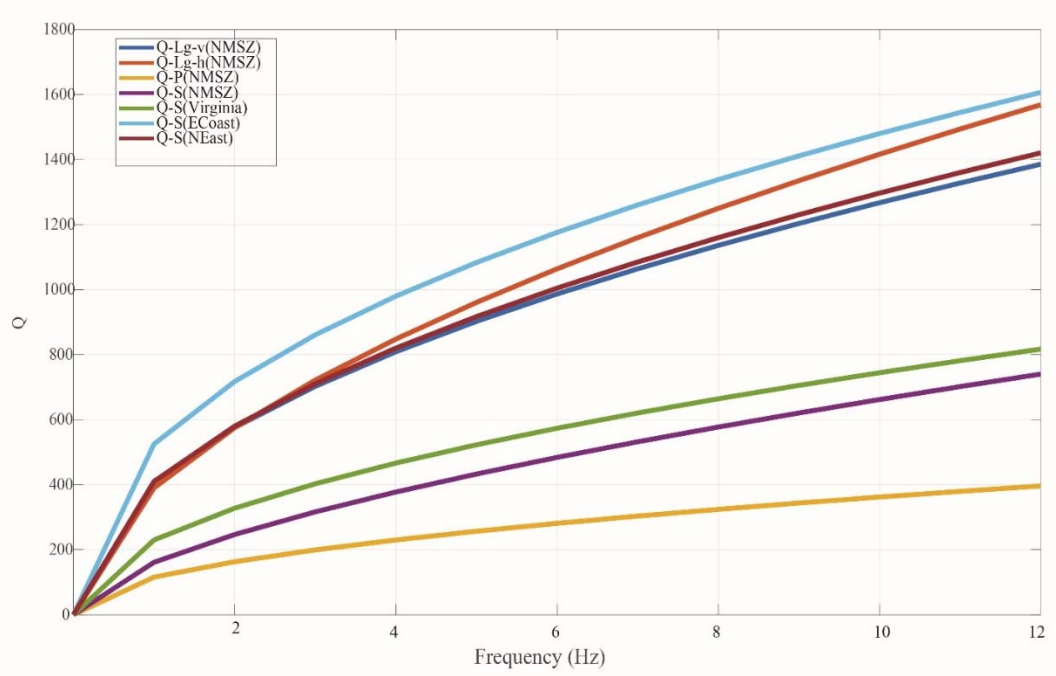


Figure 5.18 (a) HVSr of local and regional events recorded in CUSSO. (b) HVSr of regional events. The black solid line is the average HVSr and the blue solid line is the weighed-average HVSr. Notice the shift in the fundamental frequency from 0.8 Hz to 0.2 Hz

5.9 Supplement figures.



Supp.Figure 5.1 Ground motion amplification at CUSSO between the ground surface and the bedrock at 580m.



Supp. Figure 5.2 The Q values of the NMSZ region and other regions in the east from previous studies (Nazemi et al., 2017; Pezeshk et al., 2017; McNamara et al., 2014; Boatwright et al., 2011).

5.10 References

- Aki, K., and Chouet, B., 1975. Origin of coda waves: source, attenuation, and scattering effects. *Journal of geophysical research*, **80**(23), 3322–3342. Wiley Online Library.
- Aki, K., and Richards, P. G., 2002. *Quantitative seismology*.
- Bisrat, S. T., DeShon, H. R., Pesicek, J., and Thurber, C., 2014. High-resolution 3-DP wave attenuation structure of the New Madrid Seismic Zone using local earthquake tomography. *Journal of Geophysical Research: Solid Earth*, **119**(1), 409–424. Wiley Online Library.
- Boore, D. M., 2003. Phase derivatives and simulation of strong ground motions. *Bulletin of the Seismological Society of America*, **93**(3), 1132–1143. U.S. Geological Survey, 345 Middlefield Rd., Menlo Park, CA 94025, United States: Seismological Society of America. DOI: 10.1785/0120020196
- Bouchon, M., 1982. The complete synthesis of seismic crustal phases at regional distances. *Journal of Geophysical Research: Solid Earth*, **87**(B3), 1735–1741. Wiley Online Library.
- Bowden, D. C., and Tsai, V. C., 2017. Earthquake ground motion amplification for surface waves. *Geophysical Research Letters*, **44**(1), 121–127. DOI: 10.1002/2016GL071885
- Carpenter, N. S., Wang, Z., Rong, M., Woolery, E. W., Hamburger, M. W., and Pavlis, G. L., 2016. Estimating Site Effect in the Central US Using Horizontal-to-Vertical Spectral Ratios from Broadband Recordings of Earthquake and Blast

Shear Waves and Ambient Noise. *AGU Fall Meeting Abstracts*.

- Carpenter, N. S., Wang, Z., Woolery, E. W., and Rong, M., 2018. Estimating Site Response with Recordings from Deep Boreholes and HVSr: Examples from the Mississippi Embayment of the Central United States. *Bulletin of the Seismological Society of America*, **108**(3A), 1199–1209. Retrieved from <http://dx.doi.org/10.1785/0120170156>
- Chiu, D.-M., and Sudama, R., 1992, March 31. Apparatus and method for realtime monitoring of network sessions in a local area network. Google Patents.
- Chun, K. Y., West, G. F., Kokoski, R. J., and Samson, C., 1987. A Novel Technique for Measuring Lg Attenuation - Results From Eastern Canada Between 1 to 10 Hz. *Bulletin of the Seismological Society of America*, **77**(2), 398–419.
- Crotwell, H. P., Owens, T. J., and Ritsema, J., 1999. The TauP Toolkit: Flexible seismic travel-time and ray-path utilities. *Seismological Research Letters*, **70**(2), 154–160. Seismological Society of America.
- Csontos, R., and Van Arsdale, R., 2008. New Madrid seismic zone fault geometry. *Geosphere*, **4**(5), 802–813. Geological Society of America.
- David von Seggern, 2010. Exploring Reflection and Transmission Coefficients in Elastic Media, (December), 1–11.
- Ducellier, A., Kawase, H., and Matsushima, S., 2013. Validation of a new velocity structure inversion method based on horizontal-to-vertical (H/V) spectral ratios of earthquake motions in the Tohoku Area, Japan. *Bulletin of the Seismological Society of America*, **103**(2 A), 958–970. BRGM, 3 avenue Claude Guillemin, BP 36009, 45060 Orléans Cedex 2, France. DOI: 10.1785/0120120214

- Dunn, M., Horton, S., DeShon, H., and Powell, C., 2010. High-resolution earthquake relocation in the New Madrid seismic zone. *Seismological Research Letters*, **81**(2), 406–413. Seismological Society of America.
- Fehr, M., Kremers, S., and Fritschen, R., 2019. Characterisation of seismic site effects influenced by near-surface structures using 3D waveform modelling. *Journal of Seismology*.
- Frankel, A., and Wennerberg, L., 1987. Energy-flux model of seismic coda: separation of scattering and intrinsic attenuation. *Bulletin of the Seismological Society of America*, **77**(4), 1223–1251. The Seismological Society of America.
- Furumura, T., and Kennett, B. L. N., 1998. On the nature of regional seismic phases ϕ III. The influence of crustal heterogeneity on the wave field for subduction earthquakes: the 1985 Michoacan and 1995 Copala, Guerrero, Mexico earthquakes, 1060–1084.
- Gallegos, A., Ranasinghe, N., Ni, J., and Sandvol, E., 2014. Lg attenuation in the central and eastern United States as revealed by the EarthScope Transportable Array. *Earth and Planetary Science Letters*, **402**(C), 187–196. Elsevier B.V. DOI: 10.1016/j.epsl.2014.01.049
- Hough, S. E., and Page, M., 2011. Toward a consistent model for strain accrual and release for the New Madrid Seismic Zone, central United States. *Journal of Geophysical Research: Solid Earth*, **116**(3), 1–17. DOI: 10.1029/2010JB007783
- Kawase, H., and Aki, K., 1989. Economical seismogram synthesis using causality with FFT. *Bulletin - Seismological Society of America*, **79**(4), 1294–1299.
- Ohsani Research Inst., Shimizu Corporation, 222 Uchisaiwai-cho, Chiyoda-ku,

- Tokyo 100, Japan, Japan. Retrieved from
<https://www.scopus.com/inward/record.uri?eid=2-s2.0-0024924956&partnerID=40&md5=a85c8d197aebb88455c615f8fa4773b8>
- Kawase, H., Nagashima, F., Matsushima, S., and Sánchez-Sesma, F. J., 2014. Application of Horizontal-To- Vertical (H/V) Spectral Ratios for Both Microtremors and Earthquake Motions Based on the Diffuse Field Theory. DOI: 10.4231/D3FT8DK3H
- Kawase, H., Nagashima, F., Nakano, K., and Mori, Y., 2018. Direct evaluation of S-wave amplification factors from microtremor H/V ratios: Double empirical corrections to “Nakamura” method. *Soil Dynamics and Earthquake Engineering*. DPRI, Kyoto University, Gokasho, Uji, Japan: Elsevier Ltd. DOI: 10.1016/j.soildyn.2018.01.049
- Kawase, H., Sánchez-Sesma, F. J., and Matsushima, S., 2011. The optimal use of horizontal-to-vertical spectral ratios of earthquake motions for velocity inversions based on diffuse-field theory for plane waves. *Bulletin of the Seismological Society of America*, **101**(5), 2001–2014. DOI: 10.1785/0120100263
- Kennett, B. L. N., and Furumura, T., 2001. Regional phases in continental and oceanic environments. *Geophysical Journal International*, **146**(2), 562–568. Blackwell Publishing Ltd Oxford, UK.
- Kham, M., Semblat, J.-F., Bard, P.-Y., and Dangla, P., 2006. Seismic site–city interaction: main governing phenomena through simplified numerical models. *Bulletin of the Seismological Society of America*, **96**(5), 1934–1951.

Seismological Society of America.

Knopoff, L., Schwab, F., and Kauselt, E., 1973. Interpretation of Lg. *Geophysical*

Journal of the Royal Astronomical Society, **33**(4), 389–404. DOI:

10.1111/j.1365-246X.1973.tb02375.x

KOBAYASHI, H., and NAGAHASHI, S., 1976. Amplification characteristics of the ground and spectral characteristics of earthquake motions on the seismic bedrock inferred from spectral characteristics of earthquake motions observed on the ground surface. *Transactions of the Architectural Institute of Japan*, **240**, 79–92. Architectural Institute of Japan.

Komatitsch, D., Liu, Q., Tromp, J., Süß, P., Stidham, C., and Shaw, J. H., 2004.

Simulations of ground motion in the Los Angeles basin based upon the spectral-element method. *Bulletin of the Seismological Society of America*, **94**(1), 187–206. DOI: 10.1785/0120030077

Komatitsch, D., Ritsema, J., and Tromp, J., 2002. The Spectral-Element Method, *Geophysical Research Letters*, **29**(July), 1737–1742.

Komatitsch, D., and Tromp, J., 1999. Introduction to the spectral element method for three-dimensional seismic wave propagation. *Geophys. J. Int.*, **139**, 809–822.

DOI: 10.1046/j.1365-246x.1999.00967.x

Langston, C. A., 2003. Local earthquake wave propagation through Mississippi embayment sediments, part I: Body-wave phases and local site responses.

Bulletin Of the Seismological Society Of America, **93**(6), 2664–2684. DOI: Doi

10.1785/0120030046

Lee, C., Wei, X., Kysar, J. W., and Hone, J., 2008. Measurement of the elastic

- properties and intrinsic strength of monolayer graphene. *science*, **321**(5887), 385–388. American Association for the Advancement of Science.
- Luo, Y., Zhu, H., Nissen-Meyer, T., Morency, C., and Tromp, J., 2009. Seismic modeling and imaging based upon spectral-element and adjoint methods. *The Leading Edge*, **28**(5), 568–574. Society of Exploration Geophysicists.
- Makra, K., and Chávez-García, F. J., 2016. Site effects in 3D basins using 1D and 2D models: an evaluation of the differences based on simulations of the seismic response of Euroseistest. *Bulletin of Earthquake Engineering*, **14**(4), 1177–1194. DOI: 10.1007/s10518-015-9862-7
- Merrill, B. M. D., Slucher, E. R., Roberts-ashby, T. L., Warwick, P. D., Blondes, M. S., Freeman, P. A., Cahan, S. M., et al., 2012. Geologic Framework for the National Assessment of Carbon Dioxide Storage Resources — Permian and Palo Duro Basins and Bend Arch-Fort Worth Basin Geologic Framework for the National Assessment of Carbon Dioxide Storage Resources.
- Motazedian, D., Hunter, J. A., Pugin, A., and Crow, H., 2011. Development of a V_s (NEHRP) map for the city of Ottawa, Ontario, Canada. *Canadian Geotechnical Journal*, **48**(3), 458–472. DOI: 10.1139/T10-081
- Myers, S., Ballard, S., Rowe, C., Wagoner, G., Antolik, M., Phillips, S., Ramirez, A., et al., 2007. Tomography and methods of travel-time calculation for regional seismic location. *Lawrence Livermore Report*, (2004). Retrieved from <papers://8a7341e4-9daa-4c0d-bcf2-2d9b813974af/Paper/p10395>
- Narayan, J. P., and Kumar, V., 2012. Numerical study of effects of synclinal basement topography on ground motion characteristics. *Proceedings of the 15th*

World Conference on Earthquake Engineering (15WCEE), Lisbon, Portugal, (Paper No. 3144), September (Vol. 2428).

- Nazemi, N., Pezeshk, S., and Sedaghati, F., 2017. Attenuation of Lg waves in the New Madrid seismic zone of the central United States using the coda normalization method. *Tectonophysics*, **712–713**, 623–633. Elsevier B.V. DOI: 10.1016/j.tecto.2017.06.026
- Nyamwandha, C. A., and Powell, C. A., 2016. Seismic anisotropy beneath the Mississippi Embayment and the New Madrid Seismic Zone: A study of shear wave splitting. *Journal of Geophysical Research: Solid Earth*, **121**(11), 8239–8253. DOI: 10.1002/2015JB012729
- Ohsaki, Y., 1979. On the significance of phase content in earthquake ground motions. *Earthquake Engineering & Structural Dynamics*, **7**(5), 427–439. Wiley Online Library.
- Oliver, J., and Ewing, M., 1958. Normal modes of continental surface waves. *Bulletin of the Seismological Society of America*, **48**(1), 33–49. The Seismological Society of America.
- Pabian, R. K., and Diffendal Jr, R. F., 1991. Late Paleozoic Cyclic Sedimentation in Southeastern Nebraska: A Field Guide.
- Pabian, R. K., Diffendal, R., and Ii, D. R. B., 2003. Southeast Nebraska Geology : Field Trip 3.
- Pavel, F., Vacareanu, R., Calotescu, I., Sandulescu, A.-M., Arion, C., and Neagu, C., 2017. Impact of spatial correlation of ground motions on seismic damage for residential buildings in Bucharest, Romania. *Natural Hazards*, **87**(2), 1167–

1187. Springer.

- Pezeshk, S., Sedaghati, F., and Nazemi, N., 2018. Near-source attenuation of high-frequency body waves beneath the New Madrid Seismic Zone. *Journal of Seismology*, **22**(2), 455–470. Journal of Seismology. DOI: 10.1007/s10950-017-9717-6
- Salinas, V., Luzón, F., García-Jerez, A., Sánchez-Sesma, F. J., Kawase, H., Matsushima, S., Suarez, M., et al., 2014. Using diffuse field theory to interpret the H/V spectral ratio from earthquake records in Cibeles seismic station, Mexico City. *Bulletin of the Seismological Society of America*, **104**(2), 995–1001. Dpt. Ingeniería del Terreno Cartográfica y Geofísica, Universitat Politècnica de Catalunya, Edifici D2 Campus Nord c/ Jordi Girona, 1-3, 08034 Barcelona, Spain: Seismological Society of America. DOI: 10.1785/0120130202
- Satoh, T., Kawase, H., and Sato, T., 1995. Evaluation of local site effects and their removal from borehole records observed in the Sendai region, Japan. *Bulletin - Seismological Society of America*, **85**(6), 1770–1789. Retrieved from <https://www.scopus.com/inward/record.uri?eid=2-s2.0-0029529846&partnerID=40&md5=0cdbea615fa71676ef155056327c4139>
- Savage, A. F., 2010, July 6. Software development tool using a structured format to generate software code. Google Patents.
- Sedaghati, F., Pezeshk, S., and Nazemi, N., 2018. Site amplification within the Mississippi embayment of the central United States: Investigation of possible differences among various phases of seismic waves and presence of basin waves. *Soil Dynamics and Earthquake Engineering*, **113**, 534–544. DOI:

10.1016/j.soildyn.2018.04.017

Stacey, R., 1988. Improved transparent boundary formulations for the elastic-wave equation. *Bulletin of the Seismological Society of America*, **78**(6), 2089–2097.

The Seismological Society of America.

Steidl, J. H., Tumarkin, A. G., and Archuleta, A. J., 1996. What is a reference site? *Bulletin of the Seismological Society of America*, **86**(6), 1733–1748. DOI:

10.1130/SPE184-p149

Storchak, D. A., Schweitzer, J., and Bormann, P., 2003. The IASPEI standard seismic phase list. *Seismological Research Letters*, **74**(6), 761–772. Seismological

Society of America.

Tromp, J., Komattisch, D., and Liu, Q., 2008. Spectral-element and adjoint methods in seismology. *Communications in Computational Physics*, **3**(1), 1–32.

Tsai, Y.-B., and Aki, K., 1969. Simultaneous determination of the seismic moment and attenuation of seismic surface waves. *Bulletin of the Seismological Society of America*, **59**(1), 275–287. The Seismological Society of America.

Wheeler, R. L., 1997. Boundary separating the seismically active Reelfoot rift from the sparsely seismic Rough Creek graben, Kentucky and Illinois. *Seismological Research Letters*, **68**(4), 586–598. Seismological Society of America.

Whiteley, J. S., Chambers, J. E., Uhlemann, S., Wilkinson, P. B., Kendall J. M., 2018.

Reviews of Geophysics Geophysical Monitoring of Moisture-Induced

Landslides : *Reviews of Geophysics REVIEW*, **57**, 1–40. DOI:

10.1029/2018RG000603

Woolery, E. W., Wang, Z., Carpenter, N. S., Street, R., and Brengman, C., 2016. The

- Central United States Seismic Observatory : Site Characterization ,
Instrumentation , and Recordings, (September 1985). DOI: 10.1785/0220150169
- Yang, J., 2001. Saturation effects on horizontal and vertical motions in a layered soil
± bedrock system due to inclined SV waves, **21**, 527–536.
- Yang, J., and Sato, T., 2000. Interpretation of seismic vertical amplification observed
at an array site. *Bulletin of the Seismological Society of America*, **90**(2), 275–
285. DOI: 10.1785/0119990068
- Yilar, E., Baise, L. G., and Ebel, J. E., 2017. Using H/V measurements to determine
depth to bedrock and Vs30 in Boston, Massachusetts. *Engineering Geology*, **217**,
12–22. DOI: 10.1016/j.enggeo.2016.12.002
- Zhang, Y., Chen, G., Zheng, L., and Li, Y., 2013. Numerical analysis of the largest
landslide induced by the Wenchuan earthquake, May 12, 2008 using DDA.
Earthquake-Induced Landslides (pp. 617–626). Springer.

6 Chapter 6: Conclusions:

This dissertation has improved the understanding of the seismological characteristics of the lithosphere beneath the Central and Eastern United States region. Two projects conducted in this region explore the regional site effect and uppermost mantle seismic structure and their implication in predicting the uppermost mantle temperature. I find that the amplification of regional seismic waves across CEUS is mainly function of topography, shallow shear wave velocity, sediment thickness. These factors are strongly frequency and ground motion type (vertical or horizontal) dependent . Increasing the geological complexity of region, increasing the difference between HVSR of ambient noise and the HVSR of earthquakes. In order to account for regional seismic phases which are affected by the deep seismic velocity structure, we recommend the weighted-average HVSR algorithm, which will weight each HVSR based on the distance and back-azimuth before calculating the average of these HVSRs.

The new results of the seismic structure of the uppermost mantle beneath CEUS show neither evidence of existing melt in this region, nor a clear correlation with the crustal province boundary. On the other hand, the results agree with previously reported seismic anomalies, such as negative Pn and Sn velocity anomalies beneath New England (e.g., Porritt et al., 2014; Schmandt and Lin, 2014), and Illinois basin; positive anomalies beneath northern mid-continent, and NMSZ. The temperature models, generated using the grid search algorithm, are different than previously reported temperature models in two distinct ways: (1) this study includes the observed

Qsn in the inversion to correct for anelasticity; (2) 8 compositional models, including two end-members representing the enriched and depleted mantle, were applied in the grid search algorithm. I found that the upper most mantle most likely was affected by metasomatism especially in the cratonic region in northern mid-continent close to Mid Continent Rift, which could have resulted in the formation of seismically slow minerals such as amphibole, phlogopite and carbonate. Results of the Temperature-Composition models suggest that seismic structure (velocity and attenuation) is insufficient to constrain detailed composition model of the uppermost mantle.

Future research can build upon these results by expanding the different algorithms. For example, the grid search inversion of mantle temperature may benefit from including another seismic parameter in the inversion, such as the density of the upper most mantle. Additionally, the regional site response project can be expanded to explore effects of topography on the seismic response in terms of the slope and the geometric shape.

Vita

Rayan Yassminh was born in Damascus, Syria. She received her BS in Geophysics from Damascus University, Syria in 2000. She worked in the Earthquake Research Center from 2001-2010. Her work focused on analyzing seismic data, deploying and maintenance seismic stations. She gained her master's degree from University of Missouri-Columbia in 2013. Her MS research focused on seismotectonic study in northern Arabian plate. She began her doctoral studies at the Geological Sciences Department, University of Missouri at spring 2014. Her research interests are the lithospheric seismic structure and regional seismic hazard.